Representations and Transformations of Odor Information in the Mouse Olfactory System

Dara L. Sosulski

Submitted in partial fulfillment of the
requirements for the degree
of Doctor of Philosophy
in the Graduate School of Arts and Sciences

Columbia University

2011

ABSTRACT

Representations and Transformations of Odor Information in the Mouse Olfactory System

Dara L. Sosulski

For a wide variety of organisms on the planet, the sense of smell is of critical importance for survival. The mouse olfactory system mediates both learned and innate odor-driven behaviors, including activities as diverse as the localization of food sources, the avoidance of predators, and the selection of mates. How a chemical stimulus in the environment ultimately leads to the generation of an appropriate behavioral response, however, remains poorly understood. All of these behaviors begin with the binding of an odorant in the external environment to receptors on sensory neurons in the olfactory epithelium. These sensory neurons transmit this odor information to neurons in the olfactory bulb via spatially stereotyped axonal projections, and a subset of these bulbar neurons, mitral and tufted cells, in turn transmit this information to a number of higher brain regions implicated in both learned and innate odor-driven behaviors, including the piriform cortex and amygdala.

Previous work has revealed that odorants drive activity in unique, sparse ensembles of neurons distributed across the piriform cortex without apparent spatial preference. The patterns of neural activity observed, however, do not reveal whether mitral and tufted cell projections from a given glomerulus to piriform are segregated or distributed, or whether they are random or determined. Distinguishing between these possibilities is important for understanding the function of piriform cortex: a random

representation of odor identity in the piriform could accommodate learned olfactory behaviors, but cannot specify innate odor-driven responses. In addition, behavioral studies in which the function of the amygdala has been compromised have found that innate odor-driven behaviors are disrupted by these manipulations while learned odor-driven behaviors are left intact, strongly suggesting a role for the amygdala in innate olfactory responses. How odor information is represented in the amygdala, as well as the amygdala's exact role in the generation of olfactory responses, however, remain poorly understood.

We therefore developed a strategy to trace the projections from identified glomeruli in the olfactory bulb to these higher olfactory centers. Electroporation of TMR dextran into single glomeruli has permitted us to define the neural circuits that convey olfactory information from specific glomeruli in the olfactory bulb to the piriform cortex and amygdala. We find that mitral and tufted cells from every glomerulus elaborate similar axonal arbors in the piriform. These projections densely fan out across the cortical surface in a homogeneous manner, and quantitative analyses fail to identify features that distinguish the projection patterns from different glomeruli. In contrast, the cortical amygdala receives spatially stereotyped projections from individual glomeruli. The stereotyped projections from each glomerulus target a subregion of the posterolateral cortical nucleus, but may overlap extensively with projections from other glomeruli.

The apparently random pattern of projections to the piriform and the determined pattern of projections to the amygdala are likely to provide the anatomic substrates for distinct odor-driven behaviors mediated by these two brain regions. The dispersed mitral and tufted cell projections to the piriform provide the basis for the generation of

previously observed patterns of neural activity and suggest a role for the piriform cortex in learned olfactory behaviors, while the pattern of mitral and tufted cell projections to the posterolateral amygdala implicate this structure in the generation of innate odor-driven behaviors.

We have also developed high-throughput methods for imaging odor-evoked activity in targeted populations of neurons in multiple areas of the olfactory system to investigate how odor information is represented and transformed by the mouse brain. We have used a modified rabies virus that drives expression of GCaMP3, a calcium-sensitive indicator of neural activity, to image odor-evoked responses from mitral and tufted cells, as well as a modified adenoassociated virus that drives expression of GCaMP3 to image odor-evoked responses from neurons in piriform cortex.

These imaging methods have permitted us to examine odor-evoked responses in a transgenic mouse where 95% of sensory neurons express a single kind of olfactory receptor (M71). In these mice, there is a 1,000-fold increase in sensory neurons expressing the M71 receptor ligand acetophenone, and a 20-fold reduction in neurons expressing olfactory receptors from the endogenous repertoire. These M71 transgenic mice provide a useful tool for examining the role that the normally stereotyped pattern of sensory neuron input to the bulb plays in olfactory processing, as well as how odor information is transformed as is moves from the sensory periphery to the cortex.

In control mice, odors evoke activity in unique ensembles of spatially distributed, narrowly tuned mitral and tufted cells, and the number of cells responding to odor increases linearly with stimulus concentration. Surprisingly, despite the fact that there is a significant decrease in sensory neuron activity in response to odors other than

acetophenone in M71 transgenics, a wide variety of odorants are able to evoke mitral and tufted cell activity in these mice. Furthermore, the number of cells responding to these odors as well as the magnitude of these odor-evoked responses are higher in M71 transgenics compared to controls. However, despite a massive increase in acetophenone-evoked sensory neuron input to the bulb in M71 transgenics, mitral and tufted cell responses to acetophenone are similar in M71 transgenics and controls. Our results provide evidence for excitatory mechanisms that amplify weak sensory neuron input as well as inhibitory mechanisms that suppress strong, pervasive odor-evoked input, suggesting that a major role of the olfactory bulb is to aid in the comprehensive detection and refinement of olfactory signals from the environment.

Despite the fact that the representation of odor in the olfactory bulb of M71 transgenic mice differs from that observed in controls, we find the representations of odor in the piriform cortex of M71 transgenic mice and controls is quantitatively indistinguishable. Our results suggest that circuits intrinsic to the piriform significantly transform the representation of odor information as it moves from the olfactory bulb to the piriform cortex. Moreover, in comparison to the olfactory bulb, the piriform encodes odor in a more sparse, distributed manner within a much narrower dynamic range. The nature of the representation of odor we observe in piriform cortex further supports a role for this area in mediating odor discrimination and associative odor-driven behaviors.

The work described in this thesis has provided insight into the way odor is represented in several areas of the mouse olfactory system, clues about how odor information is transformed as it passes through the brain, and the role that different areas of the olfactory system play in odor-driven perception and behavior. In the future, the

novel techniques and methods described in this thesis can be applied to the study of many different areas of the mammalian brain, giving our work the potential to have a significant impact on our understanding of how patterns of neural activity may ultimately underlie the generation of perceptions, emotions, and behaviors.

TABLE OF CONTENTS

LIST OF FIGURES

CHAPTER 3: USING A MOUSE WITH A "MONOCLONAL" NOSE TO EXAMINE THE REPRESENTATIONS AND TRANSFORMATIONS OF ODOR INFORMATION IN THE MOUSE OLFACTORY SYSTEM

CHAPTER 4: SUMMARY AND CONCLUSIONS

APPENDIX A: CHAPTER 2 METHODS

ACKNOWLEDGEMENTS

Unfair as it may be, some people are just born lucky. I'm one of those people. The experiences I've had over the past six years are a fine example of this: after getting a degree in political theory and enjoying myself far too much in college, I somehow managed to get into Columbia's Neurobiology and Behavior PhD program, then got to work with some of the best scientists in the world, once again had far too much fun, and wound up having more success than I could ever have reasonably expected. Shame on me.

First and foremost, I want to thank my parents, who have been endlessly loving and supportive over the past three decades, and my four younger siblings, who have been endlessly annoying over the past three decades (just kidding).

I'm forever grateful for the advice I received from the people at Harvard who assured me that life doesn't end at 21, and that it wasn't totally crazy to switch fields from political science to neuroscience. Drs. Robert Kirshner, Melissa Franklin, and Bert Vaux, as well as my friends Laura Berger and Yanni Poulakos—thank you.

Thanks to Zachary Mainen, for giving me a chance to work in his laboratory at Cold Spring Harbor from 2003-2005. You were a great mentor who somehow managed to whip me into shape as an experimental neuroscientist, and you gave me perhaps the best piece of advice I've ever received: "Learn how to program in Matlab."

My deepest thanks to the outstanding collaborators I've had over the past few years, especially Sandeep Robert Datta and Alexander Fleischmann. You've both meant a tremendous amount to me as colleagues, mentors, examples of how science should be done, and finally, as friends, and I'm grateful for the time we got to spend together. We'll always have Paris. And Boston, Massachusetts.

Thanks to Columbia's doctoral program in Neurobiology and Behavior, for not only admitting me but also providing a great environment in which to work and live, as well as the thousands of dollars I used to take seminar speakers out to really nice restaurants. And special shout-outs to Alla Kerzner, John Koester, and Carol Mason—you made everything a lot easier, and a lot more enjoyable.

Thanks to the National Institutes of Health, the Howard Hughes Medical Institute, the Foundation for the National Institutes of Health through the Grand Challenges in Global Health Initative, and the European Molecular Biology Organization for their generous and ongoing financial support.

Thanks to my classmates and program-mates at Columbia for an enjoyable few years in New York City; that was a lot of beer we just drank. Also, thanks to all of the people that I've shared benches, bays, rooms, and microscopes with, and who have become good friends over the years—Ed Schwartz, Kevin Franks, Kim Simpson, Sean Luo, Vanessa Ruta, Marco Russo, Tim Machado, Adam Hantman, Felicity Gore, Stanley Aladi, and Yonghua Sun, I'll miss you.

A big thank you to Phyllis Kisloff, Miriam Gutierrez, Adriana Nemes, Monica Mendelsohn, Konrad Konrdratowicz, and Barbara Han—you made it much, much easier to deal with the administrative details of lab life; my eternal thanks.

Thanks to Drs. Eric Kandel and Daniel Salzman, for serving on my committees; your time, effort, and scientific input have been very much appreciated.

Thanks to Dr. Leslie Vosshall, for providing scientific inspiration as well as an external member for my thesis committee; you deserve some kind of lifetime achievement award for agreeing to do this for so many of Richard's graduate students.

A tremendous thank you to Tom Jessell, who has provided advice and recommendations many times, as well as a great lab with lots of wonderful people just across the hall.

And finally, to Richard; it's not an exaggeration to say that I have no idea where I would be today without your support, guidance, and care, but I'm pretty sure it would involve far fewer Nature papers, bottles of Veuve Clicquot, and French fries. The years I've spent in the Axel lab have been the most enjoyable of my life—they've been challenging, rewarding, frustrating, enlightening, exhausting, and absolutely thrilling, and after five years of it, I still love going to your lab every day. It has been an honor and a pleasure to work for you, and I'll miss you terribly. Thank you for everything.

DEDICATION

To my mother and father; for their unending love and support.

CHAPTER 1

INTRODUCTION

As long as human beings have existed, we have wondered about the origins of our thoughts, perceptions, memories, and behaviors (Kandel et al., 2000). For thousands of years the mind was thought to occupy the realm of the spiritual, a divine and immortal thing impossible to dissect using empirical means. Those beliefs began to change during the Scientific Revolution of the 16th and 17th centuries, when man slowly came to be viewed as a material thing whose physiology could be explained using the laws of physics and mathematics (Huyser et al., 2007). A few hundred years later this approach was finally brought to bear on the problem of the mind, as the first modern neuroscientists began to use anatomical, physiological and behavioral techniques to illuminate the biological basis of how the brain works.

Over the past hundred years, tremendous advances in our understanding of the development and function of the nervous system have come not from the study of humans, but a diverse array of model organisms including worms, sea slugs, fruit flies, fish, birds, mice, rats, cats and monkeys, to name just a few. Even the simplest of these organisms can exhibit complex behavioral responses; the nematode *C. elegans*, a blind and deaf worm with only 302 neurons, displays a natural attraction to food sources and local environments it finds optimally hospitable, and can even learn to associate particular locations with rewarding stimuli (Hobert, 2003; de Bono and Maricq, 2005).

The mouse *Mus musculus* has proven to be a particularly useful model organism for those interested in how the brain works, thanks to its high neurobiological homology to humans, our ability to apply a wide range of molecular, physiological and imaging techniques to the study of its nervous system, and the diverse multitude of behaviors it exhibits (Costantini and Lacy, 1981; Gordon and Ruddle, 1981; Gossen et al., 1995; Bockamp et al., 2002; Strand et al., 2007; Dombeck et al., 2007; Fox, 2007; Luo et al., 2008; Harvey et al., 2009). Many of the most robust and sophisticated of these behaviors are mediated by the sense of smell, including both learned behaviors, such as remembering the location of a particularly rich food source, as well as innate behaviors like the avoidance of predators and the selection of mates (Abraham et al., 2004; Brennan and Kendrick, 2006; Mainen, 2006; Kobayakawa et al., 2007). The array of tools available for studying the mouse brain, in combination with the variety of learned and innate odor-driven behaviors it displays, make the mouse olfactory system a potentially transformative model for understanding the biological basis of sensory processing, perception, memory, and behavior.

The Anatomy and Function of the Early Mouse Olfactory System

The mammalian olfactory system affords animals the ability to recognize and discriminate a very large number of odors (Buck and Axel, 1991). Although the anatomy and physiology of the olfactory system had been under investigation for nearly 200 years (Fig. 1), at the end of the 21st century it remained unknown how the universe of odorants in the world around us was detected by the olfactory system. This question was finally

answered by the discovery of an extremely large multigene family encoding 7-transmembrane receptors that are expressed selectively at the olfactory sensory periphery (Buck and Axel, 1991). These receptors, which are expressed on the dendrites of primary sensory neurons located in the olfactory epithelium in the nasal cavity, directly bind to odorant molecules in the environment (Saito et al., 1998; DeMaria and Ngai, 2010). These olfactory receptors therefore enable olfactory sensory neurons to convert a chemical signal in the environment into an electrical signal that can be propagated to the rest of the brain.

Nearly 1,000 genes encoding olfactory receptor proteins have been presently identified in the olfactory system of the mouse (Dulac and Axel, 1995; Liberles and Buck, 2006; Rivière et al., 2009). The quantity and diversity of these olfactory receptor proteins underlies the mouse's ability to detect and recognize a vast number of chemical stimuli (Zhang and Firestein, 2002). In addition, olfactory receptors that bind to odors with important social, physiological and behavioral meaning to rodents have recently been identified, including receptors tuned to compounds enriched in the urine of male mice or stressed mice and ligands related to disease and inflammation (Liberles and Buck, 2006; Rivière et al., 2009). Each olfactory sensory neuron chooses to express only one of these ~1,000 genes, and once selected, these receptors are thought to elicit a feedback signal that stabilizes this choice, thus ensuring that only a single kind of olfactory receptor is expressed during the lifetime of a neuron (Chess et al., 1994; Young and Trask, 2002; Zhang and Firestein, 2002; Serizawa et al., 2003; Shykind et al., 2004; Lewcock and Reed, 2004; Nguyen et al., 2007). Each olfactory receptor can bind to several odorants, and in turn, odorants can bind to several kinds of olfactory receptors

(Malnic et al., 1999). As a consequence, olfactory sensory neurons can have fairly broad stimulus tuning, often responding to a structurally and perceptually diverse set of odors (Araneda et al., 2000; Tan et al., 2010).

The olfactory epithelium is divided into four expression zones along its dorsal/ventral axis, and the expression of an olfactory receptor is limited to the sensory neurons in a single one of these zones (Ressler et al., 1993; Vassar et al., 1993; Fig. 2). Within these zones, however, olfactory sensory neurons expressing different receptors are intermingled in a stochastic manner (Ressler et al., 1993). This anatomic organization leads to a spatially disperse, combinatorial representation of odor information at the level of the olfactory epithelium (Malnic et al., 1999). A given odor will evoke activity in an ensemble of neurons that is spatially distributed across the sensory sheet, and different odors will evoke activity in distinct but overlapping combinations of olfactory sensory neurons.

The diverse collection of olfactory receptors expressed by the mouse therefore provides a biological basis for the detection of ligands that have the ability to drive a wide range of innate and learned odor-driven responses. However, even monomolecular odorants activate multiple olfactory receptor types (Malnic et al., 1999; Saito et al., 2009), and information about a given odor in the environment is therefore encoded in a combinatorial fashion. The combinatorial nature of sensory representations at the level of the epithelium greatly expands the capacity of the mammalian olfactory system to represent information about odors. While a coding strategy in which each receptor is specifically tuned to respond to a single kind of odorant would provide a straightforward way to link a given odor with a specific percept or behavioral response (e.g. a “labeled-

line" code), it would also limit the number of odors an animal could detect to the number of olfactory receptors in its repertoire. Rather, a combinatorial code allows for the detection and perception of an exponentially greater number of stimuli: even if each odorant were encoded by only three olfactory receptors, the number of odorants that could theoretically be discriminated would be nearly one billion (Malnic et al., 1999).

Olfactory sensory neurons project their axons out of the nasal cavity to the olfactory bulb, an outgrowth of the forebrain that serves as the first relay station for odor information in the brain (Shepherd, 1994). These axons bundle together as they make their way to the olfactory bulb, and the terminations of all of the sensory neurons that express the same receptor target the same two spatial points, called glomeruli, at the bulbar surface (Vassar et al., 1993; Ressler et al., 1994; Mombaerts et al., 1996; Fig. 3). This pattern of sensory neuron projections to the olfactory bulb is genetically hardwired: the axons of the olfactory sensory neurons expressing a given receptor target the same two glomeruli in the same spatial location in every animal, thereby generating a topographic map of sensory neuron input to the bulb (Mori and Sakano, 2011).

This hardwired, spatially organized pattern of sensory neuron projections shapes the way odor information is represented in the olfactory bulb. Functional imaging studies have demonstrated that each odor drives activity in a unique combination of glomeruli (Meister and Boenhoeffer, 2001; Wachowiak and Cohen, 2001; Bozza et al., 2004). At concentrations of odor encountered in the natural environment, this activity is sparse, with fewer than 5% of glomeruli responding (Lin et al., 2006). Furthermore, these topographic patterns of odor-evoked activity are stereotyped, with minimal variation in the location and number of responsive glomeruli across animals (Belluscio and Katz,

2001; Bozza et al., 2004; Fig. 4). Thus, the distributed, overlapping representation of odor apparent in the sensory epithelium is transformed into a sparse, convergent topographic representation of odor at the surface of the olfactory bulb: one can determine which odor an animal has encountered simply by looking at the pattern of glomeruli that are active.

For many years, it was believed that the spatially stereotyped organization of olfactory receptor neuron projections provided the anatomical basis for a chemotopic map of odor information in the bulb (Mori et al., 1999; Mori et al., 2006; Johnson and Leon, 2007). Previous studies using local increases in blood flow as an indicator of neural activity suggested that glomeruli with similar odor tuning were located near one another, and that odors belonging to different chemical families (e.g. thiols, aldehydes) activated glomeruli at different locations in the bulb (Uchida et al., 2000; Meister and Bonhoeffer, 2001; Takahashi et al., 2004). This chemotopic organization was thought to enable the sharpening of stimulus tuning and odor perception via short-range inhibitory interactions between neurons responding to similar odorants (Meister and Bonhoeffer, 2001).

Recently, however, work employing large stimulus sets and indicators of neural activity that are expressed exclusively in sensory neurons have found little evidence of chemotopic organization in the mouse olfactory bulb on scales smaller than ~1 mm (Soucy et al., 2009). If this topographic glomerular map does not reflect a meaningful organization of odor information for local sensory processing, then what role does it play in olfactory perception and behavior? Interestingly, a recent study has proposed an alternate role for the spatial organization of sensory neuron input to the bulb. Behavioral experiments using mice with genetic ablations of different portions of the glomerular map

have demonstrated that glomeruli located in the dorsolateral region of the olfactory bulb are exclusively responsible for mediating innate behavioral responses to a predator odor (TMT), while more ventrally situated glomeruli were able to mediate learned behavioral associations with this odor, but not the innate response (Kobayakawa et al., 2007).

These results suggest a role for this hardwired, stereotyped glomerular organization not in the generation of a systematically varying chemotopic map of odor information, but rather, in the establishment of parallel circuits for mediating innate and learned olfactory behaviors (Mainen, 2007). Moreover, these observations suggest that the mouse olfactory system may exploit the reliability and simplicity of signal processing in a labeled-line coding scheme, while also enjoying the flexibility and expanded computational capacity provided by a combinatorial coding regime. For instance, while the knowledge that a given receptor was activated may not provide enough information to determine which odor is present in the external environment, the location of the axonal terminations of the sensory neurons expressing that receptor may reveal whether that receptor mediates innate odor-driven aversion. It is likely that the sensory neurons projecting to different parts of the olfactory bulb will activate divergent circuits downstream of the olfactory bulb that mediate hardwired, stereotyped odor-evoked behaviors or more general olfactory perception and learning, respectively.

Although much is known about how odors are represented at the level of input to the olfactory bulb, less is known about how odor information is represented and processed in its deeper layers. There are six distinctly organized laminae within the olfactory bulb, and each layer contains a unique complement of cell types and cell processes, raising the possibility that the complex, spatially organized circuitry of the

bulb engenders specific local computations and transformations of odor information (Shepherd, 1994; Fig. 5).

Most superficial is the olfactory nerve layer (ONL), containing the axons of the olfactory sensory neurons projecting to the bulb, and directly underneath the ONL lies the glomerular layer (GL) (Shepherd, 1994). In addition to serving as the substrate for the topographic map of sensory neuron input, the organization of the glomerular layer provides the anatomical framework for a number of processes thought to be important for odor perception and behavior. Olfactory sensory neurons converge onto individual glomeruli at a ratio of about 25,000:1 (Shepherd, 1994), and this massive convergence of sensory neuron input is thought to assist in the amplification of weak sensory signals at the periphery (Cleland and Linster, 1999; Maresh et al., 2008). Furthermore, glomeruli themselves are complex, heterogeneous spheres of neuropil, consisting of the axon termini of olfactory sensory neurons, the apical dendrites of the projection neurons of the olfactory bulb (mitral and tufted cells), the processes of local interneurons, and fibers from cells that provide centrifugal input to the bulb (Shepherd, 1994; Fletcher and Chen, 2011). Electrical interactions that serve to synchronize mitral cell responses to sensory neuron input take place within the confines of the glomerulus (Schoppa and Westbrook, 2002; Fadool et al., 2004). In addition, dendritic spillover of glutamate released by mitral cells that connect to the same glomerulus can enhance the excitability of these neurons (Nicoll and Jahr, 1982; Isaacson, 1999; Schoppa and Westbrook, 2001; Christie and Westbrook, 2006). These mechanisms are thought to further boost the gain of odor-evoked activity in the bulb, thereby strengthening the signal these mitral and tufted cells project to higher brain regions.

In addition to glomeruli, the GL contains a diverse class of local neurons called juxtaglomerular (JG) cells, of which there are three types: external tufted (ET) cells, which have a single dendrite that arborizes in one glomerulus, periglomerular (PG) cells, which have short dendrites that can arborize in one or multiple glomeruli, and short axon (SA) cells, which have dendrites that contact several glomeruli and long interglomerular processes that can extend over distances of hundreds of microns (Aungst et al., 2003; Kiyokage et al., 2010). Most JG cells are GABAergic, but dopaminergic JG cells have also been identified (Kosaka et al., 1998; Hayar et al., 2004; Parrish-Aungst et al., 2007; Kiyokage et al., 2010).

Sensory neuron excitation can drive activity in JG cells via both monosynaptic and polysynaptic connections, and JG cell activity has been demonstrated to influence odor-evoked activity in the olfactory bulb in several ways (Shepherd, 1994). PG cell-mediated feedback inhibition can reduce stimulus-evoked transmitter release from sensory neurons, and is able to scale with stimulus strength (Aroniadou-Anderjaska et al., 2000; McGann et al., 2005; Wachowiak et al., 2005; Fleischmann et al., 2008). In addition, JG neurons can mediate feedforward inhibition that acts across glomeruli, as well as the inhibition of mitral cell firing over both short and long distances (Aungst et al., 2003; Murphy et al., 2005; Shao et al., 2009). It has been suggested that these inhibitory microcircuits perform a number of computational roles, including sharpening the tuning of projection neuron responses (Yokoi et al., 1995), aiding in the detection of weak sensory stimuli, and providing a form of gain control that prevents a stimulus from saturating the dynamic range of postsynaptic neurons (Olsen and Wilson, 2008).

Below the glomerular layer is the external plexiform layer (EPL), containing the lateral dendrites of projection neurons, the dendrites of granule cells, and small populations of excitatory tufted cells and inhibitory interneurons (Hamilton et al., 2005). The EPL also contains axon terminals from centrifugal fibers, which provide input to the bulb from neuromodulatory centers like the noradrenergic locus coeruleus, the serotonergic raphe nucleus, and the cholinergic horizontal limb of the diagonal band of Broca (Fletcher and Chen, 2011). These centrifugal inputs have been implicated in mediating a number of effects in the olfactory bulb, including the modulation of mitral cell sensitivity, the sharpening of mitral and tufted cell tuning, and the regulation of synaptic release from olfactory sensory neurons, as well as in behaviors such as odor discrimination, sensory detection, and odor memory (Doucette et al., 2007; Shea et al., 2008; Chaudhury et al., 2009; Petzold et al., 2009). Overall, the effects of these centrifugal inputs remain largely uncharacterized, but they are well poised to mediate a flexible modulation of bulbar inputs and outputs commensurate with perceptual and behavioral demands.

Ventral to the EPL is the mitral cell layer (MCL), which contains the cell bodies of mitral and internal tufted cells, the projection neurons of the olfactory bulb (Shepherd, 1994). These mitral and tufted cells each extend an apical dendrite into a single glomerulus, where they receive input from olfactory sensory neurons, and project their axons out of the bulb to several higher brain areas, providing odor information to a number of regions including the anterior olfactory nucleus, the olfactory tubercle, the piriform cortex, the entorhinal cortex, and the amygdala (Sosulski et al., 2011).

Extracellular and intracellular recordings have demonstrated that mitral and tufted cells respond to a small set of odors that can be structurally and perceptually diverse (Imamura et al., 1992; Katoh et al., 1993; Nagayama et al., 2004; Egaña et al., 2005; Lin et al., 2005; Yokoi et al., 1995; Davison and Katz, 2007; Matsumoto et al., 2009). Recent work suggests that, at stimulus concentrations likely to be encountered in the natural environment, the tuning of these mitral and tufted cells is determined in large part by the olfactory sensory neurons from which they receive excitatory input (Tan et al., 2010). However, the odor information ultimately propagated to higher brain regions by these neurons can still be shaped by a number of local circuit mechanisms in the bulb, including feedback inhibition of sensory neuron input via periglomerular cells, intraglomerular inhibition mediated by various juxtaglomerular cells, and lateral and self-excitation via electrical coupling and dendritic glutamate spillover at the glomerulus and apical dendrite (Aroniadou-Anderjaska et al., 2000; Aungst et al., 2003; McGann et al., 2005; Wachowiak et al., 2005; Fleischmann et al., 2008). Moreover, it has been demonstrated that mitral and tufted cell activity can be strongly influenced by the physiological state of an animal, as well olfactory learning and engagement in a behavioral task (Kay and Laurent, 1999; Rinberg et al., 2006; Tsuno et al., 2008; Doucette et al., 2011).

Finally, beneath the MCL are the internal plexiform layer (IPL) and granule cell layer (GCL); while both layers contain the axonal terminations of centrifugal fibers, the IPL contains the dendritic processes of several cell types, while the GCL contains the densely packed cell bodies of inhibitory interneurons called granule cells (Shepherd, 1994). Each granule cell vertically extends a dendritic process that ramifies and

terminates in the EPL, and these processes are the site of dendrodendritic synapses between granule cells and the lateral dendrites of mitral cells that have the ability to modulate the output of mitral and tufted cells by means of a powerful feedback inhibition (Jahr and Nicoll, 1980; Yokoi et al., 1995; Isaacson and Strowbridge, 1998; Margrie et al., 2001). Granule cells are also a major target of centrifugal input to the bulb, and provide a means by which top-down inputs from the locus coeruleus, horizontal limb of the diagonal band of Broca, and piriform cortex can modulate the activity of mitral and tufted cells (Jahr and Nicoll, 1982; Kunze et al., 1992; Pressler et al., 2007; Mouret et al., 2009).

In summary, mitral and tufted cells serve as the substrate for an olfactory sensory input to the brain that can be flexibly modulated based on sensory conditions, perceptual demands, behavioral states, and previously learned associations. The existence of numerous local interneurons and circuit mechanisms that have the ability to shape odor-evoked activity as it passes through the bulb suggests that the representation of odor information in the mitral cell layer may be significantly different from that observed in the more dorsal glomerular layer. Moreover, mitral and tufted cells are the sole output neurons of the bulb, providing all olfactory sensory input to the rest of brain (Davison and Katz, 2007). Similar to the way that the organization of sensory neuron input to the bulb shapes the representation of odor information in the bulb, the nature of mitral and tufted cell projections to downstream brain regions may constrain the way odor information is represented by these areas. A determination of the pattern of mitral and tufted cell projections to these areas may provide insight into the roles these higher brain areas play in olfactory perception and behavior.

Although many computational functions have been attributed to the complex intrinsic circuitry of the olfactory bulb, few studies have directly demonstrated the functional impact these local circuits have on olfactory processing, perception and behavior. Much of the previously aforementioned work has been performed in slice recording preparations with electrical stimulation as a substitute for odor-evoked activity, making it unclear whether similar effects are observed in an *in vivo* setting. In addition, many of these studies have employed extracellular and intracellular electrophysiology techniques to examine neural activity in the bulb, which only permits the investigation of odor-evoked responses in one or a handful of randomly selected, unidentified neurons at a time. The development of high-throughput methods that allow for the readout of neuronal activity from identified cell types *in vivo* in the mouse olfactory bulb, such as the imaging of specific neural populations using calcium-sensitive indicators of neural activity (Ohki et al., 2005; Tian et al., 2009), would greatly enhance our understanding of how the bulb represents and transforms information about odor.

One of the largest impediments to definitively demonstrating the functional role of these local circuits has been the lack of molecular tools that permit the targeted manipulation of neuronal subtypes in the olfactory bulb. Several studies have used genetic methods to examine the effect of eliminating the function of the entire population of olfactory sensory neurons on odor-driven behaviors (Leypold et al., 2002; Stowers et al., 2002; Luo et al., 2003; Lin et al., 2005; Mandiyan et al., 2005), but only a few methods for selectively manipulating the neurons of the olfactory bulb have been successfully employed thus far (Fadool et al, 2004; Christie et al., 2005; Abraham et al., 2010; Tobin et al., 2010). However, the past few years have seen a rapid increase in the

number of molecular tools available for the functional manipulation of specific neurons in a spatially and temporally controlled way, such as channelrhodopsin-2 and halorhodopsin (Boyden et al., 2005; Zhang et al., 2007; Luo et al., 2008). Moreover, there has been a dramatic expansion in the number of vehicles that can be used to deliver such reagents to select populations of neurons, like two-photon targeted electroporation and high-efficiency, low-toxicity viral vectors (Dittgen et al., 2004; Judkewitz et al., 2009; Marshel et al., 2010; Wall et al., 2010; Osakada et al., 2011). These tools are just beginning to be applied to the study of olfaction (Arenkiel et al., 2007; Dhawale et al., 2010), but promise to play key roles in the dissection of information processing in the bulb.

Finally, most of the aforementioned studies have used relatively coarse behavioral assays to measure olfactory function in mice with altered bulb circuitry (Leypold et al., 2002; Stowers et al., 2002; Fadool et al., 2004; Mandiyan et al., 2005; Kimchi et al., 2007; Kobayakawa et al., 2007). The development of behavioral paradigms that permit a more rigorous quantification of parameters such as stimulus detection thresholds, odor sampling time, response speed, and response accuracy, as well as tighter control over stimulus delivery and stimulus quality (e.g. concentration, composition of odor stimuli) will be necessary to tease apart the potentially subtle computational and perceptual effects of altering olfactory bulb circuit function (Uchida and Mainen, 2003; Abraham et al., 2004; Semmelhack and Wang, 2009).

The Anatomy and Function of Mouse Olfactory Cortex

Using the Golgi method of silver impregnation, Santiago Ramon y Cajal first demonstrated that mitral and tufted cells project out of the olfactory bulb to higher regions of the brain (Cajal, 1909). Subsequent studies have employed a number of retrograde and anterograde anatomical tracing tools, including horseradish peroxidase (HRP) (Haberly and Price, 1977; Scott et al., 1980; Ojima et al., 1984), Phaseolus vulgaris Leucoagglutinin (PHA-L) (Buonviso et al., 1991), dextran-conjugated fluorescent dyes (Yan et al., 2008; Nagayama et al., 2010; Sosulski et al., 2011), modified rabies virus (Miyamichi et al., 2011), and sindbis virus (Ghosh et al., 2011) to show that mitral and tufted cells provide input to a number of areas downstream of the bulb. These areas include the anterior olfactory nucleus, olfactory tubercle, piriform cortex, amygdala, and lateral entorhinal cortex (Fig. 6).

The genetically hardwired, stereotyped nature of sensory neuron projections to the bulb implies that the spatial position of an individual glomerulus has inherent meaning for olfactory perception and odor-evoked responses (Mainen, 2007). The topographic organization of odor information observed in the olfactory bulb, therefore, is likely to be of critical importance for perception and behavior, but it remains largely unknown whether the hardwired, stereotyped representation of odor seen in the bulb is recapitulated via mitral and tufted cell projections to higher olfactory areas. Determining whether the topographic organization seen in the bulb is maintained via stereotyped, spatially organized mitral and tufted cell projections to these higher olfactory areas would provide insight into the perceptual and behavioral roles of these regions. A stereotyped pattern of mitral and tufted cell projections to these areas suggests a role in mediating hardwired associations of odor stimuli with a perceptual valence or a behavioral

response, while a distributed, random representation of odor information could accommodate learned olfactory behaviors or memories. The nature of mitral and tufted cell projections to these higher brain areas, as well as the roles these regions play in olfactory perception, memory and behavior, however, remain poorly understood.

The anterior olfactory nucleus (AON) lies in between the olfactory bulb and piriform cortex (Brunjes et al., 2005). Projections from the olfactory bulb to the AON are topographically organized in a coarse fashion—mitral and tufted cells located in the dorsal bulb project to the dorsal aspect of the AON, while mitral and tufted cells located in the ventral bulb project to the ventral AON (Yan et al., 2008; Ghosh et al., 2011; Miyamichi et al., 2011). The function of this organization of olfactory input is unclear, but appears to assist in a precise exchange of information between the left and right bulbs; neurons in the AON of one hemisphere project to the contralateral olfactory bulb in a spatially stereotyped manner, linking neurons associated with the same glomerulus in each bulb (Yan et al., 2008).

Few studies have examined how the AON represents and processes information about odors. Extracellular and intracellular recordings have demonstrated that neurons in the AON are more broadly tuned to olfactory stimuli than mitral and tufted cells (Boulet et al., 1978). In addition, it has been shown that AON neurons display stronger responses to a mixture of odorants compared to what would be predicted based on a simple sum of responses to the mixture components presented individually (Lei et al., 2006). Recently, one study observed that neurons in the AON can respond with excitation when odors are delivered to the ipsilateral nostril, but inhibition when the same odors are delivered to the contralateral nostril (Kikuta et al., 2010).

Taken together, the anatomical and functional data suggests that the AON serves to integrate odor information it receives from individual olfactory bulb neurons, likely from both hemispheres of the brain, and that this integration may underlie the ability to recognize complex olfactory stimuli as well as the ability to localize odor sources in space (Rajan et al., 2006). Furthermore, due to its reciprocal and bilateral connections with the olfactory bulb and the piriform cortex, the AON is well poised to modulate the flow of olfactory information both within and across the cerebral hemispheres. Ultimately, however, how odor information is represented by the AON, as well as what role the AON plays in olfactory perception and behavior remain largely open questions.

Just caudal of the AON lies the olfactory tubercle (OT), part of the ventral striatum (Ubeda-Bañon et al., 2007). The OT receives a wealth of input from a diverse complement of brain areas involved in sensory processing (retinal ganglion cells, auditory cortex, olfactory bulb, olfactory cortex), neuromodulation (raphe nucleus, horizontal limb of the diagonal band of Broca, locus coeruleus), emotion (cortical and medial amygdala), reward (ventral tegmental area, nucleus accumbens) and memory (hippocampus) (White, 1965; Haberly and Price, 1977; Fallon, 1978; Zahm and Heimer, 1985; Mick et al., 1993; Groenwegen et al., 1987; Johnston et al., 2000; Kuntzle et al., 2005; Budinger et al., 2006; Del-Fava et al., 2007; Ikemoto et al., 2007; Usunoff et al., 2009; Wesson and Wilson, 2011). Despite the fact that the OT receives dense projections from the olfactory bulb as well as input from the AON, piriform cortex, entorhinal cortex and cortical amygdala, exceedingly few studies have examined odor-evoked responses in the OT. However, extracellular recordings performed in anaesthetized rats have shown

that OT neurons do display odor-evoked responses, and that these cells can respond to one or several odorants (Murakami et al., 2005; Wesson and Wilson, 2011).

Much work needs to be done before an understanding of how olfactory information is represented in the OT, as well as what role the OT may be playing in the generation of olfactory perceptions and behaviors, is achieved. However, the diverse array of inputs the OT receives from brain areas involved in sensory processing, neuromodulation, and reward suggest that this region is well poised to play a key role in the association of odors with information about reward or the physiological state of an animal.

Lying nearly 10 millimeters caudal to the olfactory bulb, the lateral entorhinal cortex is the most posterior brain area that receives direct projections from mitral and tufted cells (Sosulski et al., 2011). Situated between the piriform cortex and hippocampus, the entorhinal cortex (EC) is anatomically and functionally divided into two areas, the medial entorhinal cortex (MEC) and the lateral entorhinal cortex (LEC) (Kerr et al., 2007). Much work on the MEC has been performed over the past decade, and these studies have strongly implicated this area in the neural coding of space and navigation (Fyhn et al., 2004; Hafting et al., 2005; Sargolini et al., 2006; Burgalossi et al., 2011).

In contrast, the function of the LEC remains almost totally unknown. Anatomical work has shown that the LEC is strongly and reciprocally connected to a number of areas that process olfactory information, including the olfactory bulb, piriform cortex, amygdala, and insula (McDonald and Mascagni, 1997; Kerr et al., 2007). The LEC also

receives weaker inputs from a number of prefrontal and temporal regions (Kerr et al., 2007). Moreover, the EC serves to link the hippocampus with the neocortex at large, providing the bulk of the cortical input to the hippocampus via the perforant pathway, and receiving one of the main outputs from the hippocampus (van Groen et al., 2003).

Only a handful of studies have examined neural responses in the LEC. Extracellular recordings have demonstrated that, unlike what is observed in the MEC, LEC neurons are not spatially selective (Fyhn et al., 2004; Henriksen et al., 2010; Yoganarasimha et al., 2010). And despite the existence of strong olfactory inputs to the LEC, exceedingly few studies have examined how olfactory stimuli are represented by this area. Using an explanted guinea pig brain preparation, work has demonstrated that neural responses in the EC can be driven by electrical stimulation of mitral and tufted cell axons in the lateral olfactory tract (LOT) (Biella and de Curtis, 2000). Additional work has found that local field potentials in the LEC can be evoked by odor stimulation (Chabaud et al., 2000).

Behavioral studies involving animals with lesions of the EC have suggested its involvement in complex odor-driven behaviors. Simple odor recognition and discrimination and the association of an odor with a particular valence do not seem to be affected by lesions of the EC (Otto et al., 1991). However, EC lesions can impact the learning of conditioned odor aversion (Ferry et al., 1999; Ferry et al., 2006), and lesions restricted to the LEC have been demonstrated to impair the learned association of an odor with a location in space (Mayeaux and Johnston, 2004).

Taken together, the existing anatomical, functional, and behavioral data suggests that the LEC plays a critical role in mediating complex olfactory behaviors, likely in large part by providing olfactory information to the hippocampus. However, despite anatomical and behavioral indications that suggest the LEC is involved in olfactory processing and learned odor-driven responses, it remains almost completely unknown at the present time how odor information is represented in the LEC, and what role this area is playing in olfactory perception and behavior.

In rodents, the amygdala consists of ~13 nuclei (Sah et al., 2003). The main olfactory bulb projects to the anterior and posterolateral cortical nuclei of the amygdala, as well as the nucleus of the lateral olfactory tract, while the accessory olfactory bulb projects to the posteromedial cortical nucleus, medial nucleus, and the bed nucleus of the accessory olfactory tract (Winans and Scalia, 1970; Scalia and Winans, 1975). Additional olfactory input to the amygdala is provided by the piriform cortex and AON, which project to the lateral, basal, and accessory basal nuclei (Sah et al., 2003). Together, this cluster of nuclei has historically been referred to as the "olfactory amygdala."

Behavioral studies involving animals with amygdala lesions have implicated this region in mediating a number of odor-driven responses. Rats with amygdala lesions show a reduced level of freezing, the cessation of all movement except that associated with breathing that is a hallmark of stimulus-driven fear, in response to cats or cat hair (Blanchard and Blanchard, 1972; Vazdarjanova et al., 2001). Amygdala lesions also impaired the consolidation and retrieval of an odor-driven conditioned fear response (Takahashi et al., 2007). In addition, lesions of the medial amygdala result in the degredation of male mating behavior (Lehman et al., 1980; Beck et al., 1982), as well as

female scent marking and the recognition of odors that drive sexual responses (Petrulis and Johnston, 1999).

Although much behavioral work has implicated the amygdala in both learned and innate olfactory behavior, little is known about how odor information is represented and processed by the amygdala. Studies have observed increased cFos expression in the medial nucleus of the amygdala after exposure to odor stimuli (del Barco-Trillo et al., 2009). In addition, extracellular recordings in the rat have shown that a large proportion of neurons in the cortical and basal nuclei of the amygdala respond to odor, and that these neurons tend to be quite broadly tuned (Cain and Bindra, 1972). Finally, extracellular recordings have found evidence of odor-responsive neurons in the basolateral nucleus of the amygdala after these stimuli were associated with a behavioral outcome through experience (Hess et al., 1997; Schoenbaum et al., 1999).

Functional imaging and physiology experiments performed on the human brain have also provided insight into the olfactory function of the amygdala. Early extracellular recording experiments demonstrated the existence of odor-responsive neurons in the human amygdala, and that the responses of these neurons were related more to the concentration of an odor stimulus as opposed to its identity (Hughes and Andy, 1979; Hudry et al., 2001). Furthermore, data from imaging experiments suggests a role for the amygdala in encoding the hedonic value as opposed to the identity of odor stimuli (Zald and Pardo, 1997; Winston et al., 2005). The results from these studies in both rodents and humans suggest that the amygdala may represent olfactory stimuli based not on their molecular or perceptual identity, but their emotional valence, and may play a role in

mediating perceptual and behavioral responses to the hedonic value of an olfactory stimulus.

Finally, the largest and most well-studied of the areas that receive direct projections from the olfactory bulb is the three-layered piriform cortex (PC). Layer I of PC contains many axons and a sparse complement of mostly GABAergic interneurons (Löscher et al., 1998; Zhang et al., 2006). Mitral and tufted cell axonal projections terminate in superficial layer I (Ia); the deeper aspect of layer I (Ib) contains associational fibers that mediate extensive recurrent connections between the principal neurons of the PC (Suzuki and Bekkers, 2007). Layer II of PC contains the numerous, densely packed cell bodies of the principal neurons of piriform, pyramidal and semilunar cells, as well as a variety of GABAergic interneurons (Protopapas and Bower, 2000; Ekstrand et al., 2001; Suzuki and Bekkers, 2006). Layer III contains a lower density of principal neuron cell bodies, as well as a high density of associational fibers. In addition to receiving direct input from the olfactory bulb, the PC also receives projections from the AON, LEC, amygdala, and a number of neuromodulatory areas (Luskin and Price, 1982). In turn, the PC provides input to a number of cortical and subcortical regions, including the olfactory bulb, striatum, hippocampal formation, thalamus, hypothalamus, and neocortex (Luskin and Price, 1983; Shepherd, 1994).

Recent work using anatomical and physiological techniques has demonstrated that individual neurons in the PC receive convergent input from mitral and tufted cells that are connected to multiple glomeruli located all over the olfactory bulb (Apicella et al., 2010; Davison and Ehlers et al., 2011; Miyamichi et al., 2011). This anatomical organization may underlie the fact that neurons in the PC can be broadly or narrowly tuned to odor,

and often respond to odorants that are molecularly and perceptually diverse (Yoshida and Mori, 2007; Zhan and Luo, 2010). In addition, nonlinear interactions are often observed in the PC; for instance, neurons that respond to an odorant presented in isolation may not respond when the same odorant is presented as part of a mixture, and PC neurons can respond to a mixture of odors with more or less activity than would be predicted by calculating the linear sum of the activity displayed in response to each odor presented individually (Barnes et al., 2008; Stettler and Axel, 2009). Finally, electrophysiology and imaging experiments have demonstrated that odorants evoke activity in sparse, spatially distributed ensembles of neurons in PC (Illig and Haberly, 2003; Rennaker et al., 2007; Poo and Isaacson, 2009; Stettler and Axel, 2009; Fig. 7). Thus, each odor is represented by the activity of a unique population of PC neurons, and this population of cells extends across the piriform with no apparent spatial preference (Stettler and Axel, 2009).

These observations suggest that although the piriform is often considered to be primary olfactory cortex, it is anatomically and functionally organized in a manner that is considerably different from other primary sensory cortices. In primary visual cortex (V1), for example, a cell responsive to a given stimulus orientation is likely to respond to lines of similar orientation but not to lines of very different orientation, and cell responsive to similar stimulus features are clustered; this organization is thought to encode spatial information about a stimulus and enable lateral inhibitory interactions that sharpen the stimulus tuning of neurons (Talbot and Marshall, 1941; Hubel and Wiesel, 1959). Olfactory information, however, does not have a meaningful representation in two-dimensional space, and neurons in the piriform cortex not only exhibit discontinuous receptive fields, but neurons responsive to a given odorant are distributed without

apparent spatial preference (Stettler and Axel, 2009). It has therefore been suggested that piriform cortex serves not to represent sensory stimuli in a usefully deconstructed manner, but rather, to assemble representations of olfactory stimuli in a way that enables the perception of complex odor "objects" (e.g. the smell of coffee, which consists of over 200 volatile odorant chemicals (Laurent, 2005)), the discrimination of different odors present in the environment, and the association of a given odor with a behavioral response (Haberly et al., 2001; Choi et al., 2011).

Indeed, the nature of these odor representations suggests a role for the piriform cortex in mediating associative olfactory perception and learned olfactory behaviors. The sparse representation of complex sensory stimuli across a large population of neurons maximizes the coding space between representations of different stimuli, increases memory capacity, and is well suited to permit the formation of learned associations through Hebbian mechanisms of synaptic plasticity (Marr, 1971; Ito et al., 2008). In line with this suggestion, work has demonstrated that PC neurons can be tuned to various aspects of a behavioral task (e.g. odor sampling, interval of motor response, interval of reward consumption) after animals have learned to perform an olfactory discrimination task (Schoenbaum and Eichenbaum, 1995). In addition, the biophysical and synaptic properties of PC neurons can change with odor experience as well as development (Barkai and Saar, 2001; Franks and Isaacson, 2005; Poo and Isaacson, 2007; Cohen et al., 2008). Finally, recent experiments using channelrhodopsin-2 to artificially activate cells in PC have demonstrated that ensembles of neurons in piriform cortex are able to drive learned associative behaviors (Choi et al., 2011).

Although the PC is by far the most studied and well understood of all of the areas in the mouse olfactory system, several questions remain unresolved. It has been well established that odors evoke activity in sparse, spatially distributed ensembles of neurons in the PC, yet it remains unclear how much of this representation is the result of feedforward input from mitral and tufted cells, and how much of this representation is the result of local circuit processing that transforms the representation of odor within the piriform itself. Recent studies have begun to shed light on the role that local interneurons play in shaping the sparse, spatially distributed representation of odor information in the piriform. Electrophysiology experiments have demonstrated that inhibition of neurons in the PC is widespread and broadly tuned, and that this inhibition serves to sparsen the representation of odor in the PC (Poo and Isaacson, 2009). Feedforward inhibition that abruptly terminates principal neuron activation in the PC has also been described; this inhibition is likely to be mediated by GABAergic interneurons that are directly activated by mitral and tufted cell input (Luna and Schoppa, 2008). Finally, recent work has demonstrated that individual pyramidal cells in piriform are weakly connected by long-range excitatory connections, providing a means by which odor information transmitted from the olfactory bulb can be distributed across the piriform cortex (Franks et al., 2011). It is therefore likely that the piriform cortex actively transforms the input it receives from the olfactory bulb into a highly sparse, distributed, decorrelated representation using a number of excitatory and inhibitory circuit mechanisms, but the exact manner by which this occurs remains to be determined.

Many more anatomical, electrophysiological, imaging, and behavioral studies must be performed in all of these higher olfactory regions to achieve a comprehensive

understanding of how odor information is represented and transformed by the mouse olfactory system, and correspondingly, what roles these areas may be playing in olfactory perception and behavior. The lack of investigation into how odor information is processed by these areas has led not only to a commensurate lack of understanding regarding their function, but also, little direction for designing meaningful, hypothesis-driven experiments for the future.

The majority of past studies aimed at understanding the role that these higher brain areas play in olfactory perception and odor-driven responses have employed fairly coarse anatomical and behavioral techniques. The aforementioned anatomical work has attempted to determine the inputs and outputs of these higher olfactory areas; these studies have almost exclusively relied on bulk tracing techniques like extracellular injections of horseradish peroxidase or fluorescent dyes into relatively large areas of the olfactory bulb or cortex. While these techniques can give a binary indication of what areas receive input or output from the location at which these tracers have been delivered, they reveal little about the nature of these projections. The development of more fine-scale anatomical tracing techniques would allow for the characterization and quantification of these patterns of input and output to and from various higher olfactory areas. The application of these more refined anatomical techniques would provide insight into the way odor information is represented by these areas, and what role these areas may be performing in olfactory perception and behavior. Furthermore, these studies would allow for the formulation of more specific hypotheses about the function of these regions that can be tested in future experiments using physiological, imaging and behavioral approaches.

In a similar vein, the aforementioned studies involving animals with permanent lesions or temporary inactivation of higher olfactory areas have suggested several perceptual and behavioral functions for these regions. Due to the coarse nature of these manipulations, however, it is difficult to come to any solid conclusions based on the data they have provided. For instance, studies have demonstrated that lesions of the LEC impair the ability of animals to remember whether odors had been presented in a particular location, and have proposed that the LEC is therefore involved in processing odor-place combinations (Mayeaux and Johnston, 2004). This approach, however, makes it impossible to disambiguate whether odor-place processing takes place in the LEC or the hippocampus, to which it provides olfactory sensory input. Teasing apart the functional roles of these regions will require more refined methods for silencing, as well as activating, their specific neuronal components.

Novel Approaches for Elucidating the Representations and Transformations of Odor Information in the Mouse Olfactory System

To further our understanding of how odor information is represented and processed by the olfactory system of the mouse, we have developed a fine-scale anatomical method that allows us to trace the projections from mitral and tufted cells connected to a single glomerulus in the olfactory bulb to a number of higher brain areas. Electroporation of dextran-conjugated fluorescent dye into a single glomerulus of the olfactory bulb under the guidance of a two-photon microscope has permitted us to elucidate the precise nature of mitral and tufted cell projections to several higher brain

regions, in particular the piriform cortex and amygdala. This novel method allows us to answer questions about the nature of these projections left previously unanswered by the coarse anatomical tools employed in the past: is the topographic glomerular organization of information observed in the olfactory bulb recapitulated in these higher brain areas? Are projections to these regions from the mitral and tufted cells connected to individual glomeruli stereotyped, or are they random? How is odor information represented and transformed by different areas of the mouse olfactory system? Finally, what can these representations and transformations tell us about the role these regions play in the generation of olfactory perceptions, emotions, memories, and behaviors?

Furthermore, this work has laid the foundation for the future development of methods that will enable the targeted manipulation of specific olfactory circuits. Studies that have employed lesions and infusions of pharmacological agents in olfactory areas have led to intriguing suggestions with regard to the perceptual and behavioral roles these areas play. However, these techniques lack the spatial and temporal refinement necessary to unambiguously dissect the function of these regions. The electroporation technique we have developed for introducing dextran-conjugated dye into the mitral and tufted cells connected to a single glomerulus can potentially be adapted for driving the expression of molecular tools like channelrhodopsin-2 or halorhodopsin (Boyden et al., 2005; Zhang et al., 2007) in the neurons connected to a single glomerulus, by substituting plasmid DNA in place of fluorescent indicator. This approach would allow for the functional and behavioral characterization of these cells, as well as their projections to higher brain regions, using the spatially and temporally controlled delivery of light to different areas of the olfactory system (Choi et al., 2011).

In addition, we have developed and applied new techniques for imaging neuronal activity at single-cell resolution in multiple areas of the mouse olfactory system. Using a novel reagent, rabies-GCaMP3, we have developed a method that allows for the targeted expression of a calcium-sensitive indicator of neural activity in hundreds of mitral and tufted cells in the olfactory bulb. We have demonstrated that this reagent can be used to examine the topographic organization of odor-evoked activity in the mitral cell layer of the bulb, as well as the general responsiveness and stimulus tuning of individual mitral and tufted cells. Moreover, we have developed methods for using a previously existing reagent, AAV-GCaMP3 (Tian et al., 2009), to record and analyze patterns of odor-evoked activity in the piriform cortex of the mouse. The methods we have developed provide novel, high-throughput ways of characterizing odor-evoked activity in targeted populations of neurons in several areas of the mouse olfactory system.

Finally, we have applied these methods in a transgenic mouse with a targeted manipulation of the stereotyped pattern of olfactory sensory neuron input to the olfactory bulb to examine the role that this anatomical organization plays in olfactory processing. The application of these new imaging techniques in a mouse with a genetically altered glomerular map (Fleischmann et al., 2008) has allowed us to gain further insight into how odor information is represented in the olfactory bulb and piriform cortex, how odor information is transformed as it passes through the mouse olfactory system, and what roles these areas are playing in odor perception and behavior.

The imaging methods we have developed are widely applicable, and will permit the examination of the topographic organization of neural activity in many brain regions, as well as the high-throughput characterization of the stimulus tuning of individual

neurons and correlations in neural activity in large populations of cells. Future experiments can use these approaches in tandem with recently developed techniques for imaging the activity of neural populations in head-fixed mice performing behavioral tasks, allowing for the correlation of observed patterns of neural activity with specific perceptual and behavioral responses (Dombeck et al., 2007).

The work described in this thesis has improved our understanding of how the mouse olfactory system represents and transforms information about odor in a number of ways. Our anatomical studies have provided insight into how information about odor is represented in a number of higher olfactory brain areas, as well as the potential roles these areas play in olfactory perception and behavior. Functional imaging experiments we have performed in the olfactory bulb and piriform cortex have suggested specific functions for local circuits in the processing of olfactory information, and ways in which olfactory information is transformed as it passes through the nervous system. Finally, many of the methods we have developed for studying the representations and transformations of information in the mouse olfactory system are widely applicable to the study of the structure and function of many areas of the mammalian brain. Our work therefore has the potential to have a significant impact on our understanding of the neural basis of perception, emotion, decision-making, and behavior.

Figure 1.

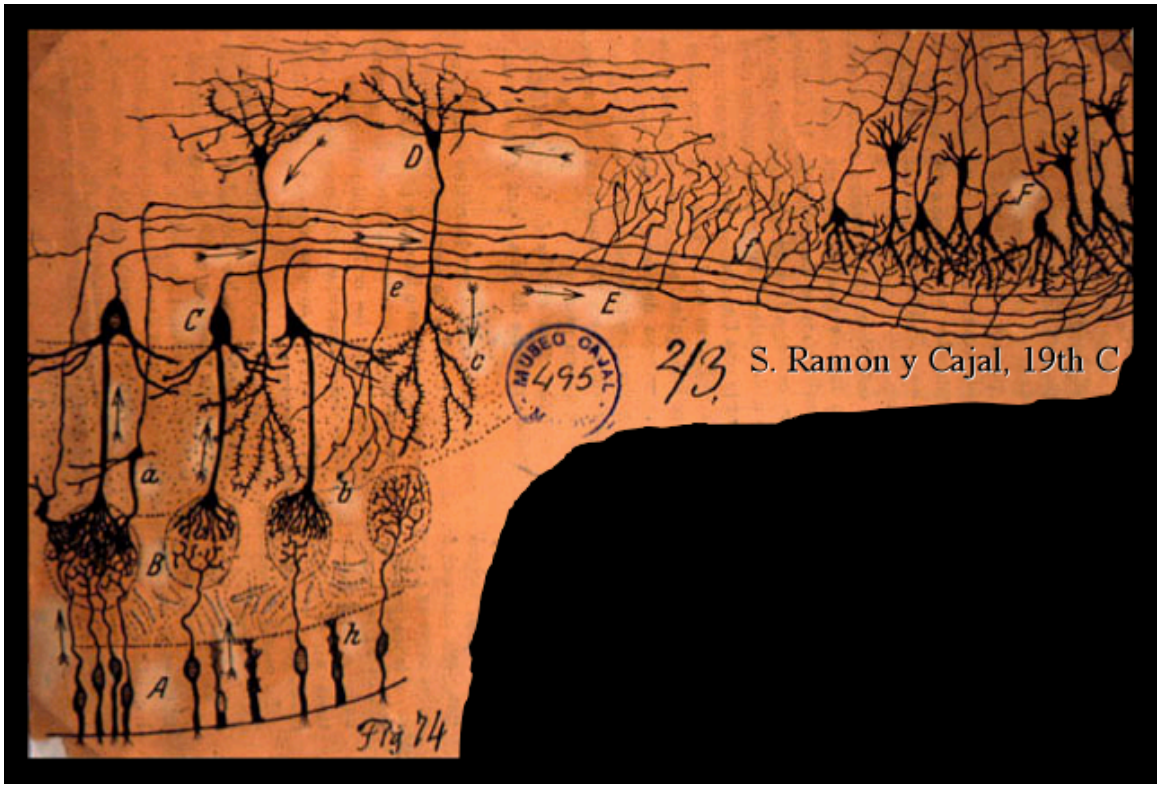

Figure 1. Drawing of mitral and tufted cells and their axonal projections to olfactory cortex by Santiago Ramon y Cajal. A drawing created by Santiago Ramon y Cajal to illustrate how the mammalian olfactory system processes odor-evoked sensory signals (mitral cells are labeled **C**). Image courtesy of Richard Axel.

Figure 2.

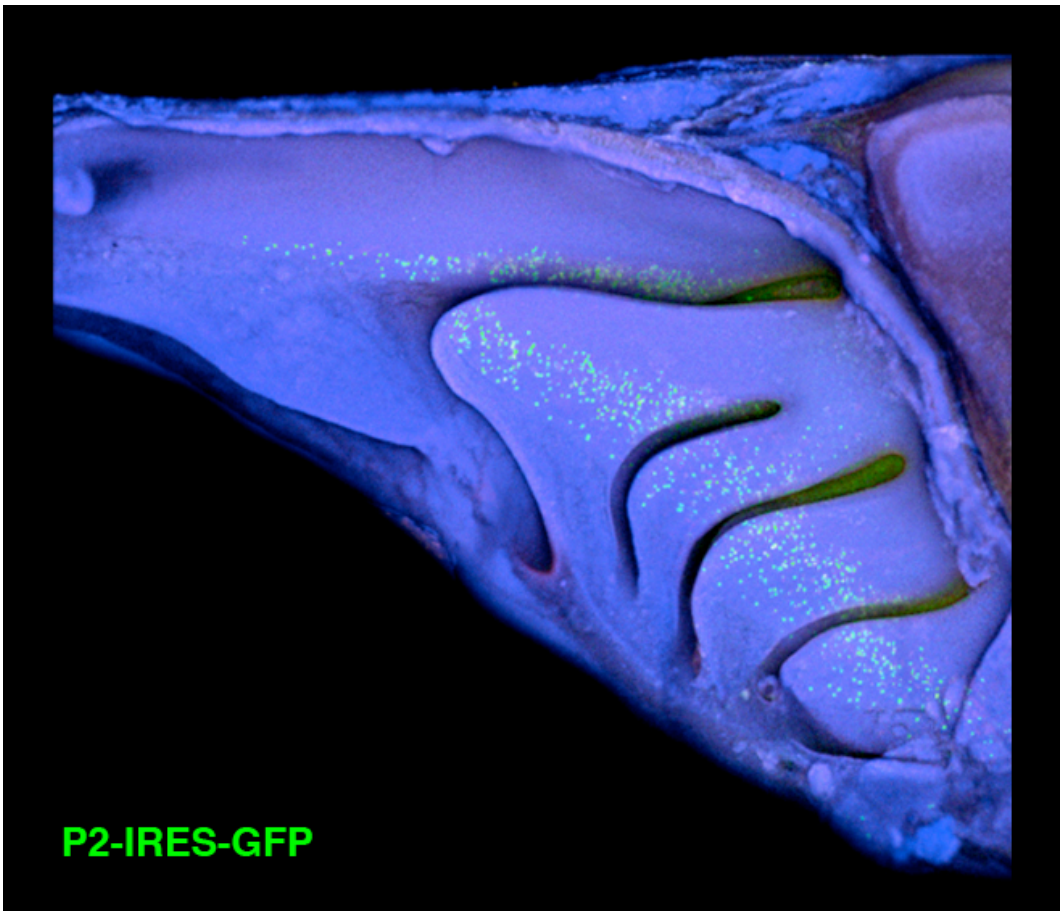

Figure 2. Sensory neurons expressing a given olfactory receptor are distributed in a stochastic manner across the olfactory epithelium. A whole-mount preparation of the olfactory epithelium from a mouse expressing GFP under control of the P2 olfactory receptor (P2-IRES-GFP mouse). Adapted from image by Ben Shykind.

Figure 3.

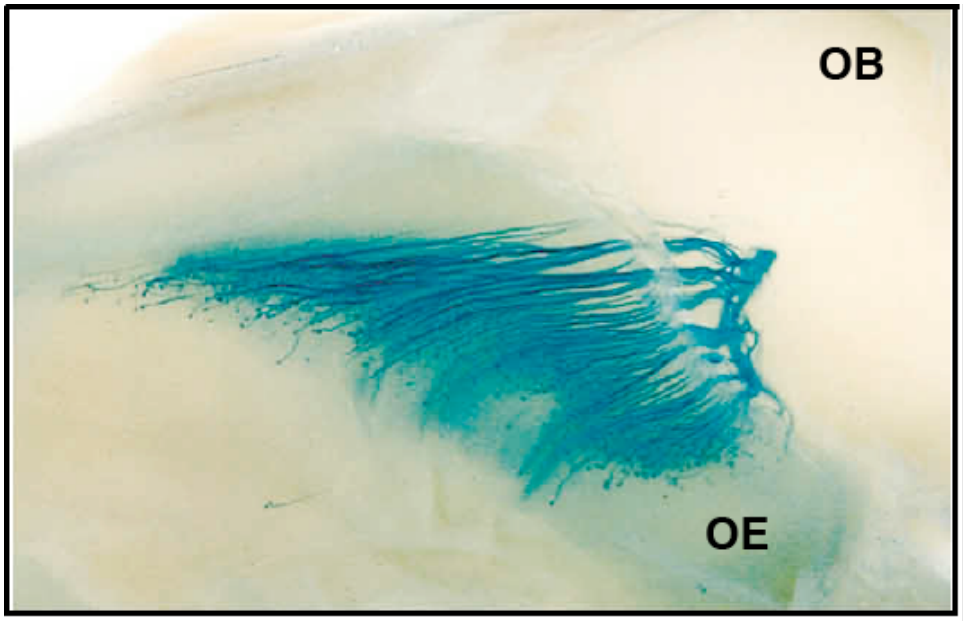

Figure 3. Olfactory sensory neurons project their axons to the bulb in a hardwired, spatially stereotyped manner. View of the olfactory epithelium (OE) and the olfactory bulb (OB) in a whole-mount preparation from a P2-IRES-tau-lacZ mouse (lacZ visualized with X-Gal staining (blue)). The terminations of all olfactory sensory neurons expressing the same receptor (in this image, the olfactory receptor P2) target the same two glomeruli at the surface of the olfactory bulb. Note that because this preparation exposes the medial surface of the epithelium, only one P2 glomerulus can be seen. Adapted from Mombaerts et al. (1996).

Figure 4.

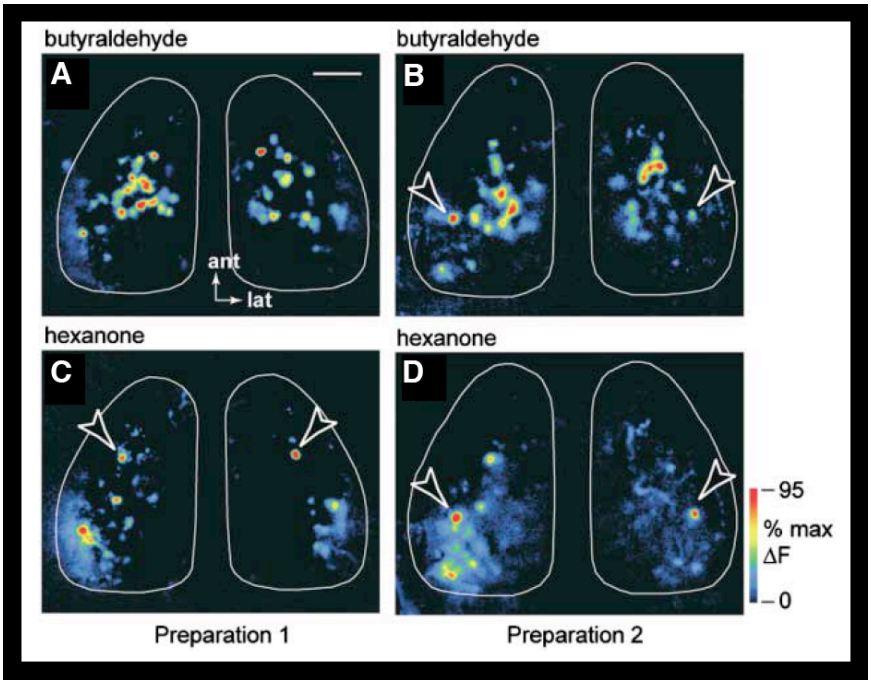
butyraldehyde
A
ant
lat
butyraldehyde
B
hexanone
C
hexanone
D
95
% max
ΔF
0
Preparation 1
Preparation 2

Figure 4. Odor-evoked patterns of glomerular activity are stereotyped across animals. (A-D) Pseudocolored maps of odor-evoked activity (in ΔF/F) on the dorsal surfaces of the olfactory bulbs of mice expressing synapto-pHluorin, a pH-sensitive indicator of synaptic release, in all olfactory sensory neurons (OMP-IRES-spH mice). **(A-B)** Pattern of glomerular activity evoked by the odorant butyraldehyde in mouse 1 **(A)** and mouse 2 **(B)**. **(C-D)** Pattern of glomerular activity evoked by the odorant hexanone in mouse 1 **(C)** and mouse 2 **(D)**. Odorant concentrations were 1% for **(A)** and **(D)**, 0.5% for **(B)**, and 1.8% for **(C)**. Adapted from Bozza et al. (2004).

Figure 5.

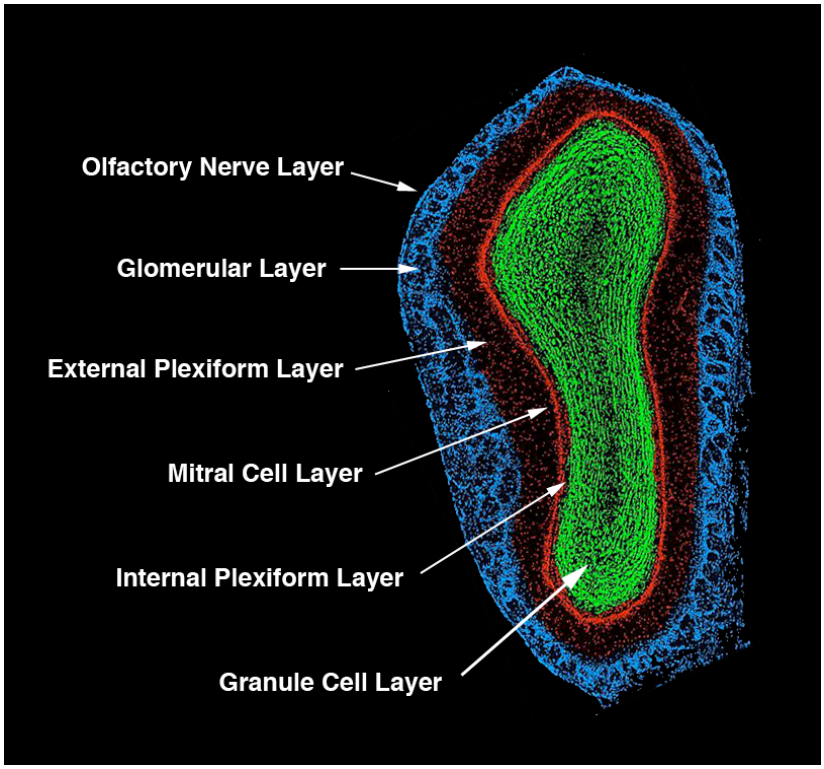
Olfactory Nerve Layer
Glomerular Layer
External Plexiform Layer
Mitral Cell Layer
Internal Plexiform Layer
Granule Cell Layer

Figure 5. The six layers of the olfactory bulb. Pseudocoloring was applied to an image of a coronal slice of the olfactory bulb counterstained for nuclei using TOTO-3 to help distinguish different layers. White arrows indicate the location of each layer. Adapted from image by Matt Valley (2006).

Figure 6.

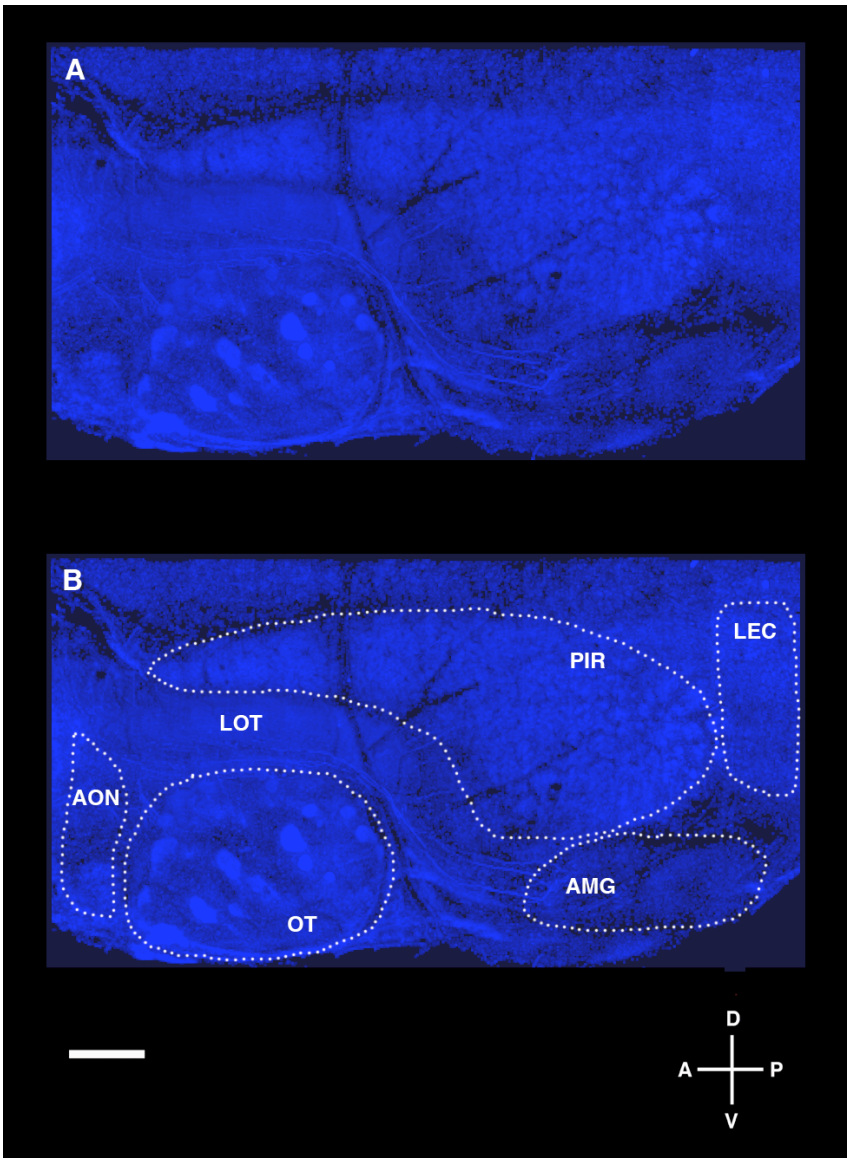

Figure 6. Projections from the olfactory bulb target a number of higher brain regions. (A) Many of the areas targeted by axonal projections from mitral and tufted cells can be visualized in a histological preparation in which a hemisphere of the mouse brain is flattened between two spaced slides and counterstained for Nissl substance using NeuroTrace 435 (blue). **(B)** The same preparation as in **(A)**, but with areas that receive projections from mitral tufted cells via the lateral olfactory tract (LOT) outlined in white (AON = anterior olfactory nucleus; OT = olfactory tubercle; PIR = piriform cortex; LEC = lateral entorhinal cortex; AMG = cortical amygdala; scale bar = 700 μM).

Figure 7.

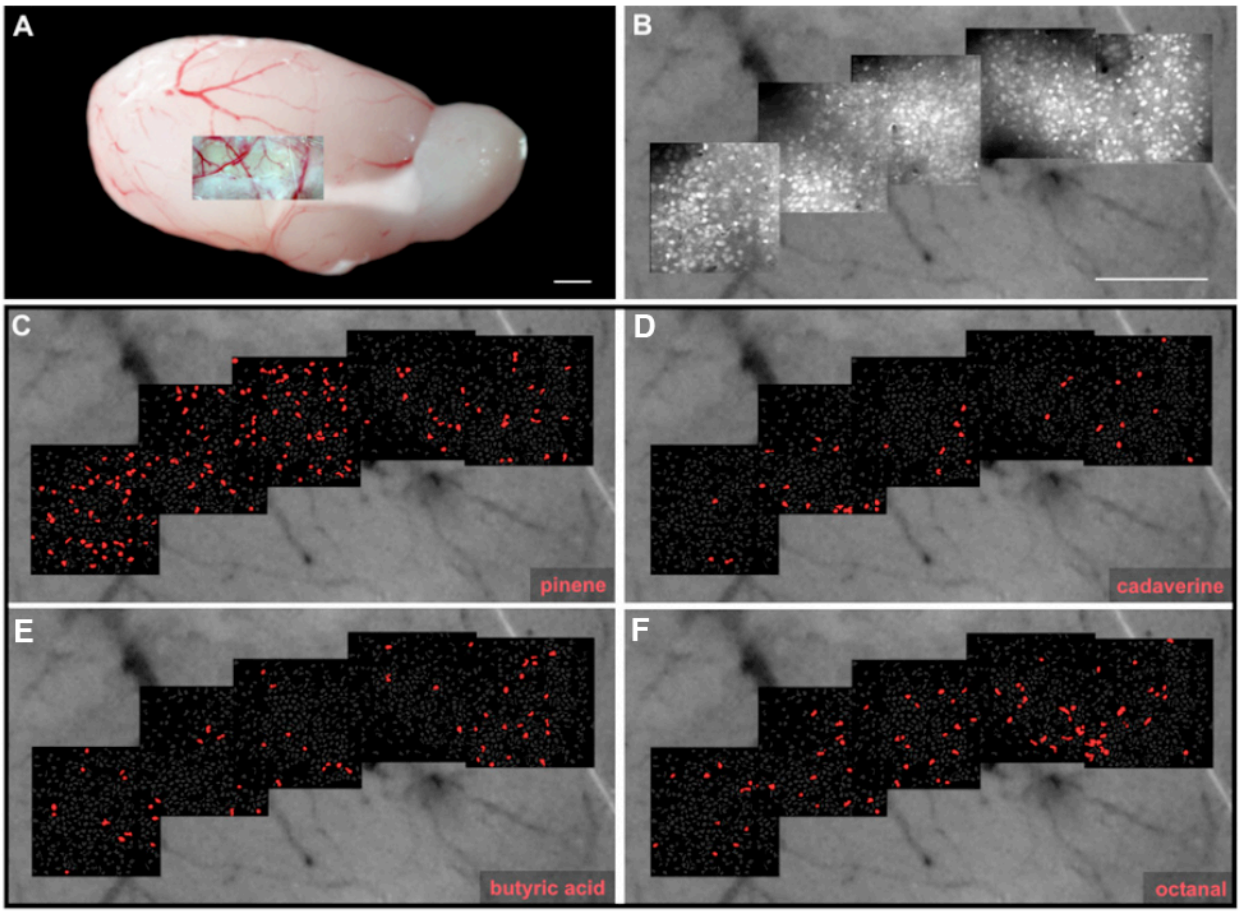

Figure 7. Different odors evoke unique patterns of activity in ensembles of neurons that are spatially distributed across the piriform cortex. (A) Ventral lateral view of a mouse cerebral hemisphere superimposed with the imaging craniotomy (scale bar = 1 mm). **(B)** Montage of images showing the baseline fluorescence of labeled cells in five contiguous imaging sites across piriform cortex (scale bar = 200 μM). **(C)** Cells responsive to four odorants (pinene, cadaverine, butyric acid, and octanal, all at a concentration of ~3 ppm in air) across the region of piriform cortex shown in panel **(B)**. Adapted from Stettler and Axel (2009).

CHAPTER 2

USING A NOVEL METHOD FOR CHARACTERIZING MITRAL AND TUFTED CELL PROJECTIONS TO REVEAL DISTINCT REPRESENTATIONS OF OLFACTORY INFORMATION IN DIFFERENT CORTICAL CENTERS

In vision and touch, information central to perception is ordered in space in the external world and this order is maintained from the peripheral sense organs to the cortex (Marshall et al., 1941; Talbot and Marshall, 1941). Olfactory information, however, does not exhibit a discernible spatial order in the physical world and this poses the question of how odors are represented in the brain. In mammals, olfactory perception is initiated by the recognition of odorant molecules by a large repertoire of receptors in the olfactory sensory epithelium (Buck and Axel, 1991). Individual olfactory sensory neurons express one of approximately 1,000 receptors (Chess et al., 1994; Malnic et al., 1999; Zhang et al., 2002; Niimura et al., 2005), and each receptor interacts with multiple odorants. Neurons expressing a given receptor, although randomly distributed within zones of the olfactory epithelium, project with precision to two spatially invariant glomeruli in the olfactory bulb (Ressler et al., 1993; Vassar et al., 1993; Ressler et al., 1994; Vassar et al., 1994; Mombaerts et al., 1996). Thus, the randomly distributed population of neurons activated by an odorant in the olfactory epithelium is consolidated into a discrete stereotyped map of glomerular activity in the olfactory bulb (Rubin and Katz, 1999; Uchida et al., 2000; Wachowiak and Cohen, 2001; Bozza et al., 2004; Lin et al., 2006).

Each glomerulus has a unique and characteristic receptive field and remains the only topographically conserved feature identified in the olfactory system. The glomerulus is therefore a fundamental unit of processing in the olfactory circuit.

How is this highly ordered map of spatially invariant glomeruli represented in the cortex? The projection neurons of the olfactory bulb, mitral and tufted cells, extend an apical dendrite into a single glomerulus and send axons to several telencephalic areas, including a significant input to the piriform cortex and cortical amygdala (Haberly and Price, 1977; Scott et al., 1980; Price, 1973; Luskin and Price, 1982; Ojima et al., 1984; Buonviso et al., 1991). Electrophysiological studies and optical imaging reveal that individual odorants activate subpopulations of neurons distributed across the piriform without spatial preference (Illig and Haberly, 2003; Rennaker et al., 2007; Stettler and Axel, 2009). The piriform therefore discards the spatial segregation of the bulb and returns to a highly dispersed organization in which different odorants activate unique ensembles of cortical neurons. However, the patterns of neural activity do not allow us to discern whether mitral and tufted cell projections from a given glomerulus to cortical neurons are segregated or distributed, and whether they are random or determined. Distinguishing between these possibilities is important for understanding odor perception because a random representation of odor identity could accommodate learned olfactory behaviors, but cannot specify innate behaviors. Rather, innate olfactory behaviors are likely to result from the activation of genetically determined, stereotyped neural circuits. The elucidation of the circuit architecture that links individual glomeruli to the piriform cortex and cortical amygdala may provide insight into the behavioral function of these brain regions.

Previous experiments have employed the injection of tracer molecules into the bulb or cortex, to relate the spatial position of projection neurons in the bulb with their targets in higher olfactory centers (Haberly and Price, 1977; Scott et al., 1980; Price, 1973; Luskin and Price, 1982; Ojima et al., 1984; Buonviso et al., 1991; see Discussion). However, these experiments predate the ability to identify specific glomeruli (Mombaerts et al., 1996), precluding a determination as to whether projections from a single mitral or tufted cell or a single glomerulus are random or stereotyped. We have therefore developed a strategy to trace the projections from identified glomeruli in the olfactory bulb to higher olfactory cortical centers.

Results

Mitral and tufted cells that innervate a single glomerulus were labeled by electroporation of tetramethylrhodamine (TMR) dextran under the guidance of a two-photon microscope. This technique labels mitral and tufted cells that innervate a single glomerulus and is sufficiently robust to allow the identification of axon termini within multiple higher order olfactory centers (Figs. 1a-1f; Fig. 2; Fig. 3). Labeling of glomeruli in the olfactory bulbs of mice that express GFP under the control of specific odorant receptor promoters permits us to examine potential stereotypy of projections from identical glomeruli (MOR 28-IRES-GFP (n = 8), MOR 1-3-IRES-GFP (n= 13), and MOR 174-9-IRES-GFP (n = 10); Shykind et al., 2004). Labeling of random unidentified glomeruli was performed in mice expressing synapto-pHluorin (OMP-IRES-spH), a fluorescent marker that allows us to visualize individual glomeruli (Bozza et al., 2004).

This permits us to sample the projection patterns from multiple different glomeruli (Fig. 1c).

Electroporation of a single glomerulus results in the labeling of 6-17 neurons in the mitral cell layer (~300 μM ventral to the surface of the bulb; mean = 9.2 +/- 0.8; Figure 1e; see Methods). A determination of the number of labeled tufted cells is more difficult since their anatomic position is not restricted to a defined layer and they are often obscured by the intense labeling of the glomerulus (Fig. 4; see Methods). The number of mitral and tufted cells that innervate a single glomerulus in the mouse has not been determined and therefore we do not know whether we are labeling all or a subset of cognate mitral and tufted cells. We have demonstrated that all mitral and tufted cells labeled in this manner innervate a single glomerulus by electroporating TMR dextran into one glomerulus and fluorescein (FITC) dextran into a neighboring glomerulus (Fig. 1d). Examination of the mitral and tufted cells following this two-color electroporation reveals either red or green mitral and tufted cells with only a rare cell labeled simultaneously with the two dyes (1/60 cells, n= 4) (Figs. 1e-1f). This labeling strategy therefore restricts incorporation of tracer to mitral and tufted cells innervating a single glomerulus.

The comparison of projection patterns from individual glomeruli was facilitated by the observation that the number of neurons and number of axons labeled was relatively constant. It is possible to count individual labeled axons within the posterior portion of the lateral olfactory tract. The more anterior axon bundle consists of axons from both mitral and tufted cells and it is thought that only the mitral cells extend more caudally to project to the posterior piriform cortex, amygdala, and entorhinal cortex

(Haberly and Price 1977; Skeen and Hall, 1977; Scott et al., 1980; Scott, 1981; Schneider and Scott, 1983). We observe that a similar number of axons comprise the posterior LOT for all glomeruli examined (mean = 8.2 +/- 0.7; Fig. 5). This value is in accord with the number of labeled cells in the mitral cell layer, suggesting that differences in projection patterns are not due to differences in the number of labeled neurons or the extent of axonal labeling.

We observe that projections from individual glomeruli extend to all major olfactory cortical regions including the accessory olfactory nucleus, piriform cortex, olfactory tubercle, cortical amygdala and lateral entorhinal cortex (Figs. 2a-2c). Visualization of the extent of axonal projections was facilitated by the development of a flattened hemi-brain preparation that enables high-resolution imaging of all olfactory centers except the anterior olfactory nucleus, which is obscured by the overlying lateral olfactory tract. Most glomeruli we have examined project to all the major olfactory cortical regions independent of the spatial location of the glomerulus within the olfactory bulb (n=21 different glomeruli in the flattened preparation; see below). While our labeling method does not allow us to unambiguously resolve the projections from single neurons, our results are in accord with recent tracing experiments demonstrating that the axons of single mitral cells split and project to several of the higher olfactory brain areas we visualize in our hemisphere preparation (Ghosh et al., 2011). Each of the different higher olfactory centers receives a qualitatively unique pattern of input from the olfactory bulb (Figs. 2b-2c, Fig. 6). In the piriform cortex a distributive representation is observed, whereas in the amygdala mitral cell projections are broad but spatially segregated.

Mitral and tufted cell axons extend to the piriform cortex via the lateral olfactory tract (LOT). We observe that axonal branches exit the LOT at right angles and extend upward to densely and diffusely project to the piriform cortex along the entire anteroposterior axis (Figs. 7a-7c). The projections from mitral and tufted cells connected to a single glomerulus exhibit dense and distributive projections to the piriform, with no apparent spatial preference in any dimension. High-resolution multiphoton imaging reveals varicosities likely to be axonal boutons (Fig. 3). The spatial distribution of these varicosities is similar in every field imaged and is independent of glomerular origin, suggesting that mitral and tufted cell synapses with piriform neurons are distributed throughout the piriform cortex (Fig. 3). The density of these varicosities within the piriform cortex is also similar regardless of the identity of the electroporated glomerulus, further suggesting that each glomerulus makes a similar number of synapses (MOR1-3: 10.2 +/- 0.57 μM of axon per varicosity; M72 (1): 9.9 +/- 0.65 and M72 (2): 10.1 +/- 0.36 μM of axon per varicosity; Fig. 8). The highly dispersed pattern of projections to the piriform cortex is observed from every glomerulus examined independent of its identity or location within the olfactory bulb (n = 21; Fig. 9). On visual inspection, the patterns of projection from two identical glomeruli are no more similar than the patterns of projection observed from two different glomeruli.

We performed hierarchical and k-means clustering to determine whether the observed patterns of projections from different glomeruli are quantitatively distinguishable (see Methods). Relevant parameters that define the pattern of projections to the piriform were extracted from aligned images. We were unable to identify any parameters, including axon fiber positions, density of TMR labeling, center of mass X

and Y coordinates and centroid X and Y coordinates, that reliably distinguish the projection patterns from different glomeruli (Fig. 10). All measured parameters were similar upon comparison of the projection patterns from identical or different glomeruli (Fig. 11).

We have also performed normalized cross correlation analysis to compare the patterns of piriform projections from different glomeruli (see Methods, Fig. 12 for detailed explanation of method and interpretation). Cross-correlation analysis can create a graphical representation of the similarity of the spatial patterning in two images. The correlograms comparing identical and distinct glomeruli display an extended region of moderate correlation (Figs. 7d-7g). These data suggest that the dispersed pattern of projections is largely homogeneous in density over several spatial scales (Fig. 13) and indicate that the patterns are similar for each of the 24 glomeruli we have examined (Figs. 7e-7f). The similarity of correlograms from identical and different glomeruli provides further evidence that the pattern of piriform projections does not differ for each of the distinct glomerulus types. Thus, the mitral cells innervating an individual glomerulus discard the insular and invariant spatial segregation of the bulb and project dense, dispersed axons to the piriform cortex with no discernible spatial bias.

We have also examined the patterns of projections of single glomeruli to the cortical amygdala. The cortical amygdala consists of three nuclei: the anterior cortical, posterolateral cortical, and posteromedial cortical nuclei (Paxinos and Franklin, 2004). Using nuclear counterstaining we can clearly identify the posteromedial nucleus and a nucleus whose position is consistent with the posterolateral nucleus. We observe relatively sparse projections anterior to the posterolateral nucleus and therefore restrict

our analysis to the posterolateral cortical nucleus. The posteromedial cortical nucleus, a major site of innervation from the accessory olfactory bulb (de Olmos et al., 1978), receives no discernible input from any of the glomeruli of the main olfactory bulb we have examined (Figs. 14a-14f, n = 33 glomeruli, see Methods).

The patterns of projection from individual glomeruli in the posterolateral nucleus reveal dense, patchy axonal projections that exhibit a focal nexus surrounded by a less dense halo of fibers (Figs. 14a-14f). Despite the diffuse nature of projections, different glomeruli appear to send fibers to anatomically distinct and spatially invariant regions of the posterolateral cortical amygdala (Figs. 14a-14f). The spatial segregation we observe is largely restricted to the mediolateral dimension. For example, projections from the MOR 1-3 glomerulus consistently occupy the most medial aspect of the posterolateral nucleus, whereas projections from the MOR28 glomerulus terminate more laterally. We have observed a tendency for dorsally situated glomeruli to project to the medial aspect of the posterolateral nucleus and more ventrally situated glomeruli to project to the lateral aspect of the nucleus (Fig. 14a-14c). This pattern, however, is not absolute; MOR 1-3 and MOR 174-9 are both dorsally situated glomeruli, but their projections target different regions of the posterolateral nucleus (Fig. 14). These conclusions are evident on visual inspection and are supported by more quantitative analysis.

K-means clustering using relevant parameters extracted from the amygdala projection patterns after image alignment (center of mass X coordinate, X position of medial-most fiber, absolute medial fiber density, ratio of lateral/medial fiber density) was performed on the projections from three identified glomeruli, MOR 1-3 (n=5), MOR 174-9 (n =5), and MOR 28 (n=4). This cluster analysis correctly assigns glomerular identity

for 79% of the samples examined (one-way MANOVA, $p = 0.0006$, $\alpha = 0.05$). Hierarchical clustering using identical parameters allows the construction of a dendrogram that segregates MOR 1-3 from MOR 174-9 and MOR 28 with 100% accuracy (Fig. 15). MOR 174-9 and MOR 28 exhibit overlapping lateral projections and discriminating this pair by hierarchical clustering is less successful; pairwise k-means clustering for these two glomeruli is able to correctly assign glomerular identity with 67% accuracy.

We have performed normalized cross-correlation analysis to further compare the projection patterns from different glomeruli. Autocorrelation generates a peak at the center of the correlogram (Fig. 14h), and cross-correlation between the projection patterns from the same glomerulus in different animals should exhibit peaks close to the center if the projections to the amygdala are spatially stereotyped (Figs. 14e-14f), whereas correlograms of projection patterns from glomeruli that exhibit different projections will generate peaks that are more distant from the correlogram center (Fig. 14g). Cross-correlation analysis reveals a single peak in the correlogram that reflects the more focal nature of projections to this brain region than in the piriform (Figs. 14e-14g). The correlograms between the projection patterns of identical glomeruli reveal peaks that exhibit a small displacement from the center (Figs 14h-14i; Fig. 16a-16c, Fig. 17a-17c). Cross-correlation using images of projection patterns from different glomeruli exhibit more varied and often very large displacements (Fig. 14j; Fig. 16d-16j, Fig. 17d-17j). These data indicate that the cortical amygdala receives spatially stereotyped projections from individual glomeruli.

Although individual glomeruli project to fixed positions, extensive overlap is observed for the projections from different glomeruli. We occasionally observe robust labeling in anterior structures such as the piriform cortex and olfactory tubercle, but only sparse label in the posterior-residing amygdala. It is therefore possible that a small subpopulation of glomeruli fail to project to the amygdala, but we cannot exclude the possibility that the absence of amygdalar projections results from sporadic failures of our labeling method.

The amygdalar projection patterns we observe differ from the insular, segregated, glomerular structures in the olfactory bulb and project to a broad but topographically conserved patch in the posterolateral cortical nucleus. The apparently random pattern of projections in the piriform and the determined pattern in the amygdala are likely to provide the anatomic substrates for distinct olfactory-driven behaviors mediated by these two brain regions.

Discussion

Insight into the logic of olfactory perception will depend upon an understanding of the how the highly ordered glomerular map is represented in higher olfactory centers. Despite a coarse chemotopy in the bulb, no discernable features of an odor are spatially mapped onto this structure. Therefore the relevant question for olfactory coding is how the brain interprets information from individual glomeruli. The organization of projections from the olfactory bulb to the cortex has been explored by performing both anterograde and retrograde dye tracing (Price, 1973; Haberly and Price, 1977; Scott et al.,

1980; Luskin and Price, 1982; Ojima et al., 1984; Buonviso et al., 1991). These experiments suggested that the bulbar map is not recapitulated in piriform cortex. For example, labeling of random single mitral cells revealed that these neurons elaborate multiple, spatially distributed tufts of axons in the piriform cortex (Ojima et al., 1984; Buonviso et al., 1991). Indeed, the labeling of a single cell assures that you are looking at projections from a single glomerulus. However, these traditional labeling methods were performed without reference to an identified glomerulus, and it was therefore impossible to discern whether projections to the cortex, regardless of their form, are stereotyped or random. Furthermore, the efficiency of labeling in experiments which label individual cells reveal a sparse pattern of axonal arborization that is far less dense and extensive than the strikingly rich projections we observe, rendering an interpretation of spatial patterning difficult at best (Buonviso et al., 1991). Finally, in none of the previous studies was sufficient labeling obtained to allow the analysis of projections to the cortical amygdala.

We have defined a neural circuit that conveys olfactory information from specific glomeruli in the olfactory bulb to the piriform cortex and the cortical amygdala. A distributive representation of neurons in the sensory epithelium is converted into a topographic map in the bulb upon the convergence of like axons onto spatially invariant glomeruli (Ressler et al., 1993; Vassar et al., 1993; Ressler et al., 1994; Mombaerts et al., 1996). The piriform discards this spatial order; axons from individual glomeruli project diffusely to the piriform without apparent spatial preference. Neurons from every glomerulus elaborate similar axonal arbors and quantitative analyses fail to identify features that may distinguish the individual projection patterns. This data is in accord

with retrograde tracings using rabies virus that reveal the convergence of multiple, spatially distributed glomeruli on a small number of piriform neurons (Miyamichi et al., 2011).

Optical imaging and electrophysiological studies of neural responses to odors reflect these anatomic transformations. Distributed neural activity in the sensory epithelium of the nose is transformed in the bulb, with each odor eliciting distinct spatial patterns of glomerular activity (Rubin and Katz, 1999; Uchida et al., 2000; Bozza et al., 2004; Wachowiak et al., 2004; Lin et al., 2006). A second transformation is apparent in the piriform cortex where individual odorants activate unique ensembles of neurons that are distributed without discernible spatial order (Illig and Haberly, 2003; Rennaker et al., 2007; Stettler and Axel, 2009). These neurons also exhibit discontinuous receptive fields; neurons within an ensemble responsive to a given odor will respond to multiple, structurally dissimilar odors (Poo and Isaacson, 2009; Stettler and Axel, 2009). The dispersed projections to the piriform provide an anatomic substrate for the generation of these patterns of neural activity.

One model consistent with both the anatomy and physiology invokes the random convergence of excitatory inputs from mitral cells onto piriform neurons such that each piriform neuron would sample a random combination of glomerular inputs. If the connections from bulb to cortex are indeed random, then the representation of the quality of an odorant or its valence in the piriform must be imposed by experience. Odorants, however, can elicit innate behavioral responses, suggesting that a second area of the brain must receive determined inputs from the olfactory bulb. The pattern of projections to the posterolateral amygdala implicates this structure in the generation of innate olfactory-

driven behaviors. This suggestion is in accord with the finding that disruption of the amygdala abrogates innate, odor-driven behaviors but leaves learned olfactory responses intact (Blanchard and Blanchard, 1972; Slotnick, 1985; Slotnick and Risser, 1990).

In the amygdala, we observe broad but spatially invariant projections that are distinct for individual glomeruli. The projections from individual glomeruli to the amygdala exhibit overlapping but stereotyped patches that differ in character from the insular segregation of like axons and dendrites in the bulb. The identification of a more dispersed map in the amygdala may afford the opportunity for the integration of information from multiple glomeruli to principal neurons of the amygdala. The locus of integration could dictate the perception of different innate odor categories as well as the nature of the behavioral response. The observation that the vast majority of glomeruli project to amygdala may reflect the fact that most odors elicit a perceptual valence often apparent in behavioral assays (Kobayakawa et al., 2007; Mandairon et al., 2009a; Mandairon et al., 2009b). Alternatively, it remains possible that the cortical amygdala, despite its stereotyped inputs, may participate in learned olfactory behaviors.

The olfactory circuits we describe in the mouse are reminiscent of the architecture of the olfactory system in *Drosophila* (Vosshall and Stocker, 2007) despite the six hundred million years of evolution that separate the two organisms. In *Drosophila*, neurons expressing a given odorant receptor are distributed throughout the antenna and converge on spatially invariant glomeruli in the antennal lobe. Information from the antennal lobe bifurcates with one branch exhibiting spatially invariant projections to the lateral horn, a brain region mediating innate olfactory behaviors. A second branch projects to the mushroom body, a structure required for learned olfactory responses. This

anatomic and functional bifurcation provides a context in which to consider the generation of the various forms of olfactory-driven behavior in both flies and mice. Our data suggest that innate olfactory behaviors derive from determined neural circuits selected over evolutionary time, whereas learned behaviors may be mediated by the selection and reinforcement of random ensembles of neurons over the life of an organism.

Figure 1.

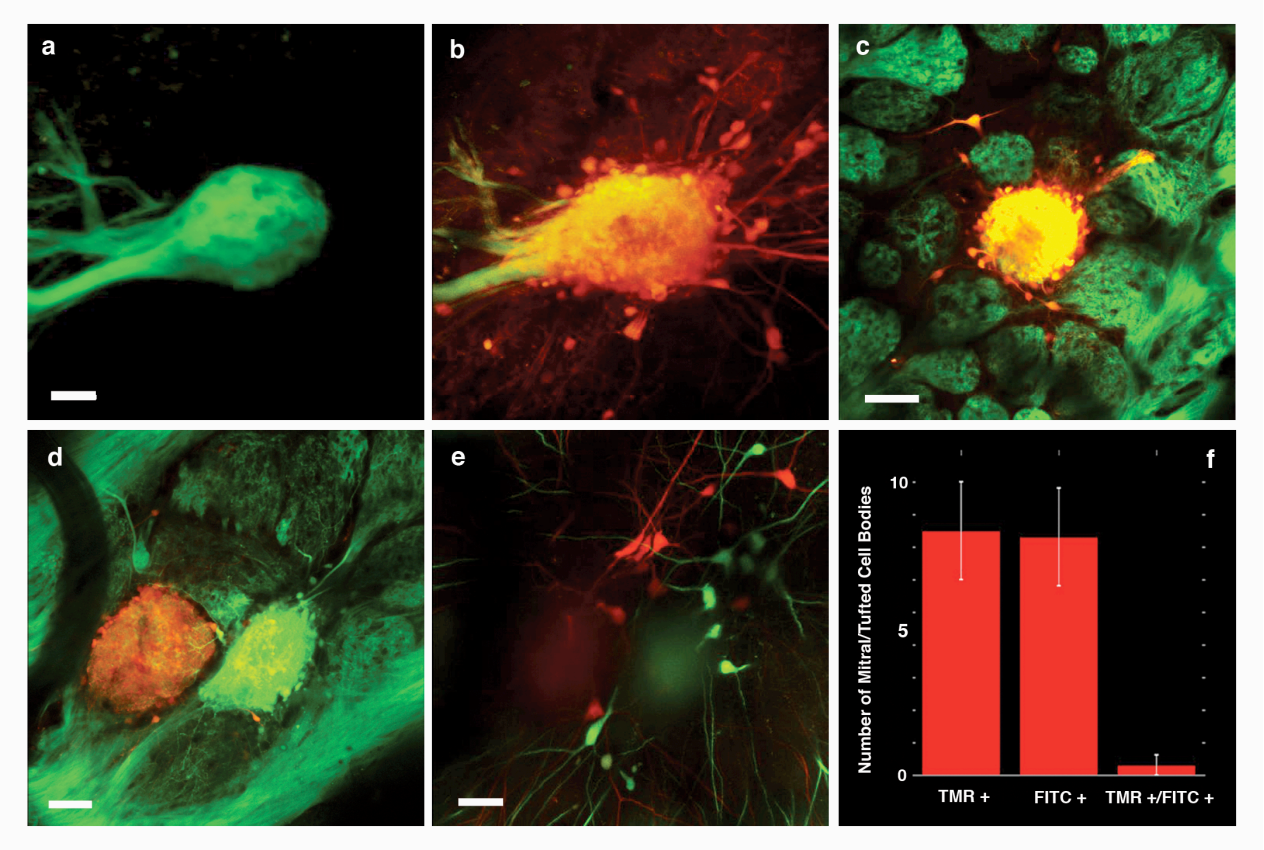
a
b
c
d
e
f
Number of Mitral/Tufted Cell Bodies
10
5
0
TMR +
FITC +
TMR +/FITC +

Figure 1. Targeted electroporation of tetramethylrhodamine (TMR) dextran labels cells that innervate a single glomerulus in the olfactory bulb. A mouse olfactory bulb in which MOR 174-9 is labeled with GFP, before **(a)** and after **(b)** electroporation with TMR dextran (scale bar = 40 μM). **(c)** Image similar to **(a)** where electroporation was performed in a mouse in which synaptopHluorin is expressed in all glomeruli (OMP-IRES-spH, green); note that labeling (red) is confined to a single glomerulus (scale bar = 85 μM). **(d)** Control experiment in an OMP-IRES-spH mouse in which neighboring glomeruli were electroporated with TMR dextran (red, left) and fluorescein dextran (green, right; scale bar = 45 μM). **(e)** Labeling of mitral cells (red, green) as a result of the experiment in **(d). (f)** Quantification of the overlap in mitral cell labeling in experiments similar to **(d)** (n = 4).

Figure 2.

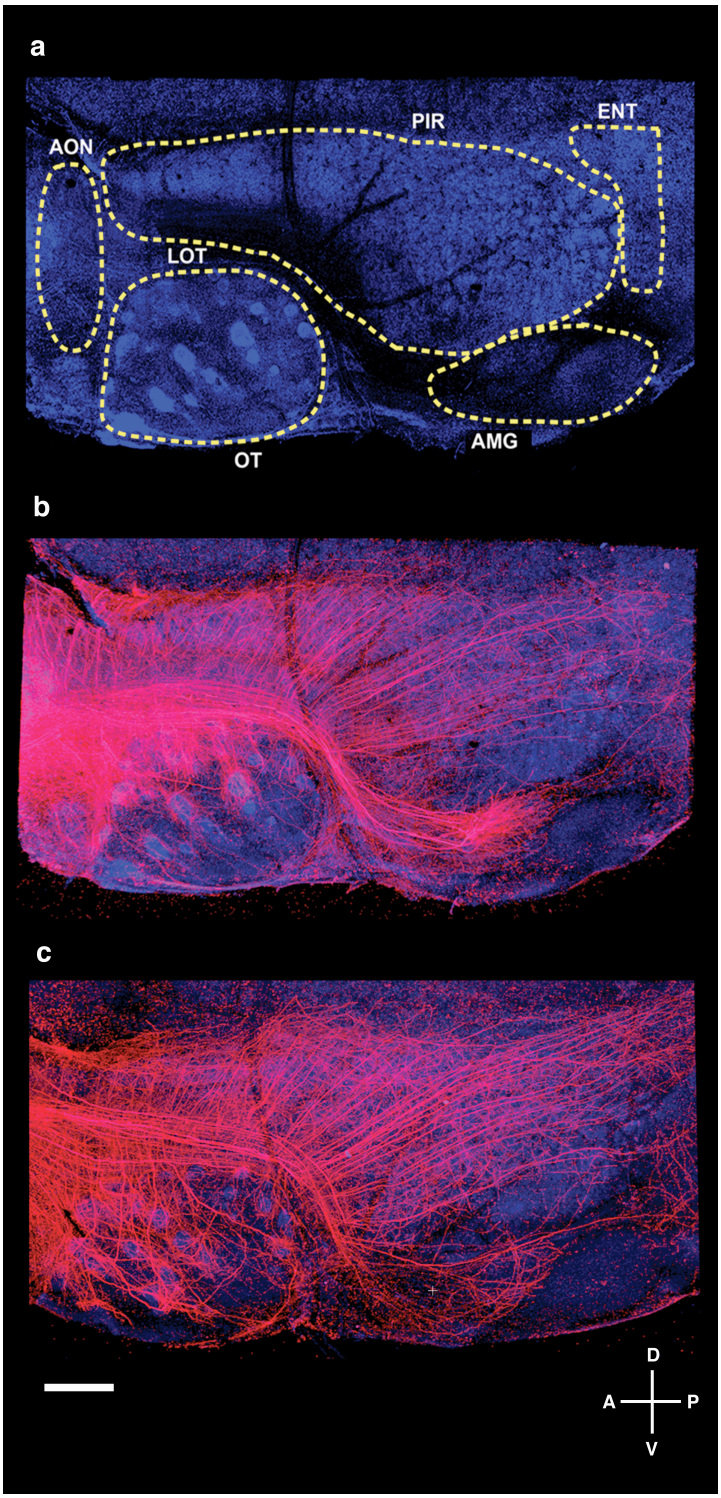

Figure 2. Mitral and tufted cells connected to a single glomerulus exhibit distinct patterns of projections to several areas of the olfactory cortex. (a) A flattened hemi-brain preparation of the olfactory cortex with nuclei identified by counterstain (blue, NeuroTrace 435) and relevant structures outlined in white (LOT = lateral olfactory tract; AON = anterior olfactory nucleus; OT = olfactory tubercle; PIR = piriform cortex; AMG = cortical amygdala; ENT = lateral entorhinal cortex). **(b)** A hemi-brain from a mouse in which a single glomerulus was electroporated with TMR-dextran (red). Note the unique pattern of projection in each of the olfactory areas. **(c)** A hemi-brain from a second mouse in which a single glomerulus was electroporated with TMR-dextran (red; scale bar = 700 μM).

Figure 3.

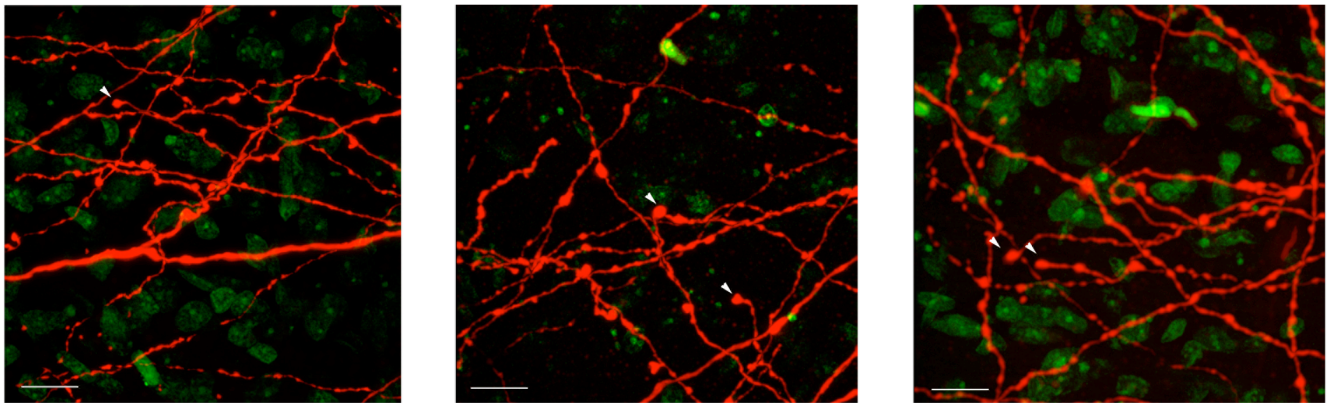

Figure 3. High-resolution multiphoton imaging of mitral and tufted cell axons within the piriform cortex. Imaging at 120x (60x objective with 2x zoom) reveals structures likely to be axonal boutons, found both at axon termini (white arrows) and periodically along the length of axonal branches that have delaminated off of the lateral olfactory tract. Two images taken from different fields of view of the projections from the M72 glomerulus from the same animal (center and right) reveal strikingly similar anatomy, with boutons found wherever axons are found across the field of view; an image (left) of the projections from the MOR1-3 glomerulus in a different animal exhibits a similar distribution of boutons. Images of 20 separate fields from three separate animals each reveal similar distributions of boutons within the piriform, suggesting that synaptic distribution within the piriform may be similar to axonal branch distribution (scale bars = 10 μM).

Figure 4.

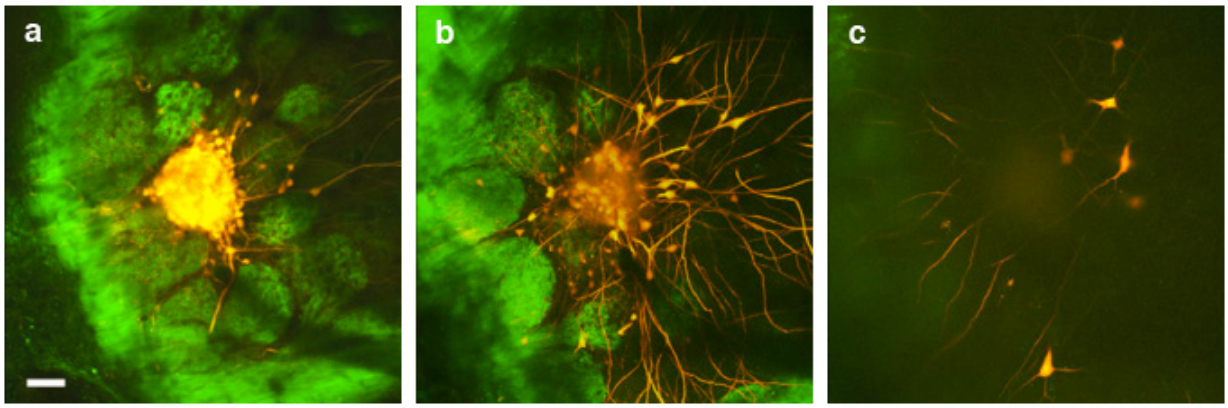

Figure 4. Examples of TMR labeling at different depths in the olfactory bulb. (a) Z-projection of images taken in the glomerular layer of a bulb in which a single glomerulus has been electroporated with TMR dextran (red). A number of labeled periglomerular cells can be seen flanking the labeled glomerulus; note that often these cell bodies cannot be disambiguated from the glomerular border (scale bar = 60 μM; green = synapto-pHluorin). **(b)** Z-projection of images taken in the external plexiform layer of the bulb. Several putative tufted cells can be seen to the right of the glomerulus. Note that the number of cells labeled, the distributed location and varying size of the cell bodies of the putative tufted cells, and the bright shadow of the labeled glomerulus make it difficult to accurately count the number of tufted cells labeled using our method. **(c)** Z-projection of images taken in the mitral cell layer of the bulb. The large cell body size, the distinct laminar location of cell bodies, and their distance from the glomerular layer (~200-300 μM) make it possible to quantify the number of labeled cells in the mitral cell layer.

Figure 5.

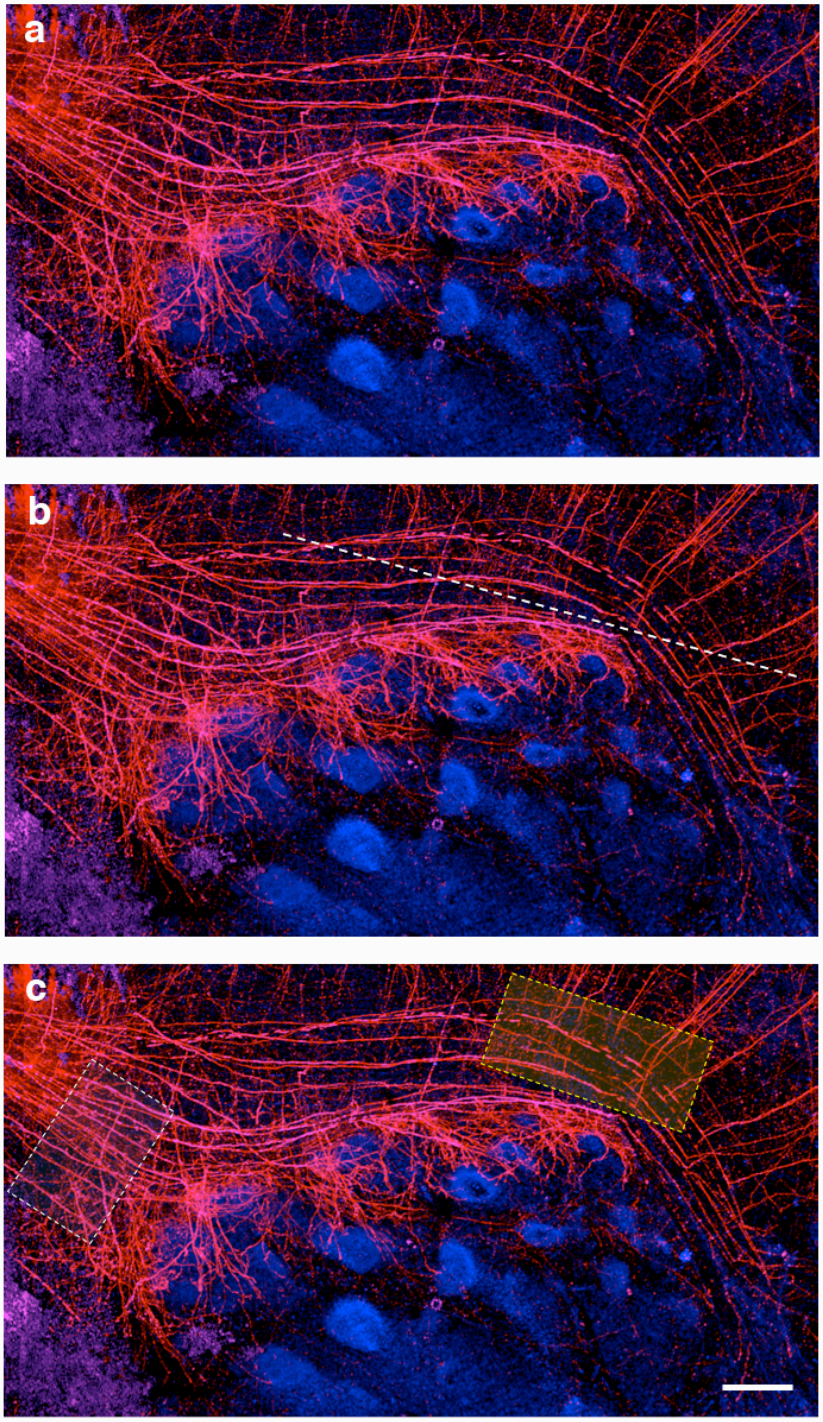

Figure 5. Putative mitral cell and tufted cell axon streams are visually distinguishable in the posterior lateral olfactory tract. (a) The appearance of the LOT after the labeling of a single glomerulus with TMR dextran (scale bar = 400 μM). **(b)** Two separate axon fiber tracts can be distinguished in the posterior aspect of the LOT (separation highlighted by dotted line). **(c)** The fibers in the superior, putative mitral cell axon tract (yellow box) are quantified to control for differences in number of axons labeled using our method. The axons in this tract can be followed all the way to the cortical nuclei of the amygdala. The number of labeled axons we count in this tract are similar to the number of labeled neurons in the mitral cell layer counted in z-stacks taken of the olfactory bulb after electroporation.

Figure 6.

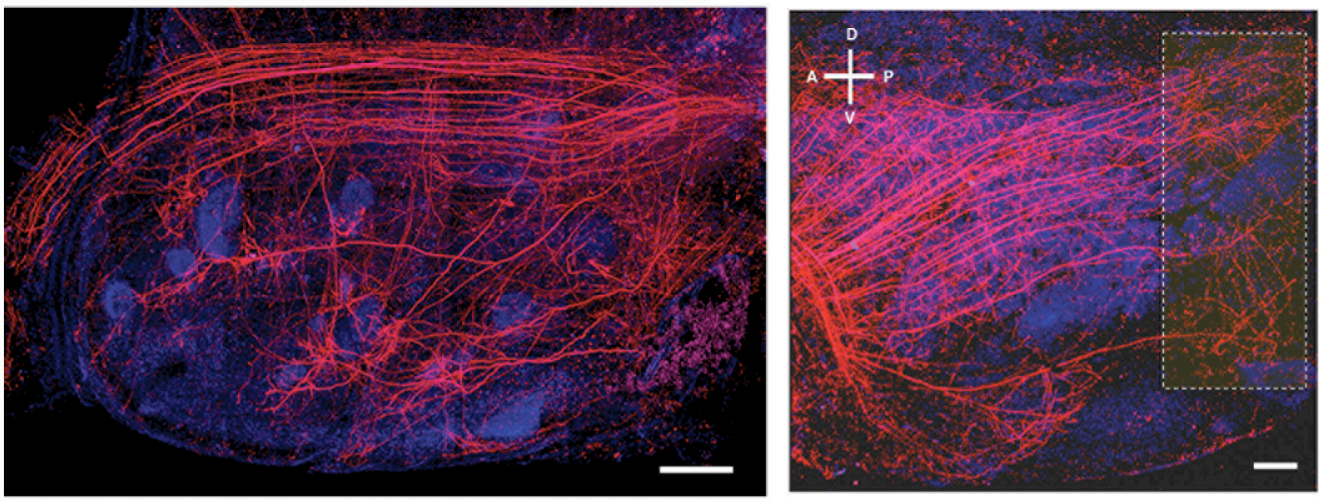

Figure 6. Mitral and tufted cells elaborate distinct patterns of projections to the olfactory tubercle and lateral entorhinal cortex. The olfactory tubercle (left) receives two kinds of projections from the bulb. First, there are projections from individual cells that terminate in a claw-like tuft, often near the islands of Calleja (bright blue circles in tubercle). A second class of projections is less elaborate, with single axonal fibers that run across the tubercle from dorsal to ventral (scale bar = 400 μM). In both cases, projections cover the entire anterior-posterior extent of the tubercle. The lateral entorhinal cortex (boxed region in right image) receives different patterns of projections to its dorsal and ventral regions; projections that target the dorsal entorhinal appear disperse, regular and homogenous, while projections that target the ventral entorhinal cortex appear organized in a less regular manner that is more nest-like or web-like (scale bar = 800 μM).

Figure 7.

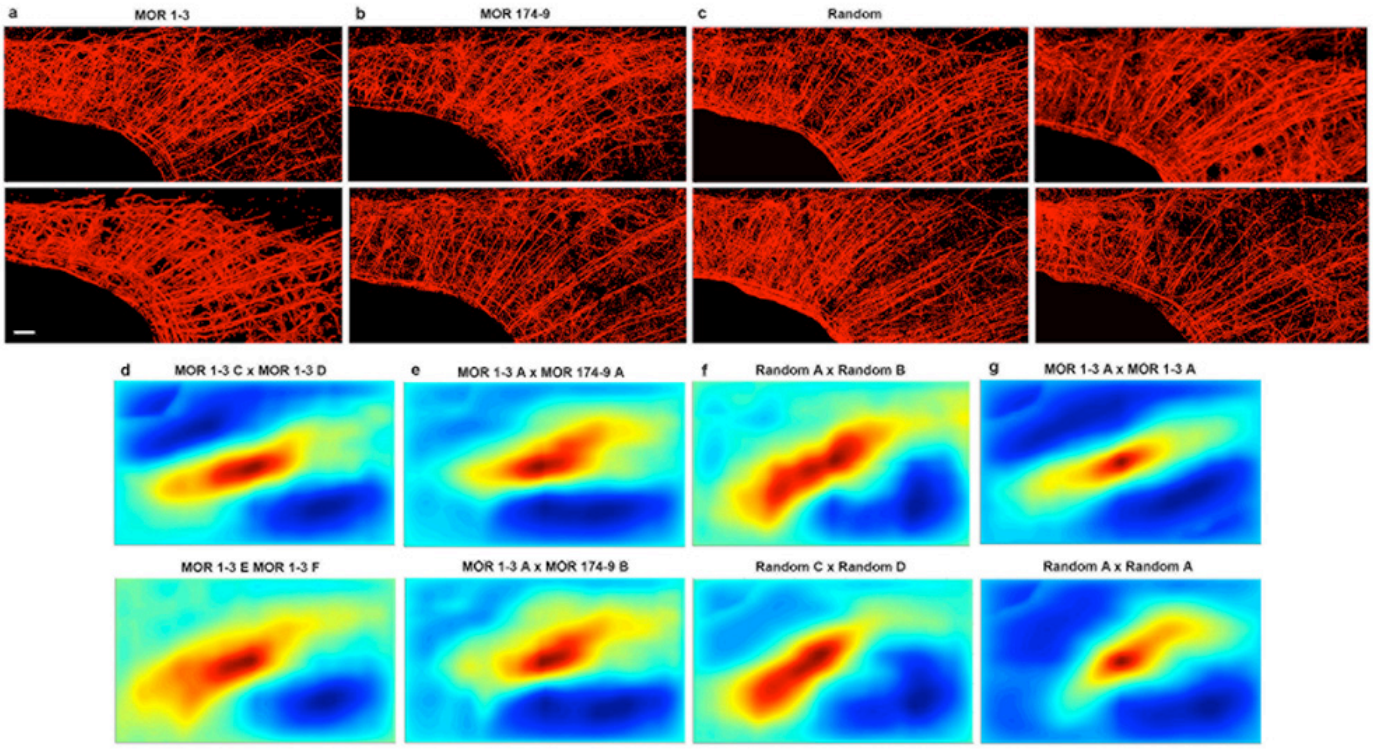
a
MOR 1-3
b
MOR 174-9
c
Random
d
MOR 1-3 C x MOR 1-3 D
e
MOR 1-3 A x MOR 174-9 A
f
Random A x Random B
g
MOR 1-3 A x MOR 1-3 A
MOR 1-3 E MOR 1-3 F
MOR 1-3 A x MOR 174-9 B
Random C x Random D
Random A x Random A

Figure 7. Projections from single glomeruli to piriform cortex are disperse, homogeneous and indistinguishable. Images of axons innervating the piriform cortex (red) from mitral and tufted cells that connect to the glomerulus corresponding to MOR 1-3 (scale bar = 500 μM) **(a)**, MOR 174-9 **(b)** or a random selection of glomeruli labeled with TMR dextran **(c)**. Correlograms plotted using the matrix of correlation coefficients generated by normalized cross-correlation of two MOR 1-3 piriforms **(d)**, a MOR 1-3 and a MOR 174-9 piriform **(e)**, and two piriforms in which random glomeruli were labeled **(f)**. Cross-correlation is performed using aligned images of projection patterns as seen in **(a)-(c)**. **(g)** Autocorrelograms generated using methods from **(d)** in which a labeled piriform is compared to itself. Note that correlograms in **(g)** are essentially indistinguishable from the correlograms in **(d)-(f)**.

Figure 8.

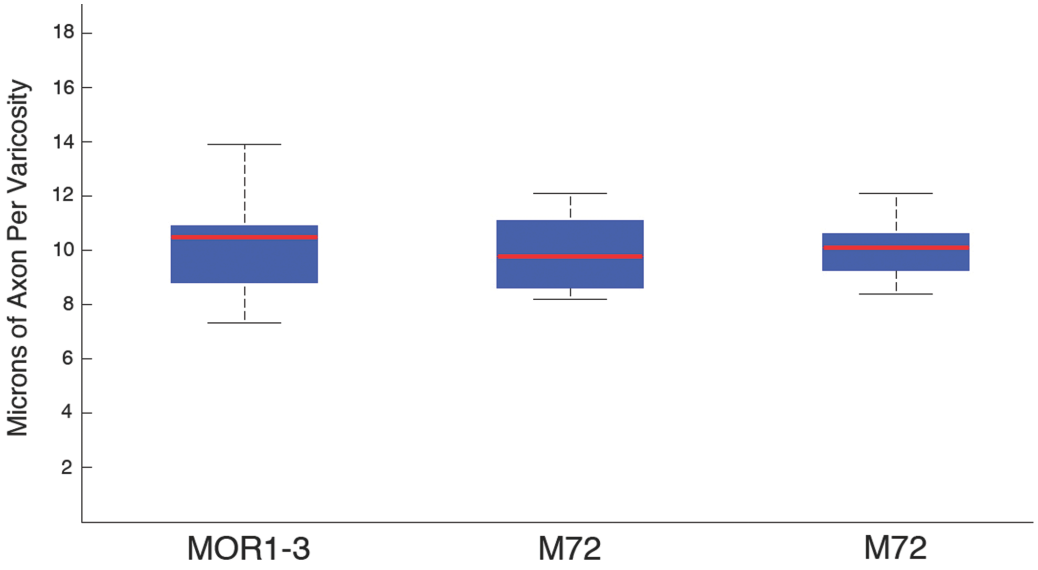
Microns of Axon Per Varicosity
18
16
14
12
10
8
6
4
2
MOR1-3
M72
M72

Figure 8. The density of axonal varicosities in the piriform cortex is independent of glomerular identity. In the box plot, black bars represent the maximum and minimum values within the dataset, the blue box represents the 25^{th} to 75^{th} percentile, and the red bar represents the mean. Mean value of microns of axon per varicosity for the 1-3 glomerulus is 10.2 +/- .57 (n = 10 fields of view, SEM), for one M72 glomerulus is 9.9 +/- .65 (n = 6 fields of view, SEM), and for a second M72 glomerulus is 10.1 +/- .36 (n = 10 fields of view, SEM). By measuring the total area of the piriform, estimating the average length of axon per imaged field of view, and measuring the area of our field of view we can calculate the total number of potential axonal boutons per glomerulus within the piriform cortex. The total area of the piriform, as assessed using the contour surface function of Imaris on images of the whole piriform, is 3.47 +/- .11 $x10^7$ μM^2 (n = 5 piriforms measured, SEM). The average number of microns of axon per field of view (at 60x) is 3644 +/- 304 μM. Our field of view with a 60x objective is 3.72 x $x10^4$ μM^2. These parameters result in a total number of boutons per glomerulus (assuming an average of 10 μM axon per bouton) of 338,892 boutons per glomerulus per piriform cortex. It is critical to note that we count as a "bouton" any structure that appears to be 50% wider or more than the adjacent axonal width; if all such structures do not represent true boutons the actual number of synapses may be lower. However, both the number of boutons per unit length axon, and the resultant total number of boutons reported here likely represent an upper bound to the amount of connectivity between any given glomerulus and the piriform cortex.

Figure 9.

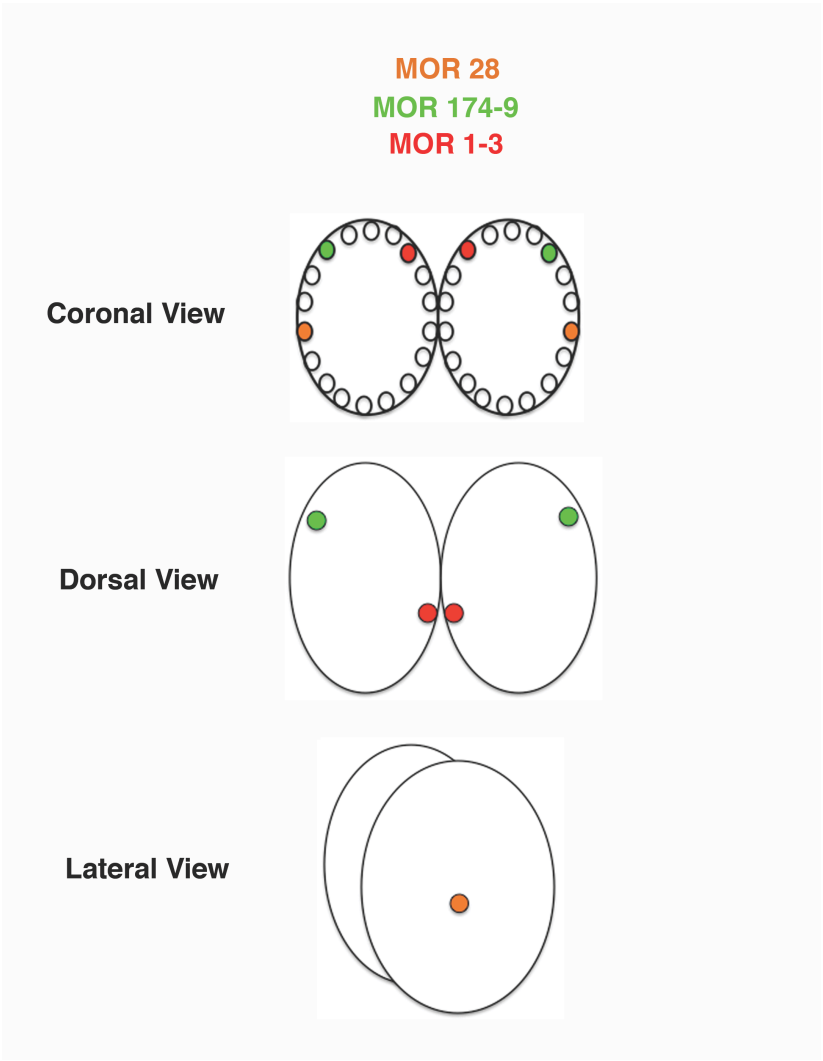

Figure 9. Schematic of the olfactory bulb location of identified glomeruli targeted in experiments.

Figure 10.

Parameters Used in K-Means Clustering	Classification Success Rate
Center of mass X-coordinate, X-coordinate of first anterior fiber, y-coordinate of last posterior fiber	55%
Center of mass X-coordinate, number of TMR-positive pixels	55%
Center of mass X-coordinate, center of mass Y-coordinate, centroid X-coordinate, centroid Y-coordinate	55%
Number of TMR-positive pixels, X-coordinate of first anterior fiber, center of mass Y-coordinate	45%
Center of mass X-coordinate, center of mass Y-coordinate	55%
Y-coordinate of last fiber, X-coordinate of first fiber	55%
Y-coordinate of last fiber, X-coordinate of first fiber, number of TMR-positive pixels	45%
Centroid X-coordinate, centroid Y-coordinate	45%
Center of mass X-coordinate, center of mass Y-coordinate, X-coordinate of first fiber	63%
Center of mass Y-coordinate, Y-coordinate of centroid, Y-coordinate of last fiber	45%
X-coordinate of centroid, Y-coordinate of centroid, number of TMR-positive pixels	55%
Number of TMR-positive pixels	55%

Figure 10. K-means clustering is unable to correctly classify piriform cortex projection patterns according to glomerular identity regardless of what combination of parameters extracted from projection patterns is used.

Figure 11.

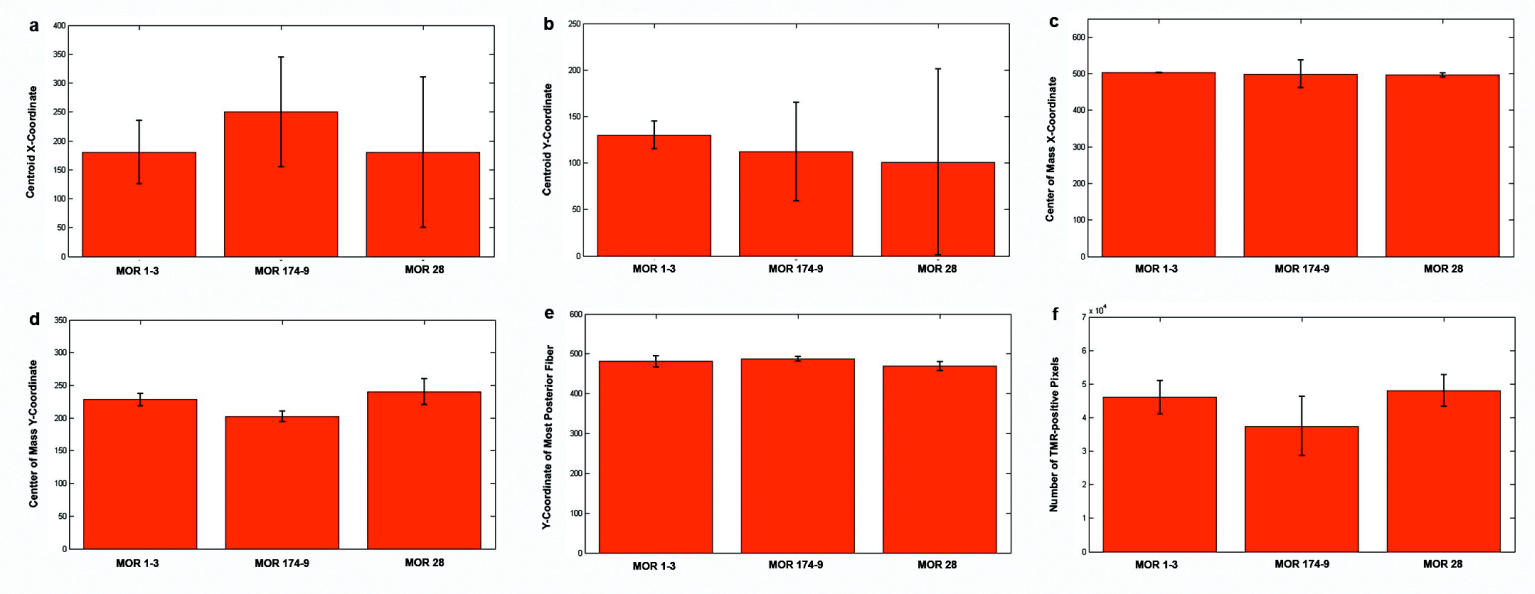
a
Centroid X-Coordinate
MOR 1-3
MOR 174-9
MOR 28
b
Centroid Y-Coordinate
MOR 1-3
MOR 174-9
MOR 28
c
Center of Mass X-Coordinate
MOR 1-3
MOR 174-9
MOR 28
d
Center of Mass Y-Coordinate
MOR 1-3
MOR 174-9
MOR 28
e
Y-Coordinate of Most Posterior Fiber
MOR 1-3
MOR 174-9
MOR 28
f
x 10^4
Number of TMR-positive Pixels
MOR 1-3
MOR 174-9
MOR 28

Figure 11. Parameters extracted from aligned piriform cortex projection patterns are similar for all samples irrespective of glomerulus type. (a) Mean X-coordinate of centroid for MOR 1-3 (n = 4), MOR 174-9 (n = 4), and MOR 28 (n = 2) piriform projection patterns. **(b)** Y-coordinate of centroid. **(c)** X-coordinate of center of mass. **(d)** Y-coordinate of center of mass. **(e)** Y-coordinate of most posterior fiber. **(f)** Number of TMR-positive pixels. All errorbars = SEM.

Figure 12.

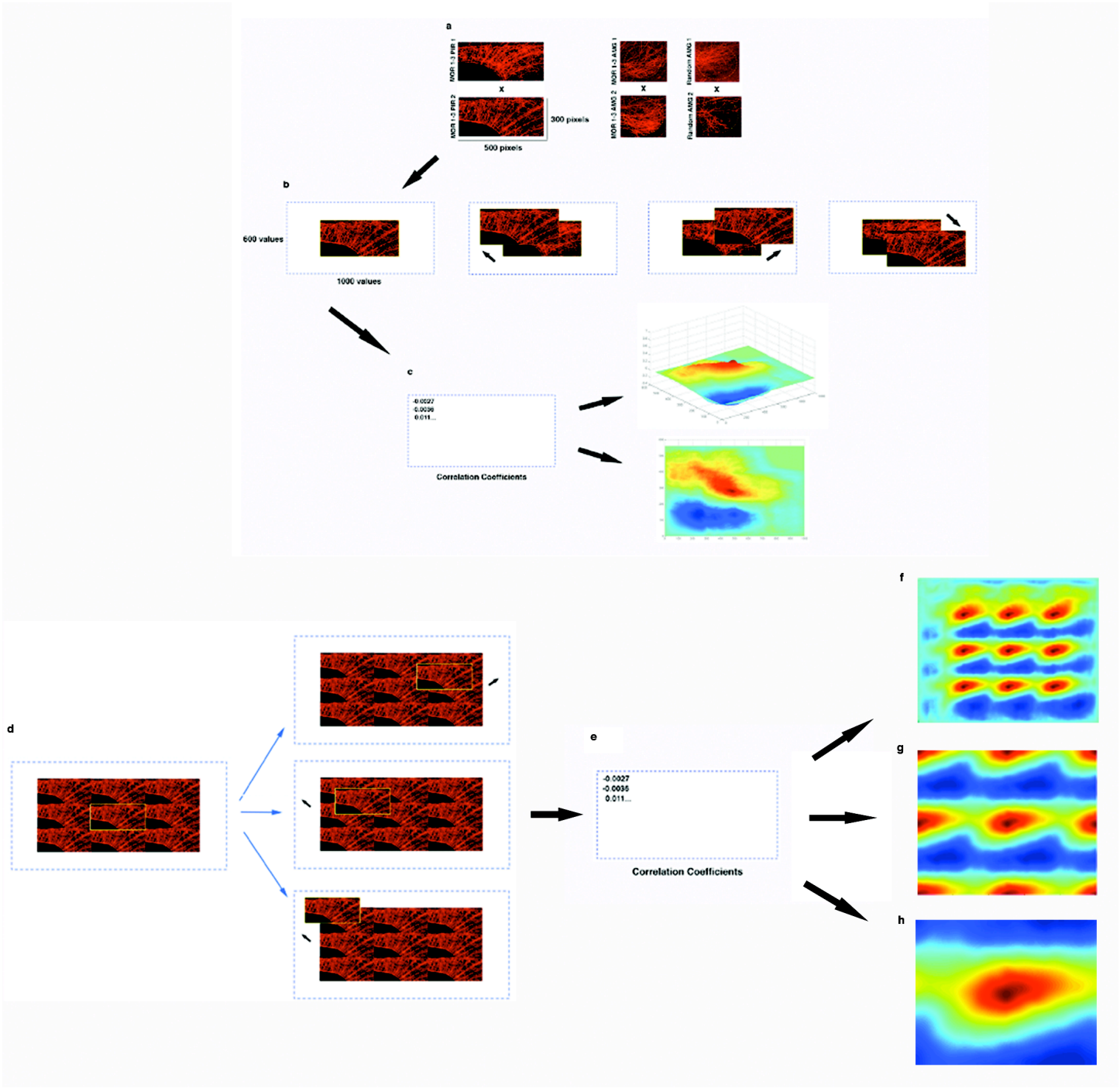
a
300 pixels
500 pixels
b
600 values
1000 values
c
Correlation Coefficients
d
e
Correlation Coefficients
f
g
h

Figure 12. Normalized cross-correlation analysis can be used to quantify the similarity of the spatial patterning in two images. (a) Examples of the images of piriform cortex and the posterolateral nucleus of the cortical amygdala used in normalized cross-correlation analysis. The source images are registered to a template image and filtered (see Methods) before being uploaded into Matlab, where they are represented as matrices of pixel values (e.g. piriform images would be represented as 500 x 300 matrices of pixel values if the images are 500 x 300 pixels in size). **(b)** The cross-correlation between the pixel values in each image is calculated when the images are directly superimposed (left-most panel) and calculated again as one image is shifted relative to the other, repeatedly in all directions (e.g. one image is shifted to the top left, top right, bottom right, and so on, as illustrated). **(c)** The result of these calculations is a matrix of correlation coefficients. The size of the matrix of correlation coefficients is the sum of the lengths of the input source and template images in each axis minus one (e.g. a 500x300 source image correlated to a 500x300 template image would result in a 999x599 correlation matrix) because such a matrix can accommodate the entire range of possible spatial shifts of one image with regard to the other, while maintaining at least one pixel worth of overlap (e.g. if images were placed side by side lengthwise, the two images would be 1000 pixels long, and 600 pixels wide if the same was done for width). These correlation coefficients range from -1 to 1, with -1 reflecting perfect anticorrelation and 1 reflecting perfect correlation of pixel values. This matrix can be plotted as a correlogram (panels on right). Two ways of displaying this correlogram are illustrated; on top, a three-dimensional correlogram is used, where the correlation coefficient values are represented on the Z-axis, and the pixel values for width and length are represented on the X and Y

axes, respectively. The data is plotted using a heatmap representation, where warm colors reflect locations of high pixel correlation, and cool colors represent areas of low correlation. Each location in the correlogram corresponds to the correlation coefficient calculated for a spatial shift of one image relative to the other (e.g. **(b)**). The bottom correlogram is simply the correlogram on top rotated 90 degrees towards the viewer. **(d)** Because normalized cross correlation analysis can be subject to edge artifacts where the two images have little overlap, we also implemented a data padding strategy to validate the data generated by traditional normalized cross correlation. By tiling the template, the source image can be slid across the entire central template tile without the source image encountering a region of zero overlap. Because of the phasic nature of the tiled template image, the overall set of pixel values in the region of overlap is held constant, and therefore the mean image pixel value and the standard deviation of image pixel values used to calculate the Pearson coefficient **(e)** are also constant as this region of the tiled image slides across the template. While the source image will slide off the template at the edges (see **d**, bottom example), the source image never leaves the tiled template image as it samples the center tile. (**f**) Output correlograms from the tiled analysis appear to be a 3x3 array, with minor errors apparent at the edges; within this array an artifact-free tile appears in the center of the correlogram, and represents the correlation between the image and the template under conditions where the image never slides off the tiled template. **(g)** To directly compare the position of the maximum correlation coefficient between this method and the zero-padding method we crop this correlogram such that it represents a similar spatial distribution of displacements. Note that the calculated values in the outer 50% of this correlogram represent displacements in which the source image overlaps

more extensively with the outer tiles in the template than with the center tile, giving this correlogram a phasic appearance. The center tile, however, clearly lacks the edge artifacts apparent at the edges of **(f)**. **(h)** Cropping out the outer 50% of displacements from the image in **(g)** generates a correlogram in which the all of the included values represent an overlap of 50% or more of pixels between the image and the central tile. In this example of cross-correlation of two piriform cortices, this correlogram reveals a single peak in the center, consistent with this brain region containing similar patterns of projection.

Figure 13.

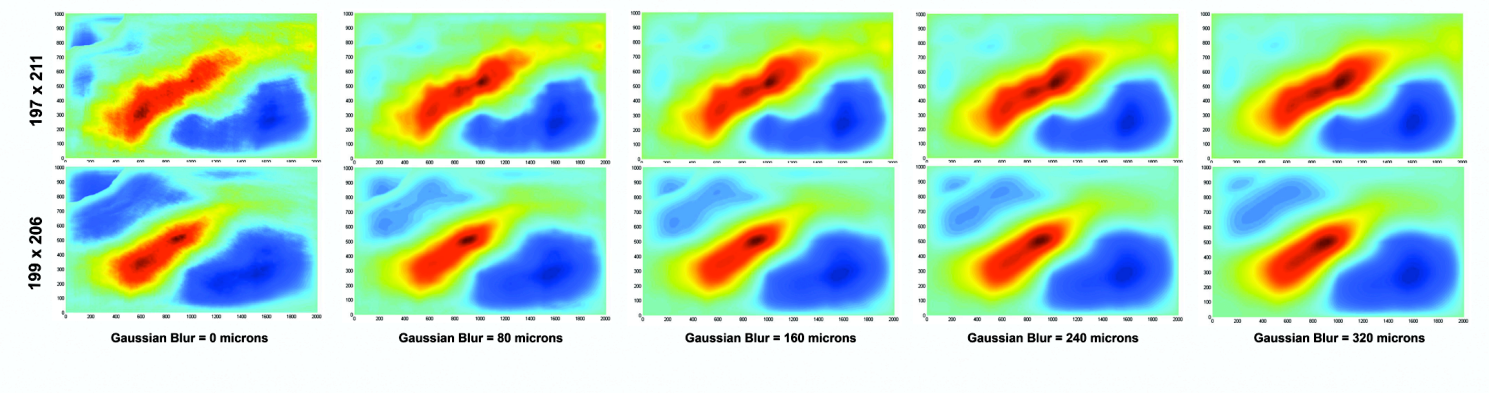
197 x 211
199 x 206
Gaussian Blur = 0 microns
Gaussian Blur = 80 microns
Gaussian Blur = 160 microns
Gaussian Blur = 240 microns
Gaussian Blur = 320 microns

Figure 13. The dispersed homogeneous pattern of projections to piriform cortex is seen across several spatial scales. (a) Correlograms from the normalized cross-correlation of two pairs of raw unblurred images of aligned piriform cortex projection patterns **(b)-(e)** Correlograms from normalized cross correlations of the same pairs of piriform projection pattern images after gaussian blurring at (**(b)** σ = 80 μM; **(c)** σ = 160 μM; **(d)** σ = 240 μM; **(e)** σ = 320 μM).

Figure 14.

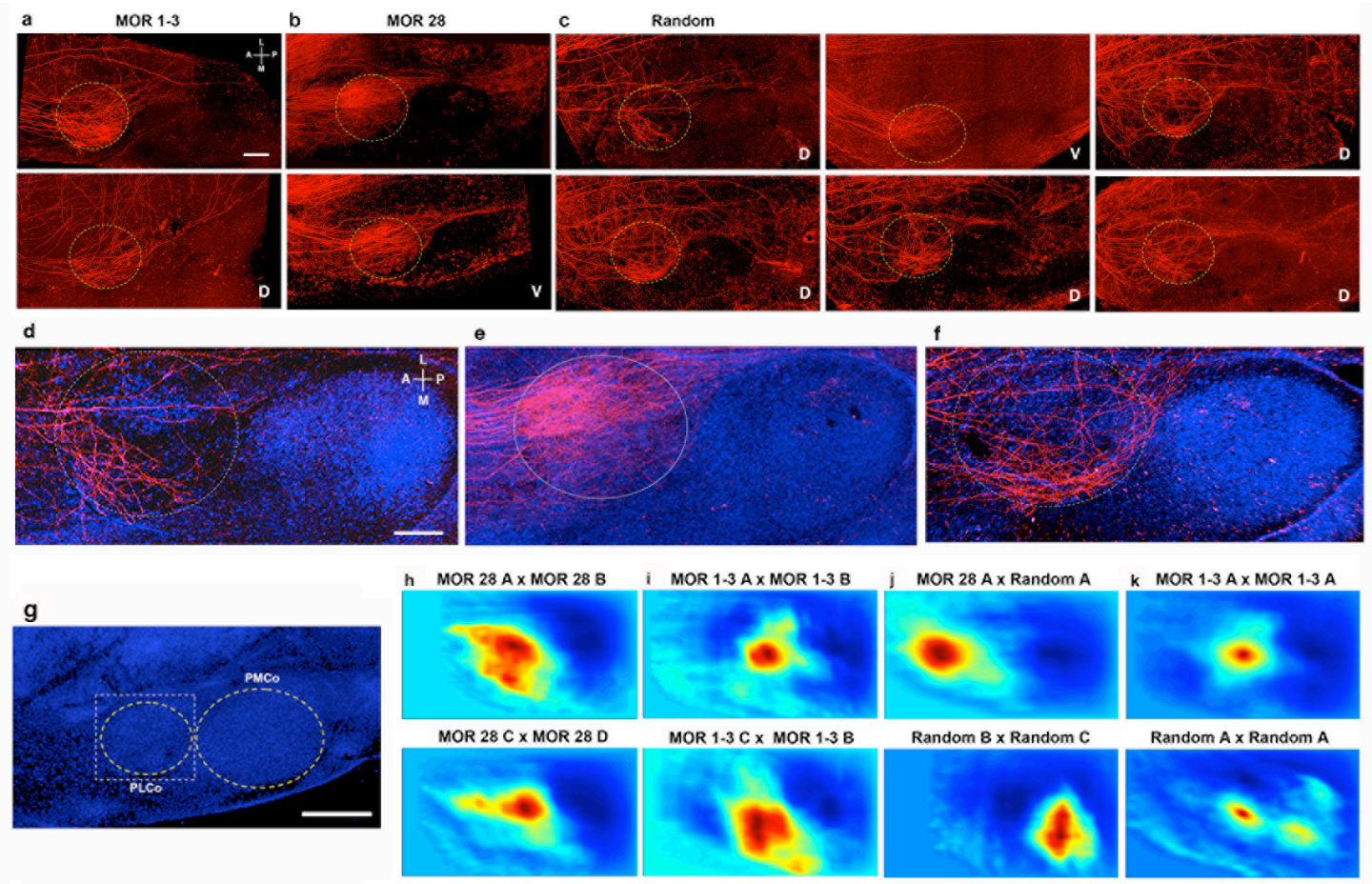
a
MOR 1-3
b
MOR 28
c
Random
D
V
d
e
f
g
PMCo
PLCo
h
MOR 28 A x MOR 28 B
i
MOR 1-3 A x MOR 1-3 B
j
MOR 28 A x Random A
k
MOR 1-3 A x MOR 1-3 A
MOR 28 C x MOR 28 D
MOR 1-3 C x MOR 1-3 B
Random B x Random C
Random A x Random A

Figure 14. Projections from single glomeruli to the cortical amygdala are broad, patchy and stereotyped. Images of the cortical amygdala reveal similar projections from the mitral and tufted cells that connect to the MOR 1-3 glomerulus in two different brains (circle = approximate posterolateral cortical nucleus boundary; scale bar = 400 μM) **(a)**, but projections that are distinct from those of mitral/tufted cells connected to the MOR 28 glomerulus **(b)** or six randomly selected glomeruli **(c)**. "D" or "V" in the bottom right corner of the image indicates whether the electroporated glomerulus was located dorsally or ventrally in the bulb. **(d)-(f)** Counterstained images from a subregion of images in **(a)-(c)** displaying a closer view of projection patterns (scale bar = 400 μM). Correlograms plotted using the matrix of correlation coefficients generated by normalized cross-correlation of MOR 28 x MOR 28 projection patterns within the cortical amygdala **(h),** MOR 1-3 x MOR 1-3 projection patterns **(i)**, or projection patterns from glomeruli of different types **(j)**. **(k)** Autocorrelograms of the PLCo from two labeled glomeruli correlated with themselves. Note that in the en bloc preparation shown here, the lateral/medial axis (indicated by the orientation bars) is synonymous with the dorsal/ventral axis, as this region of brain is curved.

Figure 15.

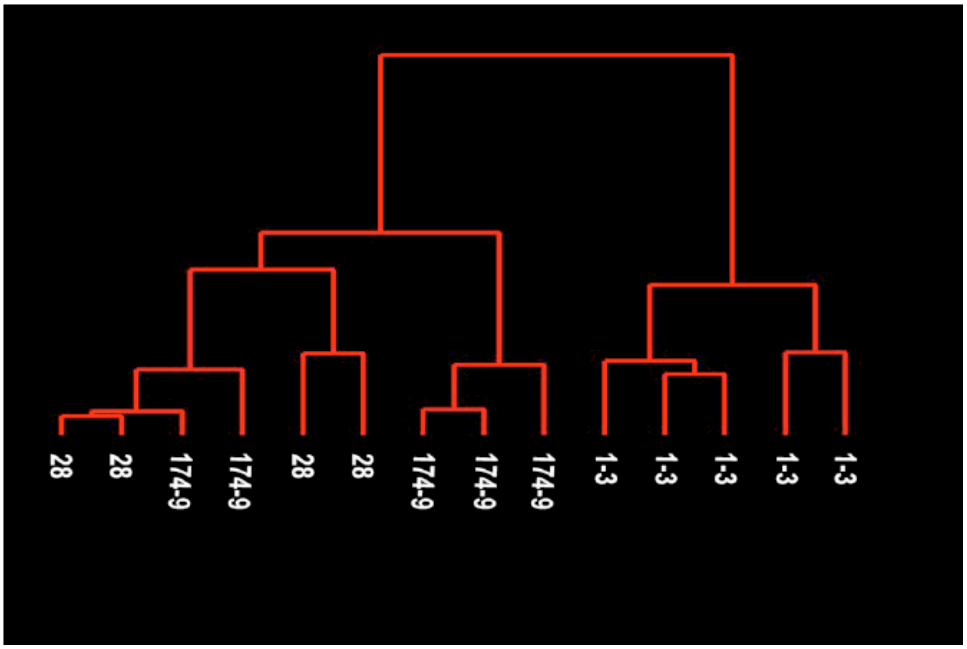

Figure 15. Hierarchical clustering illustrates the discriminability of amygdala projection patterns from three identified glomeruli. Projections from the MOR 1-3 glomerulus are more medial and easily distinguishable from the more lateral, overlapping projection patterns from MOR 28 and MOR 174-9.

Figure 16.

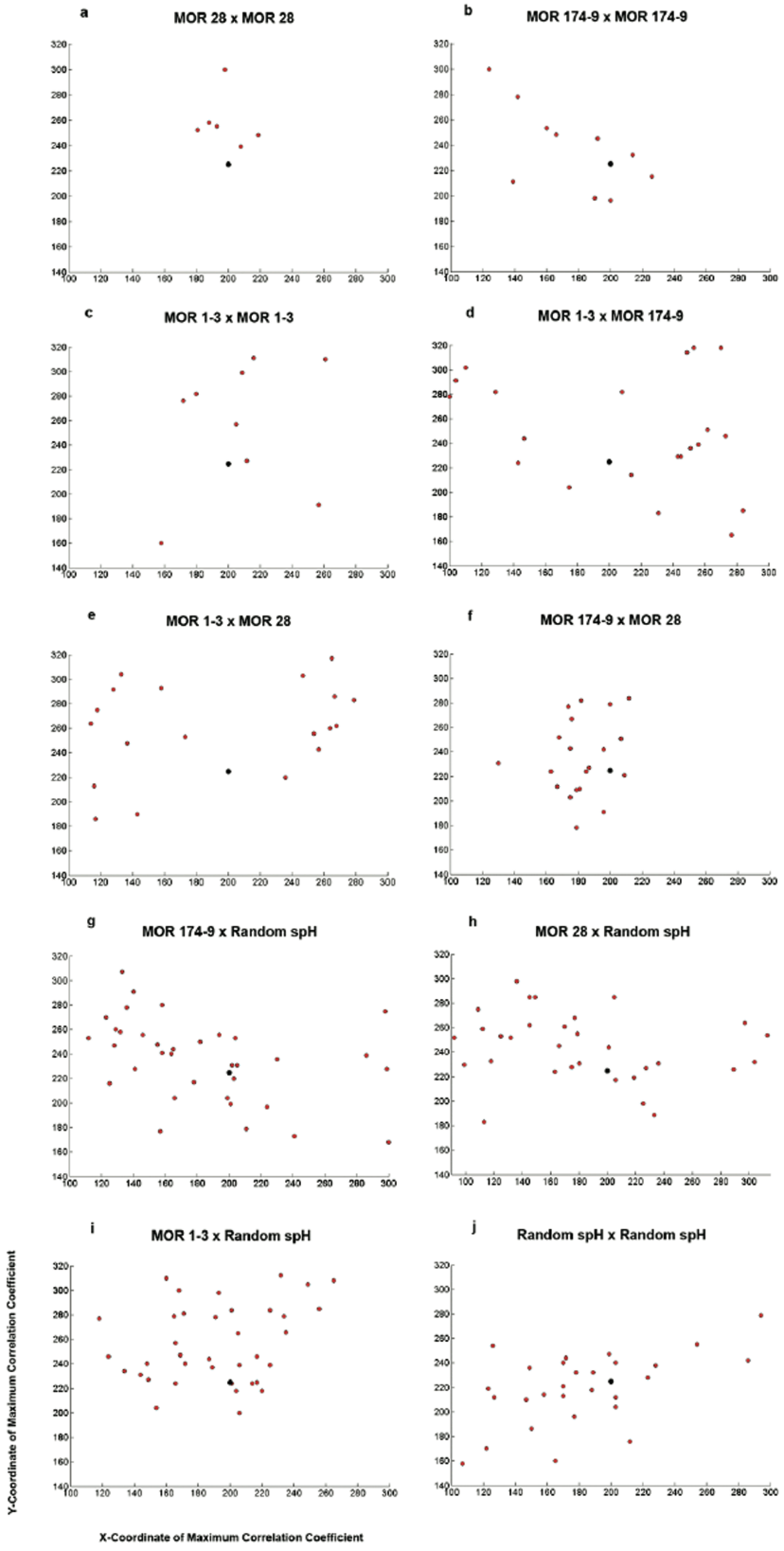
a
MOR 28 x MOR 28
b
MOR 174-9 x MOR 174-9
c
MOR 1-3 x MOR 1-3
d
MOR 1-3 x MOR 174-9
e
MOR 1-3 x MOR 28
f
MOR 174-9 x MOR 28
g
MOR 174-9 x Random spH
h
MOR 28 x Random spH
i
MOR 1-3 x Random spH
j
Random spH x Random spH
Y-Coordinate of Maximum Correlation Coefficient
X-Coordinate of Maximum Correlation Coefficient

Figure 16. Correlograms generated by the normalized cross-correlation of posterolateral amygdala innervation patterns are more similar within than across glomerulus types when using two single images as the inputs for cross-correlation analysis. The location of the maximum correlation coefficient value in cross-correlograms is closer to the center of the correlogram (represented by black dot) and more homogeneous when cross-correlation is performed on two images from the same glomerulus **(a)-(c)** than when cross-correlation is performed using images from two different glomeruli **(d)-(j)**. **(f)** Note that MOR 28 x MOR 174-9 distances are similar to those seen for within-glomerulus comparisons; this is in accord with the large degree of overlap seen in the pattern of projections from these glomeruli in the posterolateral amygdala.

Figure 17.

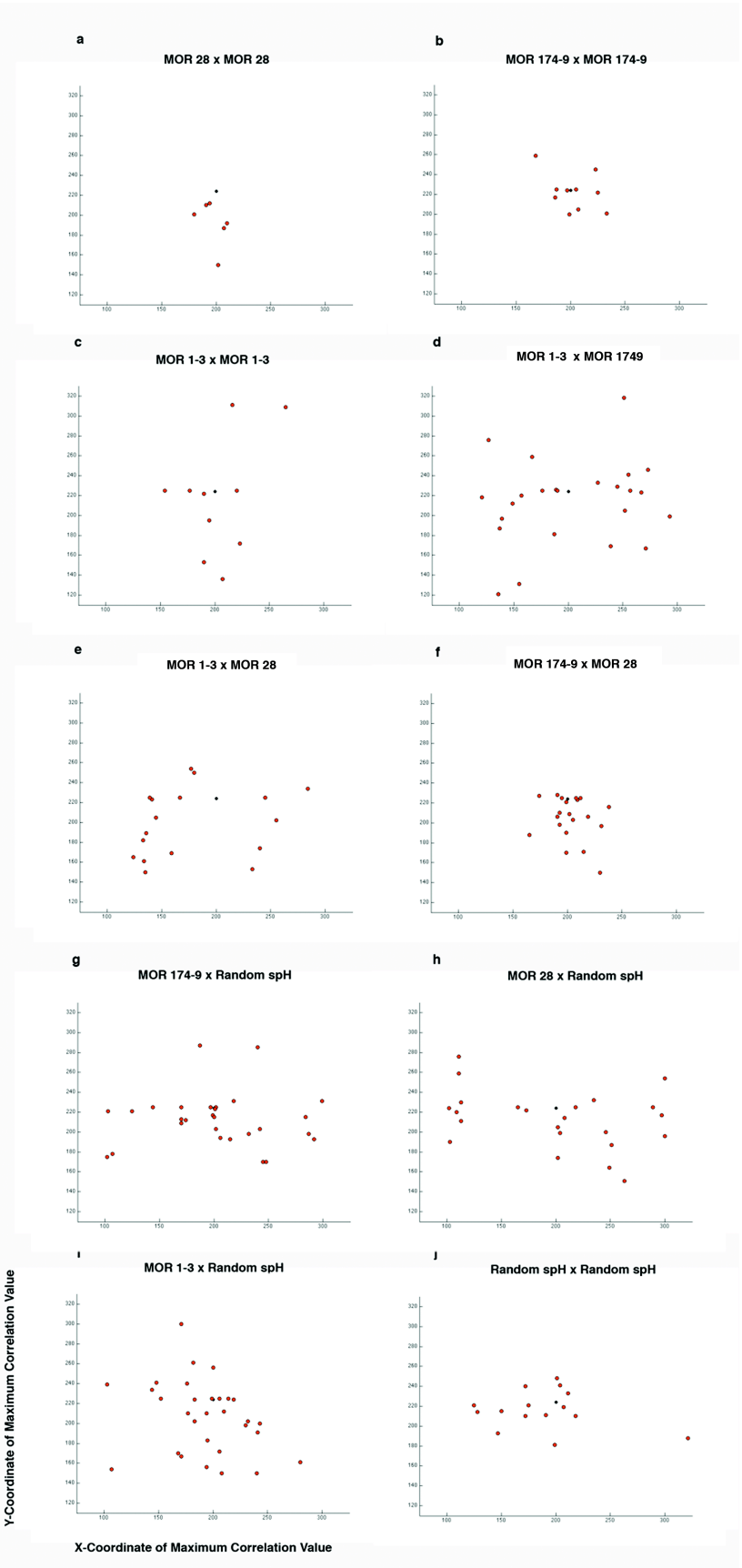
a
MOR 28 x MOR 28
b
MOR 174-9 x MOR 174-9
c
MOR 1-3 x MOR 1-3
d
MOR 1-3 x MOR 1749
e
MOR 1-3 x MOR 28
f
MOR 174-9 x MOR 28
g
MOR 174-9 x Random spH
h
MOR 28 x Random spH
i
MOR 1-3 x Random spH
j
Random spH x Random spH
Y-Coordinate of Maximum Correlation Value
X-Coordinate of Maximum Correlation Value

Figure 17. Correlograms generated by the normalized cross-correlation of posterolateral amygdala innervation patterns are more similar within than across glomerulus types when using a single source image and a 3x3 tiled template image as the inputs for cross-correlation analysis. The location of the maximum correlation coefficient value in cross-correlograms is closer to the center of the correlogram (represented by black dot) and more homogeneous when cross-correlation is performed on two images from the same glomerulus **(a)-(c)** than when cross-correlation is performed using images from two different glomeruli **(d)-(j)**. Note the qualitative and quantitative similarity of the scatterplots generated using two different modes of normalized cross-correlation analysis (Fig. 16, Fig. 17).

CHAPTER 3

USING A MOUSE WITH A "MONOCLONAL" NOSE TO EXAMINE THE REPRESENTATIONS AND TRANSFORMATIONS OF ODOR INFORMATION IN THE MOUSE OLFACTORY SYSTEM

All sensory systems have evolved for the sake of a single purpose: to extract information from the external environment, and to process this information so it can be used to guide behaviors that are critical for survival. Olfactory perception begins with the detection of odors in the world around us by primary sensory neurons in the olfactory epithelium. These neurons bind to chemical stimuli in the environment via receptors located on their dendrites, and convert an external chemical signal into an electrical one that is then transmitted to the brain. Individual olfactory sensory neurons express only one of ~1,000 odorant receptor genes, and neurons that express different kinds of odorant receptors are intermingled at the level of the olfactory epithelium (Buck and Axel, 1991; Ressler et al., 1993; Vassar et al., 1993). Functionally, this anatomic organization leads to a topographically disperse, combinatorial representation of odor at the level of the epithelium in which different odors evoke unique, spatially distributed patterns of activity in ensembles of neurons across the sensory sheet.

These olfactory sensory neurons project their axons to the olfactory bulb, the first relay station for olfactory information in the brain, and all the neurons expressing a given receptor project to two topographically fixed loci, called glomeruli, in the bulb (Ressler et al., 1994; Mombaerts et al., 1996). This pattern of olfactory sensory neuron projections

is conserved between different individuals and provides a two-dimensional representation of receptor identity at the surface of the olfactory bulb. Imaging studies reveal that this spatially invariant pattern of sensory neuron projections engenders a topographically organized "map" of odor-evoked activity in the bulb: different odors elicit distinct spatial patterns of glomerular responses, and these stimulus-specific patterns of activation are stereotyped across animals (Uchida et al., 2000; Belluscio and Katz, 2001; Meister and Bonhoeffer, 2001; Wachowiak and Cohen, 2001). Most odorants at native concentrations activate fewer than 5% of the glomeruli in the olfactory bulb, leading to odor representations in the glomerular layer of the bulb that are relatively sparse (Lin et al., 2006). These sparse, spatially invariant patterns of glomerular activity may reflect a feature critical for the processing of olfactory information in the brain.

Many have suggested that this striking anatomical and functional glomerular organization underlies several forms of information processing in the olfactory bulb. The massive convergence of olfactory sensory neurons on their glomerular targets is thought to aid in the detection of weak odor-driven activity, as well as to increase signal-to-noise ratios by averaging out uncorrelated noise in the signals relayed by olfactory sensory neurons (Laurent, 1999). In addition, electrical interactions that serve to synchronize mitral cell responses to sensory neuron input take place within the confines of the glomerulus (Schoppa and Westbrook, 2001; Fadool et al., 2004), and dendritic spillover of glutamate released by mitral cells that connect to the same glomerulus can enhance the excitability of these neurons (Nicoll and Jahr, 1982; Isaacson, 1999; Christie and Westbrook, 2006). Both of these mechanisms are thought to further boost the gain of

odor-evoked activity in the bulb, thereby strengthening the signal these mitral cells project to higher brain regions.

Past work has also provided evidence for a number of inhibitory interactions made possible by the glomerular organization of the bulb. Feedback inhibition mediated by periglomerular cells can reduce stimulus-evoked transmitter release from sensory neurons and scale with the strength of an odor stimulus (Aroniadou-Anderjaska et al., 2000; McGann et al., 2005; Wachowiak et al., 2005). Moreover, different subtypes of juxtaglomerular neurons can mediate a feedforward inhibition that acts across glomeruli, as well as the inhibition of mitral cell firing over both short and long distances via interglomerular projections (Aungst et al., 2003; Murphy et al., 2005; Shao et al., 2009). Finally, in addition to inhibition at the level of the glomerulus, mitral and tufted cell responses can also be modulated by GABAergic granule cell input. Granule cells extend a dendritic process into the external plexiform layer of the bulb, where they form dendrodendritic synapses on the lateral dendrites of mitral cells (Shepherd, 1994). These dendrodendritic synapses allow granule cells to modulate the stimulus tuning and output of mitral and tufted cells by means of a powerful, spatially defined feedback inhibition (Jahr and Nicoll, 1980; Yokoi et al., 1995; Isaacson and Strowbridge, 1998; Margrie et al., 2001).

The glomerular organization of the bulb has therefore been proposed to enable the refinement of mitral and tufted cell tuning by providing an anatomical substrate for a number of local circuit processes, including sharpening the tuning of projection neuron responses (Yokoi et al., 1995), aiding in the detection of weak sensory stimuli, and providing a form of gain control that prevents a stimulus from saturating the dynamic

range of postsynaptic neurons (Olsen and Wilson, 2008). In turn, this refinement of mitral and tufted cell activity is thought to aid in odor detection, odor discrimination, and sensory-evoked associative learning by strengthening the stimulus-evoked signal that is propagated to higher brain regions, minimizing overlap in the representations of different odors, and maximizing decorrelation between patterns of odor-evoked activity (Barlow, 1972; Ito et al., 2008). However, the difficulty of making targeted manipulations of this circuitry, as well as the lack of high-throughput functional readouts to detect the effects of specific alterations, has made it challenging to determine the functional relevance of these motifs with regard to how the olfactory bulb represents and transforms odor information, and how these representations and transformations influence olfactory perception and behavior.

Results

Previously, we generated a mouse with a "monoclonal nose" in which greater than 95% of all olfactory sensory neurons express the acetophenone-responsive M71 receptor to investigate the perceptual and behavioral impact of altering the stereotyped organization of olfactory sensory neuron input to the bulb (Fleischmann et al., 2008). To generate this M71 transgenic mouse, we first created mouse lines bearing the construct tet_o-M71-IRES-tau-lacZ. In these mice, the odorant receptor M71 and the marker tau-lacZ are both under control of a promoter, tet_o, that activates gene transcription upon binding the tet-transactivator (tTA) protein (Gossen et al., 1995; Fig. 1a; see Methods). These transgenic lines were then crossed with a previously generated mouse strain in

which the tet-transactivator tTA is under the control of the olfactory marker protein (OMP) promoter (OMP-IRES-tTA mice; Yu et al., 2004). Because OMP is expressed in all mature olfactory sensory neurons, tTA is also expressed in all olfactory sensory neurons in OMP-IRES-tTA mice. Finally, M71 transgenic mice are generated by crossing tet_o-M71-IRES-tau-lacZ mice with OMP-IRES-tTA mice; these mice express both the M71 receptor and tau-lacZ marker protein in olfactory sensory neurons (Fig. 1a, 1c-1d, 1f-1h, 1j-1l).

Staining for the tau-lacZ marker protein demonstrates that lacZ is extensively expressed in the olfactory sensory epithelia in these M71 transgenic mice (Fig. 1c-1d). The pattern of lacZ expression in these M71 transgenic mice is comparable to that observed when the tau-lacZ protein is expressed in all olfactory sensory neurons via the OMP promoter (OMP-IRES-tau-lacZ mice, Mombaerts et al., 1996; Fig. 1b). Furthermore, staining with antibody shows widespread expression of the M71 receptor in the olfactory epithelia (Fig. 1g-1h, 1k-1l). Quantification of the number of sensory neurons in the main olfactory epithelium that express receptors other than M71 demonstrates that only ~5% of sensory neurons continue to express endogenous receptors (Fig. 2). Therefore, the M71 receptor is expressed in approximately 95% of olfactory sensory neurons in these transgenic mice.

Electrophysiology experiments have demonstrated that these M71 receptors are functional. Single cell recordings performed using a dissociated epithelium preparation indicate that the odor-evoked responses and biophysical properties of sensory neurons expressing the M71 receptor are nearly identical in M71 transgenic mice and controls (K-W Yau et al., unpublished data). In addition, we examined odor-evoked sensory neuron

activity at the population level by performing field potential recordings from the olfactory epithelia (electroolfactogram recordings) of M71 transgenic mice and controls. In control mice, acetophenone evoked a much smaller response than that which was evoked by a mixture of five odorants (carvone, lyral, limonene, isoeugenol, and heptanal at a concentration of 10 μM each; Fig. 3a, 3c). In contrast, acetophenone produced a dramatically larger response than the odorant mixture in M71 transgenic animals (Fig. 3b, 3c). This 160-fold change in the ratio of the field potential is likely to result from the dramatic increase in the frequency of sensory neurons expressing the acetophenone-responsive M71 receptor. These data demonstrate that exogenously expressed M71 receptors function in a manner that is indistinguishable from normally expressed M71 receptors and render the olfactory epithelium exquisitely sensitive to acetophenone (Fleischmann et al., 2008).

Staining for tau-lacZ and the M71 receptor in the olfactory bulb reveals that the axons from M71-expressing neurons course over the entire surface of the main olfactory bulb and innervate large numbers of glomeruli in M71 transgenic mice (Fig. 4a-4b, 4e-4f). The size of individual glomeruli remained comparable between M71 transgenic and control bulbs (Fig. 4j-4l, 4n-4p). When the pattern of projections from the ~5% of neurons that continue to express the P2 receptor in M71 transgenic mice was examined by crossing mice bearing a genetically modified allele of the P2 receptor (P2-IRES-GFP; Gogos et al., 2000) into the M71 transgenic background, these neurons projected their axons to the location of the P2 glomerulus observed in controls (Fig. 4i-4p). Thus, the olfactory bulb of M71 transgenic mice receives much diminished but normally targeting

sensory input from cells expressing endogenous receptors, and superimposed on this map are the pervasive projections from neurons driven to express the M71 receptor.

We performed functional imaging experiments to examine whether this altered pattern of olfactory sensory neuron projections is reflected in the pattern of odor-evoked glomerular activity in the bulb of M71 transgenic mice. M71 transgenic mice were crossed with mice expressing synapto-pHluorin, a pH-sensitive fluorescent indicator of synaptic release, in all olfactory sensory neurons (OMP-spH mice; Bozza et al., 2004). Two-photon imaging in these mice permitted us to monitor presynaptic glomerular activity in response to odor. In controls, individual odors (ethyl acetate, isoamyl acetate, eugenol and acetophenone) at a concentration of 1% (vol./vol. dilution) typically activated two to three glomeruli per field (~30 glomeruli total) with a $\Delta F/F$ of 5% (Fig. 5a-5d). In contrast, exposure of M71 transgenic animals to ethyl acetate, isoamyl acetate or eugenol failed to elicit a discernable glomerular response, likely a consequence of the marked reduction in sensory input from neurons expressing the endogenous receptor repertoire (Fig. 5f-5h). However, exposure of the M71 transgenic mice to 1% acetophenone resulted in the activation of an average of 51% of glomeruli imaged (Fig. 5i), and exposure to 10% acetophenone evoked activity in 75% of glomeruli in M71 transgenic mice (Fig. 5j).

Interestingly, the level of acetophenone-evoked activity in transgenic mice (1% odor, $\Delta F/F = 1.9\%$; 10% odor, $\Delta F/F = 1.8\%$) was substantially lower than acetophenone-induced glomerular activity in controls (1% odor, $\Delta F/F = 6.5\%$; 10% odor, $\Delta F/F = 5.9\%$), suggesting that inhibition of synaptic release is likely occurring at sensory axon termini in M71 transgenics. GABAergic periglomerular cells have been shown to inhibit

transmitter release from olfactory sensory neurons via $GABA_B$ receptors expressed on sensory neuron axon termini (Aroniadou-Anderjaska et al., 2000; McGann et al., 2005; Murphy et al., 2005; Vucinic et al., 2006). We therefore examined odor-evoked activity in the presence or absence of the $GABA_B$ receptor antagonist CGP46381. In control mice, odor-evoked responses to all odors tested exhibited only modest elevations in glomerular activity (13.3%) in the presence of CGP46381 (Fig. 5k-5l). In contrast, in CGP46381-treated M71 transgenic mice we observed a dramatic enhancement in the level of acetophenone-evoked glomerular activity (210% to 1% and 170% to 10%), as well as the recruitment of additional active glomeruli (90% of glomeruli active to both 1% and 10% acetophenone; Fig. 5m-5n). However, we still failed to observe significant changes in fluorescence in response to any other odor tested in M71 transgenic mice. Taken together, these results demonstrate that there is a significant decrease in presynaptic glomerular activity in response to all odors tested other than acetophenone, a significant increase in acetophenone-evoked sensory neuron input to the bulb, and active suppression of this widespread acetophenone-evoked input by GABAergic presynaptic inhibition in M71 transgenic mice.

Finally, the perceptual and behavioral consequence of these alterations in odor-evoked input to the bulb was examined using an assay for olfactory discrimination. M71 transgenic mice and littermate controls were trained to discriminate between pairs of odorants using a go/no-go behavioral assay (Abraham et al., 2004). For this go/no-go task, mice learn to associate one odor in the pair (the CS+) with the delivery of a water reward, and respond by moving to lick at a water delivery spout when the odor is presented; the other odor in the pair (the CS-) becomes associated with the lack of water

reward, and the animal learns to withhold movement to the water spout and licking when this odor is presented (Fig. 6). Using this paradigm, M71 transgenic mice could be trained to discriminate different odorants despite a 20-fold reduction in neurons expressing the endogenous receptor repertoire (Fig. 7a-7b, 7d-7e). However, M71 transgenic mice show decreased performance on an associative olfactory discrimination task when challenged with perceptually similar odors (Fig. 7c, 7f). Finally, these mice were unable to learn to discriminate acetophenone from air in the go/no-go assay, despite a 1000-fold increase in neurons expressing the M71 receptor (Fig. 7g-7i). These results demonstrate that, although M71 transgenic mice are able to detect and discriminate odors that widely differ in their molecular and perceptual characteristics, the ability of these mice to tell more similar odors apart is impaired. Furthermore, while these mice are able to detect and discriminate some odorants, M71 transgenic mice appear to be unable to smell the M71 receptor ligand acetophenone.

This transgenic model affords us the opportunity to examine the functional impact of genetically altering the stereotyped pattern of sensory neuron input to glomeruli on the processing of odor information by the olfactory bulb. While previous studies have revealed the way odor information is represented in these M71 transgenic mice at the level of input to the olfactory bulb, it is unclear how the bulbar circuitry deals with this altered pattern of odor-evoked activity, and how this pattern of odor information is represented at the level of output from the olfactory bulb. What happens to the way odor information is processed by the bulb when this sparse, stereotyped map of input is changed into a dense, homogeneous one? What does this tell us about how information about odor is transformed as it passes from the input layer to the output layer of the bulb?

Finally, what does this tell us about the role the olfactory bulb plays in olfactory perception and behavior?

We have performed two-photon imaging of odor-evoked activity at single-cell resolution in the olfactory bulb of M71 transgenic mice to examine the functional impact of altering the stereotyped pattern of sensory neuron input to glomeruli on the processing of odor information by the olfactory bulb. We have developed a method for imaging the responses of large populations of mitral and tufted cells, the output neurons of the olfactory bulb, via retrograde labeling with a novel rabies virus-conjugated calcium indicator. A modified rabies virus lacking a gene required for the production of infectious viral particles was used to drive expression of the calcium indicator GCaMP3 in mitral and tufted cells (SADΔG-GCaMP3) (Wickersham et al., 2010; Osakada et al., 2011; see Methods). Capitalizing on the fact that rabies virus enters neurons via components of the nerve terminal (Lentz et al., 1982; Lafon, 2008; Thoulouze et al., 1998; Shnell et al., 2010; see Methods), we made multiple injections of rabies-GCaMP3 virus into the region of olfactory cortex underneath the lateral olfactory tract, a fiber bundle containing the axons of mitral and tufted cells projecting to higher brain regions. After the injection procedure is complete, animals recover for 5-8 days to allow for robust expression of GCaMP3 before imaging is performed. Because this modified rabies virus lacks the gene encoding its viral glycoprotein, it is unable to spread transsynaptically, thereby restricting expression of GCaMP3 to the neurons directly infected via their axonal terminations during our injection procedure (Wickersham et al., 2007).

Using this method, we are able to routinely express GCaMP3 in hundreds of mitral and tufted cells in the olfactory bulb (Fig. 8a; mean = 40 +/- 3 cells per field of

view (~501.8 μM^2), max = 104 cells; min = 9 cells; n = 48 sites). Mitral and tufted cells infected with rabies-GCaMP3 using this method are homogeneously distributed across the olfactory bulb in a spatially unbiased manner (Fig. 8a-8c). We often observe several GCaMP3-expressing mitral and tufted cells projecting to the same glomerulus (Fig. 8b). Moreover, the cell bodies of neurons labeled with GCaMP3 are located in and just above the mitral cell layer of the bulb, demonstrating that this rabies-GCaMP3 virus allows us to selectively label the mitral and tufted projection neurons of the olfactory bulb (Fig. 8a-8b).

Mitral and tufted cells infected with rabies-GCaMP3 display robust stimulus-locked responses to odor, often reaching up to ~100% $\Delta F/F$ in response to high stimulus concentrations (Fig. 9b-9c, 9e-9f). These odor-evoked responses were consistent across trials (Fig. 9b, 9e), and increased in a linear fashion as the stimulus concentration was increased (Fig. 9c, 9f). Furthermore, we observed a similar number of cells responding to odor, as well as similar stimulus tuning in individual neurons, regardless of whether 5, 6 or 7 days had elapsed since infection (Fig. 10a-10b; (number of cells responding: mean p value = 0.1535; stimulus tuning: mean p value = 0.3337)). Finally, little evidence of cell death or toxicity was observed through 8 days post infection, suggesting that the function of mitral and tufted cells infected with rabies-GCaMP3 is largely unperturbed (Fig. 10c). Therefore, we have developed a high-throughput method that allows us to characterize odor-evoked activity in a targeted population of bulbar neurons, the mitral and tufted cells, using a novel rabies-GCaMP3 virus. Because mitral and tufted cells provide the sole output of the olfactory bulb (Davison and Katz, 2007), this technique permits us to

elucidate the representation of odor information that is propagated to a number of higher brain regions.

In control mice, we find that odors at low concentrations (1/10,000 vol./vol. dilution) typically evoke sparse, spatially distributed patterns of activity in 5-10% of mitral and tufted cells (Fig. 11a-11o; Fig. 12a; n = 4). Furthermore, we observe mitral and tufted cell responses to a variety of structurally and perceptually diverse odors tested regardless of whether the neurons are located in the posterior, medial, or anterior dorsal olfactory bulb (15 odors at 1/10,000 vol./vol. concentration; data not shown). Different odors could evoke activity in neurons that were located in distinct spatial locations within an imaging site (Fig. 11b, 11j, 11m). However, we found that mitral and tufted cells responsive to a given odor were often distributed across the site imaged (Fig. 11e, 11i, 11n, 11o). Increasing the concentration of odor typically increased the number of stimulus-responsive mitral and tufted cells in a linear fashion, with up to 60% of neurons responding at the highest concentrations tested (1/100 vol./vol., Fig. 11p-11x; Fig. 12b; n = 4).

Mitral and tufted cells generally displayed narrow stimulus tuning at low concentrations of odor, in accord with previously published results from electrophysiological recordings (Davison and Katz, 2007; Tan et al., 2010; Fig. 12c; Fig. 13a-13b). Most of the neurons we observed failed to respond to any of the 15 odors in the stimulus set used to probe selectivity (51%), while the majority of odor-responsive neurons displayed an increase in fluorescence to 1-4 stimuli (36%; Fig. 12c). However, we also observed a small population of more broadly tuned mitral and tufted cells. While the majority of these more broadly tuned neurons (10%) responded to 5-10 of the 15

odors presented, 4% of cells responded to 11-15 stimuli (Fig. 12c). In addition, mitral and tufted cells became increasingly broadly tuned as stimulus concentration was increased, an observation that is in accord with the increase in the number of cells that respond to each odor at higher concentrations (Fig. 12b; Fig. 13c-13d; n = 3). These observations are indicative of a representation of odor in the mitral cell layer of the bulb that is sparse and spatially distributed at low stimulus concentrations, and becomes increasingly more overlapping as odor magnitude is increased. Moreover, these data suggest that the representation of odor in the mitral cell layer of the bulb is largely determined by feedforward input from olfactory sensory neurons.

In M71 transgenic mice, there is a 20-fold reduction in sensory neurons expressing the endogenous receptor repertoire (Fig. 2). In addition, we were unable to detect glomerular responses to a variety of non-acetophenone odorants when imaging olfactory sensory neuron activity in these transgenic animals (Fig. 5). Nonetheless, we observed robust mitral and tufted cell responses to odor in M71 transgenic mice (Fig. 14b-14c, 14e- 14f). Responses of mitral and tufted cells in M71 transgenic mice were locked to stimulus delivery, and were reliable across trials (Fig. 14b, 14e). In addition, odor-evoked responses in mitral and tufted cells increased in a linear fashion as stimulus concentration was increased (Fig. 14b-14c, 14e-14f). Furthermore, the magnitude of these responses could reach ~100% $\Delta F/F$ on a given trial (Fig. 14b, 14e). These observations indicate that individual mitral and tufted cell responses to odor are similar in M71 transgenics and controls.

Strikingly, we were able to identify mitral and tufted cells responsive to every odor tested in these M71 transgenic mice (Fig. 15a-15o; Fig. 1d; n = 3). We observed

mitral and tufted cell responses to a diverse panel of odorants in M71 transgenic mice regardless of whether the neurons were located in the posterior, medial, or anterior dorsal olfactory bulb (15 odors at 1/10,000 vol./vol. concentration; data not shown). Similar to what we observed in control mice, different odors could evoke activity in neurons located in distinct locations at a given imaging site (Fig. 15a, 15d). However, cells responsive to odor were often distributed across a given imaging location (Fig. 15b, 15h, 15i). These data demonstrate that, despite a drastic reduction in sensory neuron activity in response to odors other than acetophenone, a wide variety of odorants are able to evoke responses from mitral and tufted cells in M71 transgenic mice.

Not only do we find that a variety of non-acetophenone odorants can evoke activity in mitral and tufted cells in M71 transgenic mice, we find that a significantly larger number of neurons are responsive to stimuli in M71 transgenics compared to controls, with up to 30% of mitral and tufted cells responding to a given odor at low concentrations (Fig. 12d; $p = 0.0168$; $n = 3$). Furthermore, increasing the concentration of odor tended to increase the number of mitral and tufted cells responsive to odor in a nonlinear fashion, with up to 80% responding to odorants at the highest stimulus concentration delivered (1/100 vol./vol., Fig. 15p-15x; Fig. 16c-16d; Fig. 12b; $n = 3$). Finally, we find that odor-evoked responses are slightly, although not significantly, greater in magnitude in M71 transgenic mice at low concentrations of odor (Fig. 17a; $p = 0.0837$). Taken together, these observations suggest the existence of circuit mechanisms intrinsic to the olfactory bulb that can powerfully amplify weak stimulus-evoked sensory neuron input.

Similar to what was observed in controls, mitral and tufted cells tend to display narrow stimulus tuning (Fig. 12f; Fig.16a-16b; $p = 0.6325$). We observed a slight increase in the number of narrowly tuned mitral and tufted cells, in accord with the increase in odor-responsive neurons seen in M71 transgenics (Fig.12f). While many mitral and tufted cells still failed to respond to any of the 15 odors in the stimulus set used to probe selectivity (37%), a greater number of neurons displayed an increase in fluorescence to 1-4 stimuli (52% of cells; Fig. 12f). Also similar to what was observed in controls, we found a small population of neurons that were more broadly tuned to odor; 8% of cells responded to 5-10 of the 15 odors presented, while 4% of cells responded to 11-15 stimuli (Fig. 12f). In addition, mitral and tufted cells in M71 mice also became increasingly broadly tuned as stimulus concentration was increased, an observation that is in accord with the dramatic increase in the number of cells that respond to each odor at higher concentrations (Fig. 16c-16d).

In M71 transgenic mice, there is a 1000-fold increase in the number of olfactory sensory neurons expressing the acetophenone-responsive M71 receptor (Fig. 1, Fig. 2). Furthermore, electrophysiological recording and imaging of olfactory sensory neuron activity has demonstrated a massive increase in the number of neurons and glomeruli responding to acetophenone (Fig. 3, Fig. 5). Despite this massive increase in acetophenone-evoked sensory neuron activity, we find that the number of mitral and tufted cells responsive to acetophenone is similar to that observed for many of the other odors tested at low concentrations in M71 transgenic mice (Fig. 12d). In addition, the spatial distribution of acetophenone-evoked responses is not different from that seen for other odors in M71 transgenic mice (Fig. 15a-15o). The magnitude of mitral and tufted

cell responses evoked by acetophenone is similar in M71 transgenics and controls (Fig. 17b; $p = 0.8067$). However, when we examined mitral and tufted cell responses to a concentration series of odors in M71 transgenics, we observed a sharp, nonlinear increase in the number of neurons responding to high concentrations of acetophenone as well as 2-hexanone, both of which have been demonstrated to activate the M71 receptor (K-W Yau et al., unpublished data; Fig. 12e; Fig. 16c-16d). These observations, as well as our previous data from functional imaging experiments (Fig. 5), suggest that inhibition is likely to be recruited at multiple levels of the olfactory bulb to suppress widespread odor-evoked activity in M71 transgenic mice.

In summary, we observe evidence of both excitatory mechanisms that serve to amplify weak sensory neuron input, as well as inhibitory mechanisms that actively suppress strong, pervasive input from olfactory sensory neurons. The combination of these excitatory and inhibitory mechanisms may prevent a particularly strong odor from evoking overwhelming excitation in the bulb, and allow for the detection of signals from weaker stimuli that may also be present.

The piriform cortex is a major target of mitral and tufted cell axons, which densely ramify in a disperse, fan-like manner across its surface (Ghosh et al. 2011; Sosulski et al., 2011). Functional imaging and electrophysiology studies indicate that a given odor will evoke activity in a sparse ensemble of neurons distributed in an apparently random fashion across the piriform (Illig and Haberly, 2003; Rennaker et al., 2007; Poo and Isaacson, 2009; Stettler and Axel, 2009). However, the degree to which this sparse, topographically disperse representation is generated by computations performed by circuits within the piriform cortex, versus the degree to which the nature of

this representation is determined by the disperse feedforward input from the olfactory bulb is just beginning to be resolved.

Because the representation of odor in the mitral cell layer of the olfactory bulb of M71 transgenic mice differs from that which we observed in controls with regard to the number of cells that respond to odor as well as the magnitude of odor-evoked responses, we reasoned that we could use these M71 transgenic mice to investigate whether the representation of odor in the piriform is dominated by feedforward input from mitral and tufted cells, or whether it is largely the result of transformations performed by local circuits within the piriform itself. We therefore used an adenoassociated virus-conjugated calcium indicator, AAV-GCaMP3, to examine how odor information is represented in the piriform cortex of M71 transgenic mice (Tian et al., 2009). Stereotaxic injections of AAV-GCaMP3 were made into the center of the piriform, and odor-evoked responses were examined 8-12 days later to allow for high levels of GCaMP3 expression before imaging (see Methods).

These AAV-GCaMP3 injections resulted in the labeling of hundreds of neurons extending over several millimeters of the piriform cortex (Fig. 18; mean = 178 cells +/- 6 per field of view (416.3 μM^2), max = 260 cells, min = cells 74; n = 56 sites). The majority of neurons labeled had cell bodies located in layer II of piriform (Fig. 18b). A small complement of GCaMP3-labeled cells was also seen in layers I and III (Fig. 18a, 18c), reflecting the known laminar distribution of neurons in piriform cortex (Shepherd, 1994). We observed robust stimulus-locked responses that were reliable across trials from piriform cortex neurons expressing GCaMP3 (Fig. 19b-19c, 19e-19f). These responses could reach as high as ~30% $\Delta F/F$ on a single trial (Fig. 19b, 19e).

At the population level, we observed a sparse, distributed representation of odor in which a given odorant evoked activity in a topographically disperse ensemble of neurons, in accord with what has previously been reported (Poo and Isaacson, 2009; Stettler and Axel, 2009; Fig. 20a-20f). Different odors reliably evoked activity in unique ensembles of piriform neurons (Fig. 20a-20f). Odors typically evoked activity in 5-15% of all piriform neurons (Fig. 20a). Moreover, this was true even when the concentration of an odor stimulus was increased over three orders of magnitude (1/10,000-1/100 vol./vol. dilution in mineral oil, Fig. 20g-20o; Fig. 21a-21b; n = 10). Interestingly, the magnitude of responses evoked by high concentrations of an odorant were often very similar to those evoked by low concentrations of the same stimulus (Fig. 19b-19c, 19e-19f). Individual neurons in piriform generally displayed narrow stimulus tuning, with the majority of cells responding to one or two odorants out of a set of six even at the highest stimulus concentrations tested (1/100 vol./vol., Fig. 21c; Fig. 22a-22b; n = 3). Response magnitudes were most often small, with the vast majority of $\Delta F/Fs$ falling below 10% (Fig. 23a). These results indicate that odors are represented in a much more sparse, decorrelated manner, and within a significantly smaller dynamic range, in the piriform cortex compared to the olfactory bulb.

Despite the fact that the representation of odor in the olfactory bulb of M71 transgenic mice differs significantly from that which we observed in controls, we find that the representation of odor in the piriform cortex of M71 transgenic mice and controls is quantitatively indistinguishable. Similar to what was observed in controls, we saw robust odor-evoked responses from piriform cortex neurons expressing GCaMP3 in M71 mice (Fig. 24b-24c, 24e-24f). In addition, these odor-evoked responses were also locked

to stimulus delivery, were reliable across trials (Fig. 24b, 24e), and could reach as high as ~30% ΔF/F on a single trial (Fig. 24b, 24e).

We observed no obvious difference in the topographic organization of odor-responsive neurons in M71 transgenics and control mice. All odors tested, including acetophenone, evoked activity in a sparse ensemble of 5-15% of neurons that was spatially distributed across the piriform cortex (Fig. 25a-25f; Fig. 21d; n = 6; p = 0.3180). Similar to what was observed in controls, this was true even when the concentration of an odor stimulus was increased over three orders of magnitude (1/10,000-1/100 vol./vol., Fig. 25g-25o; Fig. 21e; n = 3; p = 0.6751). Again, the magnitude of responses evoked by high concentrations of an odorant were often very similar to those evoked by low concentrations of the same stimulus (Fig. 24b-24c, 24e-24f). Similar to what was observed in controls, neurons in the piriform cortex of M71 transgenic mice most often displayed narrow stimulus tuning (Fig. 21f; Fig. 26a-26b; p = 0.8827). The distribution of response magnitudes was nearly indistinguishable in M71 transgenics and controls, with most odor-evoked responses falling below 10% ΔF/F (Fig. 23a; p = 0.5156). Moreover, even when responses to acetophenone were analyzed separately, the distribution of response magnitudes remained similar in M71 mice and controls (Fig. 23b; p = 0.2086).

These results suggest that the intrinsic circuits of the piriform significantly transform the representation of odor information as it moves from the olfactory bulb to the piriform cortex. In comparison to the olfactory bulb, the piriform cortex represents odor in a sparser, more decorrelated manner within a much narrower dynamic range, and this representation of odor is highly consistent even in the face of large fluctuations in input. The nature of this representation of odor, with its limited overlap between

ensembles of neurons responsive to different stimuli and narrow dynamic range, may allow for the successful perception and discrimination of odors even in the face of a rapidly changing sensory environment.

Discussion

The mammalian olfactory system mediates a variety of learned and innate olfactory behaviors, and understanding how the detection of an odor in the environment leads to the generation of a behavioral response depends upon an understanding of how odor information is represented and transformed as it moves from the sensory periphery to the highest regions of the brain. We have performed functional imaging of odor-evoked responses in the olfactory bulb and piriform cortex of transgenic mice with a "monoclonal" nose to investigate how odor information is represented and transformed by these areas, and correspondingly, what role these areas may be performing in olfactory perception and behavior.

Our observations of cells responsive to a wide variety of odors, a larger number of odor-responsive mitral and tufted cells, and an increase in the magnitude of responses in M71 transgenic mice all point to the existence of circuit mechanisms with the ability to greatly amplify stimulus-evoked activity. It has long been argued that the basic organization of the olfactory bulb glomerulus, with its massive convergence of olfactory sensory neuron input, electrical coupling between mitral cells connected to the same glomerulus, and self-excitation of intraglomerular mitral cell assemblies, is designed to improve odorant signal detection, but data in direct support of this point has been lacking

(Nicoll and Jahr 1982; Isaacson 1999; Margrie et al 2001; Schoppa and Westbrook 2001; Schoppa and Westbrook 2002; Urban and Sakmann 2002; Fadool et al., 2004; Murphy et al., 2004; Chen and Shepherd 2005; Christie et al. 2005). Our genetic approach has allowed us to selectively alter the ratio of sensory neuron convergence onto glomeruli, while leaving postsynaptic circuit features such as electrical coupling and mitral cell self-excitation unperturbed. Therefore, our results directly demonstrate a role for the anatomical convergence of sensory neuron input to glomeruli in the amplification of signals from olfactory sensory neurons as well as the perceptual detection of weak odor stimuli.

In M71 transgenic mice, the similarity of mitral and tufted cell responses evoked by acetophenone and other odors suggests that powerful inhibitory mechanisms exist within the bulb to prevent runaway excitation evoked by strong sensory inputs to the glomerular layer. Past work has provided evidence for the existence of feedback inhibition mediated by GABAergic periglomerular cells in the bulb that reduces stimulus-evoked transmitter release from sensory neurons and scales with stimulus strength (Aroniadou-Anderjaska et al., 2000; McGann et al., 2005; Murphy et al., 2005; Vucinic et al., 2006). Our previous work indicates that in M71 transgenic mice, GABAergic feedback inhibition of sensory neuron transmitter release serves to significantly reduce the amount of acetophenone-evoked excitatory drive to the mitral and tufted cells of the bulb (Fleischmann et al., 2008). This presynaptic inhibition is likely to suppress sensory neuron activity in response to acetophenone across the surface of the bulb in a global manner.

In addition to presynaptic inhibition of sensory neuron activity, mitral and tufted cell responses can also be modulated by GABAergic granule cell input. Granule cells extend a dendritic process into the external plexiform layer of the bulb, where they form dendrodendritic synapses on the lateral dendrites of mitral cells (Shepherd, 1994). These dendrodendritic synapses allow granule cells to modulate the stimulus tuning and output of mitral and tufted cells by means of a powerful feedback inhibition (Jahr and Nicoll, 1980; Yokoi et al., 1995; Isaacson and Strowbridge, 1998; Margrie et al., 2001). Interestingly, recent work has demonstrated the existence of an activity-dependent lateral inhibition mediated by granule cells that preferentially targets neurons displaying correlated stimulus-evoked activity (e.g. similar odor tuning), and operates only when mitral and tufted cell activity is neither too low nor too high (Arevian et al., 2008). This inhibitory mechanism could explain why, despite the dense, homogenous nature of acetophenone-evoked sensory neuron input to the bulb, we do not observe a dense, homogenous pattern of mitral and tufted cell responses to acetophenone. Moreover, it provides an explanation regarding why we do observe widespread acetophenone-evoked mitral and tufted cell responses at the highest stimulus concentrations, which likely drive these neurons to fire above the range of activity for which this inhibition is observed. Future experiments can begin to tease apart the inhibitory mechanisms that shape the bulbar representation of odor in M71 transgenics by examining odor-evoked periglomerular cell and granule cell activity in these mice using bulbar injection of AAV-GCaMP3.

In the piriform cortex, we find that odor-evoked responses in M71 transgenics are quantitatively indistinguishable from those we observe in controls for a variety of

measures. In both M71 transgenics and controls, each odor tested at a variety of concentrations evoked activity in a sparse, spatially distributed ensemble of neurons. Moreover, the similarity of the representation of odor in the piriform cortex of M71 transgenics and controls, as well as the narrow dynamic range of odor-evoked responses revealed by using multiple concentrations of odor, demonstrates that the representation of odor information in the piriform is highly consistent even in the face of dramatic fluctuations in input. These results suggest that circuits intrinsic to the piriform cortex transform the representation of odor information it receives from the mitral and tufted cells of the bulb into a highly sparse, topographically disperse representation in which odor-evoked activity is kept within a small dynamic range.

These observations are in line with a number of recent studies of the intrinsic circuitry of the piriform cortex. Electrophysiology experiments have demonstrated that inhibition of neurons in the PC is widespread and broadly tuned, and that this inhibition serves to sparsen the representation of odor in the PC (Poo and Isaacson, 2009). A form of feedforward inhibition mediated by GABAergic neurons that receive direct input from mitral and tufted cells has also been described (Luna and Schoppa, 2008). This inhibition abruptly terminates principal neuron activation in the piriform cortex, which may play a role in keeping odor-evoked piriform activity in a small dynamic range. Recent work has also provided evidence for an activity-dependent feedforward inhibition mediated by GABAergic neurons activated by input from pyramidal cells within the piriform itself (Franks et al., 2011; Poo and Isaacson, 2011). This locally mediated inhibition has the ability to further sparsen activity evoked by mitral and tufted cell input. Finally, recent work has demonstrated that individual pyramidal cells in piriform are weakly connected

by long-range excitatory connections, providing a means by which odor information transmitted from the olfactory bulb can be further distributed across the piriform cortex (Franks et al., 2011).

The piriform cortex, therefore, does not passively receive its representation of odor from the axonal projections of mitral and tufted cells but actively transforms input from the bulb into a highly sparse, distributed, decorrelated representation of its own using a number of excitatory and inhibitory circuit mechanisms. The sparse, distributed representation of odor information we observe in the piriform minimizes overlap between stimuli, maximizes decorrelation between patterns of odor-evoked activity, and may enhance not only the discrimination of odor stimuli but also enhance sensory-evoked associative learning (Barlow, 1972; Ito et al., 2008).

Taken together, our results demonstrate that information about odors is significantly transformed as it passes through the mouse olfactory system from the sensory periphery to the cerebral cortex, and the unique nature of these transformations suggests distinct functional roles for the olfactory bulb and piriform cortex in olfactory processing, perception and behavior. The representations and transformations of odor information we observe in the olfactory system of the mouse bear great similarity to those that have been reported in both the zebrafish and the fruit fly, suggesting that despite vast differences in terrestrial environments and millions of years of evolutionary time, the principles that underlie olfactory processing remain largely the same (Perez-Orive et al., 2002; Wilson et al., 2004; Assisi et al., 2007; Yaksi et al., 2007; Turner et al., 2008; Yaksi et al., 2009). In all three organisms the representation of odor information is significantly transformed as it passes from the sensory periphery to higher olfactory

areas, with representations shifting from a convergent, overlapping representation of odor information to a sparser, more topographically disperse representation with a smaller dynamic range. These distinct representations of olfactory information are likely to reflect the unique functional roles of these areas, from aiding in the detection and discrimination of the vast universe of chemical stimuli in the environment around us to mediating the formation of olfactory associations that underlie olfactory perception, memory and behavior.

Figure 1.

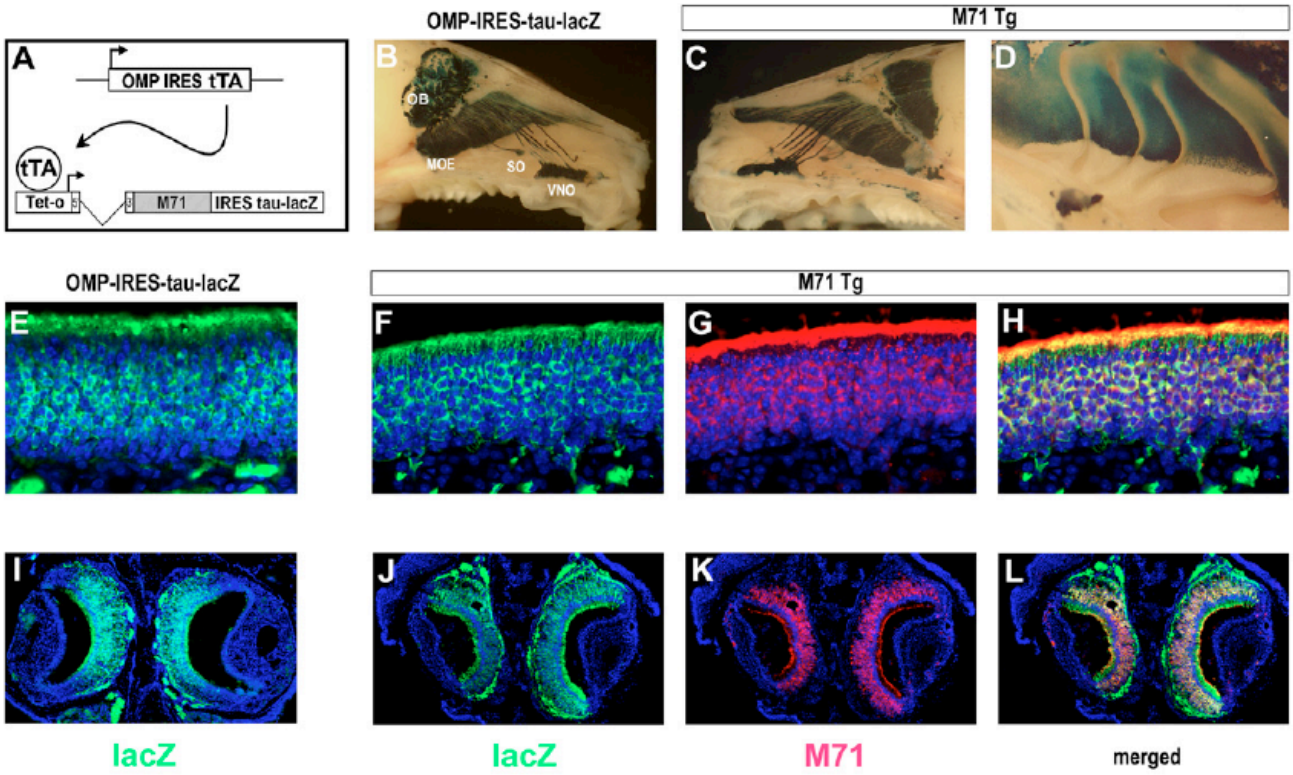
A
OMP IRES tTA
tTA
Tet-o
M71
IRES tau-lacZ
OMP-IRES-tau-lacZ
B
OB
MOE
SO
VNO
M71 Tg
C
D
OMP-IRES-tau-lacZ
E
M71 Tg
F
G
H
I
J
K
L
lacZ
lacZ
M71
merged

Figure 1. Expression of the tet_O-IRES-tau-lacZ transgene in olfactory sensory epithelia. (A) Schematic of the genetic strategy to express the M71 odorant receptor in all olfactory sensory neurons. The transgene tet_O-M71-IRES-tau-lacZ can be activated in all olfactory sensory neurons by the expression of tTA from the OMP-IRES-tTA locus. **(B)** Expression of OMP-IRES-tau-lacZ (detected by X-gal staining, blue) marks olfactory sensory neurons in a whole-mount preparation in: the main olfactory epithelium (MOE), septal organ (SO), and vomeronasal organ (VNO), as well as in axons of sensory neurons from these areas as they project to the main olfactory bulb (OB) and accessory olfactory bulb. **(C)** The expression of the M71 transgene in all of the sensory epithelia detected by X-gal staining (blue) of a whole-mount preparation. **(D)** Expression of the M71 transgene across all zones of the MOE as detected by X-gal staining in a whole-mount preparation. **(E)** Immunohistochemical detection of the expression of lacZ (green) in coronal sections through the olfactory epithelium of control, OMP-IRES-tau-lacZ mice, counterstained with TOTO-3 (blue). **(F-H)** Immunohistochemical detection of the expression of lacZ (green) in coronal sections through the olfactory epithelium of M71 transgenic mice. **(F)** Staining with antibody to lacZ (green). **(G)** Staining with antibody directed against the M71 receptor (red). **(H)** Merged fields of **(F)** and **(G)**. Nuclei are counterstained with TOTO-3 (blue). **(I)** Immunohistochemical detection of the expression of lacZ (green) in coronal sections through the VNO of control OMP-IRES-tau-lacZ mice, counterstained with TOTO-3 (blue). **(J-L)** Immunohistochemical detection of the expression of lacZ and M71 in coronal sections through the VNO of M71 transgenic mice. **(J)** Staining with antibody to lacZ (green). **(K)** Staining with antibody directed against the M71 receptor (red). **(L)** Merged fields of **(J)** and **(K)**. Nuclei are counterstained with TOTO-3 (blue).

Figure 2.

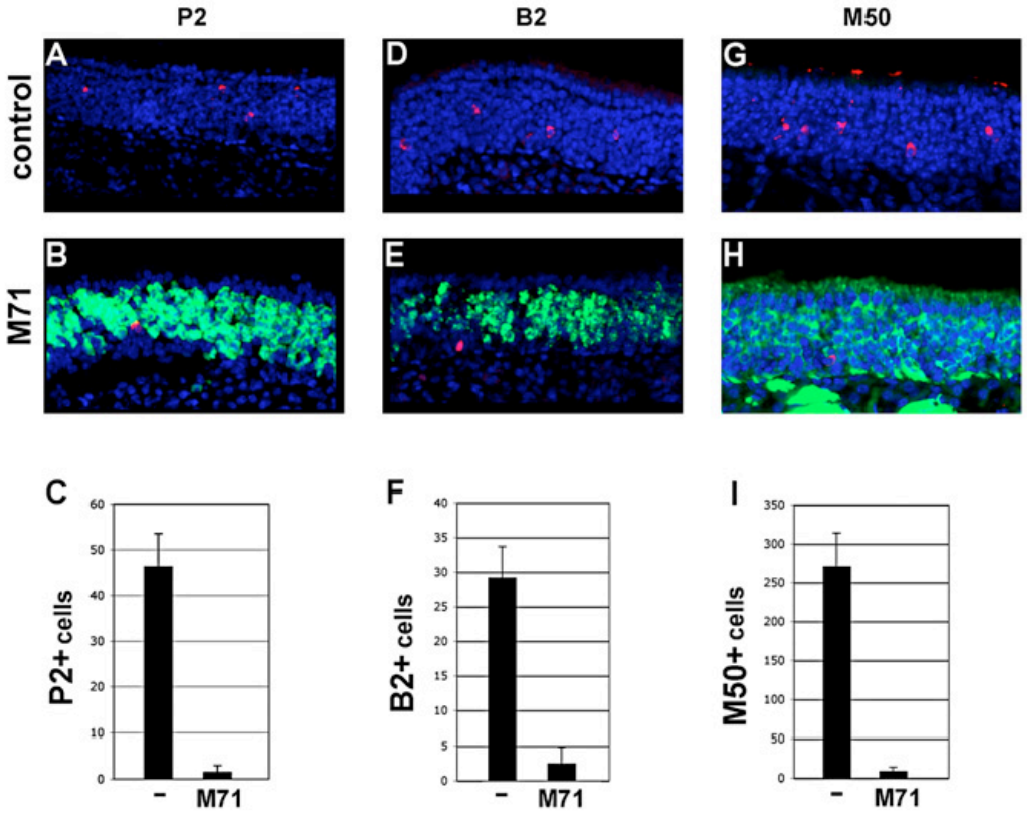
P2
B2
M50
control
M71
A
B
C
D
E
F
G
H
I
P2+ cells
B2+ cells
M50+ cells
-
M71

Figure 2. Expression of the endogenous odorant receptor genes in M71 transgenic and control mice detected in coronal sections through the main olfactory epithelium. Average number of cells expressing the endogenous OR gene per section (n = 10) is shown for each receptor in the graphs below. **(A and B)** Two-color RNA in situ hybridization with differentially labeled riboprobes, lacZ (green) and OR P2 (red), in sections from control **(A)** and M71 transgenic **(B)** mice. Nuclei are counterstained with TOTO-3 (blue). **(C)** P2+ cells in controls = 46.5 +/- 7.1 (SD); in M71 transgenics = 1.6 +/- 1.4 (SD). **(D and E)** Two-color RNA in situ hybridization with differentially labeled riboprobes, lacZ (green) and OR B2 (red), in sections from control **(D)** and M71 transgenic mice **(E)**. **(F)** B2+ cells in controls = 29.2 +/- 4.1 (SD); in M71 transgenics = 2.5 +/- 1.7 (SD). **(G and H)** Immunohistochemical detection of lacZ and OR M50. Antibody directed against lacZ (green) and M50 (red) in sections from control **(G)** and M71 transgenic mice **(H)**. **(I)** M50+ cells in controls = 271 +/- 43 (SD); in M71 transgenics = 8.8 +/- 5.2 (SD). Nuclei are counterstained with TOTO-3 (blue).

Figure 3.

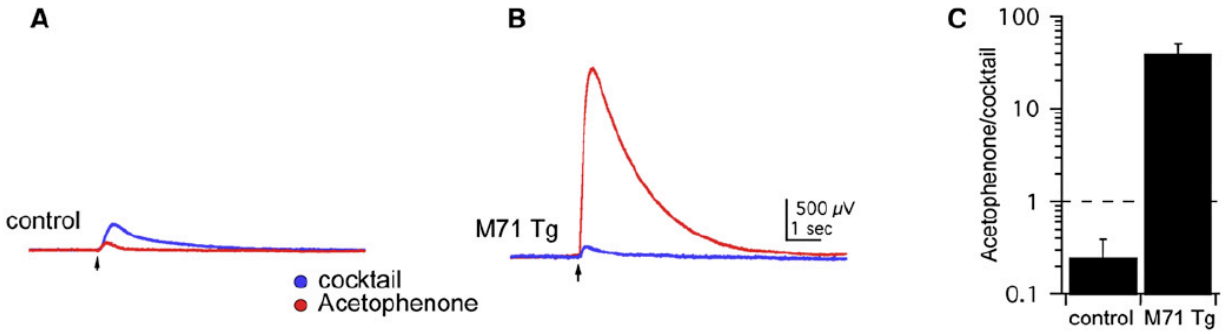
A
control
cocktail
Acetophenone
B
M71 Tg
500 μV
1 sec
C
100
10
1
0.1
Acetophenone/cocktail
control
M71 Tg

Figure 3. Odor-evoked activity in the epithelium of M71 transgenic mice. (A-C) Representative electroolfactogram (EOG; e.g. epithelium field potential) recordings from control **(A)** and M71 transgenic **(B)** mice in response to either a cocktail of odorants (blue) or to acetophenone (red). **(C)** Acetophenone sensitivity in M71 transgenic mice and control mice, expressed as the ratio of integrated EOG responses to acetophenone and to an odorant cocktail.

Figure 4.

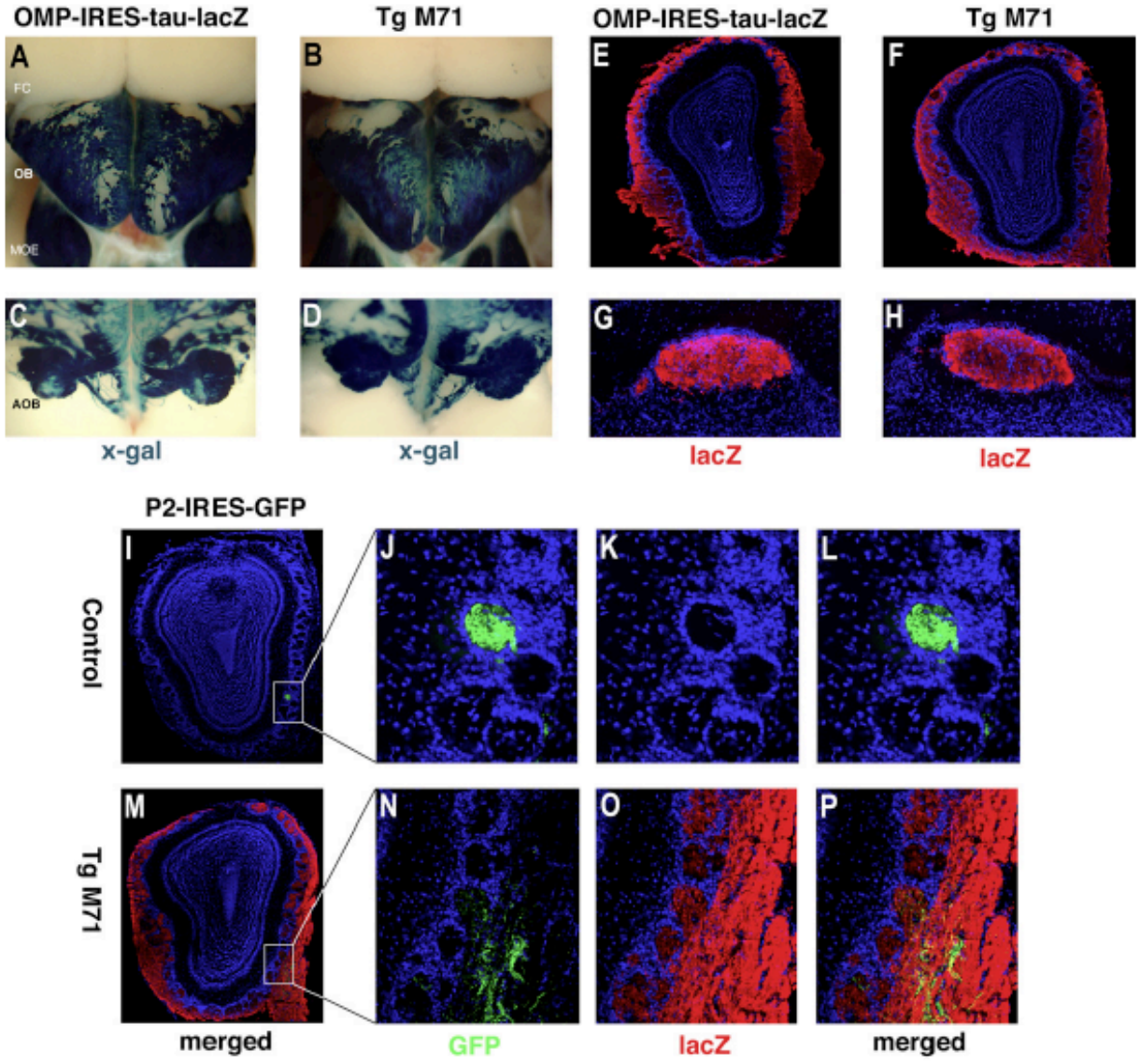
OMP-IRES-tau-lacZ
Tg M71
OMP-IRES-tau-lacZ
Tg M71
A
FC
OB
MOE
B
E
F
C
AOB
D
G
H
x-gal
x-gal
lacZ
lacZ
P2-IRES-GFP
Control
I
J
K
L
Tg M71
M
N
O
P
merged
GFP
lacZ
merged

Figure 4. Pervasive innervation of the olfactory bulb in M71 transgenic mice. (A) Dorsal view of an X-gal stained (blue) whole-mount preparation revealing the olfactory bulb (OB), main olfactory epithelium (OE), and frontal cortex (FC) of a control OMP-IRES-tau-lacZ animal reveals the extent of sensory neuron input to the bulb. **(B)** Dorsal view of an X-gal stained whole-mount preparation of an M71 transgenic animal. **(C)** Dorsocaudal view of an X-gal stained whole-mount preparation of a control OMP-IRES-tau-lacZ animal reveals the extent of sensory input to the accessory olfactory bulb (AOB). **(D)** Dorsocaudal view of an X-gal stained whole-mount preparation of an M71 transgenic animal. **(E)** Immunohistochemical staining with antibody directed against lacZ (red) of a coronal section through the main olfactory bulb of a control OMP-IRES-tau-lacZ animal, counterstained for nuclei with TOTO-3 (blue). **(F)** Immunohistochemical detection of lacZ+ fibers (red) in a coronal section through the main olfactory bulb of an M71 transgenic animal. **(G)** Immunohistochemical staining with antibody directed against lacZ (red) of a coronal section through the accessory olfactory bulb of a control OMP-IRES-tau-lacZ animal, counterstained for nuclei with TOTO-3 (blue). **(H)** Immunohistochemical detection of lacZ+ fibers (red) in a coronal section through the olfactory bulb of an M71 transgenic animal. **(I-P)** Diminished sensory input from fibers expressing endogenous OR and co-innervation of glomeruli in M71 transgenic animals. **(I)** Coronal sections of the olfactory bulb of P2-IRES-GFP control mice reveal P2 axons converging to form a single glomerulus, as visualized by antibody to GFP (green) and TOTO-3 nuclear counterstain (blue) in low-power and **(J-L)** high-power images of the boxed region in **(I)**. **(M)** In a low-power image of a coronal section through the olfactory bulb of an M71 transgenic animal, also bearing the P2-IRES-GFP allele, diminished

numbers of P2+ axons (green) converge on the P2 glomerulus in the presence of lacZ+ axons (red). **(N-P)** High-power images of boxed region in **(M)** reveal co-innervation of the P2 glomerulus, as detected by anti-GFP antibody (green, **(N)**), by lacZ+ fibers detected by antiserum to lacZ (red, (**O)**) and merged in **(P)**. Nuclei are counterstained by TOTO-3 (blue).

Figure 5.

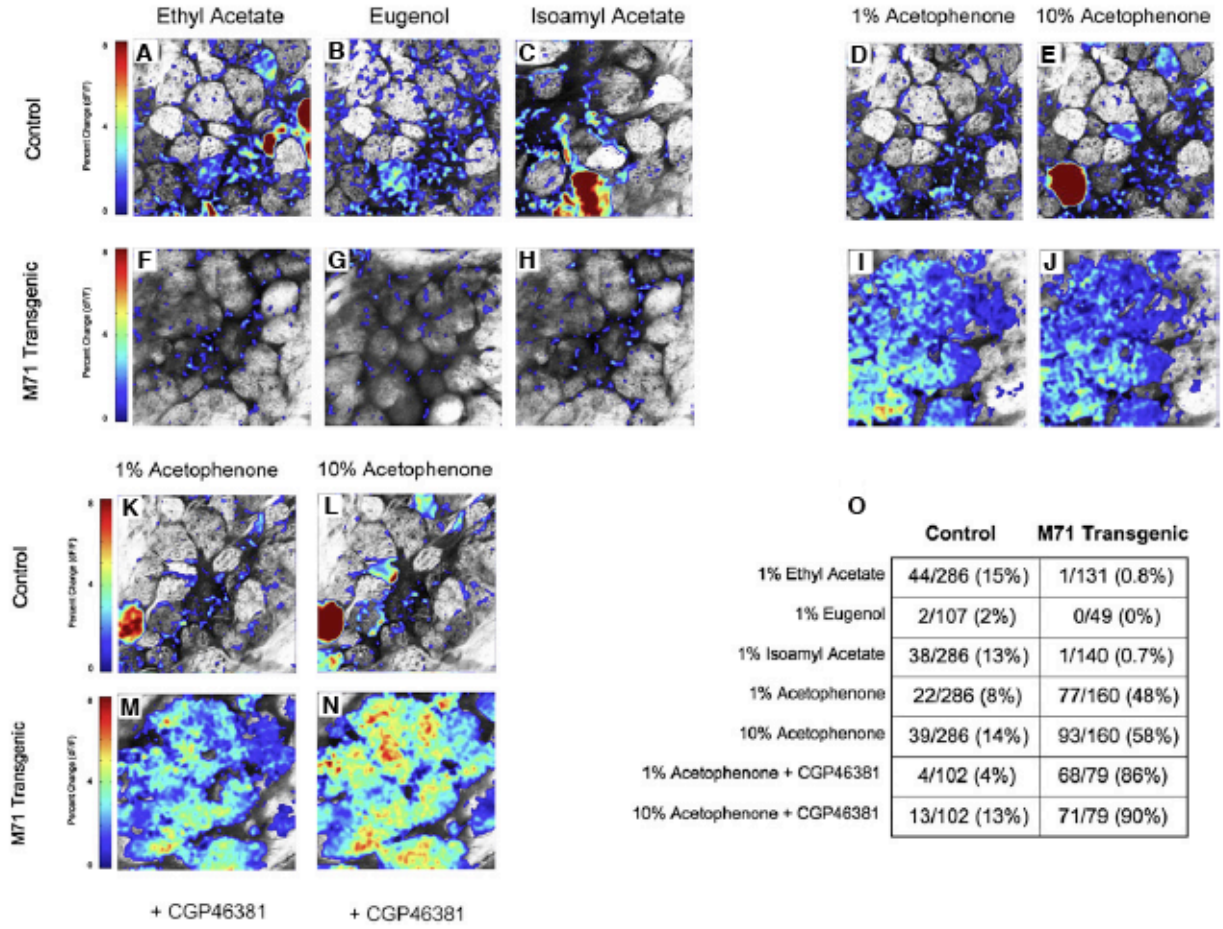

O

	Control	M71 Transgenic
1% Ethyl Acetate	44/286 (15%)	1/131 (0.8%)
1% Eugenol	2/107 (2%)	0/49 (0%)
1% Isoamyl Acetate	38/286 (13%)	1/140 (0.7%)
1% Acetophenone	22/286 (8%)	77/160 (48%)
10% Acetophenone	39/286 (14%)	93/160 (58%)
1% Acetophenone + CGP46381	4/102 (4%)	68/79 (86%)
10% Acetophenone + CGP46381	13/102 (13%)	71/79 (90%)

Figure 5. Odor-evoked activity in the olfactory bulb of M71 transgenic mice. (A-N) Two-photon imaging of odor-evoked activity in the olfactory bulb in response to 1% ethyl acetate, 1% eugenol, and 1% isoamyl acetate in control **(A-C)** and M71 transgenic animals **(F-H)**. Pseudocolored heat maps show mean percent change in fluorescence ($\Delta F/F$) for each odor. Activity evoked by 1% acetophenone and 10% acetophenone in control **(D-E)** and M71 transgenic animals **(I-J)**. Activity evoked by 1% and 10% acetophenone in the presence of the $GABA_B$-receptor antagonist CGP46381 in control **(K-L)** and M71 transgenic bulbs **(M-N)**; same image fields as before antagonist application, as shown in **(D-E)** and **(I-J)**. **(O)** Summary table of the fraction of glomeruli responding to each odor in control and M71 transgenic mice.

Figure 6.

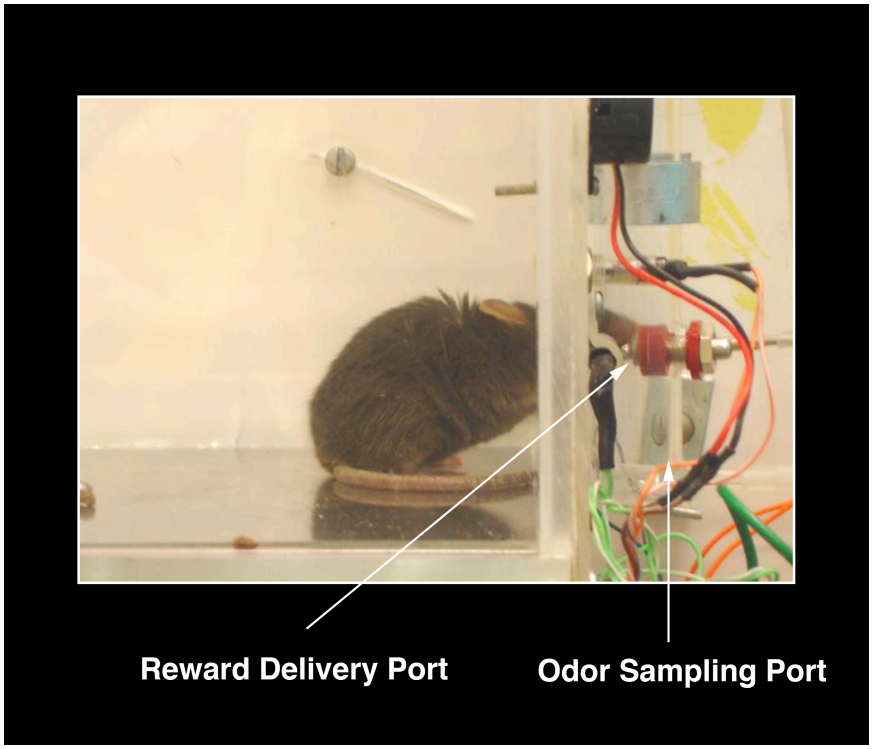

Figure 6. Schematic of the behavioral chamber used for the go/no-go odor pair discrimination task. Animals are trained to poke their nose into an odor sampling port (gray), where a brief puff of odor is delivered via a computer-controlled olfactometer. Depending on the identity of the odor stimulus (CS+ or CS-), the animal must decide whether to lick at a reward delivery port (CS+) or withhold licking at the reward port (CS-). Correct responses result in the delivery of water at the reward delivery port. Animals were water restricted (~1-1.5 ml per day) to maintain 85-90% of baseline weight for 1 week prior to behavioral training and testing.

Figure 7.

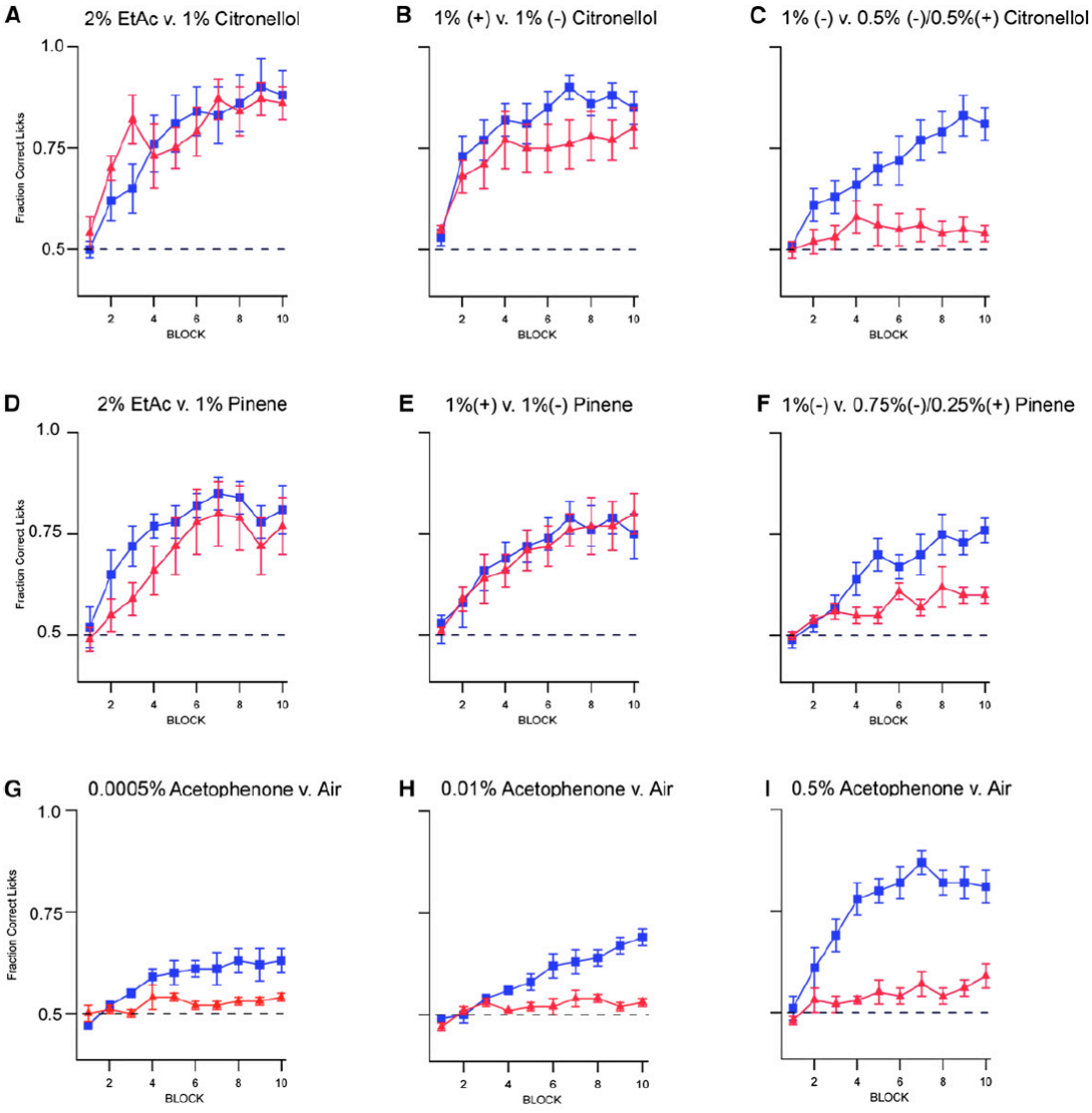
A
2% EtAc v. 1% Citronellol
B
1% (+) v. 1% (-) Citronellol
C
1% (-) v. 0.5% (-)/0.5%(+) Citronellol
D
2% EtAc v. 1% Pinene
E
1%(+) v. 1%(-) Pinene
F
1%(-) v. 0.75%(-)/0.25%(+) Pinene
G
0.0005% Acetophenone v. Air
H
0.01% Acetophenone v. Air
I
0.5% Acetophenone v. Air
Fraction Correct Licks
1.0
0.75
0.5
2
4
6
8
10
BLOCK

Figure 7. M71 transgenic mice display deficits in olfactory discrimination. (A-C) Control mice (blue) can discriminate between 2% ethyl acetate and 1% citronellol **(A)**, between 1% (+) citronellol and 1% (-) citronellol **(B)**, and between 1% (-) citronellol and a mix of 0.5% (+) citronellol/0.5%(-) citronellol **(C)**. M71 transgenic mice (red) can discriminate between 2% ethyl acetate and 1% citronellol **(A)** and between 1% (+) citronellol and 1% (-) citronellol **(B)**, but they fail to discriminate between 1% (-) citronellol and a mix of 0.5% (+) citronellol/0.5% (-) citronellol **(C)**. **(D-F)** Control mice (blue) can discriminate between 2% ethyl acetate and 1% pinene **(D)**, between 1% (+) pinene and 1% (-) pinene **(E)**, and between 1% (-) pinene and a mix of 0.25% (+) pinene/0.75% (-) pinene **(F)**. M71 transgenic mice (red) can discriminate between 2% ethyl acetate and 1% pinene **(D)** and between 1% (+) pinene and 1% (-) pinene **(E)**, but they fail to discriminate between 1% (-) pinene and a mix of 0.25% (+) pinene/0.75% (-) pinene **(F)**. **(G-I)** Control mice (blue) show increasing accuracy in the discrimination of acetophenone and air (no odor stimulus) as acetophenone concentration is increased from 0.0005% to 0.5%. M71 transgenic mice (red) fail to discriminate between acetophenone and air at all concentrations tested.

Figure 8.

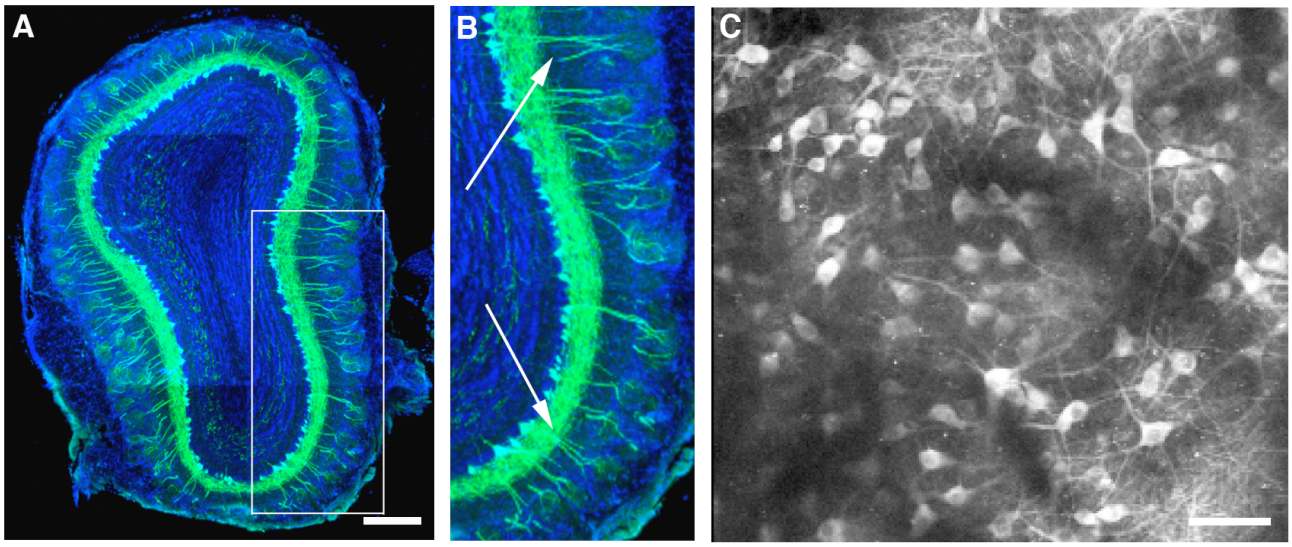

Figure 8. Cortical injection of a modified rabies virus permits the targeted expression of GCaMP3 in the mitral and tufted cells of the olfactory bulb. (A) Coronal section from the olfactory bulb of a mouse with rabies-GCaMP3 injected into olfactory cortex. Robust expression of GCaMP3 (green) is seen in mitral and tufted cells starting at ~5 days post infection. Note the undiminished expression of GCaMP3 in cell bodies as well as throughout the apical and basal dendrites of mitral and tufted cells. Slices were counterstained for Nissl substance using NeuroTrace 435 (blue) (scale bar = 300 μM). **(B)** Zoomed-in view of boxed region in **(A)** emphasizing the innervation of individual glomeruli by the dendrites of multiple GCaMP3+ mitral and tufted cells (white arrows). Also note that cellular GCaMP3 labeling is restricted to the mitral cell layer of the olfactory bulb. **(C)** Two-photon image of the cell bodies and lateral dendrites of GCaMP3+ neurons in the mitral cell layer of the dorsal olfactory bulb (arial view; scale bar = 75 μM).

Figure 9.

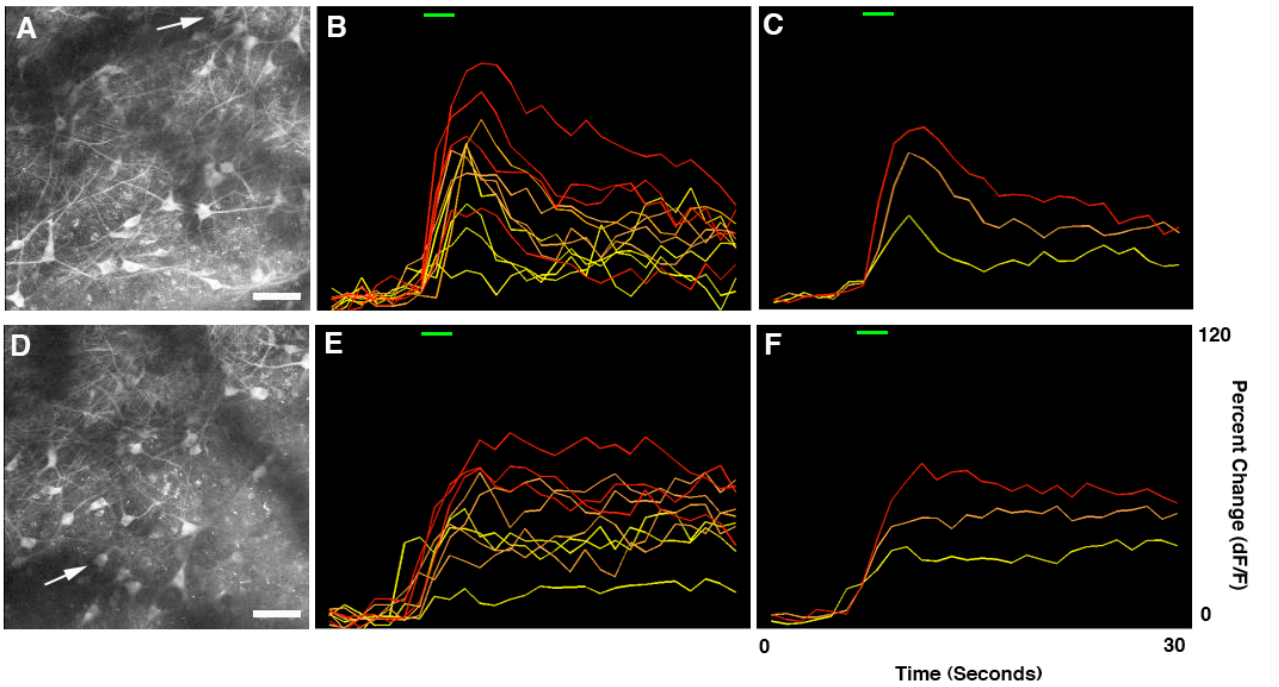

Figure 9. Odor-evoked responses in mitral and tufted cells infected with rabies-GCaMP3 are robust and reliable. (A) Two-photon image of the resting fluorescence of mitral and tufted cells infected with rabies-GCaMP3 (scale bar = 75 μM). **(B)** Odor-evoked responses (in ΔF/F) from the neuron indicated with the white arrow in **(A)** for each of four presentations of an odorant at three different concentrations (ethyl acetate; yellow = 1/10,000; orange = 1/1,000; red = 1/100, vol./vol. dilutions in mineral oil). Green bar indicates odor delivery period (2 seconds). **(C)** Average odor-evoked response across the four trials plotted in **(B)**. **(D)** Two-photon image of the resting fluorescence of mitral and tufted cells infected with rabies-GCaMP3 in a different animal than that used in **(A-C)** (scale bar = 75 μM). **(E)** Odor-evoked responses (in ΔF/F) from the neuron indicated with the white arrow in **(D)** for each of four presentations of an odorant at three different concentrations (2-hexanone; yellow = 1/10,000; orange = 1/1,000; red = 1/100, vol./vol. dilutions in mineral oil). Green bar indicates odor delivery period (2 seconds). **(F)** Average odor-evoked response across the four trials plotted in **(E)**.

Figure 10.

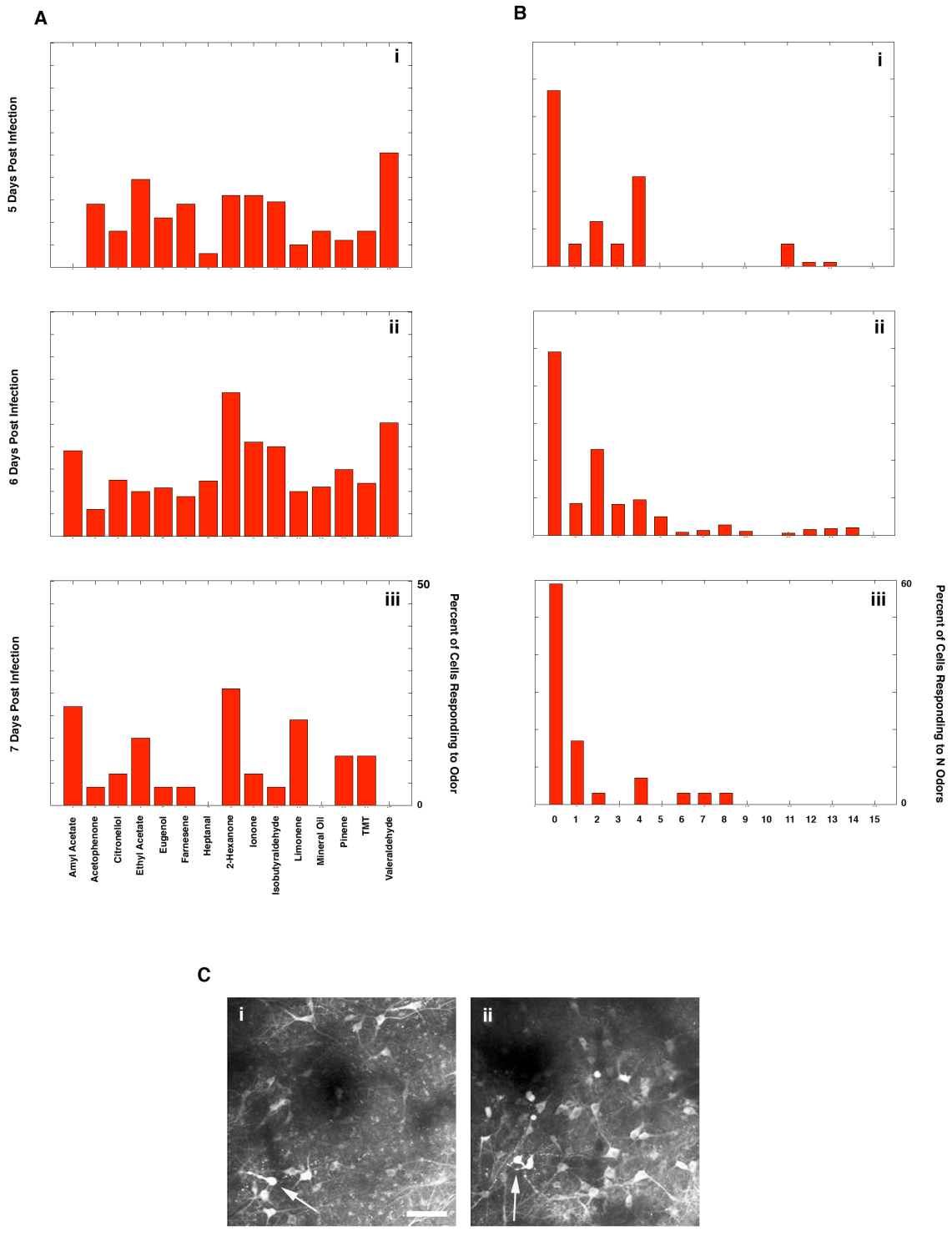
A
B
C
i
ii
iii
5 Days Post Infection
6 Days Post Infection
7 Days Post Infection
Percent of Cells Responding to Odor
Percent of Cells Responding to N Odors
50
0
60
0 1 2 3 4 5 6 7 8 9 10 11 12 13 14 15
Amyl Acetate
Acetophenone
Citronellol
Ethyl Acetate
Eugenol
Farnesene
Heptanal
2-Hexanone
Ionone
Isobutyraldehyde
Limonene
Mineral Oil
Pinene
TMT
Valeraldehyde

Figure 10. Rabies-GCaMP3 does not perturb mitral and tufted cell function. (A) The percent of mitral and tufted cells that respond to odor is similar regardless of whether 5 **(Ai)**, 6 **(Aii)**, or 7 **(Aiii)** days had elapsed since injection of rabies-GCaMP3. **(B)** The breadth of tuning of individual cells is similar regardless of whether 5 **(Bi)**, 6 **(Bii)**, or 7 **(Biii)** days had elapsed since injection of rabies-GCaMP3. **(C)** Evidence of "blebbing," a sign of stress or cell death, was rarely seen; when blebbing was observed **(Ci-Cii**, white arrows), it was only seen at 8 days post-injection or later (scale bar = 85 μM). Note that all mitral and tufted cell imaging experiments were performed 5-7 days after rabies-GCaMP3 injections.

Figure 11.

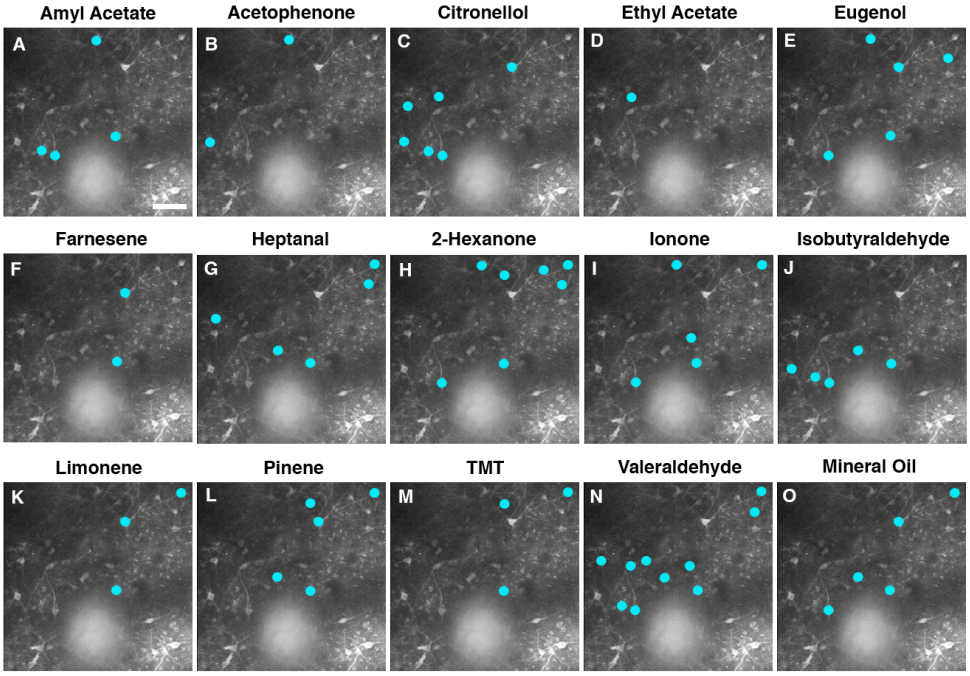
Amyl Acetate
Acetophenone
Citronellol
Ethyl Acetate
Eugenol
A
B
C
D
E
Farnesene
Heptanal
2-Hexanone
Ionone
Isobutyraldehyde
F
G
H
I
J
Limonene
Pinene
TMT
Valeraldehyde
Mineral Oil
K
L
M
N
O

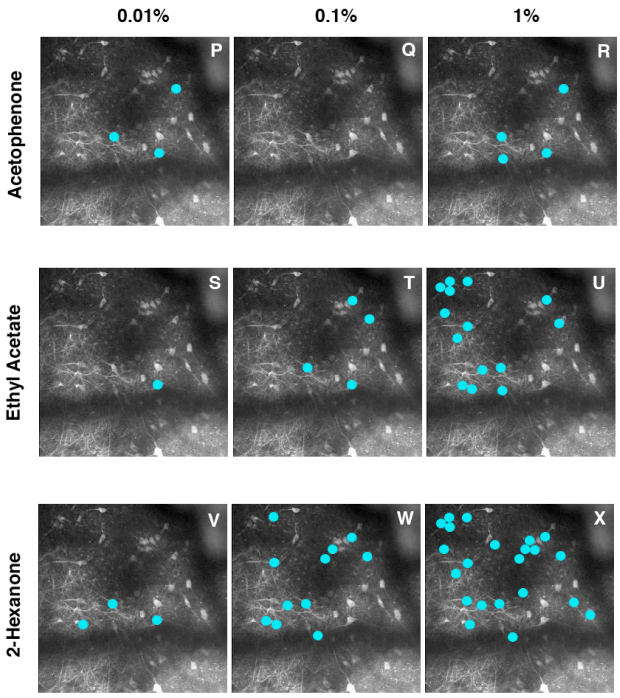
0.01%
0.1%
1%
Acetophenone
P
Q
R
Ethyl Acetate
S
T
U
2-Hexanone
V
W
X

Figure 11. Different odors are represented by spatially distributed, overlapping ensembles of mitral and tufted cells. (A-O) Topographic patterns of mitral and tufted cell responses to 15 different odorants at a low stimulus concentration (blue dots = responsive neurons; 1/10,000 vol./vol. dilution in mineral oil) (scale bar = 85 μM). **(P-X)** Topographic patterns of mitral and tufted cell responses to 3 odorants at multiple stimulus concentrations (blue dots = responsive neurons; 1/10,000 **(P,S,V)**, 1/1,000 **(Q,T,W)** and 1/100 **(R,U,X)** vol./vol. dilutions of pure odorants in mineral oil).

Figure 12.

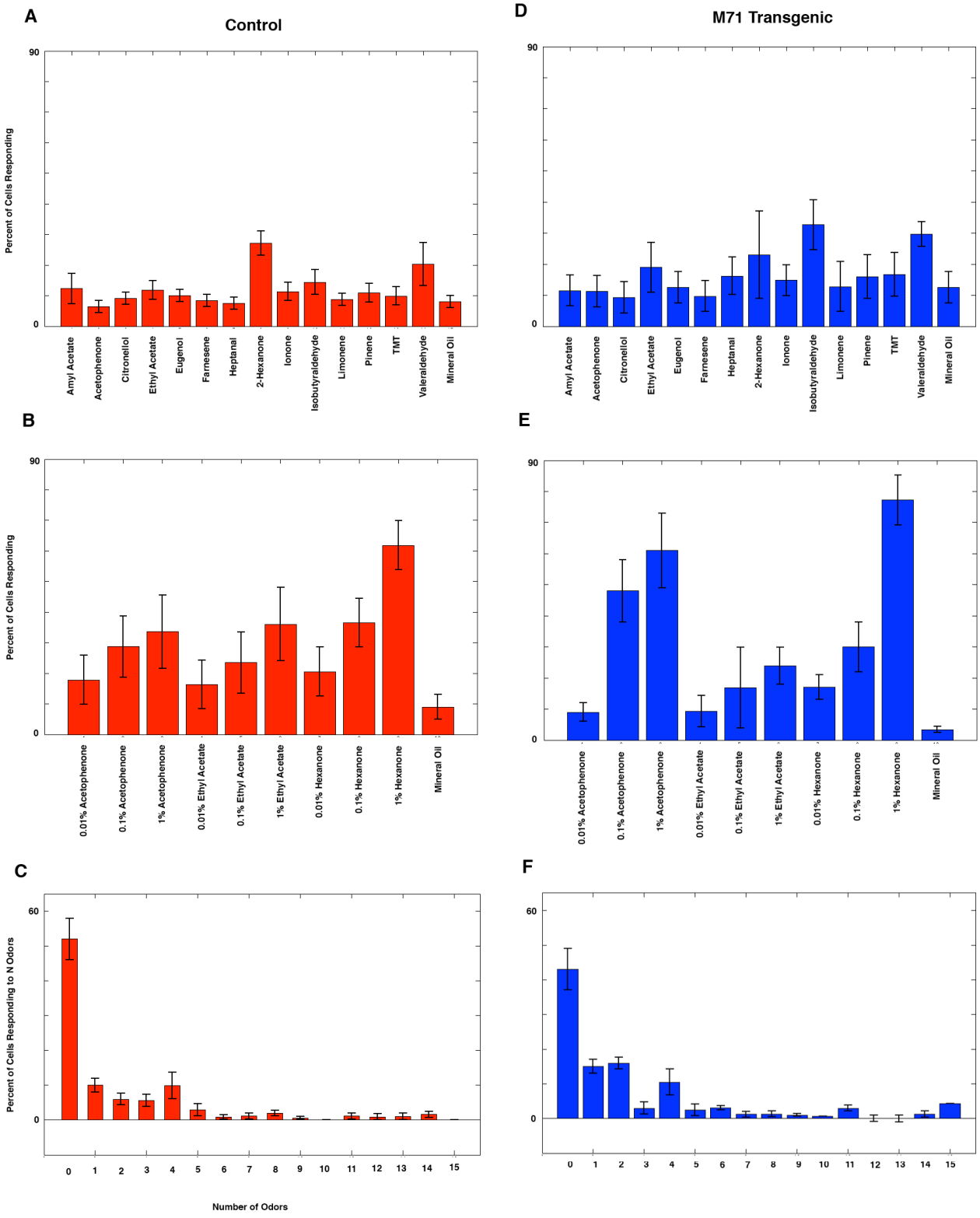
A
Control
Percent of Cells Responding
90
0
Amyl Acetate
Acetophenone
Citronellol
Ethyl Acetate
Eugenol
Farnesene
Heptanal
2-Hexanone
Ionone
Isobutyraldehyde
Limonene
Pinene
TMT
Valeraldehyde
Mineral Oil
D
M71 Transgenic
B
0.01% Acetophenone
0.1% Acetophenone
1% Acetophenone
0.01% Ethyl Acetate
0.1% Ethyl Acetate
1% Ethyl Acetate
0.01% Hexanone
0.1% Hexanone
1% Hexanone
E
C
Percent of Cells Responding to N Odors
60
0 1 2 3 4 5 6 7 8 9 10 11 12 13 14 15
Number of Odors
F

Figure 12. Quantification of odor-evoked mitral and tufted cell responses in control mice and M71 transgenics. (A) The percent of mitral and tufted cells responding to 15 different odors at a low concentration in control mice (1/10,000 vol./vol. dilution in mineral oil). **(B)** The percent of mitral and tufted cells responding to 3 different odors at 3 concentrations as well as mineral oil in control mice (1/10,000, 1/1,000, and 1/100 vol./vol. dilution in mineral oil). **(C)** The percent of mitral and tufted cells that respond to a given number of odors (e.g. breadth of stimulus tuning) when 15 odors at 1/10,000 vol./vol. concentration were used in control mice. **(D)** The percent of mitral and tufted cells responding to 15 different odors at a low concentration in M71 transgenic mice (1/10,000 vol./vol. dilution in mineral oil). **(E)** The percent of mitral and tufted cells responding to 3 different odors at 3 concentrations as well as mineral oil in M71 transgenic mice (1/10,000, 1/1,000, and 1/100 vol./vol. dilution in mineral oil). **(F)** The percent of mitral and tufted cells that respond to a given number of odors (e.g. breadth of stimulus tuning) when 15 odors at 1/10,000 vol./vol. concentration were used in M71 transgenic mice. Errorbars = SEM.

Figure 13.

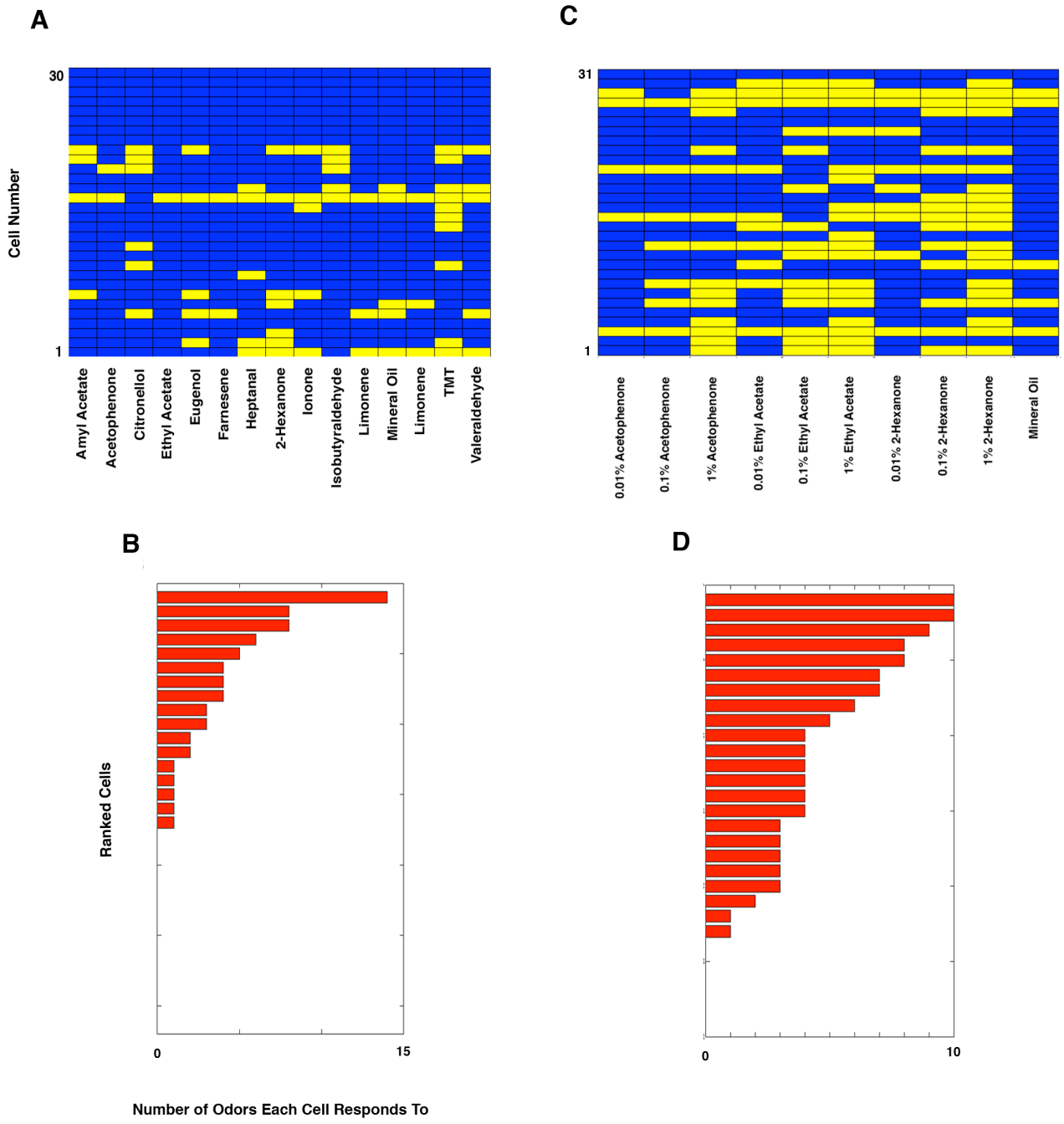
A
30
1
Cell Number
Amyl Acetate
Acetophenone
Citronellol
Ethyl Acetate
Eugenol
Farnesene
Heptanal
2-Hexanone
Ionone
Isobutyraldehyde
Limonene
Mineral Oil
Limonene
TMT
Valeraldehyde
C
31
1
0.01% Acetophenone
0.1% Acetophenone
1% Acetophenone
0.01% Ethyl Acetate
0.1% Ethyl Acetate
1% Ethyl Acetate
0.01% 2-Hexanone
0.1% 2-Hexanone
1% 2-Hexanone
Mineral Oil
B
Ranked Cells
0
15
Number of Odors Each Cell Responds To
D
0
10

Figure 13. Mitral and tufted cells can be broadly or narrowly tuned to odor stimuli. **(A)** A binary response matrix illustrating the odor tuning of each cell at a low stimulus concentration at one imaging site in a control mouse (1/10,000 vol./vol. dilution in mineral oil; yellow square = cell responds to odor; blue square = cell does not respond to odor). **(B)** A ranked bar plot of the same cells in **(A)** with respect to the number of odors each cell responds to. **(C)** A binary response matrix illustrating the odor tuning of each cell at 3 different odor concentrations at one imaging site in a control mouse (1/10,000, 1/1,000 and 1/100 vol./vol. dilution in mineral oil; yellow square = cell responds to odor; blue square = cell does not respond to odor). **(D)** A ranked bar plot of the same cells in **(C)** with respect to the number of odors each cell responds to. Note the increase in both the number of cells responding to odor as well as the number of odors that individual cells respond to as the stimulus concentration is increased.

Figure 14.

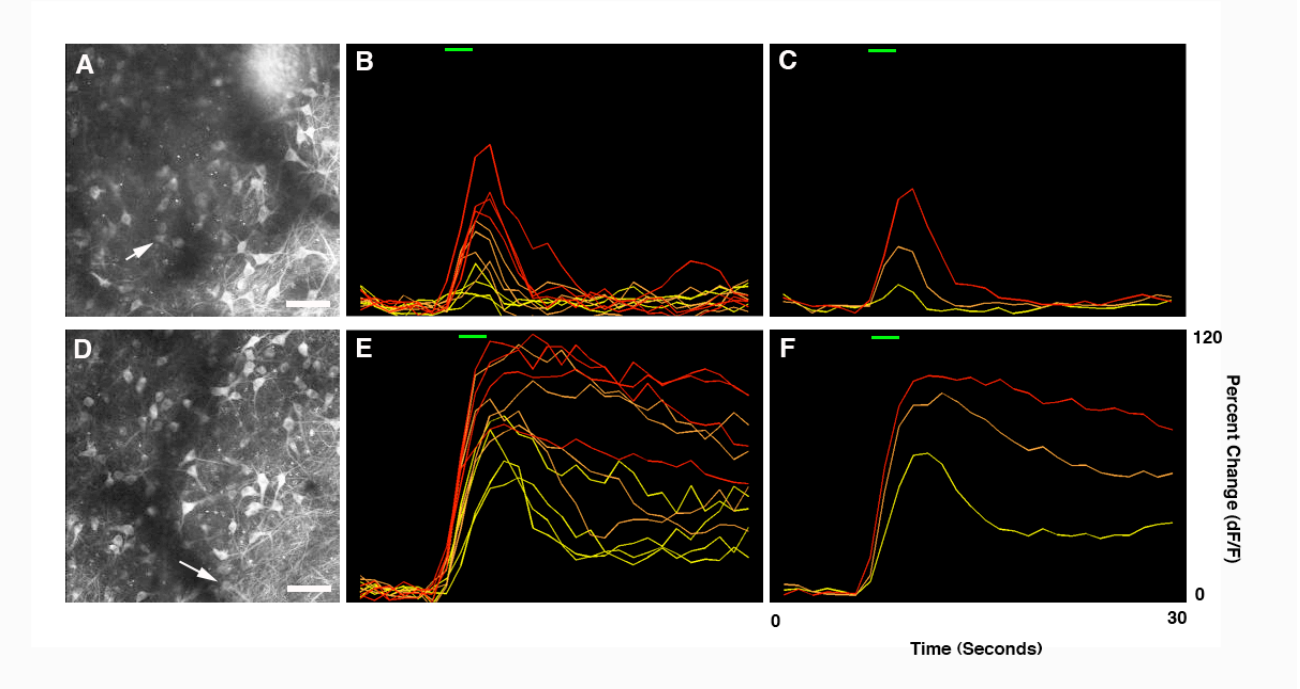

Figure 14. Odor-evoked responses in mitral and tufted cells infected with rabies-GCaMP3 in M71 transgenic mice are robust and reliable. (A) Two-photon image of the resting fluorescence of mitral and tufted cells in the bulb of an M71 transgenic mouse infected with rabies-GCaMP3 (scale bar = 85 μM). **(B)** Odor-evoked responses (in ΔF/F) from the neuron indicated with the white arrow in **(A)** for each of four presentations of an odorant at three different concentrations (acetophenone; yellow = 1/10,000; orange = 1/1,000; red = 1/100, vol./vol. dilutions in mineral oil). Green bar indicates odor delivery period (2 seconds). **(C)** Average odor-evoked response across the four trials plotted in **(B)**. **(D)** Two-photon image of the resting fluorescence of mitral and tufted cells infected with rabies-GCaMP3 in a different animal than that used in **(A-C)** (scale bar = 85 μM). **(E)** Odor-evoked responses (in ΔF/F) from the neuron indicated with the white arrow in **(D)** for each of four presentations of an odorant at three different concentrations (ethyl acetate; yellow = 1/10,000; orange = 1/1,000; red = 1/100, vol./vol. dilutions in mineral oil). Green bar indicates odor delivery period (2 seconds). **(F)** Average odor-evoked response across the four trials plotted in **(E)**.

Figure 15.

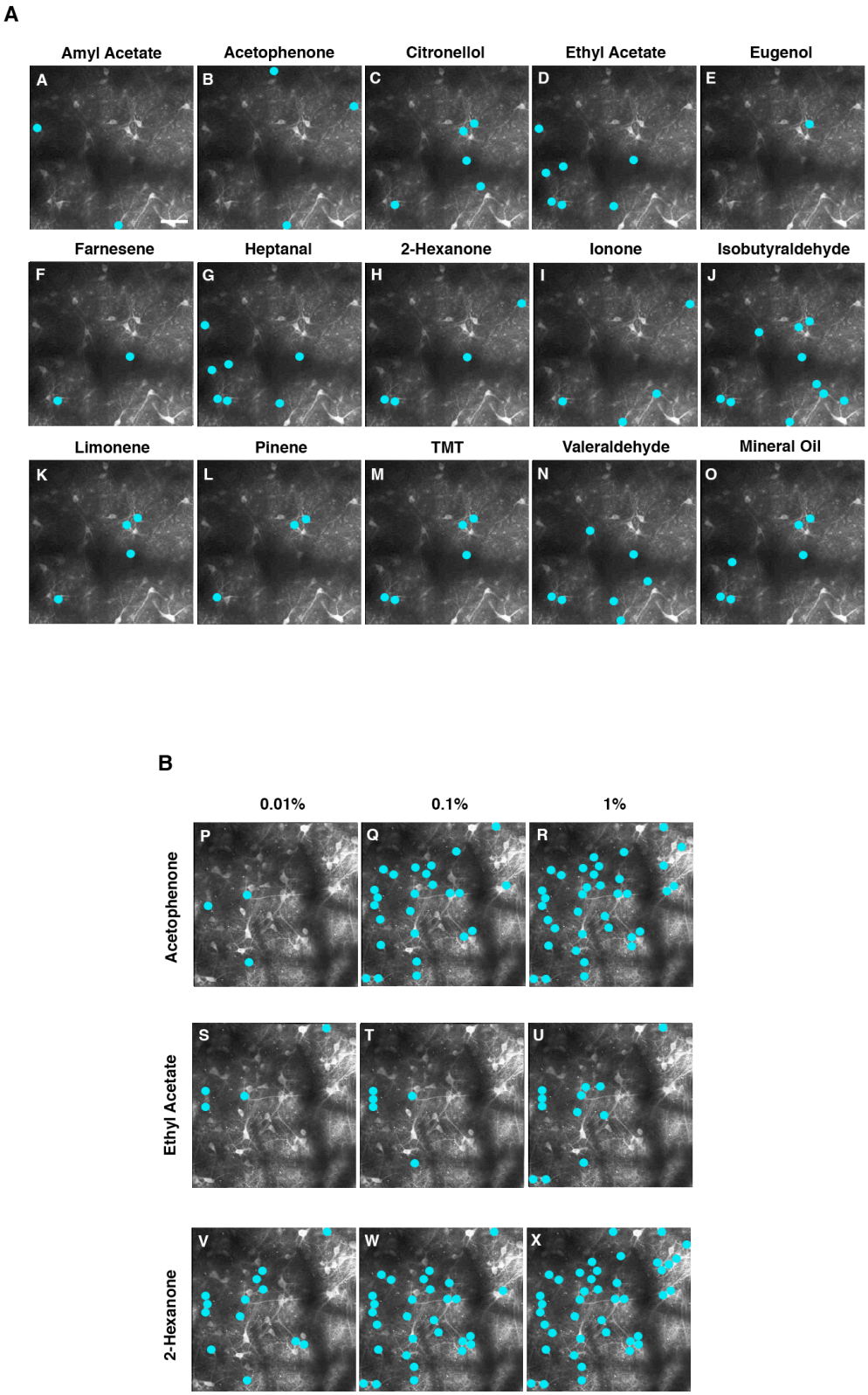
A
Amyl Acetate
Acetophenone
Citronellol
Ethyl Acetate
Eugenol
A
B
C
D
E
Farnesene
Heptanal
2-Hexanone
Ionone
Isobutyraldehyde
F
G
H
I
J
Limonene
Pinene
TMT
Valeraldehyde
Mineral Oil
K
L
M
N
O
B
0.01%
0.1%
1%
Acetophenone
P
Q
R
Ethyl Acetate
S
T
U
2-Hexanone
V
W
X

Figure 15. Mitral and tufted cells in M71 transgenic mice can respond to a variety of different odorants. (A-O) Topographic patterns of mitral and tufted cell responses to 15 different odorants at a low stimulus concentration in M71 transgenic mice (blue dots = responsive neurons; 1/10,000 vol./vol. dilution in mineral oil) (scale bar = 85 μM). **(P-X)** Topographic patterns of mitral and tufted cell responses to 3 odorants at multiple stimulus concentrations in M71 transgenic mice (blue dots = responsive neurons; 1/10,000 **(P,S,V)**, 1/1,000 **(Q,T,W)** and 1/100 **(R,U,X)** vol./vol. dilutions of pure odorants in mineral oil).

Figure 16.

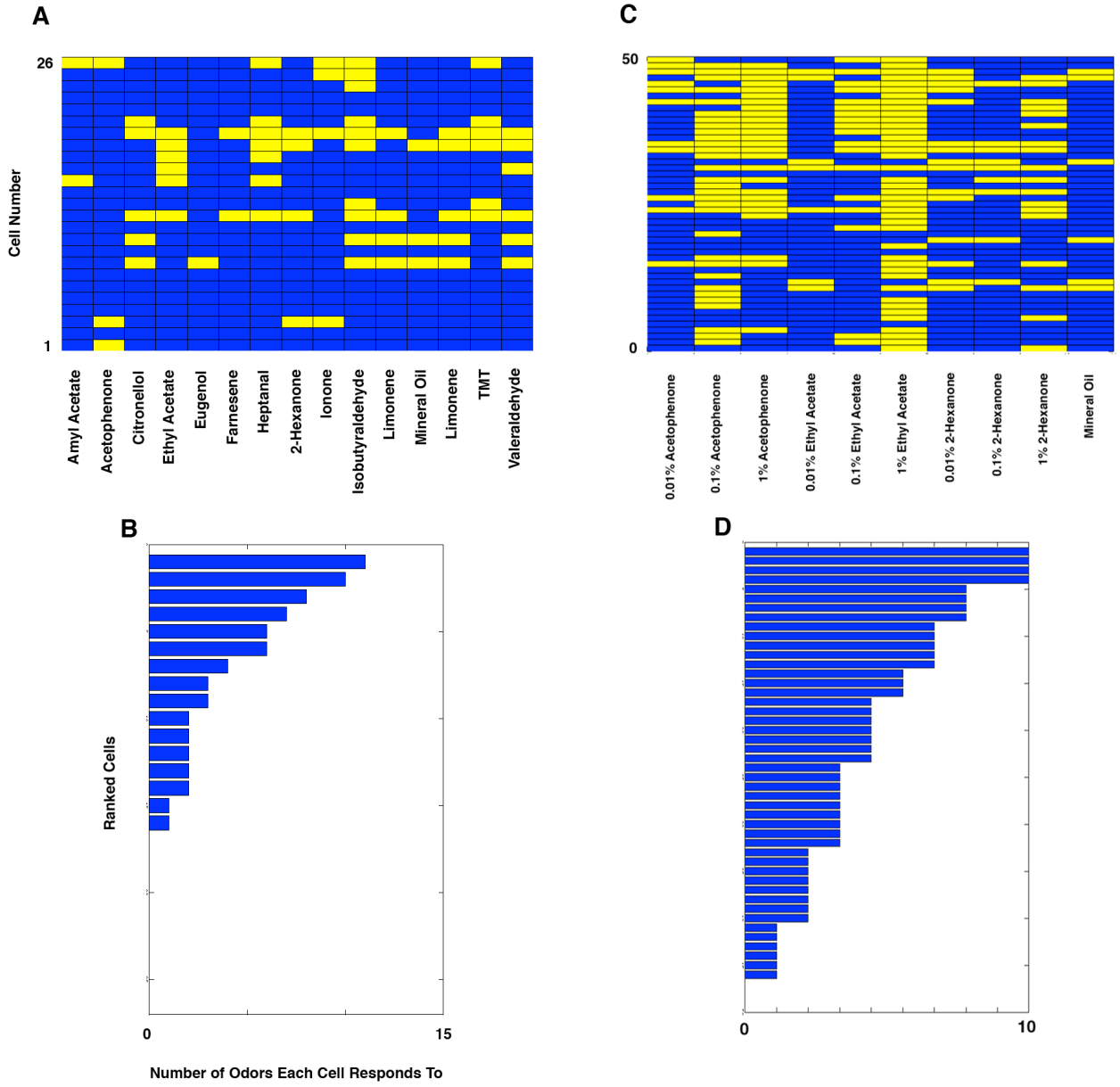
A
26
1
Cell Number
Amyl Acetate
Acetophenone
Citronellol
Ethyl Acetate
Eugenol
Farnesene
Heptanal
2-Hexanone
Ionone
Isobutyraldehyde
Limonene
Mineral Oil
Limonene
TMT
Valeraldehyde
C
50
0
0.01% Acetophenone
0.1% Acetophenone
1% Acetophenone
0.01% Ethyl Acetate
0.1% Ethyl Acetate
1% Ethyl Acetate
0.01% 2-Hexanone
0.1% 2-Hexanone
1% 2-Hexanone
Mineral Oil
B
Ranked Cells
0
15
Number of Odors Each Cell Responds To
D
0
10

Figure 16. Mitral and tufted cells in M71 transgenic mice can be broadly or narrowly tuned to odor stimuli. (A) A binary response matrix illustrating the odor tuning of each cell at a low stimulus concentration at one imaging site in an M71 transgenic mouse (1/10,000 vol./vol. dilution in mineral oil; yellow square = cell responds to odor; blue square = cell does not respond to odor). **(B)** A ranked bar plot of the same cells in **(A)** with respect to the number of odors each cell responds to. **(C)** A binary response matrix illustrating the odor tuning of each cell at 3 different odor concentrations at one imaging site in an M71 transgenic mouse (1/10,000, 1/1,000 and 1/100 vol./vol. dilution in mineral oil; yellow square = cell responds to odor; blue square = cell does not respond to odor). **(D)** A ranked bar plot of the same cells in **(C)** with respect to the number of odors each cell responds to. Note the increase in both the number of cells responding to odor as well as the number of odors that individual cells respond to as the stimulus concentration is increased.

Figure 17.

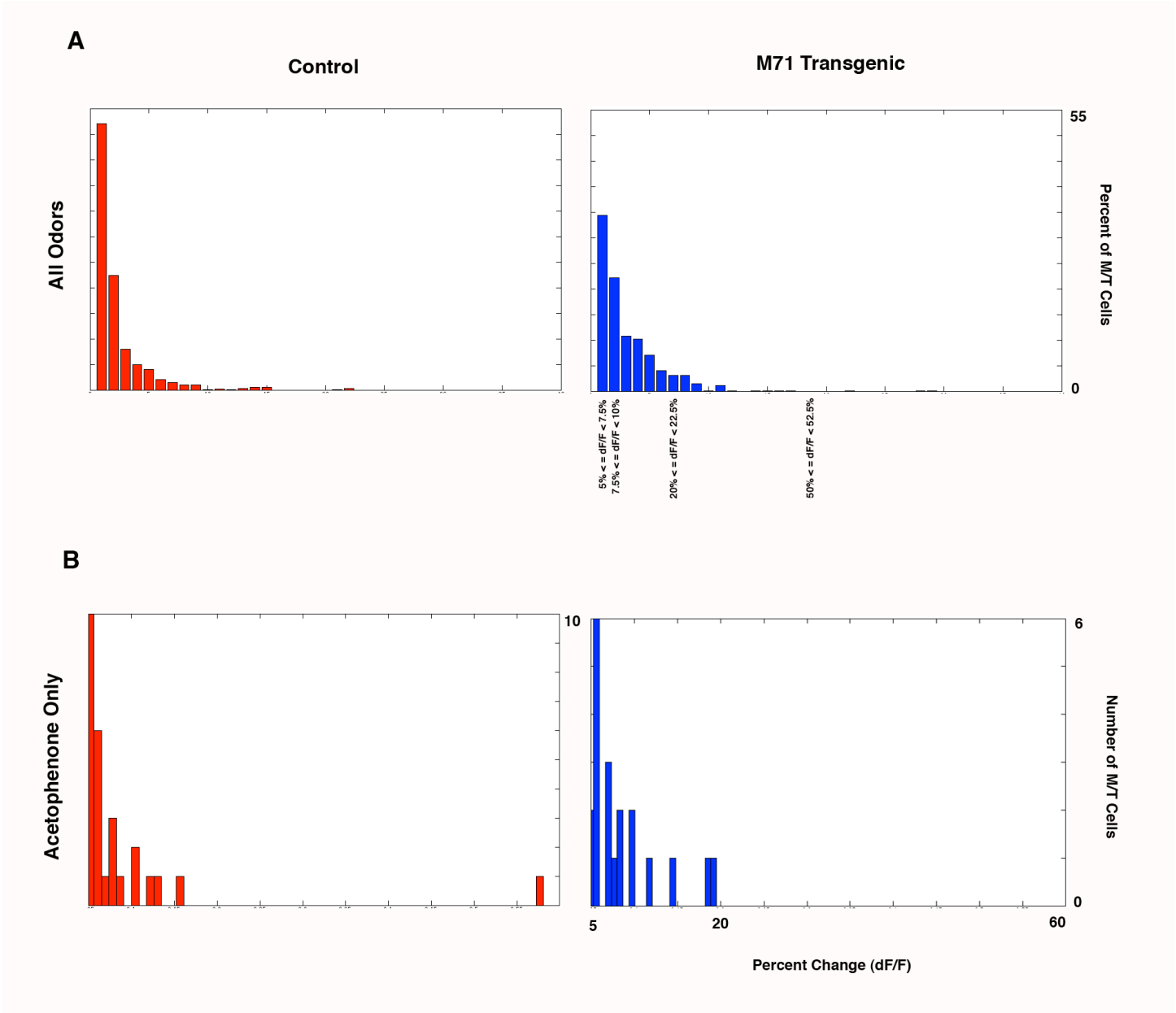
A
Control
M71 Transgenic
All Odors
55
0
Percent of M/T Cells
5% < = dF/F < 7.5%
7.5% < = dF/F < 10%
20% < = dF/F < 22.5%
50% < = dF/F < 52.5%
B
Acetophenone Only
10
6
0
5
20
60
Number of M/T Cells
Percent Change (dF/F)

Figure 17. The magnitude of odor-evoked mitral and tufted cell responses is greater in M71 transgenics than controls. (A) The percent of cells with ΔF/Fs falling within a given interval, plotted in intervals of 2.5% ΔF/F (e.g. 2.51%-5%, 5.01%-7.5%, etc.) in controls (left, red) and M71 transgenics (right, blue; responses to all odors at 1/10,000 vol.vol. concentration, 15 odor set). **(B)** Histograms plotting the frequency of ΔF/Fs for neurons in response to acetophenone only in controls (left, red) and transgenics (right, blue).

Figure 18.

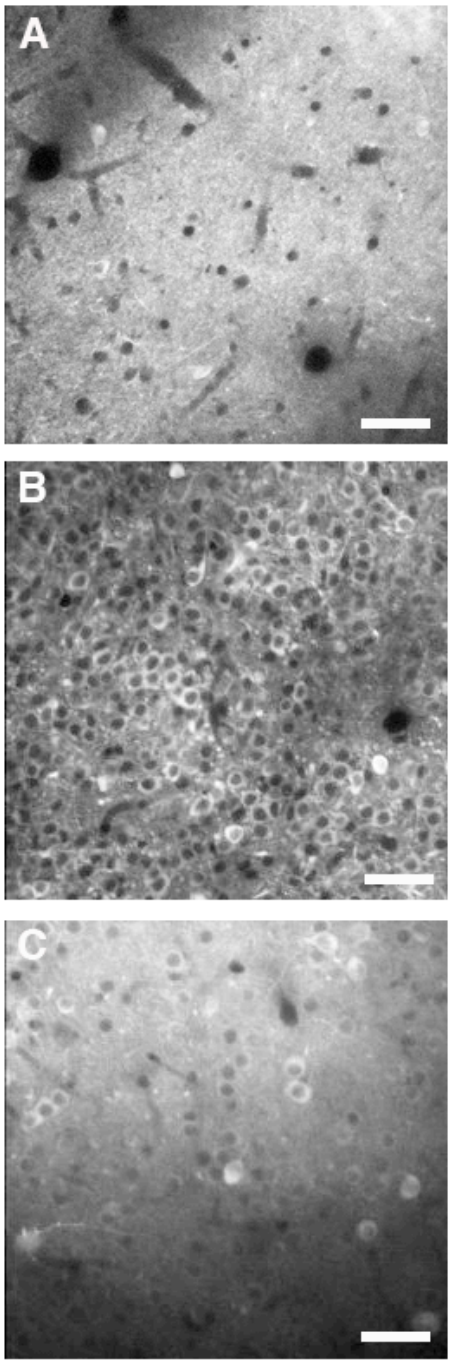

Figure 18. Cortical injection of an AAV-GCaMP3 virus permits the expression of GCaMP3 in piriform cortex neurons. (A-C) Injections of AAV-GCaMP3 virus centered in layer II of piriform cortex lead to sparse labeling of neurons in layer I of piriform **(A)**, dense labeling in layer II **(B)**, and moderate cellular labeling of neurons in layer III of piriform cortex **(C)** (scale bars = 40 μM). While the nature of this labeling may be due to the targeting of these injections to layer II, because AAV is able to infect cells located millimeters away from the injection site, it is more likely to reflect the known distribution of cell bodies in the piriform cortex.

Figure 19.

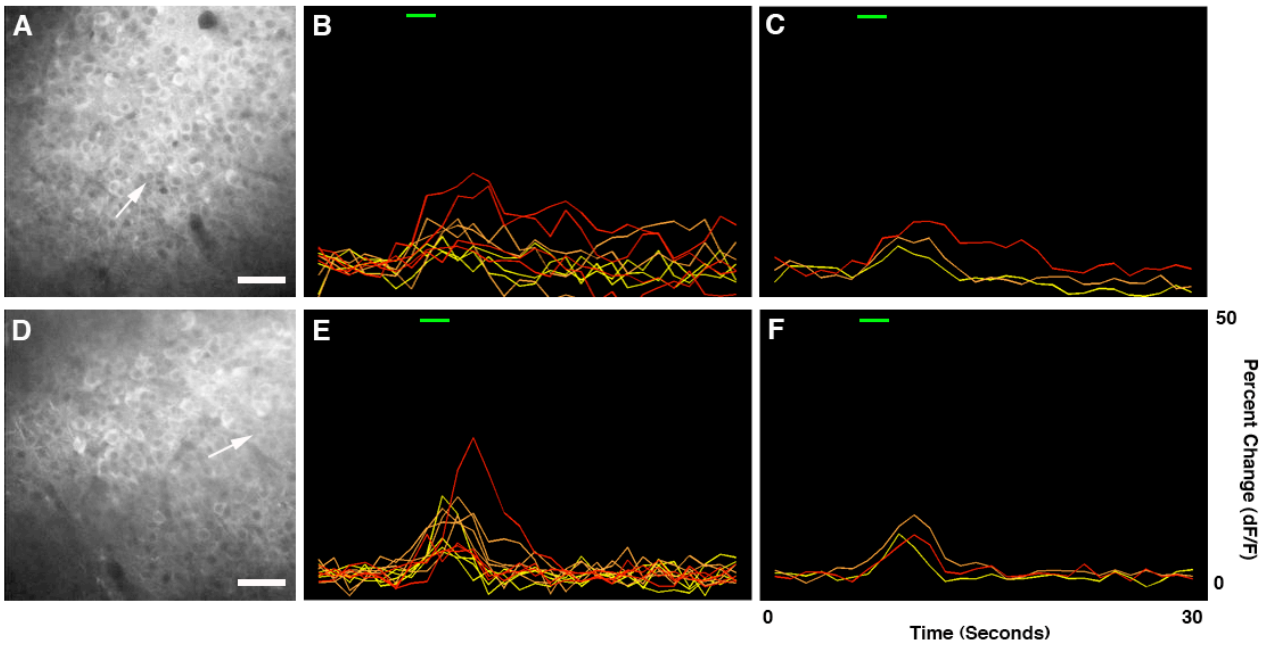

Figure 19. Odor-evoked responses in piriform neurons infected with AAV-GCaMP3 are robust and reliable. (A) Two-photon image of the resting fluorescence of piriform cortex neurons infected with AAV-GCaMP3 (scale bar = 45 μM). **(B)** Odor-evoked responses (in ΔF/F) from the neuron indicated with the white arrow in **(A)** for each of four presentations of an odorant at three different concentrations (isoamyl acetate; yellow = 1/10,000; orange = 1/1,000; red = 1/100, vol./vol. dilutions in mineral oil). Green bar indicates odor delivery period (2 seconds). **(C)** Average odor-evoked response across the four trials plotted in **(B)**. **(D)** Two-photon image of the resting fluorescence of piriform neurons infected with AAV-GCaMP3 in a different animal than that used in **(A-C)** (scale bar = 45 μM). **(E)** Odor-evoked responses (in ΔF/F) from the neuron indicated with the white arrow in **(D)** for each of four presentations of an odorant at three different concentrations (2-hexanone; yellow = 1/10,000; orange = 1/1,000; red = 1/100, vol./vol. dilutions in mineral oil). Green bar indicates odor delivery period (2 seconds). **(F)** Average odor-evoked response across the four trials plotted in **(E)**.

Figure 20.

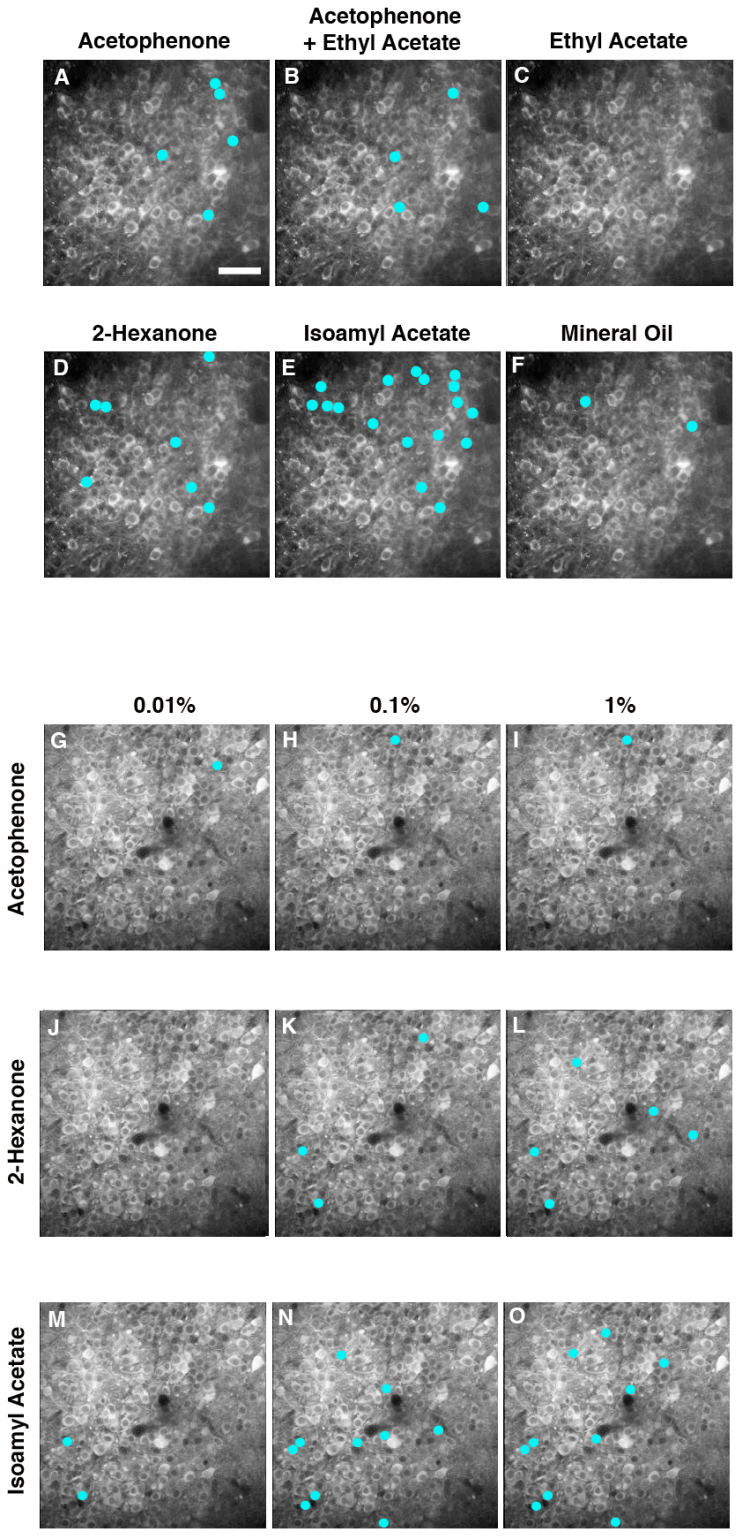
Acetophenone
Acetophenone + Ethyl Acetate
Ethyl Acetate
A
B
C
2-Hexanone
Isoamyl Acetate
Mineral Oil
D
E
F
0.01%
0.1%
1%
Acetophenone
G
H
I
2-Hexanone
J
K
L
Isoamyl Acetate
M
N
O

Figure 20. Different odors are represented by sparse, spatially distributed ensembles of neurons in the piriform cortex. (A-F) Topographic patterns of mitral and tufted cell responses to 6 different odorants at a high stimulus concentration (blue dots = responsive neurons; 1/100 vol./vol. dilution in mineral oil) (scale bar = 75 μM). **(G-O)** Topographic patterns of piriform neuron responses to 3 odorants at multiple stimulus concentrations (blue dots = responsive neurons; 1/10,000 **(G,J,M)**, 1/1,000 **(H,K,N)** and 1/100 **(I,L,O)** vol./vol. dilutions of pure odorants in mineral oil).

Figure 21.

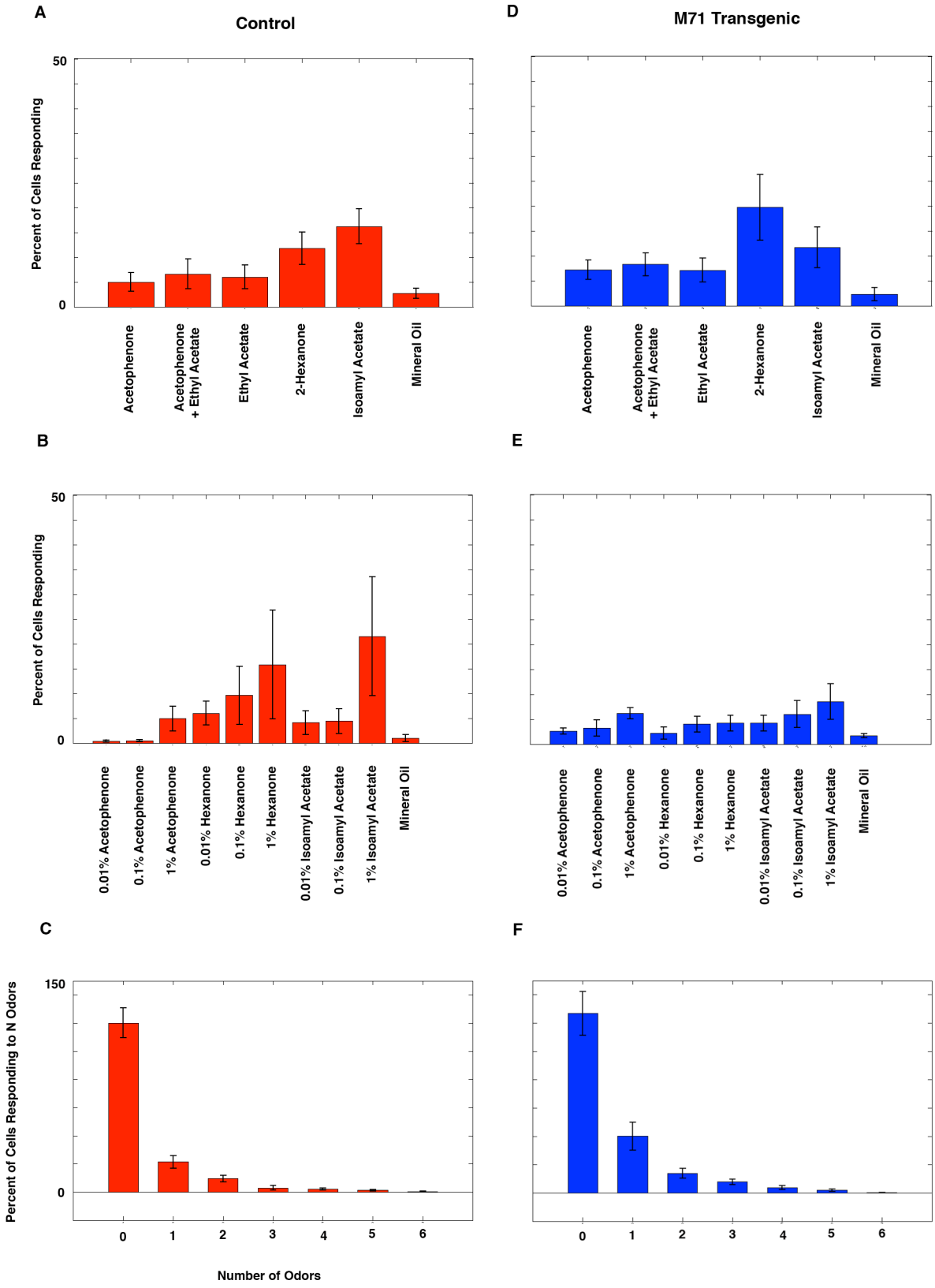
A
Control
D
M71 Transgenic
Percent of Cells Responding
50
0
Acetophenone
Acetophenone + Ethyl Acetate
Ethyl Acetate
2-Hexanone
Isoamyl Acetate
Mineral Oil
B
E
0.01% Acetophenone
0.1% Acetophenone
1% Acetophenone
0.01% Hexanone
0.1% Hexanone
1% Hexanone
0.01% Isoamyl Acetate
0.1% Isoamyl Acetate
1% Isoamyl Acetate
C
F
Percent of Cells Responding to N Odors
150
0
1
2
3
4
5
6
Number of Odors

Figure 21. Quantification of odor-evoked piriform neuron responses in control mice and M71 transgenics. (A) The percent of piriform cortex neurons responding to 6 different odors at a high concentration in control mice (1/100 vol./vol. dilution in mineral oil). **(B)** The percent of piriform cortex neurons responding to 3 different odors at 3 concentrations as well as mineral oil in control mice (1/10,000, 1/1,000, and 1/100 vol./vol. dilution in mineral oil). **(C)** The percent of piriform neurons that respond to a given number of odors (e.g. breadth of stimulus tuning) when 6 odors at 1/100 vol./vol. concentration were used in control mice. **(D)** The percent of piriform neurons responding to 6 different odors at a high concentration in M71 transgenic mice (1/100 vol./vol. dilution in mineral oil). **(E)** The percent of piriform neurons responding to 3 different odors at 3 concentrations as well as mineral oil in M71 transgenic mice (1/10,000, 1/1,000, and 1/100 vol./vol. dilution in mineral oil). **(F)** The percent of piriform neurons that respond to a given number of odors (e.g. breadth of stimulus tuning) when 6 odors at 1/100 vol./vol. concentration were used in M71 transgenic mice. Errorbars = SEM.

Figure 22.

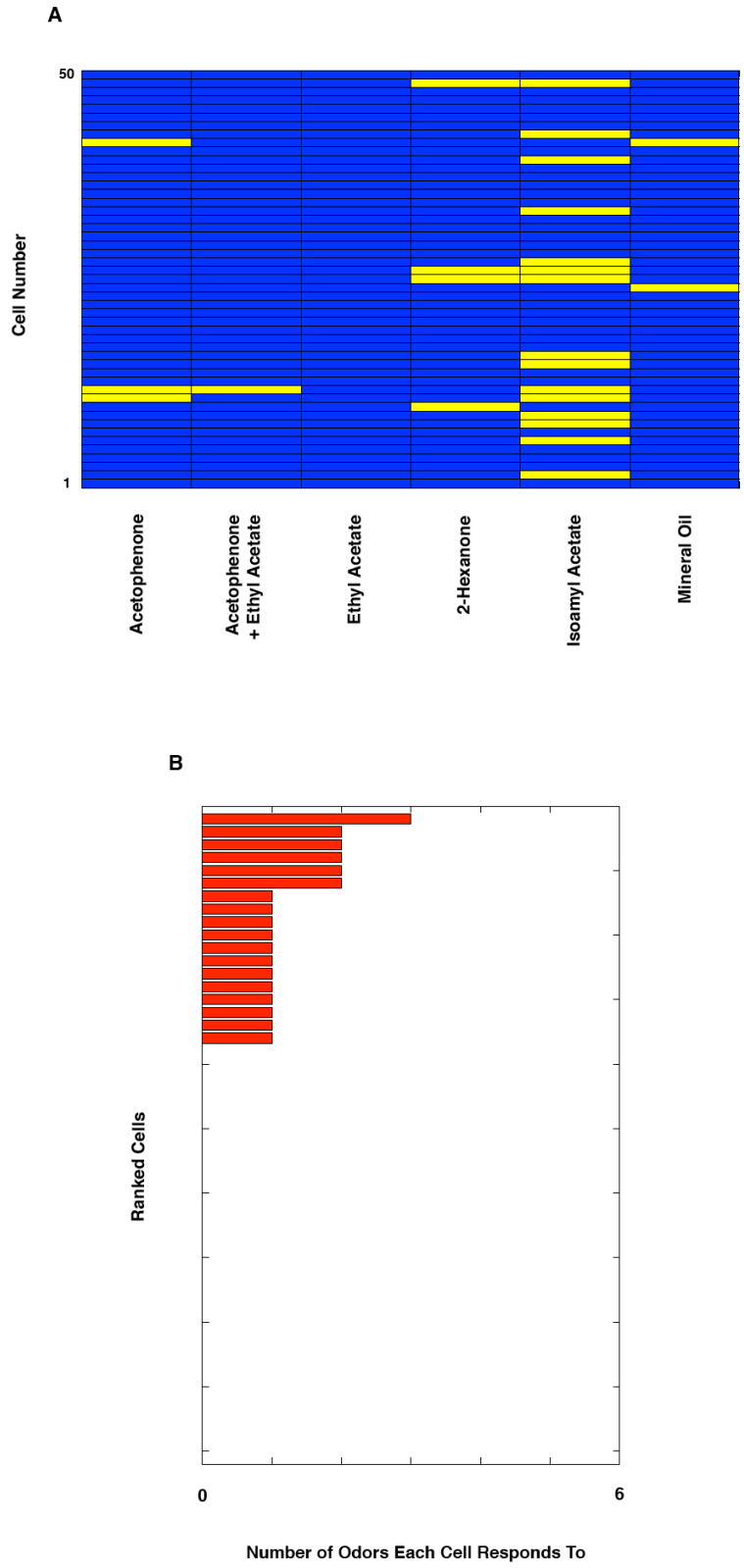
A
50
1
Cell Number
Acetophenone
Acetophenone + Ethyl Acetate
Ethyl Acetate
2-Hexanone
Isoamyl Acetate
Mineral Oil
B
Ranked Cells
0
6
Number of Odors Each Cell Responds To

Figure 22. Piriform neurons in control mice can be broadly or narrowly tuned to odor stimuli. (A) A binary response matrix illustrating the odor tuning of each cell at a high stimulus concentration at one imaging site in a control mouse (1/100 vol./vol. dilution in mineral oil; yellow square = cell responds to odor; blue square = cell does not respond to odor). **(B)** A ranked bar plot of the same cells in **(A)** with respect to the number of odors each cell responds to.

Figure 23.

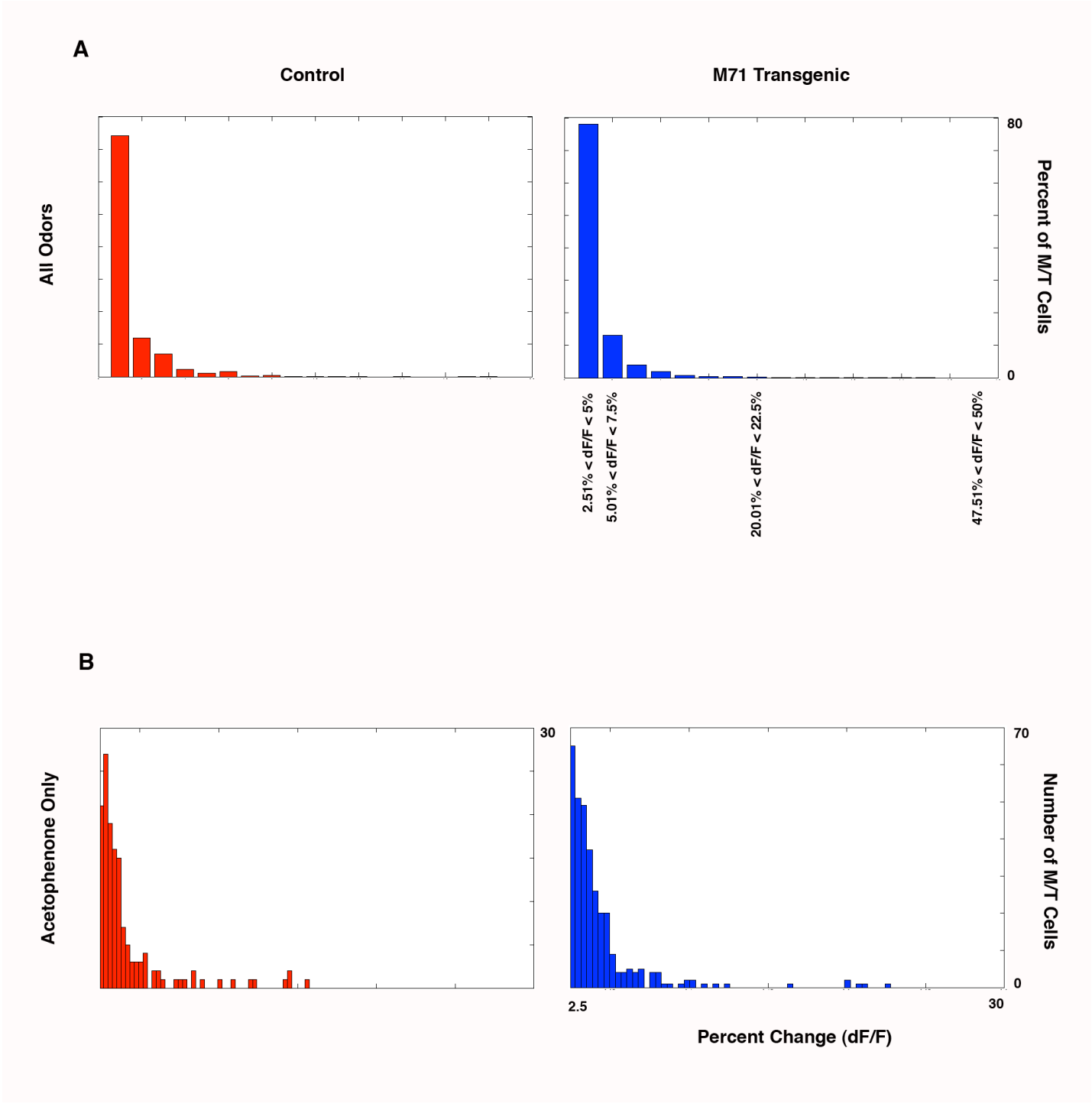
A
Control
M71 Transgenic
All Odors
Percent of M/T Cells
80
0
2.51% < dF/F < 5%
5.01% < dF/F < 7.5%
20.01% < dF/F < 22.5%
47.51% < dF/F < 50%
B
Acetophenone Only
Number of M/T Cells
30
70
0
2.5
30
Percent Change (dF/F)

Figure 23. The magnitude of odor-evoked responses in piriform neurons is similar in M71 transgenics and controls. (A) The percent of cells with ΔF/Fs falling within a given interval, plotted in intervals of 2.5% ΔF/F (e.g. 2.51%-5%, 5.01%-7.5%, etc.) in controls (left, red) and M71 transgenics (right, blue; 1/100 vol./vol. concentration, 6 odor set). **(B)** Histograms plotting the frequency of ΔF/Fs for neurons in response to acetophenone only in controls (left, red) and transgenics (right, blue).

Figure 24.

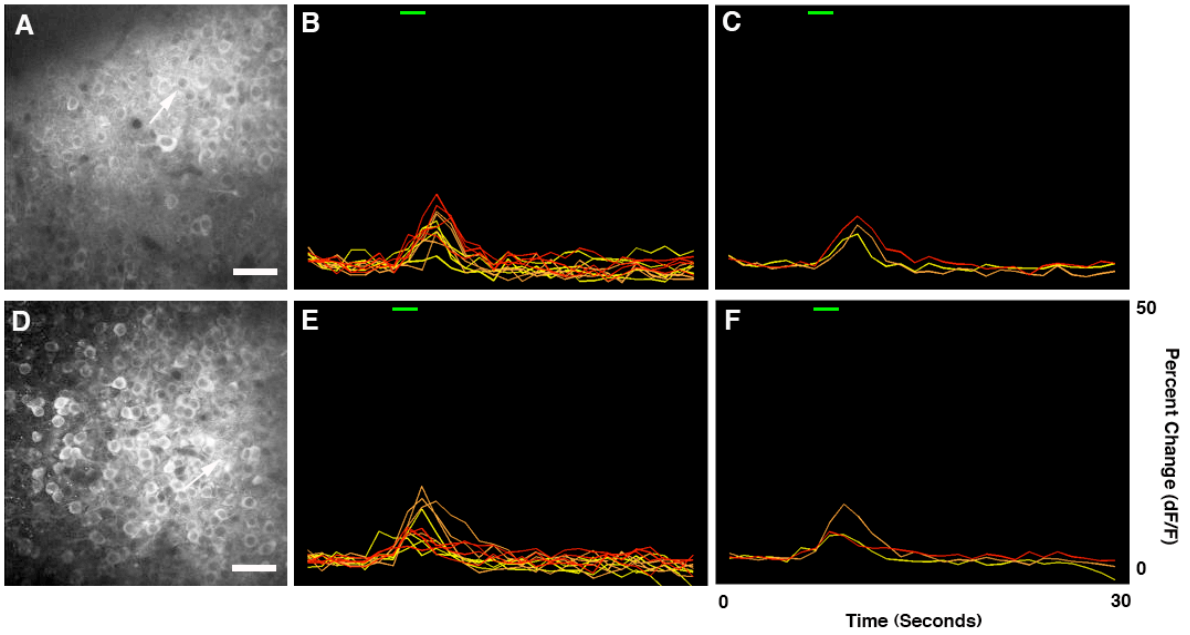

Figure 24. Odor-evoked responses in piriform neurons infected with AAV-GCaMP3 in M71 transgenic mice are robust and reliable. (A) Two-photon image of the resting fluorescence of piriform cortex neurons in M71 transgenic mice infected with AAV-GCaMP3 (scale bar = 45 μM). **(B)** Odor-evoked responses (in ΔF/F) from the neuron indicated with the white arrow in **(A)** for each of four presentations of an odorant at three different concentrations (acetophenone; yellow = 1/10,000; orange = 1/1,000; red = 1/100, vol./vol. dilutions in mineral oil). Green bar indicates odor delivery period (2 seconds). **(C)** Average odor-evoked response across the four trials plotted in **(B)**. **(D)** Two-photon image of the resting fluorescence of piriform neurons infected with AAV-GCaMP3 in a different M71 transgenic animal than that used in **(A-C)** (scale bar = 45 μM). **(E)** Odor-evoked responses (in ΔF/F) from the neuron indicated with the white arrow in **(D)** for each of four presentations of an odorant at three different concentrations (isoamyl acetate; yellow = 1/10,000; orange = 1/1,000; red = 1/100, vol./vol. dilutions in mineral oil). Green bar indicates odor delivery period (2 seconds). **(F)** Average odor-evoked response across the four trials plotted in **(E)**.

Figure 25.

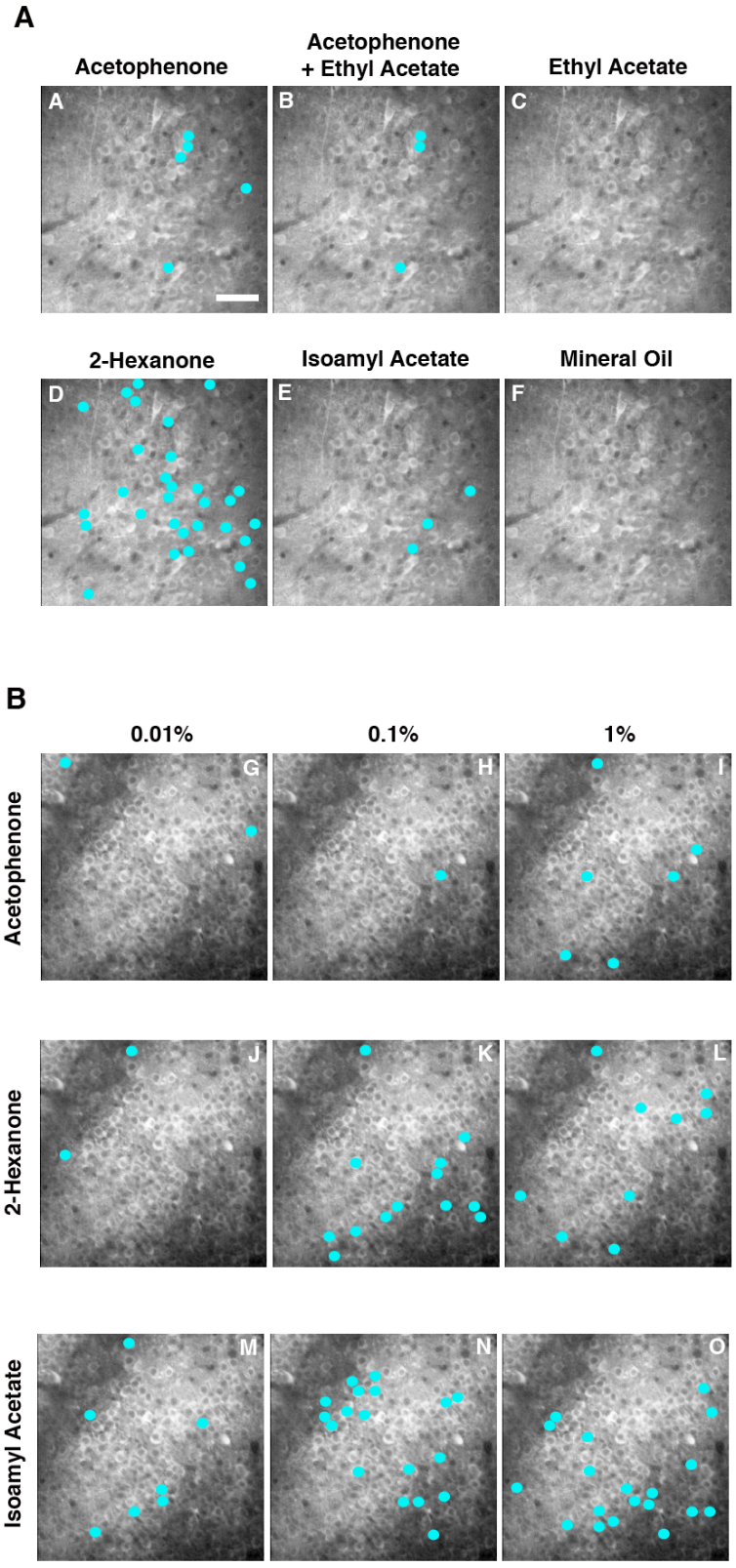
A
Acetophenone
Acetophenone + Ethyl Acetate
Ethyl Acetate
A
B
C
2-Hexanone
Isoamyl Acetate
Mineral Oil
D
E
F
B
0.01%
0.1%
1%
Acetophenone
G
H
I
2-Hexanone
J
K
L
Isoamyl Acetate
M
N
O

Figure 25. Different odors are represented by sparse, spatially distributed ensembles of neurons in the piriform cortex of M71 transgenic mice. (A-F) Topographic patterns of mitral and tufted cell responses to 6 different odorants at a high stimulus concentration (blue dots = responsive neurons; 1/100 vol./vol. dilution in mineral oil) (scale bar = 75 μM). **(G-O)** Topographic patterns of piriform neuron responses to 3 odorants at multiple stimulus concentrations (blue dots = responsive neurons; 1/10,000 **(G,J,M)**, 1/1,000 **(H,K,N)** and 1/100 **(I,L,O)** vol./vol. dilutions of pure odorants in mineral oil).

Figure 26.

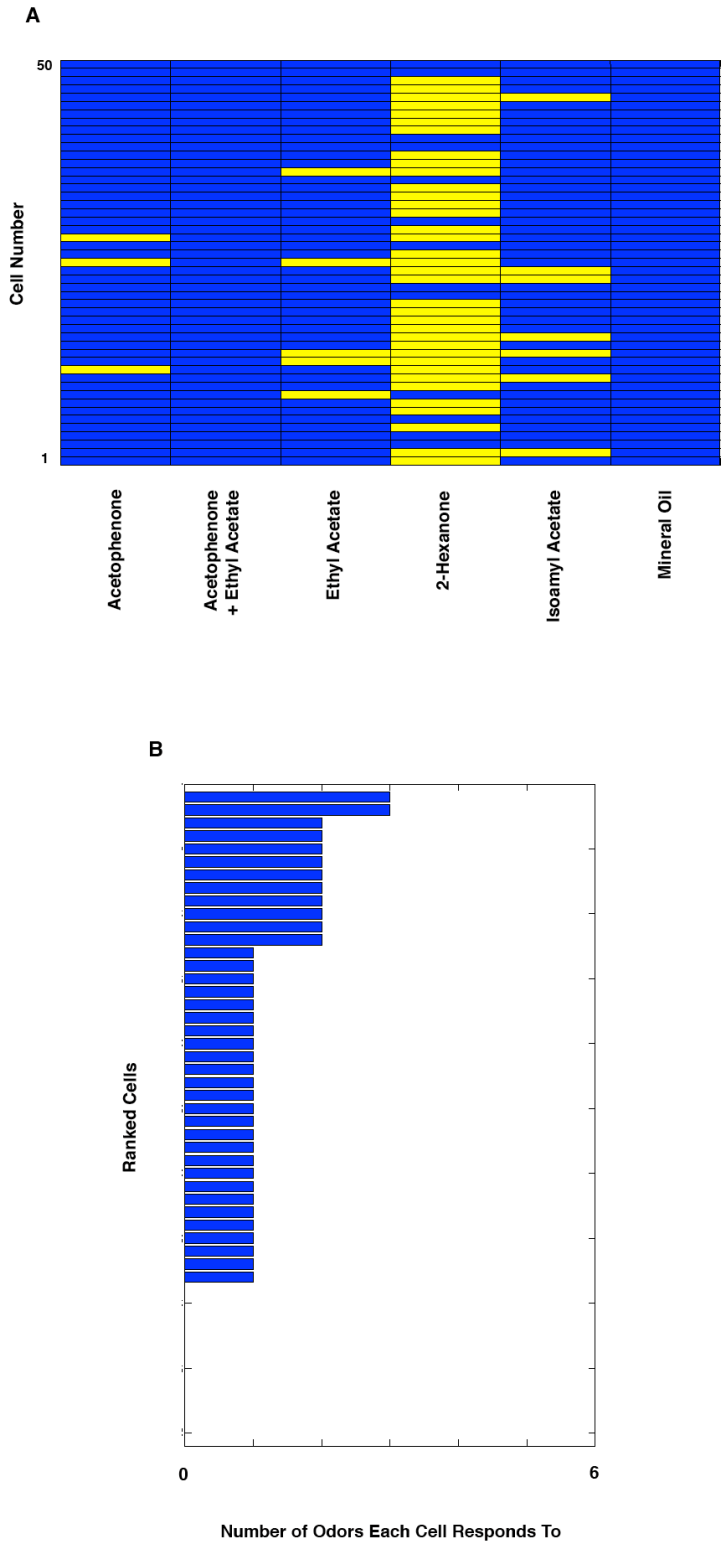
A
50
1
Cell Number
Acetophenone
Acetophenone + Ethyl Acetate
Ethyl Acetate
2-Hexanone
Isoamyl Acetate
Mineral Oil
B
Ranked Cells
0
6
Number of Odors Each Cell Responds To

Figure 26. Piriform neurons in M71 transgenic mice can be broadly or narrowly tuned to odor stimuli. (A) A binary response matrix illustrating the odor tuning of each cell at a high stimulus concentration at one imaging site in an M71 transgenic mouse (1/100 vol./vol. dilution in mineral oil; yellow square = cell responds to odor; blue square = cell does not respond to odor). **(B)** A ranked bar plot of the same cells in **(A)** with respect to the number of odors each cell responds to.

CHAPTER 4

SUMMARY AND CONCLUSIONS

For a wide variety of organisms on the planet, the sense of smell is of critical importance for survival. The mouse olfactory system mediates both learned and innate odor-driven behaviors, including activities as diverse as the localization of food sources, the avoidance of predators, and the selection of mates. How a chemical stimulus in the environment can ultimately lead to the generation of an appropriate behavioral response, however, remains poorly understood.

All of these behaviors begin with the binding of an odorant in the external environment to receptors on sensory neurons in the olfactory epithelium. These olfactory sensory neurons transmit this odor information to neurons in the olfactory bulb via stereotyped axonal projections, and a subset of these olfactory bulb neurons, mitral and tufted cells, in turn transmit this information via their axons to a number of higher brain regions implicated in learned and innate odor-driven responses, including the piriform cortex and amygdala.

Studies using electrophysiology and optical imaging techniques have revealed that individual odorants drive activity in unique, sparse ensembles of neurons that are distributed across the piriform without apparent spatial preference. The patterns of neural activity observed, however, do not reveal whether mitral and tufted cell projections from a given glomerulus to piriform cortex neurons are segregated or distributed, and whether they are random or determined. Distinguishing between these possibilities is important

for understanding the functional role of piriform cortex, as well as perception and behavior more generally: a random representation of odor identity in the piriform cortex could accommodate learned olfactory behaviors, but cannot specify innate odor-driven responses.

Rather, innate olfactory behaviors are likely to result from the activation of genetically determined, stereotyped neural circuits. Behavioral studies in which the normal function of the amygdala has been compromised by lesion or inactivation have found that innate, odor-driven behaviors are disrupted by these manipulations, but learned odor-driven behaviors are left intact, strongly suggesting a role for this area in innate olfactory responses (Blanchard and Blanchard, 1972; Slotnick, 1985; Slotnick and Risser, 1990). However, how odor information is represented in the amygdala, as well as the amygdala's exact role in the generation of innate olfactory responses, remain largely undefined.

We developed a strategy to trace the projections from identified glomeruli in the olfactory bulb to higher olfactory cortical centers. This technique has permitted us to define the neural circuits that convey olfactory information from specific glomeruli in the olfactory bulb to the piriform cortex and cortical amygdala. We find that mitral and tufted cells from every glomerulus elaborate similar axonal arbors in the piriform. These projections densely fan out across the cortical surface in a homogeneous manner, and quantitative analyses fail to identify features that distinguish the projection patterns from different glomeruli. In contrast, the cortical amygdala receives spatially stereotyped projections from individual glomeruli. The stereotyped projections from each glomerulus

target a subregion of the posterolateral cortical nucleus, but may overlap extensively with projections from other glomeruli.

The apparently random pattern of projections to the piriform and the determined pattern of projections to the amygdala are likely to provide the anatomic substrates for distinct odor-driven behaviors mediated by these two brain regions. The disperse, homogeneous organization of axonal projections from all mitral and tufted cells to the piriform cortex make it possible for any neuron in the piriform to receive input from any glomerulus in the olfactory bulb. If synaptic connections between mitral and tufted cells and piriform neurons are made at random, this anatomic organization could explain both the unique, apparently random nature of the ensembles of neurons that represent odors in the piriform, as well as the observation that piriform neurons often respond to a perceptually and chemically diverse complement of odors (Stettler and Axel, 2009). The representation of stimulus information in the piriform cortex therefore differs from that observed in other neocortical sensory areas, where cells are tuned to particular, continuously varying stimulus features and show spatial patterning on macroscopic as well as microscopic scales (Mountcastle, 1957; Hubel and Weisel, 1959; Okhi et al., 2005; Sato et al., 2007; Rothschild et al., 2010).

If the ensemble of neurons that encode the identity of an odor in the piriform cortex is random, then the representation of a given odor in the piriform will vary from animal to animal. It is therefore impossible for these representations of odor to mediate innate, hardwired perceptions or behaviors. Rather, these representations of odor in the piriform must be associated with perceptual or behavioral meaning through experience. It is this kind of coding strategy that makes the brain such a powerful substrate for

perception, memory, and behavior: because it would be inefficient and potentially deleterious to hardwire a behavioral output to every possible sensory input, the brain instead allows for the flexible association of a stimulus with a response to be formed as a consequence of experience.

A similar kind of coding strategy may be employed in the hippocampus, an area that has long been implicated in associative learning and memory. Like the piriform cortex, the hippocampus is a paleocortex consisting of a densely packed central layer of neurons flanked above and below by less densely populated cellular layers, laminarly well-defined afferent inputs, and extensive associative inputs between the neurons located in layer II (Shepherd, 1994; Haberly, 2001). Although more work needs to be done in both areas to establish causal links between structure and function, the striking anatomic similarity between the piriform cortex and hippocampus suggests that this kind of organization may be an optimal one for supporting flexible, experience-dependent associative learning, memory and behavior.

However, there are indeed behaviors whose appropriate execution are critical for the survival of an animal even upon its first encounter with a stimulus, such as the avoidance of predators. Instead of a random neural representation of these stimuli, one would expect a genetically hardwired organization of information that is stereotyped across animals to mediate these innate odor-driven responses. In the mouse olfactory system, we observe a pattern of mitral and tufted cell projections to the posterolateral nucleus of the cortical amygdala that is spatially targeted and invariant across individuals. These projections were distinct for each glomerulus, although projections from different glomeruli could display extensive overlap. In line with results from studies on the human

amygdala's role in olfactory processing and perception, this pattern of mitral and tufted cell projections to the amygdala may provide a substrate for the automatic association of odors with an innate hedonic valence, or behavioral value.

Due to limitations in the number of glomeruli we were able to sample as well as occassional failures in our labeling method, it is impossible to rule out the possibility that some glomeruli in the main olfactory bulb do not project to the cortical amygdala. However, the vast majority of glomeruli, from both dorsal and lateral regions of the olfactory bulb, whose projections we examined sent axons to the posterolateral nucleus of the amygdala. Interestingly, a similar organization is observed in the fruit fly *Drosophila melanogaster*. The lateral horn, a region thought to mediate innate odor-driven responses, is likely to receive projections from all glomeruli in the antenal lobe of the fly (Jefferis et al., 2007). Furthermore, it has been demonstrated that projections from glomeruli responsive to fruit odors and projections from glomeruli that respond to pheromones target different regions of the lateral horn, suggesting that the olfactory inputs to this area are topographically organized with respect to biological value (Jefferis et al., 2007).

An understanding of the meaning of the pattern of mitral and tufted cell projections to the amygdala will require experiments that similarly allow us to correlate anatomical structure with perceptual and behavioral function. Along these lines, future experiments can use the anatomical tracing method we have developed in combination with behavior and functional imaging techniques. Behavioral work has demonstrated that a number of naturally occurring monomolecular odorants possess an innate valence to mice; these odors include compounds released by predators such as foxes, weasels and cats, which evoke innate fear or avoidance responses by mice, as well as compounds

released by conspecifics that evoke innate attraction or aggression (Vernet-Maury et al., 1984; Lin et al., 2005; Brennan and Kendrick, 2006; Kobayakawa et al., 2007; Haga et al., 2010; Ferrero et al., 2011).

We are currently using behavioral assays to characterize the innate valence of odors to mice (Kobayakawa et al., 2007; Semmelhack and Wang, 2009) (Fig. 1). These assays permit the quantification of parameters such as odor investigation time, time spent near and far from the odorant, and amount of time spent freezing, which in turn allow us to classify a given odorant as innately aversive, innately attractive, or innately neutral to mice. We have used these assays to identify a number of innately aversive odorants, including TMT, a compound from fox feces that has been shown in a number of studies to evoke innate fear responses in mice, and components of cat urine, 3-Mercapto-3-methylbutan-1-ol (3-Merc) and 4-Methoxy-2-methylbutane-2-thiol (MMB), whose behavioral relevance had not been previously established (Fig. 2).

Furthermore, we have used the panel of innately aversive odorants identified using these assays in functional imaging experiments to map the patterns of glomerular responses to these odors. Using CCD imaging of odor-evoked glomerular activity in mice expressing synapto-pHluorin, the pH-sensitive indicator of synaptic release, in all olfactory sensory neurons (Bozza et al., 2004), we find that these innately aversive odorants evoke activity in a sparse ensemble of glomeruli on the dorsolateral and lateral surfaces of the olfactory bulb (Fig. 3). These representations remain sparse over increases in odor concentrations over several orders of magnitude (Fig. 3), and are stereotyped across mice (Fig. 4).

Using these techniques, we have identified the small number of glomeruli that respond to these innately relevant odors at near-threshold concentrations (Fig. 3, Fig. 4). Future experiments can use the maps of odor-responsive glomeruli we have generated to guide the electroporation of TMR dextran into glomeruli that respond to odors with defined valences, such as the aversive odor TMT. This approach will permit the labeling and characterization of mitral and tufted cell projections from functionally identified glomeruli to multiple regions of the olfactory cortex, allowing the further exploration of the functional role of the topography of mitral and tufted cell projections to the cortical amygdala. In addition, we are developing a method that will allow us to express channelrhodopsin-2 in single, functionally identified glomeruli via electroporation of plasmid DNA. This technique will allow us to determine which glomeruli responsive to innately relevant odors are able to drive behavioral responses, as well as which downstream brain areas, including the amygdala, can mediate these responses using the spatially targeted delivery of light to different locations on mitral and tufted cell dendrites and axons.

The stereotyped glomerular organization of input to the bulb is a hallmark of the mammalian olfactory system. Although many have implicated this organization in increasing the ability of the olfactory system to detect weak sensory signals via intraglomerular convergence and excitation and the refinement of mitral and tufted cell tuning via inhibitory interactions, direct evidence for the functional role of this anatomical arrangement has been lacking. In addition, although the diversity and complexity of local circuits in the olfactory bulb has been well established, the functional role of this anatomical sophistication is largely unknown.

Using a transgenic mouse with a "monoclonal" nose, we were able to gain insight into the way odor information is represented and transformed by the olfactory bulb. In control mice, odors evoke activity in unique ensembles of spatially distributed, narrowly tuned mitral and tufted cells, and the number of cells responding increases linearly with odor concentration. Surprisingly, despite the fact that there is a significant decrease in presynaptic glomerular activity in response to odors other than acetophenone in M71 transgenics, a wide variety of odorants are able to evoke activity in mitral and tufted cells in these mice. Furthermore, the number of cells responding to these odors, particularly at the highest concentrations, and the magnitude of these odor-evoked responses are higher in M71 transgenics compared to control mice. However, despite a massive increase in acetophenone-evoked sensory neuron input to the bulb in M71 mice, mitral and tufted cell responses to acetophenone are similar in terms of the number of cells responding as well as their spatial distribution in M71 transgenics and controls. Our observations suggest that a major role of the glomerular organization of the olfactory bulb is to aid in the comprehensive detection of the wide variety of odor stimuli in the environment by amplifying weak sensory inputs while suppressing strong inputs.

Past work has demonstrated that odor information is represented by unique ensembles of topographically distributed neurons in piriform cortex. Whether this representation arises largely as a consequence of the disperse pattern of feedforward input the piriform receives from mitral and tufted cells, or whether this representation is uniquely computed by local circuits in the piriform cortex, however, is just beginning to be understood. Because the representation of odor in the mitral cell layer of the olfactory bulb of M71 transgenic mice is uniquely different from that which we observe in

controls, we used these M71 transgenic mice to investigate whether the representation of odor in the piriform is dominated by feedforward input from the bulb or is largely the result of transformations performed by circuits within the piriform.

Despite the fact that the representation of odor in the olfactory bulb of M71 transgenic mice differs from that which we observed in controls, we find that the representation of odor in the piriform cortex of M71 transgenic mice and controls is quantitatively indistinguishable. Our results suggest that circuits intrinsic to the piriform cortex significantly transform the representation of odor information it receives from the mitral and tufted cells of the bulb into a highly sparse, topographically disperse representation in which odor-evoked activity is kept within a small dynamic range. The sparse, distributed representation of odor information we observe in the piriform minimizes overlap between stimuli, maximizes decorrelation between patterns of odor-evoked activity, and may enhance not only the discrimination of odor stimuli but also sensory-evoked associative learning. Together, our results demonstrate that information about odors is significantly transformed as it passes through the mouse olfactory system from the sensory periphery to the cerebral cortex, and the unique nature of these transformations suggest distinct functional roles for the olfactory bulb and piriform cortex in olfactory processing, perception and behavior.

In the future, a mechanistic determination of the circuit mechanisms underlying these transformations and representations in the olfactory bulb will depend on the targeted manipulation of different cellular elements. Injecting AAV-GCaMP3 into the center of the bulb leads to the labeling of hundreds of periglomerular and granule cells (Fig. 5). The nature of this labeling permits us to selectively measure odor-evoked

responses in these different classes of inhibitory neurons, which will allow us to determine whether the inhibition of acetophenone-evoked signals we observe in M71 transgenic mice takes place at the level of input to the bulb via periglomerular cells, whether inhibition takes place at the level of output from the bulb via granule cells, or whether a combination of these inhibitory mechanisms are at work in these mice. Furthermore, by pairing the ability to image the odor-evoked activity of mitral and tufted, periglomerular, and granule cells afforded by the rabies-GCaMP3 and AAV-GCaMP3 viruses with pharmacological manipulation (e.g. blocking or eliminating inhibition), we can further tease apart the roles that these different kinds of neurons play in the representation and transformation of odor information by the olfactory bulb.

Elucidating how the bulb represents and transforms information about odor has been particularly challenging not only because of the diversity and complexity of circuits in the olfactory bulb, but also because of a lack of high-throughput techniques for recording neuronal activity in the bulb. Using a novel virus-conjugated calcium indicator, rabies-GCaMP3, we have developed a new high-throughput technique for imaging the odor-evoked activity of large populations of mitral and tufted cells in the mouse olfactory bulb. This virus enables us to drive high expression of GCaMP3 in mitral and tufted cells in a spatially unbiased manner, and simultaneously image odor-evoked responses in hundreds of cells. In the future, this technique will allow for imaging of mitral and tufted cell responses to be performed in a variety of different preparations, including in awake mice engaged in behavioral tasks (Dombeck et al., 2007). Furthermore, expression of GCaMP3 in these mitral and tufted cells is stable enough to permit the investigation of the changes that occur during olfactory learning and experience.

Finally, future experiments can use this rabies-GCaMP3 method to investigate how odor information is represented and transformed by many other areas of the mouse olfactory system. For instance, although olfactory memories can be some of the most vivid recollections people possess, it is unclear how these memories arise. Previous work suggests that the hippocampus is critical for the formation as well as the expression of associations between odor memories (Eichenbaum, 1998; Alvarez et al., 2002; Fortin et al., 2002), and it has been demonstrated that all olfactory sensory input to the hippocampus is mediated by projections from the lateral entorhinal cortex (Kerr et al., 2007). To investigate the representation of odor in the entorhinal cortex, the representation of odor information that is projected to the hippocampus, and what role these areas may play in the formation of sensory memories, one could inject rabies-GCaMP3 into the hippocampus and perform imaging experiments in the lateral entorhinal cortex similar to those we have described in the olfactory bulb.

Over the past five years, we have used a combination of genetic, anatomic, imaging, and behavioral techniques to elucidate how the mouse olfactory system represents and transforms information about odors, and how these representations and transformations may underlie the role these areas play in the generation of sensory perceptions and behaviors. Although the mouse olfactory system is able to mediate a diverse and complex array of behaviors critical for survival, it is also a relatively shallow system: only two synapses exist between primary olfactory sensory neurons and the principal neurons of higher brain regions implicated in learning, emotion, and memory. These features make it an invaluable model system for cellular, behavioral and systems neurobiology, and by continuing to dissect the function of the mouse olfactory system,

we will gain insight into one of the greatest questions in neuroscience: how patterns of electrical activity generated by neural circuits in the brain are able to engender perceptions, thoughts, memories, and behaviors, and how the mind ultimately arises out of a complicated mass of a hundred billion cells.

Figure 1.

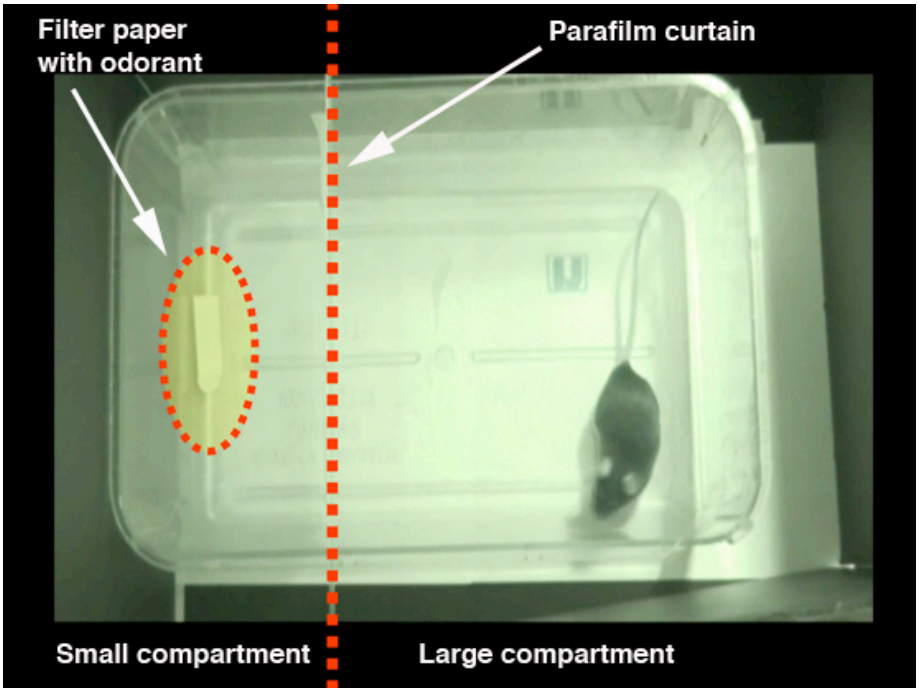
Filter paper
with odorant
Parafilm curtain
Small compartment
Large compartment

Figure 1. Schematic of the partitioned behavior arena used for determining the innate relevance of odorants. The arena consists of a clean Plexiglas cage divided into a large and small compartment with a moveable curtain made of parafilm (red dotted line). After a 5-minute habituation period in which the animal is allowed to freely explore the arena, a piece of filter paper with 50 µl of odorant is placed into the small compartment (yellow circle). The animal's response to this odorant over the first 3 minutes after delivery of the stimulus is then quantified post hoc by measuring the time the animal spends investigating (sniffing) the filter paper, the time the animal spends in the small and large compartments, and the time the animal spends freezing (the cessation of all movement except for that associated with breathing).

Figure 2.

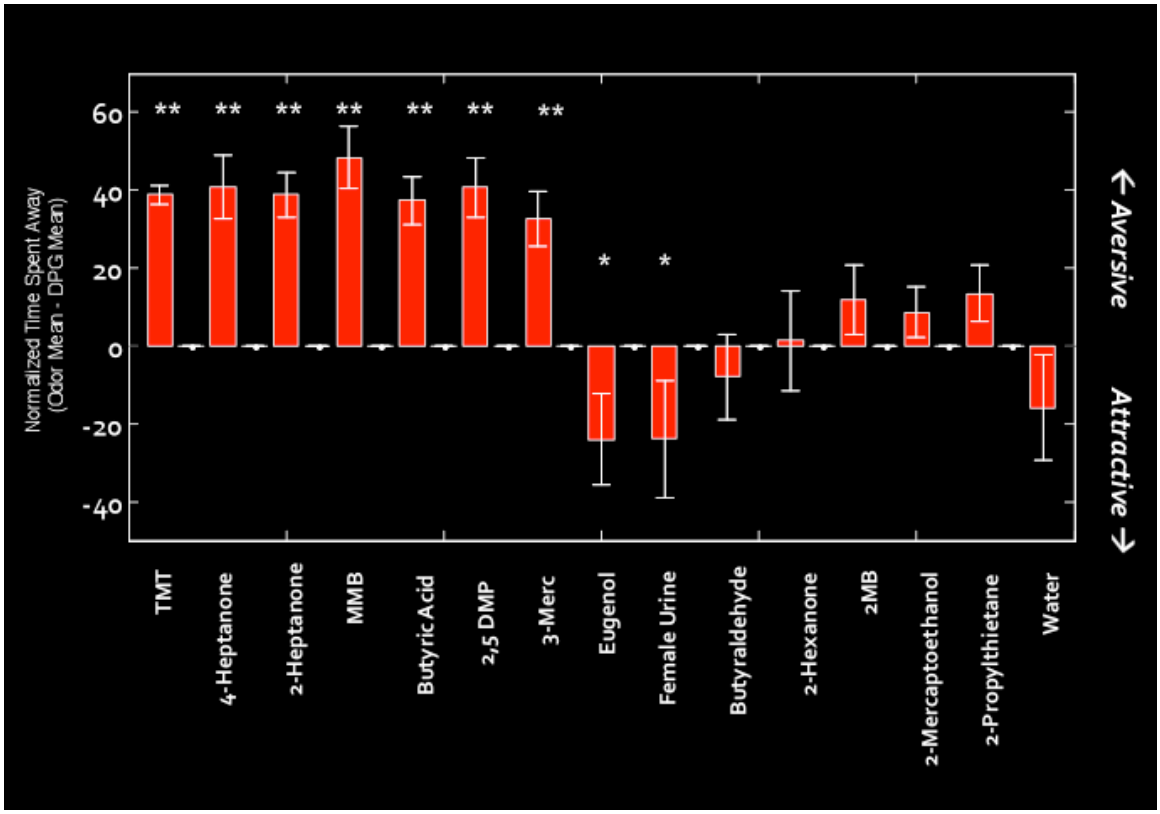
Normalized Time Spent Away
(Odor Mean - DPG Mean)
60
40
20
0
-20
-40
**
**
**
**
**
**
**
*
*
← Aversive
Attractive →
TMT
4-Heptanone
2-Heptanone
MMB
Butyric Acid
2,5 DMP
3-Merc
Eugenol
Female Urine
Butyraldehyde
2-Hexanone
2MB
2-Mercaptoethanol
2-Propylthietane
Water

Figure 2. The partitioned behavior arena can be used to classify the innate relevance of odors to mice. Plotted is the normalized time the animal spends in the large compartment of the arena (away from the odor), which is calculated by subtracting the average time the mouse spends in the large compartment when an odorless diluent is presented on the filter paper from the average time the mouse spends in the large compartment when the test odor stimulus is presented in the filter paper. The resulting number is positive if the animal spends more time in the large compartment of the arena, and negative if the animal spends more time in the small compartment of the arena. Odors are classified as innately aversive if this number is significantly positive, innately attractive if this number is significantly negative, and innately neutral if this number is not significantly negative or positive (Student's t-test; * = significant at $\alpha = 0.05$; ** = significant at $\alpha = 0.01$).

Figure 3.

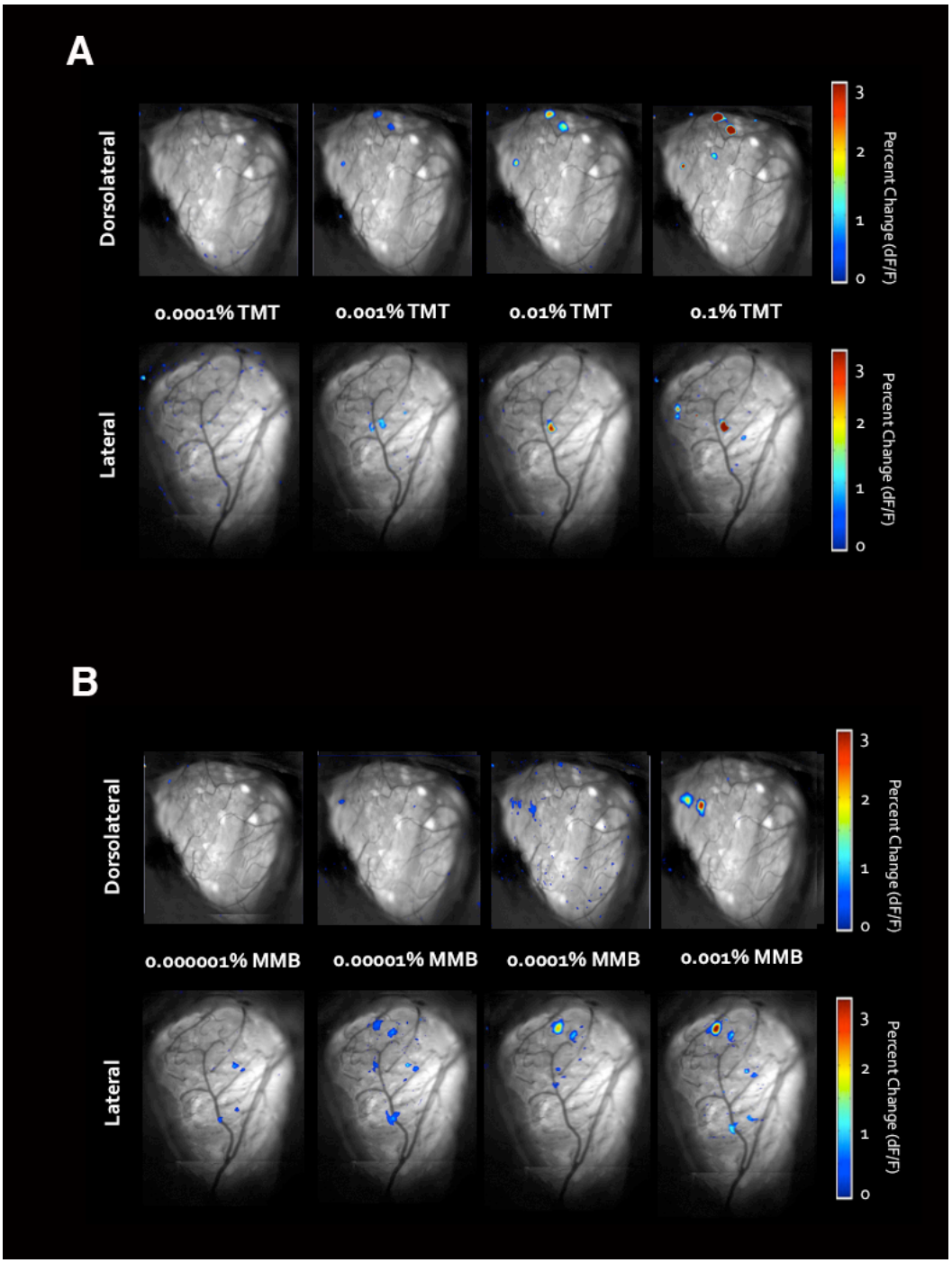
A
Dorsolateral
0.0001% TMT
0.001% TMT
0.01% TMT
0.1% TMT
Lateral
Percent Change (dF/F)
3
2
1
0
B
Dorsolateral
0.000001% MMB
0.00001% MMB
0.0001% MMB
0.001% MMB
Lateral

Figure 3. Innately aversive odorants evoke activity in a sparse ensemble of glomeruli on the dorsolateral and lateral surfaces of the olfactory bulb. (A) The innately aversive odorant TMT, produced by the anal gland of the fox, evokes activity in ~3 glomeruli on the dorsal (top row) and lateral (bottom row) surfaces of the olfactory bulb at near-threshold concentrations. The ensemble of glomeruli responding to TMT remains sparse even when the stimulus concentration is increased over several orders of magnitude. **(B)** The innately aversive odorant MMB, found in cat urine, evokes activity in ~2 glomeruli on the dorsal (top row) and lateral (bottom row) surfaces of the olfactory bulb at near-threshold concentrations. The ensemble of glomeruli responding to MMB remains sparse even when the stimulus concentration is increased over several orders of magnitude.

Figure 4.

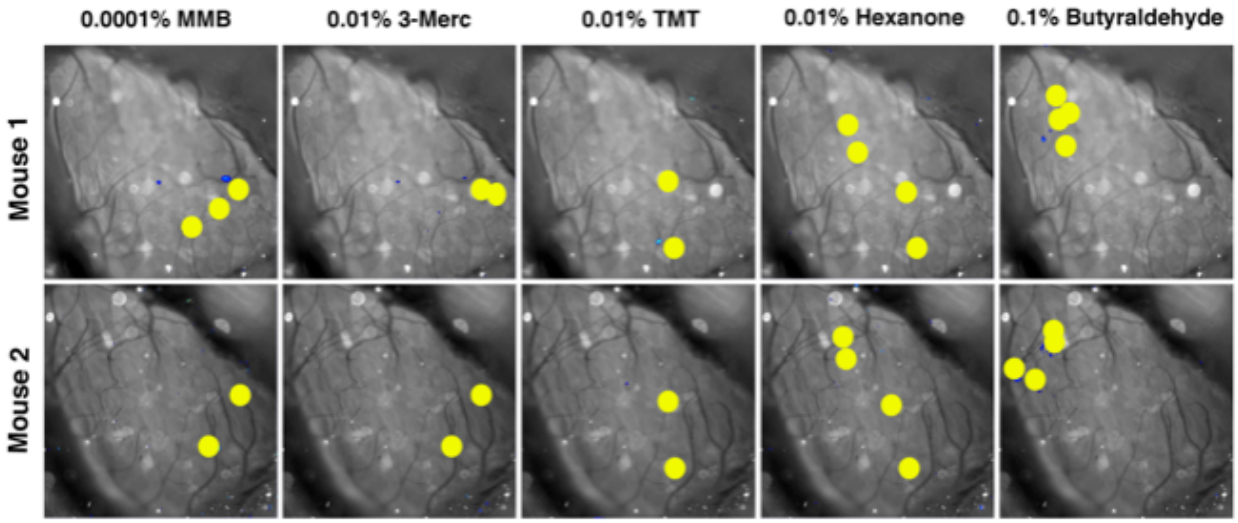
0.0001% MMB
0.01% 3-Merc
0.01% TMT
0.01% Hexanone
0.1% Butyraldehyde
Mouse 1
Mouse 2

Figure 4. Innately aversive odorants evoke activity in a sparse ensemble of glomeruli that is stereotyped across mice. The ensembles of glomeruli activated on the dorsolateral surface of the olfactory bulb by five odors at near-threshold concentrations (four innately aversive odorants, TMT, MMB, 3-Merc, and 2-Hexanone, as well as the innately neutral odor butyraldehyde) are similar in two different mice (top row, bottom row). The location of each odor-responsive glomerulus is marked with a yellow dot.

Figure 5.

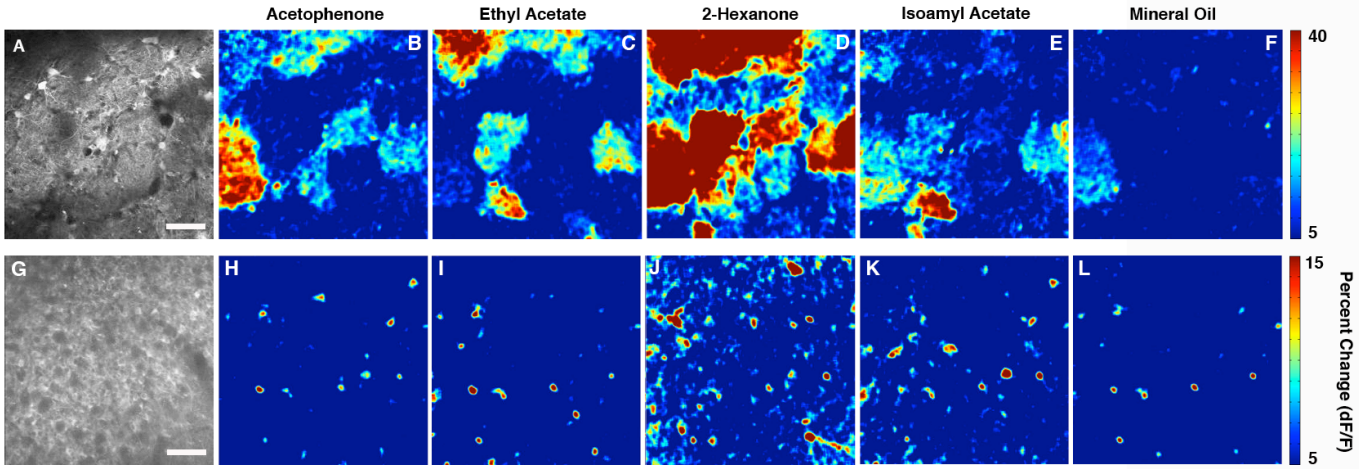
Acetophenone
Ethyl Acetate
2-Hexanone
Isoamyl Acetate
Mineral Oil
A
B
C
D
E
F
40
5
G
H
I
J
K
L
15
5
Percent Change (dF/F)

Figure 5. AAV-GCaMP3 can be used to image odor-evoked responses of periglomerular and granule cells. (A) Two-photon image of the resting fluorescence of periglomerular cells infected with AAV-GCaMP3 (scale bar = 85 μM). **(B-F)** Periglomerular cell responses to the delivery of acetophenone **(B)**, ethyl acetate **(C)**, 2-hexanone **(D)**, isoamyl acetate **(E)**, and mineral oil **(F)** (all presented at a concentration of 1/100 vol./vol. dilution in mineral oil). **(G)** Two-photon image of the resting fluorescence of granule cells infected with AAV-GCaMP3 (scale bar = 85 μM). **(H-L)** Granule cell responses to the delivery of acetophenone **(H)**, ethyl acetate **(I)**, 2-hexanone **(J)**, isoamyl acetate **(K)**, and mineral oil **(L)** (all presented at a concentration of 1/100 vol./vol. dilution in mineral oil).

REFERENCES

Abraham, N.M. *et al.* Maintaining accuracy at the expense of speed: stimulus similarity defines odor discrimination time in mice. *Neuron* **5**, 865-76 (2004).

Abraham, N.M. *et al.* Synaptic inhibition in the olfactory bulb accelerates odor discrimination in mice. *Neuron* **3**, 399-411 (2010).

Alvarez, P., Wendelken, L., & Eichenbaum, H. Hippocampal lesions impair performance in an odor-odor association task independently of spatial context. *Neurobiol Learn Mem* **2**, 470-6 (2002).

Apicella, A., Yuan, Q., Scanziani, M. & Isaacson, J.S. Pyramidal cells in piriform cortex receive convergent input from distinct olfactory bulb glomeruli. *J Neurosci* **42**, 14255-60 (2010).

Araneda, R.C., Kini, A.D. & Firestein, S. The molecular receptive range of an odorant receptor. *Nat Neurosci* **12**, 1248-55 (2000).

Arankiel, B.R. *et al.* In vivo light-induced activation of neural circuitry in transgenic mice expressing channelrhodopsin-2. *Neuron* **2**, 205-18 (2007).

Arevian, A.C., Kapoor, V. & Urban N.N. Activity-dependent gating of lateral inhibition in the mouse olfactory bulb. *Nat Neurosci* **1**, 80-7 (2008).

Aroniadou-Anderjaska, V., Zhou, F.M., Priest, C.A., Ennis, M. & Shipley, M.T. Tonic and synaptically evoked presynaptic inhibition of synaptic input to the rat olfactory bulb via GABA(B) heteroreceptors. *J Neurophysiol* **3**, 1194-203 (2000).

Assisi, C., Stopfer, M., Laurent, G. & Bazhenov, M. Adaptive regulation of sparseness by feedforward inhibition. *Nat Neurosci* **9**, 1176-84 (2007).

Aungst, J.L. *et al.* Centre-surround inhibition among olfactory bulb glomeruli. *Nature* **6967**, 623-9 (2003).

Barkai, E. & Saar, D. Cellular correlates of olfactory learning in the rat piriform cortex. *Rev Neurosci* **2**, 111-20 (2001).

Barlow, H.B., Narasimhan, R. & Rosenfeld, A. Visual pattern analysis in machines and animals. *Science* **49**, 567-75 (1972).

Barnes, D.C., Hofacer, R.D., Zaman, A.R., Rennaker, R.L. & Wilson, D.A. Olfactory perceptual stability and discrimination. *Nat Neurosci* **12**, 1378-80 (2008).

Beck, J., Fonberg, E. & Korczynski, R. The effect of medial amygdala lesions on instrumental sexual responses in male rats. *Acta Neurobiol Exp (Wars)* **4-5**, 427-32 (1982).

Belluscio, L & Katz, L.C. Symmetry, stereotypy and topography of odorant representations in mouse olfactory bulbs. J Neurosci 6, 2113-22 (2001).

Biella, G. & de Curtis, M. Olfactory inputs activate the medial entorhinal cortex via the hippocampus. *J Neurophysiol* **4**, 1924-31 (2000).

Blanchard, D. C. & Blanchard, R. J. Innate and conditioned reactions to threat in rats with amygdaloid lesions. *J Comp Physiol Psychol* **81**, 281-290 (1972).

Bockamp, E *et al.* Of mice and models: improved animal models for biomedical research. *Physiol Genomics* **3**, 115-32 (2002).

Bodyak, N. & Slotnick, B. Performance of mice in an automated olfactometer: odor detection, discrimination and odor memory. *Chem Senses* **6**, 637-45 (1999).

Boulet, M., Daval, G. & Leveteau, J. Qualitative and quantitative odour discrimination by mitral cells as compared to anterior olfactory nucleus cells. *Brain Res* **1**, 123-34 (1978).

Boyden, E.S., Zhang, F., Bamberg, E., Nagel, G., & Deisseroth, K. Millisecond-timescale, genetically targeted optical control of neural activity. *Nat Neurosci* **9**. 1263-8 (2005).

Bozza, T., McGann, J. P., Mombaerts, P. & Wachowiak, M. In vivo imaging of neuronal activity by targeted expression of a genetically encoded probe in the mouse. *Neuron* **42**, 9-21 (2004).

Brennan, P.A. & Kendrick, M.M. Mammalian social odours: attraction and individual recognition. *Philos Trans R Soc Lond B Biol Sci* **1476**, 2061-78 (2006).

Brunjes P.C., Illig, K.R. & Meyer, E.A. A field guide to the anterior olfactory nucleus (cortex). *Brain Res Brain Res Rev* **2**, 305-35 (2005).

Buck, L. & Axel, R. A novel multigene family may encode odorant receptors: a molecular basis for odor recognition. *Cell* **65**, 175-187 (1991).

Budinger, E., Heil, P., Hess, A. & Scheich, H. Multisensory processing via early cortical stages: Connections of the primary auditory cortical field with other sensory systems. *Neuroscience* **4**, 1065-83 (2006).

Bunting, M., Bernstein, K.E., Greer, J.M., Capecchi, M.R. & Thomas, K.R. Targeting genes for self-excision in the germ line. *Genes Dev* **12**, 1524-8 (1999).

Buonviso, N., Revial, M. F. & Jourdan, F. The Projections of Mitral Cells from Small Local Regions of the Olfactory Bulb: An Anterograde Tracing Study Using PHA-L (Phaseolus vulgaris Leucoagglutinin). *Eur J Neurosci* **3**, 493-500 (1991).

Burgalossi, A *et al.* Microcircuits of functionally identified neurons in the rat medial entorhinal cortex. *Neuron* **4**, 773-86 (2011).

Cain, D.P. & Bindra, D. Responses of amygdala single units to odors in the rat. *Exp Neurol* **1**, 98-110 (1972).

Cajal, S.R. Histologie du systeme nerveux de l'homme et des vertebres. A. Maloine, Paris (1909).

Chabaud, P. *et al.* Exposure to behaviorally relevant odour reveals differential characteristics in rat central olfactory pathways as studied through oscillatory activities. *Chem Senses* **5**, 561-73 (2000).

Chen, W.R. & Shepherd, G.M. The olfactory glomerulus: a cortical module with specific functions. *J Neurocytol* **3-5**, 353-60 (2005).

Chess, A., Simon, I., Cedar, H. & Axel, R. Allelic inactivation regulates olfactory receptor gene expression. *Cell* **78**, 823-834 (1994).

Chaudhury, D., Escanilla, O. & Linster, C. Bulbar acetylcholine enhances neural and perceptual odor discrimination. *J Neurosci* **1**, 52-60 (2009).

Choi, G.B. *et al.* Driving opposing behaviors with ensembles of piriform neurons. *Cell* (in press) (2011).

Christie, J.M. *et al.* Connexin36 mediates spike synchrony in olfactory bulb glomeruli. *Neuron* **5**, 761-72 (2005).

Christie, J.M. & Westbrook, G.L. Lateral excitation within the olfactory bulb. *J. Neurosci* **8**, 2269-77 (2006).

Cleland, T.A. & Linster, C. Concentration tuning mediated by spare receptor capacity in olfactory sensory neurons: A theoretical study. *Neural Comput* **7**, 1673-90 (1999).

Cohen, Y., Reuveni, I., Barkai, E. & Maroun, M. Olfactory learning-induced long-lasting enhancement of descending and ascending synaptic transmission to the piriform cortex. *J Neurosci* **26**, 6664-9 (2008).

Costantini, F. & Lacy, E. Introduction of a rabbit beta-globin gene into the mouse germ line. *Nature* **5836**, 92-4 (1981).

Datta, S.R. *et al.* The Drosophila pheromone cVA activates a sexually dimorphic neural circuit. *Nature* **7186**, 473-7 (2008).

Davison, I.G. & Katz L.C. Sparse and selective odor coding by mitral/tufted neurons in the main olfactory bulb. *J Neurosci* **8**, 2091-101 (2007).

Davison, I.G. & Ehlers, M.D. Neural circuit mechanisms for pattern detection and feature combination in olfactory cortex. *Neuron* **1**, 82-94 (2011).

De Bono, M. & Maricq, A.V. Neuronal substrates of complex behaviors in C. elegans. *Annu Rev Neurosci* **28**, 451-501 (2005).

DeMaria, S. & Ngai, J. The cell biology of smell. *J Cell Biol* **3**, 443-52 (2010).

de Olmos, J., Hardy, H. & Heimer, L. The afferent connections of the main and the accessory olfactory bulb formations in the rat: an experimental HRP-study. *J Comp Neurol* **181***,* 213-244 (1978).

DelBarco-Trillo, J., Gulewicz, K. & Johnston, R.E. Medial amygdala involvement in discrimination of same-species and closely-related-species male stimuli in estrous female Mesocricetus hamsters. *Behav Neurosci* **4**, 758-63 (2009).

Del-Fava, F., Hasue, R.H., Ferreria, J.G. & Shammah-Lagnado, S.J. Efferent connections of the rostral linear nucleus of the ventral tegmental area in the rat. *Neuroscience* **3**, 1059-76 (2007).

Dhawale A.K., Hagiwara, A., Bhalla, U.S., Murthy, V.N. & Albeanu, D.F. Non-redundant odor coding by sister mitral cells revealed by light addressable glomeruli in the mouse. *Nat Neurosci* **11**, 1404-12 (2010).

Dittgen, T. *et al.* Lentivirus-based genetic manipulations of cortical neurons and their optical and electrophysiological monitoring in vivo. *Proc Natl Acad Sci U S A* **52**, 18206-11 (2004).

Dombeck, D.A., Khabbaz, A.N., Collman, F., Adelman, T.L. & Tank, D.W. Imaging large-scale neural activity with cellular resolution in awake, mobile mice. *Neuron* **1**, 43-57 (2007).

Doucette, W., Milder, J. & & Restrepo, D. Adrenergic modulation of olfactory bulb circuitry affects odor discrimination. *Learn Mem* **8**, 539-47 (2007).

Doucette, W. *et al.* Associative cortex features in the first olfactory brain relay station. *Neuron* **6**, 1176-87 (2011).

Dulac, C. & Axel, R. A novel family of genes encoding putative pheromone receptors in mammals. *Cell* **2**, 195-206 (1995).

Egaña, J.L., Aylwin, M.L. & Maldonado, P.E. Odor response properties of neighboring mitral/tufted cells in the rat olfactory bulb. *Neuroscience* **3**, 1069-80 (2005).

Eichenbaum, H. Using olfaction to study memory. *Ann N Y Acad Sci* **855**, 657-69 (1998).

Ekstrand, J.J., Domroese, M.E., Feig, S.L., Illig, K.R. & Haberly, L.B. Immunocytochemical analysis of basket cells in rat piriform cortex. *J Comp Neurol* **3**, 308-28 (2001).

Emmenlauer, M. *et al.* XuvTools: free, fast and reliable stitching of large 3D datasets. *J Microsc* **1**, 42-60 (2009).

Fadool, D.A. *et al.* Kv1.3 channel gene-targeted deletion produced “Super-Smeller Mice” with altered glomeruli, interacting scaffolding proteins, and biophysics. *Neuron* **3**, 389-404 (2004).

Fallon, J.H., Riley, J.N., Sipe, J.C. & Moore, R.Y. The islands of Calleja: organization and connections. *J Comp Neurol* **2**, 375-95 (1978).

Ferrero et al. Detection and avoidance of a carnivore odor by prey. *Proc Natl Acad Sci U S A* **27**, 11235-40 (2011).

Ferry, B., Wirth, S. & Di Scala, G. Functional interaction between entorhinal cortex and basolateral amygdala during trace conditioning of odor aversion in the rat. *Behav Neurosci* **1**, 118-25 (1999).

Ferry, B., Ferreira, G., Traissard, N. & Majchrzak, M. Selective involvement of the lateral entorhinal cortex in the control of the olfactory memory trace during conditioned odor aversion in the rat. *Behav Neurosci* **5**, 1180-6 (2006).

Fleischmann, A. *et al.* Mice with a "monoclonal nose": perturbations in an olfactory map impair odor discrimination. *Neuron* **6**, 1068-81 (2008).

Fletcher, M.L. & Chen, W.R. Neural correlates of olfactory learning: Critical role of centrifugal neuromodulation. *Learn Mem* **11**, 561-70 (2010).

Fortin, N.J., Agster, K.L. & Eichenbaum, H.B. Critical role of the hippocampus in memory for sequences of events. *Nat Neurosci* **5**, 458-62 (2002).

Fox, J.G. *The mouse in biomedical research.* 2nd ed. London: Elsevier, 2007.

Franks, K.M. & Isaacson, J.S. Synapse-specific downregulation of NMDA receptors by early experience: a critical period for plasticity of sensory input to the olfactory cortex. *Neuron* **1**, 101-14 (2005).

Franks, K.M. *et al.* Recurrent circuitry dynamically shapes the activation of piriform cortex. *Neuron* (in press), (2011).

Fyhn, M., Molden, S., Witter, M.P., Moser, E.I. & Moser, M.B. Spatial representation in the entorhinal cortex. *Science* **5688**, 1258-64 (2004).

Ghosh S. *et al.* Sensory maps in the olfactory cortex defined by long-range viral tracing of single neurons. *Nature* **7342**, 217-20 (2011).

Gogos, J.A., Osborne, J., Nemes, A., Mendelsohn, M. & Axel, R. Genetic ablation and restoration of the olfactory topographic map. *Cell* **4**, 609-20 (2000).

Gossen M. *et al.* Transcriptional activation by tetracyclines in mammalian cells. *Science* **5218**, 1766-9 (1995).

Gordon, J.W. & Ruddle, F.H. Integration and stable germ line transmission of genes injected into mouse pronuclei. *Science* **4526**, 1244-6 (1981).

Haberly, L.B. Parallel-distributed processing in olfactory cortex: new insights from morphological and physiological analysis of neuronal circuitry. *Chem Senses* **5**, 551-76 (2001).

Haberly, L. B. & Price, J. L. The axonal projection patterns of the mitral and tufted cells of the olfactory bulb in the rat. *Brain Res* **129**, 152-157 (1977).

Hafting, T., Fyhn, M., Molden, S., Moser, M.B. & Moser, E.I. Microstructure of a spatial map in the entorhinal cortex. *Nature* **7052**, 801-6 (2005).

Haga, S. *et al.* The male mouse pheromone ESP1 enhances female sexual receptive behaviour through a specific vomeronasal receptor. *Nature* **7302**, 118-22 (2010).

Hamilton, K.A. *et al.* Properties of external plexiform layer interneurons in mouse olfactory bulb slices. *Neuroscience* **3**, 819-29 (2005).

Harvey, C.D., Collman, F., Dombeck, D.A. & Tank, D.W. Intracellular dynamics of hippocampal place cells during virtual navigation. *Nature* **7266**, 941-6 (2009).

Hayar, A., Karnup, S., Ennis, M. & Shipley, M.T. External tufted cells: a major excitatory element that coordinates glomerular activity. *J Neurosci* **30**, 6676-85 (2004).

Henriksen, E.J. *et al.* Spatial representation along the proximodistal axis of CA1. *Neuron* **1**, 127-37 (2010).

Hess, U.S., Gall, C.M., Granger, R. & Lynch, G. Differential patterns of c-fos mRNA expression in amygdala during successive stages of odor discrimination learning. *Learn Mem* **3**, 262-83 (1997).

Hobert, O. Behavioral plasticity in C. elegans: paradigms, circuits, genes. *J Neurobiol* **1**, 203-23 (2003).

Hubel, D.H. & Wiesel, T.N. Receptive fields of single neurones in the cat's striate cortex. *J Physiol* **148**, 574-91 (1959).

Hudry, J., Ryvlin, P., Royet, J.P. & Mauguiere, F. Odorants elicit evoked potentials in the human amygdala. *Cereb Cortex* **7**, 619-27 (2001).

Hughes, J.R. & Andy, O.J. The human amygdala. I. Electrophysiological responses to odorants. *Electroencephalogr Clin Neurophysiol* **4**, 428-43 (1979).

Huyser, S., McKeithen, A. & Pearson, J. "Rene Descartes (1596-1650)." Historical Collections :: Vaulted Treasures. 2007. Historical Collections at the Claude Moore Health Sciences Library, University of Virginia. August 20, 2011 < http://historical.hsl.virginia.edu/treasures/descartes.html>.

Ikemoto, S. Dopamine reward circuitry: two projection systems from the ventral midbrain to the nucleus accumbens-olfactory tubercle complex. *Brain Res Rev* **1**, 27-78 (2007).

Illig, K. R. & Haberly, L. B. Odor-evoked activity is spatially distributed in piriform cortex. *J Comp Neurol* **457**, 361-373 (2003).

Imamura, K., Mataga, N. & Mori, K. Coding of odor molecules by mitral/tufted cells in rabbit olfactory bulb. I. Aliphatic compounds. *J Neurophysiol* **6**, 1986-2002 (1992).

Isaacson, J.S. Glutamate spillover mediates excitatory transmission in the rat olfactory bulb. *Neuron* **2**, 377-84 (1999).

Isaacson, J.S. & Strowbridge, B.W. Olfactory reciprocal synapses: dendritic signaling in the CNS. *Neuron* **4**, 749-61 (1998).

Ito I, Ong R.C., Raman B. & Stopfer, M. Sparse odor representation and olfactory learning. *Nat Neurosci.* **10**, 1177-84 (2008).

Jahr, C.E. & Nicoll, R.A. Dendrodendritic inhibition: demonstration with intracellular recording. *Science* **4438**, 1473-5 (1980).

Jahr, C.E. & Nicoll, R.A. Noradrenergic modulation of dendrodendritic inhibition in the olfactory bulb. *Nature* **5863**, 227-9 (1982).

Jefferis, G.S. *et al.* Comprehensive maps of Drosophila higher olfactory centers: spatially segregated fruit and pheremone representation. *Cell* **6**, 1187-203 (2007).

Johnston, D.M., Illig, K.R., Behan, M. & Haberly, L.B. New features of connectivity in piriform cortex visualized by intracellular injection of pyramidal cells suggest that "primary" olfactory cortex functions like "association" cortex in other sensory systems. *J Neurosci* **20**, 6974-6982 (2000).

Judkewitz, B., Rizzi, M., Kitamura, K., & Häusser, M. Targeted single-cell electroporation of mammalian neurons in vivo. *Nat Protoc* **6**, 862-9 (2009).

Kandel, E.R., Schwartz, J.H. & Jessell, T.M., ed. *Principles of Neural Science*, 4th ed. New York: McGraw-Hill, 2000.

Katoh, K., Koshimoto, H., Tani, A. & Mori, K. Coding of odor molecules by mitral/tufted cells in rabbit olfactory bulb II: Aromatic compounds. *J. Neurophysiol* **5**, 2161-75 (1993).

Kay, L.M. & Laurent, G. Odor- and context-dependent modulation of mitral cell activity in behaving rats. *Nat Neurosci* **11**, 1003-9 (1999).

Kerr, K.M., Agster, K.L., Furtak, S.C. & Burwell, R.D. Functional neuroanatomy of the parahippocampal region: the lateral and medial entorhinal areas. *Hippocampus* **9**, 697-708 (2007).

Kikuta, S. *et al.* From the Cover: Neurons in the anterior olfactory nucleus pars externa detect right or left localization of odor sources. *Proc Natl Acad Sci U S A* **27**, 12363-8 (2010).

Kimchi, T., Xu, J. & Dulac, C. A functional circuit underlying male sexual behaviour in the female mouse brain. *Nature* **7157**, 1009-14 (2007).

Kiyokage, E. *et al.* Molecular identity of periglomerular and short-axon cells. *J Neurosci* **3**, 1185-96 (2010).

Kobayakawa, K. *et al.* Innate versus learned odour processing in the mouse olfactory bulb. *Nature* **450**, 503-508 (2007).

Kosaka, K., Toida, K., Aika, Y. & Kosaka, T. How simple is the organization of the olfactory glomerulus?: the heterogenaity of so-called periglomerular cells. *Neurosci Res* **2**, 101-10 (1998).

Kunze, W.A., Shafton, A.D., Kern, R.E. & McKenzie, J.S. Intracellular responses of olfactory bulb granule cells to stimulating the horizontal diagonal band nucleus. *Neuroscience* **2**, 363-9 (1992).

Kuntzle, H. An extrahippocampal projection from the dentate gyrus to the olfactory tubercle. *BMC Neurosci* **6**, 1-10 (2005).

Lafon, M. Rabies virus receptors. *BMC Proceedings* **2** (Suppl. I):S26 (2008).

Laurent, G. A systems perspective on early olfactory coding. *Science* **5440**, 723-8 (1999).

Laurent, G. Olfaction: A Window into the Brain. *Engineering & Science*, No. ½ (2005).

Lehman, M.N., Winanas, S.S. & Powers, J.B. Medial nucleus of the amygdala mediates chemosensory control of male hamster sexual behavior. *Science* **4469**, 557-60 (1980).

Lei, H., Mooney, R. & Katz, L.C. Synaptic integration of olfactory information in mouse anterior olfactory nucleus. *J Neurosci* **46**, 12023-32 (2006).

Lentz, T.L., Burrage, T.G., Smith, A.L., Crick, J. & Tignor, G.H. Is the acetylcholine receptor a rabies virus receptor? *Science* **4529**, 182-4 (1982).

Lewcock, J.W. & Reed, R.R. A feedback mechanism regulates monoallelic odorant receptor expression. *Proc Natl Acad Sci U S A* **4**, 1069-74 (2004).

Leypold, B.G. *et al.* Altered sexual and social behaviors in trp2 mutant mice. *Proc Natl Acad Sci U S A* **9**, 6376-81 (2002).

Liberles, S.D. & Buck, L.B. A second class of chemosensory receptors in the olfactory epithelium. *Nature* **7103**, 645-50 (2006).

Lin, D.Y., Zhang S.Z., Block, E. & Katz L.C. Encoding social signals in the mouse main olfactory bulb. *Nature* **7032**, 470-7 (2005).

Lin, D. Y., Shea, S. D. & Katz, L. C. Representation of natural stimuli in the rodent main olfactory bulb. *Neuron* **50**, 937-949 (2006).

Lomvardas, S. *et al.* Interchromosomal interactions and olfactory receptor choice. *Cell* **2**, 403-13 (2006).

Löscher, W., Lehmann, H. & Ebert, U. Differences in the distribution of GABA- and GAD-immunoreactive neurons in the anterior and posterior piriform cortex of rats. *Brain Res* **1**, 21-31 (1998).

Luna, V.M. & Schoppa, N.E. GABAergic circuits control input-spike coupling in the piriform cortex. *J Neurosci* **35**, 8851-9 (2008).

Luo M., Fee M.S. & Katz, L.C. Encoding pheromonal signals in the accessory olfactory bulb in behaving mice. *Science* **5610**, 1196-201 (2003).

Luo, L., Callaway, E.M. & Svoboda, K. Genetic dissection of neural circuits. *Neuron* **5**, 634-60 (2008).

Luskin, M. B. & Price, J. L. The distribution of axon collaterals from the olfactory bulb and the nucleus of the horizontal limb of the diagonal band to the olfactory cortex, demonstrated by double retrograde labeling techniques. *J Comp Neurol* **209**, 249-263 (1982).

Luskin, M.B. & Price, J.L. The topographic organization of associational fibers of the olfactory system in the rat, including centrifugal fibers to the olfactory bulb. *J Comp Neurol* **3**, 264-91 (1983).

Mainen, Z.F. Behavioral analysis of olfactory coding and computation in rodents. *Curr Opin Neurobiol* **4**, 429-34 (2006).

Mainen, Z.F. The main olfactory bulb and innate behavior: different perspectives on an olfactory scene. *Nat Neurosci* **12**, 1511-2 (2007).

Malnic, B., Hirono, J., Sato, T. & Buck, L. B. Combinatorial receptor codes for odors. *Cell* **96**, 713-723 (1999).

Mandairon, N. *et al.* A computer-assisted odorized hole-board for testing olfactory perception in mice. *J Neurosci Methods* **180**, 296-303 (2009).

Mandairon, N., Poncelet, J., Bensafi, M. & Didier, A. Humans and mice express similar olfactory preferences. PLoS One 4, e4209, doi:10.1371/journal.pone.ooo4209 (2009).

Mandiyan, V.S., Coats, J.K. & Shah, N.M. Deficits in sexual and aggressive behaviors in Cnga2 mutant mice. *Nat Neurosci* **12**, 1660-2 (2005).

Maresh, A., Rodriguez Gil D., Whitman, M.C. & Greer, C.A. Principles of glomerular orgnaization in the human olfactory bulb—implications for odor processing. *PLoS One* **7**, e2640 (2008).

Margrie, T.W., Sakmann, B. & Urban, N.N. Action potential propagation in mitral cell lateral dendrites is decremental and controls recurrent and lateral inhibition in the olfactory bulb. *Proc Natl Acad Sci USA* **1**, 319-24 (2001).

Marr, D. Simple memory: a theory for archicortex. *Philos Trans R Soc Lond B Biol Sci* **841**, 23-81 (1971).

Marshall, W.H., Woolsey, C.N. & Bard, P. Observations on cortical simatic sensory mechanisms of cat and monkey. *J. Neurophysiol.* **4**, 1-24 (1941).

Marshel, J.H., Mori, T., Nielsen, K.J. & Callaway, E.M. Targeting single neuronal networks for gene expression and cell labeling in vivo. *Neuron* **4**, 562-74 (2010).

Matsumoto, H., Kashiwadani, H., Nagao, H., Aiba, A. & Mori, K. Odor-induced persistent discharge of mitral cells in the mouse olfactory bulb. *J Neurophysiol* **4**, 1890-900 (2009).

Mayeaux, D.J. & Johnston, R.E. Discrimination of social odors and their locations: role of lateral entorhinal area. *Physiol Behav* **4**, 653-62 (2004).

McDonald, A.J. & Mascagni, F. Projections of the lateral entorhinal cortex to the amygdala: a Phaseolus vulgaris leucoagglutinin study in the rat. *Neuroscience* **2**, 445-59 (1997).

McGann, J.P. *et al.* Odorant representations are modulated by intra- but not interglomerular presynaptic inhibition of olfactory sensory neurons. *Neuron* **6**, 1039-53 (2005).

Meister, M & Bonhoeffer, T. Tuning and topography in an odor map on the olfactory bulb. *J Neurosci* **4**, 1351-60 (2001).

Mick, G., Cooper, H. & Mangin, M. Retinal projection to the olfactory tubercle and basal telencephalon in primates. *J Comp Neurol* **2**, 205-19 (1993).

Miyamichi, K. *et al.* Cortical representations of olfactory input by trans-synaptic tracing. *Nature* **7342**, 191-6 (2011).

Mombaerts, P. *et al.* Visualizing an olfactory sensory map. *Cell* **87**, 675-686 (1996).

Mori, K., Nagao, H. & Yoshihara, Y. The olfactory bulb: coding and processing of odor molecule information. *Science* **5440**, 711-5 (1999).

Mori, K., Takahashi, Y.K., Igarashi, K.M. & Yamaguchi, M. Maps of odorant molecular features in the Mammalian olfactory bulb. *Physiol Rev* **2**, 409-33 (2006).

Mori, K. & Sakano, H. How is the olfactory map formed and interpreted in the mammalian brain? *Annu Rev Neurosci* **34**, 467099 (2011).

Mountcastle, V.B. Modality and topographic properties of single neurons of cat's somatic sensory cortex. *J Neurophysiol* **4**, 408-34 (1957).

Mouret, A., Murray, K. & Lledo, P.M. Centrifugal drive onto local inhibitory interneurons of the olfactory bulb. *Ann N Y Acad Sci* **1170**, 239-54 (2009).

Murakami, M., Kashiwadani, H., Kirino, Y. & Mori, K. State-depdenent sensory gating in olfactory cortex. *Neuron* **2**, 285-96 (2005).

Murphy G.J., Glickfield L.L., Balsen Z, & Isaacson, J.S. Sensory neuron signaling to the brain: properties of synaptic release from olfactory nerve terminals. *J Neurosci* **12**, 3023-30 (2004).

Murphy G. J., Darcy D.P. & Isaacson, J.S. Intraglomerular inhibition: signaling mechanisms of an olfactory microcircuit. *Nat Neurosci* **3**, 354-64 (2005).

Nagayama, S., Takahashi, Y.K., Yoshihara, Y. & Mori, K. Mitral and tufted cells differ in the decoding manner of odor maps in the rat olfactory bulb. *J Neurophysiol* **6**, 2532-40 (2004).

Nagayama, S. *et al.* Differential axonal projection of mitral and tufted cells in the main olfactory bulb. *Front Neural Circuits* **4**. pii: 120 (2010).

Nicoll, R.A. & Jahr, C.E. Self-excitation of olfactory bulb neurones. *Nature* **5856** 441-4 (1982).

Niimura, Y. & Nei, M. Evolutionary changes of the number of olfactory receptor genes in the human and mouse lineages. *Gene* **346**, 23-28 (2005).

Nguyen, M.Q., Zhou, Z., Marks, C.A., Ryba, N.J. & Belluscio, L. Prominent roles for odorant receptor coding sequences in alleleic exclusion. *Cell* **5**, 1009-17 (2007).

Ohki, K., Chung, S., Ch'ng, Y.H., Kara, P. & Reid, R.C. Functional imaging with cellular resolution reveals precise micro-architecture in visual cortex. *Nature* **7026**, 597-603 (2005).

Ojima, H., Mori, K. & Kishi, K. The trajectory of mitral cell axons in the rabbit olfactory cortex revealed by intracellular HRP injection. *J Comp Neurol* **230**, 77-87 (1984).

Olsen, S.R. & Wilson, R.I. Lateral presynaptic inhibition mediates gain control in an olfactory circuit. *Nature* **7190**, 956-60 (2008).

Osakada, F. *et al.* New rabies virus variants for monitoring and manipulating activity and gene expression in defined neural circuits. Neuron **4**, 617-31 (2011).

Otto, T., Schottler, F., Staubli, U., Eichenbaum, H. & Lynch, G. Hippocampus and olfactory discrimination learning: effects of entorhinal cortex lesions on olfactory learning and memory in a successive-cue, go-no-go task. *Behav Neurosci* **1**, 111-9 (1991).

Parrish-Aungst, S., Shipley, M.T., Erdelyi, F., Szabo, G. & Puche, A.C. Quantitative analysis of neuronal diversity in the mouse olfactory bulb. *J Comp Neurol* **6**, 825-36 (2007).

Paxinos, G. & Franklin, K. B. J. *The mouse brain in stereotaxic coordinates*. Compact 2nd edn (Elsevier Academic Press, 2004).

Perez-Orive, J. *et al.* Oscillations and sparsening of odor representations in the mushroom body. *Science* **5580**, 359-65 (2002).

Petrulis, A. & Johnston, R.E. Lesions centered on the medial amygdala impair scent-marking and sex-odor recognition but spare discrimination of individual odors in female golden hamsters. *Behav Neurosci* **2**, 345-57 (1999).

Petzold, G.C., Hagiwara, A. & Murthy, V.N. Serotonergic modulation of odor input to the mammalian olfactory bulb. *Nat Neurosci* **6**, 784-91 (2009).

Poo, C. & Isaacson, J.S. An early critical period for long-term plasticity and structural modification of sensory synapses in olfactory cortex. *J Neurosci* **28**, 7553-8 (2007).

Poo, C. & Isaacson, J. S. Odor representations in olfactory cortex: "sparse" coding, global inhibition, and oscillations. *Neuron* **62**, 850-861 (2009).

Poo, C. & Isaacson, J.S. A major role for intracortical circuits in the strength and tuning of odor-evoked excitation in olfactory cortex. *Neuron* (in press), (2011).

Pressler, R.T., Inoue, T. & Strowbridge, B.W. Muscarinic receptor activation modulates granule cell excitability and potentiates inhibition onto mitral cells in the rat olfactory bulb. *J Neurosci* **41**, 10969-81 (2007).

Price, J. L. An autoradiographic study of complementary laminar patterns of termination of afferent fibers to the olfactory cortex. *J Comp Neurol* **150**, 87-108 (1973).

Protopapas, A.D. & Bower, J.M. Physiological characterization of layer III non-pyramidal neurons in piriform (olfactory) cortex of rat. *Brain Res* **1**, 1-11 (2000).

Rajan, R., Clement, J.P. & Bhalla, U.S. Rats smell in stereo. *Science* **5761**, 666-70 (2006).

Rennaker, R. L., Chen, C. F., Ruyle, A. M., Sloan, A. M. & Wilson, D. A. Spatial and temporal distribution of odorant-evoked activity in the piriform cortex. *J Neurosci* **27**, 1534-1542 (2007).

Ressler, K. J., Sullivan, S. L. & Buck, L. B. A zonal organization of odorant receptor gene expression in the olfactory epithelium. *Cell* **73**, 597-609 (1993).

Ressler, K. J., Sullivan, S. L. & Buck, L. B. Information coding in the olfactory system: evidence for a stereotyped and highly organized epitope map in the olfactory bulb. *Cell* **79**, 1245-1255 (1994).

Rinberg, D., Koulakov, A & Gelperin, A. Sparse odor coding in awake behaving mice. *J Neurosci* **34**, 8857-65 (2006).

Rivière, S., Challet, L., Fluegge, D., Spehr, M. & Rodriguez, I. Formyl peptide receptor-like proteins are a novel family of vomeronasal chemosensors. *Nature* **7246**, 574-7 (2009).

Rothschild, G., Nelken, I. & Mizrahi, A. Functional organization and population dynamics in the mouse primary auditory cortex. *Nat Neurosci* **3**, 353-60 (2010).

Rubin, B. D. & Katz, L. C. Optical imaging of odorant representations in the mammalian olfactory bulb. *Neuron* **23**, 499-511 (1999).

Sah, P., Faber, E.S., Lopez De Armentia, M. & Power, J. The amygdaloid complex: anatomy and physiology. *Physiol Rev* **3**, 803-34 (2003).

Saito, H., Mimmack, M., Kishimoto, J., Keverne, E.B. & Emson, P.C. Expression of olfactory receptors, G-proteins and AxCAMs during the development and maturation of olfactory sensory neurons in the mouse. *Brain Res Dev Brain Res* **1**, 69-81 (1998).

Saito, H., Chi, Q., Zhuang, H., Matsunami, H. & Mainland, J.D. Odor coding by a Mammalian receptor repertoire. *Sci Signal* **60**, ra9 (2009).

Sargolini, F. *et al.* Conjunctive representation of position, direction, and velocity in entorhinal cortex. *Science* **5774**, 758-62 (2006).

Sato, T.R., Gray N.W., Mainen Z.F. & Svoboda, K. The functional microarchitecture of the mouse barrel cortex. *PLoS Biol* **7**, e189 (2007).

Scalia, F. & Winans, S.S. The differential projections of the olfactory bulb and accessory olfactory bulb in mammals. *J Comp Neurol* **1**, 31-55 (1975).

Schneider, S. P. & Scott, J. W. Orthodromic response properties of rat olfactory bulb mitral and tufted cells correlate with their projection patterns. *J Neurophysiol* **50**, 1983.

Schnell, M.J., McGettigan, J.P., Wirblich, C. & Papaneri, A. The cell biology of rabies virus: using stealth to reach the brain. *Nat Rev Microbiol* **1**, 51-61 (2010).

Schoenbaum, G. & Eichenbaum, H. Information coding in the rodent prefrontal cortex. I. Single-neuron activity in orbitofrontal cortex compared with that in pyriform cortex. *J Neurophysiol* **2**, 733-50 (1995).

Schoenbaum, G., Chiba, A.A. & Gallagher, M. Neural encoding in orbitofrontal cortex and basolateral amygdala during olfactory discrimination learning. *J Neurosci* **5**, 1876-84 (1999).

Schoppa, N.E. & Westbrook, G.L. Glomerulus-specific synchronization of mitral cells in the olfactory bulb. *Neuron* **4**, 639-51 (2001).

Schoppa, N.E. & Westbrook, G.L. AMPA autoreceptors drive correlated spiking in olfactory bulb glomeruli. *Nat Neurosci* **11**, 1194-202 (2002).

Scott, J. W. Electrophysiological identification of mitral and tufted cells and distributions of their axons in the olfactory system of the rat. *J Neurophysiol* **46**, 1981.

Scott, J. W., McBride, R. L. & Schneider, S. P. The organization of projections from the olfactory bulb to the piriform cortex and olfactory tubercle in the rat. *J Comp Neurol* **194**, 519-534 (1980).

Semmelhack, J.L. & Wang, J.W. Select Drosophila glomeruli mediate innate olfactory attraction and aversion. *Nature* **7244**, 218-23 (2009).

Serizawa, S. *et al.* Negative feedback regulation ensures the one receptor-one olfactory neuron rule in mouse. *Science* **5653**, 2088-94 (2003).

Shao, Z., Puche, A.C., Kiyokage, E., Szabo, G. & Shipley M.T. Two GABAergic intraglomerular circuits differentially regulate tonic and phasic presynaptic inhibition of olfactory nerve terminals. *J. Neurophysiol* **4**, 1988-2001 (2009).

Shea, S.D., Katz L.C. & Mooney, R. Noradrenergic induction of of odor-specific neural habituation and olfactory memories. *J Neurosci* **42**, 10711-9 (2008).

Shepherd, G.M., ed. *The synaptic organization of the brain*, 5th ed. New York: Oxford University Press, 2004.

Shykind, B. M. *et al.* Gene switching and the stability of odorant receptor gene choice. *Cell* **117**, 801-815 (2004).

Skeen, L. C. & Hall, W. C. Efferent projections of the main and the accessory olfactory bulb in the tree shrew (Tupaia glis). *J Comp Neurol* **172**, 1-35 (1977).

Slotnick, B. M. Olfactory discrimination in rats with anterior amygdala lesions. *Behav Neurosci* **99***,* 956-963 (1985).

Slotnick, B. M. & Risser, J. M. Odor memory and odor learning in rats with lesions of the lateral olfactory tract and mediodorsal thalamic nucleus. *Brain Res* **529**, 23-29 (1990).

Sosulski, D.L., Bloom, M.L., Cutforth, T., Axel, R., & Datta, S.R. Distinct representations of olfactory information in different cortical centres. *Nature* **7342**, 213-(2011).

Soucy, E.R., Albeanu, D.F., Fantana, A.L., Murthy, V.N. & Meister, M. Precision and diversity in an odor map in the olfactory bulb. *Nat Neurosci* **2**, 210-20 (2009).

Stettler, D. D. & Axel, R. Representations of odor in the piriform cortex. *Neuron* **63**, 854-864 (2009).

Stowers, L., Holy T.E., Meister, M., Dulac, C. & Koentges, G. Loss of sex discrimination and male-male aggression in mice deficient for TRP2. *Science* **5559**, 1493-500 (2002).

Strand, A.D. *et al.* Conservation of region gene expression in mouse and human brain. *PLoS Genet* **4**, e59 (2007).

Suzuki, N. & Bekkers, J.M. Neural coding by two classes of principal cells in the mouse piriform cortex. *J Neurosci* **46**, 11938-47 (2006).

Suzuki, N. & Bekkers, J.M. Inhibitory interneurons in the piriform cortex. *Clin Exp Pharmacol Physiol* **10**, 1064-9 (2007).

Takahashi, Y.K., Kurosaki, M., Hirono, S. & Mori, K. Topographic representation of odorant molecular features in the rat olfactory bulb. *J Neurophysiol* **4**, 2413-27 (2004).

Takahashi, L.K., Hubbard, D.T., Lee, I., Dar, Y. & Sipes, S.M. Predator odor-induced conditioned fear involves the basolateral and medial amygdala. *Behav Neurosci* **1**, 100-10 (2007).

Talbot, S. A. & Marshall, W. H. Physiological studies on neural mechanisms for visual localization and discrimination. *Am. J. Ophthalamol.* **24**, 1255-1263 (1941).

Tan, J., Savigner, A., Ma, M. & Luo, M. Odor information processing by the olfactory bulb analyzed in gene-targeted mice. *Neuron* **6**, 912-26 (2010).

Thoulouze, M.I. *et al.* The neural cell adhesion molecule is a receptor for rabies virus. *J Virol* **9**, 7181-90 (1998).

Tian, L. *et al.* Imaging neural activity in worms, flies and mice with improved GCaMP calcium indicators. *Nat Methods* **12**, 875-81 (2009).

Tobin, V.A. *et al.* An intrinsic vasopressin system in the olfactory bulb is involved in social recognition. *Nature* **7287**, 413-7 (2010).

Tsuno, Y., Kashiwadani, H. & Mori, K. Behavioral state regulation of dendrodendritic synaptic inhibition in the olfactory bulb. *J Neurosci* **37**, 9227-38 (2008).

Turner, G.C., Bazhenov, M. & Laurent, G. Olfactory representations by Drosophila mushroom body neurons. *J Neurophysiol* **2**, 734-46 (2008).

Ubeda-Bañon, I. *et al.* Projections from the posterolateral olfactory amygdala to the ventral striatum: neural basis for reinforcing properties of chemical stimuli. *BMC Neurosci* Nov 29, 8-103 (2007).

Uchida, N., Takahashi, Y. K., Tanifuji, M. & Mori, K. Odor maps in the mammalian olfactory bulb: domain organization and odorant structural features. *Nat Neurosci* **3**, 1035-1043 (2000).

Uchida, N. & Mainen, Z.F. Speed and accuracy of olfactory discrimination in the rat. *Nat Neurosci* **11**, 1224-9 (2003).

Urban, N.N. & Sakmann, B. Reciprocal intraglomerular excitation and intra- and interglomerular lateral inhibition between mouse olfactory bulb mitral cells. *J Physiol* **2**, 355-67 (2002).

Usunoff, K.G. *et al.* Efferent projections of the anterior and posterodorsal regions of the medial nucleus of the amygdala in the mouse. *Cells Tissues Organs* **5**, 256-85 (2009).

Van Groen, T., Miettinen, P. & Kadish, I. The entorhinal cortex of the mouse: organization of the projection to the hippocampal formation. *Hippocampus* **1**, 133-49 (2003).

Vazdarjanova, A., Cahill, L. & McGaugh, J.L. Disrupting basolateral amygdala function impairs unconditioned freezing and avoidance in rats. *Eur J Neurosci* **4**, 709-18 (2001).

Vassar, R., Ngai, J. & Axel, R. Spatial segregation of odorant receptor expression in the mammalian olfactory epithelium. *Cell* **74**, 309-318 (1993).

Vassar, R. *et al.* Topographic organization of sensory projections to the olfactory bulb. *Cell* **79**, 981-991 (1994).

Vernet-Maury, E., Polak E.H. & Demael, A. Structure-activity relationship of stress-inducing odorants in the rat. *J Chem Ecol* **7**, 1001-1018 (1984).

Vosshall, L. B. & Stocker, R. F. Molecular architecture of smell and taste in Drosophila. *Annu Rev Neurosci* **30**, 505-533 (2007).

Vucinic, D., Cohen, L.B., & Kosmidis, E.K. Interglomerular center-surround inhibition shapes odorant-evoked input to the mouse olfactory bulb in vivo. *J. Neurophysiol* **3**, 1881-7 (2006).

Wachowiak, M. & Cohen, L. B. Representation of odorants by receptor neuron input to the mouse olfactory bulb. *Neuron* **32**, 723-735 (2001).

Wachowiak, M., Denk, W. & Friedrich, R. W. Functional organization of sensory input to the olfactory bulb glomerulus analyzed by two-photon calcium imaging. *Proc Natl Acad Sci U S A* **101**, 9097-9102 (2004).

Wachowiak, M. *et al.* Inhibition of olfactory receptor neuron input to olfactory bulb glomeruli mediated by suppression of presynaptic calcium influx. *J Neurophysiol* **4**, 2700-12 (2005).

Wall, N.R., Wickersham, I.R., Cetin, A., De La Parra, M. & Callaway, E.M. Monosynaptic circuit tracing in vivo through Cre-dependent targeting and complementation of modified rabies virus. *Proc Natl Acad Sci U S A* **50**, 21848-53 (2010).

Wesson, D.W. & Wilson, D.A. Sniffing out the contributions of the olfactory tubercle to the sense of smell: hedonics, sensory integration, and more? *Neurosci Biobehav Rev* **3**, 655-68 (2011).

White, L.E. Olfactory bulb projections of the rat. *Anat. Rec.* **152**, 465-479 (1965).

Wickersham, I.R. *et al.* Monosynaptic restriction of transsynaptic tracing from single, genetically targeted neurons. *Neuron* **5**, 639-47 (2007).

Wickersham, I.R., Sullivan, H.A. & Seung, H.S. Production of glycoprotein-deleted rabies viruses for monosynaptic tracing and high-level gene expression in neurons. *Nat Protoc* **3**, 595-606 (2010).

Wilson, R.I., Turner, G.C. & Laurent, G. Transformation of olfactory representations in the Drosophila antennal lobe. *Science* **5656**, 366-70 (2004).

Winans, S.S. & Scalia, F. Amygdaloid nucleus: new afferent input from the vomeronasal organ. *Science* **955**, 330-2 (1970).

Winston, J.S., Gottfried, J.A., Kilner, J.M. & Dolan, R.J. Integrated neural representations of odor intensity and affective valence in human amygdala. *J Neurosci* **39**, 8903-7 (2005).

Yaksi, E., Judkewitz, B. & Friedrich, R.W. Topological reorgnization of odor representations in the olfactory bulb. *PLoS Biol* **7**, e178 (2007).

Yaksi, E., von Saint Paul, F., Niessing, J., Bundschuh, S.T. & Friedrich, R.W. Transformations of odor representations in target areas of the olfactory bulb. *Nat Neurosci* **4**, 474-82 (2009).

Yan, Z. *et al.* Precise circuitry links bilaterally symmetric olfactory maps. *Neuron* **4**, 613-24 (2008).

Yoganarasimha, D., Rao, G. & Knierim, J.J. Lateral entorhinal neurons are not spatially selective in cue-rich environments. *Hippocampus* doi: 10.1002/hipo.20893 (2010).

Yokoi, M., Mori K., & Nakanishi S. Refinement of odor molecule tuning by dendrodendritic synaptic inhibition in the olfactory bulb. *Proc Natl Acad Sci USA* **8**, 3371-5 (1995).

Yoshida, I. & Mori, K. Odorant category profile selectivity of olfactory cortex neurons. *J Neurosci* **34**, 9105-14 (2007).

Young, J.M. & Trask, B.J. The sense of smell: genomics of vertebrate odorant receptors. *Hum Mol Genet* **10**, 1153-60 (2002).

Yu, R. *et al*. Spontaneous neural activity is required for the establishment and maintenance of the olfactory sensory map. *Neuron* **4**, 553-66 (2004).

Zald, D.H. & Pardo, J.V. Emotion, olfaction, and the human amygdala: amygdala activation during aversive olfactory stimulation. *Proc Natl Acad Sci U S A* **8**, 4119-24 (1997).

Zahm, D.S. & Heimer, L. Synaptic contacts of ventral striatal cells in the olfactory tubercle of the rat: correlated light and electron microscopy of anterogradely transported Phaseolus vulgaris-leucoagglutinin. *Neurosci Lett* **2**, 169-75 (1985).

Zhan, C. & Luo, M. Diverse patterns of odor representation by neurons in the anterior piriform cortex of awake mice. *J Neurosci* **49**, 16662-72 (2010).

Zhang, C., Szabo, G., Erdelyi, F., Rose, J.D. & Sun, Q.Q. Novel interneuronal network in the mouse posterior piriform cortex. *J Comp Neurol* **6**, 1000-15 (2006).

Zhang. F. *et al.* Multimodal fast optical interrogation of neural circuitry. *Nature* **7136**, 633-9 (2007).

Zhang, X. & Firestein, S. The olfactory receptor gene superfamily of the mouse. *Nat Neurosci* **5**, 124-133 (2002).

APPENDIX A

CHAPTER 2 METHODS

Surgery. Mice were anaesthetized with ketamine/xylazine (100 mg/kg / 10 mg/kg, Sigma-Aldrich), and temperature was maintained at 37 º C on a feedback-controlled heating pad (Fine Science Tools). The scalp was removed, and membrane overlying the skull was cleared using a microblade (Roboz). An aluminum headpost cut from square bar (Small Parts, Inc.) was attached to the skull using RelyX luting cement (Henry Schein). The borders of the exposure were covered with silicone sealant (VWR). For dorsal glomeruli, the skull overlying the olfactory bulb was thinned using a dental drill (KaVo) and removed with forceps, and the dura was peeled back using fine forceps (Roboz). For lateral glomeruli, the skin overlying the cheek and zygomatic bone was removed, and vessels were cauterized (Fine Science Tools). The muscle attached to the zygomatic was peeled away, and the bone was removed with microscissors (Roboz). The eye and surrounding tissue was removed with microscissors; bleeding was stopped using gelfoam (Henry Schein), and animals were administered 0.7 cc Ringer's solution (Henry Schein). The skull overlying the bulb was thinned and removed, and the dura peeled away. After electroporation, the bulb was coverslipped and covered in 2% agarose (Sigma-Aldrich), the exposure was covered in lidocaine jelly (Henry Schein) and then silicone sealant. Buprenorphine (0.05 mg/kg, Henry Schein) was administered after the animal could right itself. Animals recovered for 5 days after electroporation, and were

then deeply anaesthetized with ketamine/xylazine and sacrificed by paraformaldehyde perfusion.

Electroporation. Animals were placed under a two-photon microscope (Ultima, Prairie Technologies), and a 16x objective was used to focus on a single glomerulus (0.8 NA, Nikon). A Ti-Sapphire laser (Coherent) was tuned to 880nm for experiments. Pulled glass pipets (Sutter, 5-6 μM tip) were backfilled with either lysine-fixable tetramethylrhodamine (TMR) dextran (3000 MW, 12.5 mg/ml in PBS) with biotin or lysine-fixable fluorescein (FITC) dextran (3000 MW, 12.5 mg/ml in PBS) with biotin (Invitrogen), and filled halfway with 0.9% w/v NaCl. The pipet was mounted on an electrode holder (WPI)/manipulator (Luigs and Neumann), and its tip directed to the three-dimensional center of a glomerulus under two-photon guidance. Current was applied to the pipet using a stimulator (50 V, 30 ms pulses, at 2 Hz, repeated 2-4 times, Grass SD-9 stimulator). The black lead of the stimulator was connected to the animal via an alligator clip on the foot. Note that while we observed robust and reliable long-range diffusion/transport of TMR dextran from labeled mitral and tufted cells to the olfactory cortex under these electroporation conditions, FITC dextran exhibited substantively less diffusion/transport (e.g. few or no labeled fibers in the LOT), which precluded the use of FITC dextran to explore axonal projections from the bulb to the cortex. Animals in which the glomerulus was not clearly labeled, the labeling was non-specific (an exceedingly rare occurrence) or in which labeled mitral cells in the mitral cell layer could not be identified during the course of the experiment were excluded from subsequent analysis.

Histological processing. Animals were sacrificed by transcardial perfusion with 13 ml PBS, followed by 10 ml 1% paraformaldehyde. Brains were extracted and processed differentially depending on the region to be imaged. For imaging of the whole olfactory cortex, the left hemisphere was discarded, and the subcortical matter of the right hemisphere was removed using forceps. Cortical tissue above the rhinal sulcus was dissected away, and guide cuts were made with a needle blade (Fine Science Tools). The ventral hemisphere (which includes all of the structures in the olfactory cortex) was then flattened between two slides separated by a 600 μM spacer constructed of #1.5 coverslips. The sample was placed in 4% paraformaldehyde overnight, and then stored in PBS until antibody staining. For imaging of the amygdala, the brain was dissected as previously described, and a needle blade was used to cut along the lateral olfactory tract to excise the olfactory tubercle; an additional cut was made above the cortical nuclei of the amygdala to excise the olfactory amygdala. We use this en bloc preparation of the amygdala to avoid distortions that occur at the ventral edge of the flattened hemi-preparation, where the cortical amygdala resides. This distortion is minimal in the center of the flattened preparation where the piriform cortex is located. The amygdala was fixed in 4% paraformaldehyde overnight, and then stored in PBS until antibody staining. Before application of antibody, samples were soaked in glycine (1.87 g/500 ml PBS, Sigma-Aldrich) for 2 hours, followed by 1 hour in PBS, 30 minutes in sodium borohydride (0.4 g/400 ml PBS, Sigma-Aldrich) and 1 hour in PBS to quench autofluorescence. The following series of antibodies and washes were then used: primary antibody for 3 days (1:500 rabbit anti-tetramethylrhodamine, Invitrogen) in block (2%

Triton X-100, 1% bovine serum albumin in PBS), wash 1 day (2% Triton X-100/PBS), secondary antibody for 2 days (1:250 goat anti-rabbit in block, Jackson Immunoresearch), wash 1 day, and tertiary antibody (1:250 TMR-conjugated donkey anti-goat in block, Jackson Immunoresearch) and counterstain (1:150 NeuroTrace 435 in block, Invitrogen) for 2 days, followed by 1 day of wash. Samples were mounted in Vectashield (Vector Labs) on a slide with the shallow end of a Lab-Tek chambered coverglass as a coverslip (NUNC).

Quantification of Cellular Labeling. Two different methods were used to quantify the efficiency of our labeling method. First, after electroporation, we acquired z-stacks from the surface of the olfactory bulb through the mitral cell layer of the bulb, and used these z-stacks to count the number of cell bodies labeled in the mitral cell layer of the olfactory bulb post hoc. We were unable to quantify the number of tufted cells labeled for technical reasons: the brightness and number of cells labeled superior to the mitral cell layer, as well as the brightness of the glomerulus, made it difficult to quantify cell bodies (Fig. 1), and the diversity in morphology and location of tufted cells made it difficult to identify them based on visual and depth criteria. Second, previous work has suggested that mitral cell axons travel superior to tufted cell axons in a segregated manner in the LOT and, unlike tufted cell axons, project to areas posterior to the anterior piriform cortex and olfactory tubercle (see Haberly et al., Brain Res 129:152, Scott et al., J. Comp Neuro 194:519, Scott, J. Neurophys 46:918, Schneider et al., J. Neurophys 50:358, Skeen et al., J. Comp Neuro 172:1). We observed that near the most posterior aspect of the olfactory tubercle, the axons of presumed mitral cells form a distinct bundle that continues to travel

past the tubercle towards the posterior piriform cortex and amygdala (Fig. 2a). Therefore, we counted axons corresponding to presumed mitral cells in the posterior aspect of the LOT using a confocal microscope (see Fig. 2). We did not quantify the number of presumed tufted cells with this method due to technical limitations: these individual axons were difficult to optically resolve due to the large number of cells labeled, the high intensity of labeling, their smaller diameter, and the more three-dimensional structure of the presumed tufted cell axon band in the LOT.

Image acquisition. Images were acquired on a Zeiss 710 confocal microscope (Zeiss) using a 10x water immersion objective (Zeiss 0.45 NA) or a Prairie In Vivo microscope using a 10x water immersion objective (Olympus 0.6 NA). In both cases images were acquired in multiphoton mode using a Coherent laser tuned to 810 nm. Zen software with a custom-written macro was used for acquisition and tiling of images online; LSM 510 software was used for tiling in the event that it needed to be performed post-hoc (Zeiss). Images were also tiled using XUVTools (Albert-Ludwigs-Universitat Freiburg, see Emmenlaur et al., J. Micro. 233:42, 2009). Images in which clearly labeled mitral cell fibers were not apparent in the lateral olfactory tract adjacent to the posterior piriform cortex were excluded from further study; in all such cases samples exhibited other signs of poor labeling (e.g. poorly filled axonal arbors).

Image alignment. During all image processing the operator was blind to the glomerular identity of the particular image stack. Z-stacks of images of en bloc preparations of the

cortical amygdala were aligned using an intensity-based, two-step, linear-nonlinear protocol. Image alignment was carried out in Statistical Parametric Mapping 8 (SPM8) (available at www.fil.ion.ucl.ac.uk/spm), an open-source software package widely used in fMRI research. SPM is validated for a variety of registration tasks, including analysis of the axonal projection patterns of olfactory projection neurons in Drosophila (see Datta et al., Nature 452: 473, 2008). The linear registration algorithm used a standard 12-parameter algorithm with Gauss-Newton optimization. The nonlinear registration modeled the spatial transformation with a set of basis functions, the discrete sine transformation (DST) and the discrete cosine transformation (DCT), of various spatial frequencies. Typically only a small number of nonlinear iterations were carried out (often less than 100) and the nonlinear regularization value was held relatively high (typically at 100, never below 1) which maximized the relative contribution of the linear alignment to the template. We generated a standardized template brain stack of the cortical amygdala by morphing 4 individual stacks onto a single high-quality image stack and then averaging the intensity of the resultant 5 individual stacks. This standardized reference stack was then used to warp all cortical amygdala stacks used in this study. Warping parameters were optimized for each image stack and the quality of warping was assessed by the overlap between the warped brain and the template image in the counterstained image channel only. The major landmarks in this preparation are the posterolateral cortical amygdala, the posteromedical cortical amygdala and the ventral edge of the posterior piriform cortex, all of which were used to judge alignment quality. Images that failed to align based on the counterstain were excluded from the dataset. After warp parameters were defined based upon the counterstained channel, the channel

containing the TMR-dextran staining was warped using identical parameters. Because after warping most of the data was contained in superficial planes, all analysis was performed on a maximum intensity projection of the warped volume. Alignment of maximal intensity projections of image stacks of the piriform cortex (which were highly anisotropic—i.e. 20,000 x 10,000 x 40—precluding accurate volumetric alignment by SPM8) was performed in Photoshop using affine commands (such as zoom and rotate) as well as the "Warp" command, using only the counterstain as a guide to position.

Statistics. All errorbars are +/- standard error of the mean (SEM). One-way MANOVA was used to test whether multivariate means of variables for different glomerulus types are different at the 0.05 significance level.

Image processing and cluster analysis. During all image processing the operator was blind to the glomerular identity of the particular image stack. Images were processed by using a semi-supervised algorithm to filament trace the raw warped image stacks using the Imaris software package (Bitplane), slightly dilating the filaments, and then using those slightly dilated filaments to mask the original raw data. Before extraction of parameters, piriform and posterolateral nucleus projection patterns were aligned using the image alignment procedure previously described. Samples that were unable to be aligned due to poor counterstain or extreme physical distortion were excluded from K-means analysis. The data were then maximally contrasted so that differences in label intensity were normalized. A number of parameters characterizing the features of the axonal

projection patterns to the piriform cortex (x and y center of mass coordinates, x and y centroid coordinates, x-coordinate of most anterior fiber, y-coordinate of most posterior fiber at LOT, number of TMR-positive pixels) and amygdala (x and y center of mass coordinates, x and y centroid coordinates, x-coordinate of medial-most fiber, absolute fiber density within the lateral and medial hemispheres of PLCo, ratio of lateral/medial fiber density to total fiber density within the PLCo) were extracted from the aligned and processed images of samples using ImageJ (NIH) and Matlab (The Mathworks). No combination of parameters led to correct classification by glomerular type for piriform images, but the following parameters could be used in various combinations with nearly equal measures of success to classify amygdala samples: X-coordinate of center of mass, X-coordinate of medial-most fiber, absolute fiber density within the medial hemisphere of PLCo, and the ratios of fiber density within the medial or lateral hemispheres to the total fiber density within the PLCo. The standardized Euclidean distance between pairs of objects in an M-by-N data matrix X, where rows of X correspond to the values of variables extracted from a single amygdala image and columns correspond to different variables, was then calculated using the "pdist" function in Matlab. The "linkage" function was then used to create a hierarchical cluster tree using the furthest distance between the clusters from the standardized Euclidean distance matrix calculated using "pdist". K-means clustering was performed using the "kmeans" function in Matlab, which partitions the points in the data matrix X into N clusters (e.g. N=3 for 3 glomeruli) by minimizing the sum, over all clusters, of the within-cluster sums of point-to-cluster centroid distances (squared Euclidean distance). The accuracy of this clustering is assessed by counting how many samples are correctly grouped together by glomerulus

type. Calculation of the density of fibers was performed by generating a Z projection of the warped and processed images, and using the contour surface function of Imaris (Bitplane) to calculate the pixel density within the lateral and medial halves of the posterolateral cortical amygdala. The boundary between the lateral and medial halves of the posterolateral nucleus was defined by the line extending straight horizontally through the semimajor axis of the posteromedial nucleus (which appears as an ellipse in the warped template brain).

Normalized cross-correlation. Images of piriform cortex and posterolateral cortical amygdala projection patterns were blurred using a Gaussian filter (PIR σ = 200 μM; AMG σ = ~70 μM), cropped to exclude areas outside the region of interest, resized (PIR = 500 x 250 pixels; AMG = 200 x 224 pixels), thresholded in Photoshop (Adobe) to binarize pixel values, and converted to grayscale in Matlab. The "normxcorr2" function in Matlab was then used to compute the normalized cross-correlation between the pixel values of two images (e.g. MOR 1-3 piriform 1 x MOR 1-3 piriform 2) (Fig. 3a). This function returns a matrix of Pearson correlation coefficients calculated using the following equation:

$$\gamma(u,v) = \frac{\sum_{x,y}\left[f(x,y) - \overline{f}_{u,v}\right]\left[t(x-u,y-v) - \overline{t}\right]}{\left\{\sum_{x,y}\left[f(x,y) - \overline{f}_{u,v}\right]^2 \sum_{x,y}\left[t(x-u,y-v) - \overline{t}\right]^2\right\}^{0.5}}$$

where

- f is the image.
- $\overline{t}$ is the mean of the template
- $\overline{f}_{u,v}$ is the mean of $f(x,y)$ in the region under the template.

By default, non-overlapping pixels in this analysis are assigned a padding value of zero; note that because the means of the template and the source image are subtracted from the pixel values, non-overlapping pixels can still potentially contribute to the correlation coefficient. This matrix of correlation coefficients is then plotted using the "surf" function in Matlab to generate correlograms (Fig. 3c), where warmer colors represent high correlation values (close to 1) and cooler colors represent anticorrelation values (close to -1). The cross-correlation between pixel values in two images was calculated when the images were directly superimposed, and calculated again as one image was shifted relative to the other until no more overlap is possible in all directions (Fig. 3b). The result of these calculations is a matrix of correlation coefficients that reflects the degree of correlation between the pixel values in two images across the entire range of shifts (until the images are completely non-overlapping), and this matrix can be plotted as a correlogram (Fig. 3c). If there is similarity in the spatial patterning in two images, there will be a peak (red color) in the correlogram that reflects correlation coefficients greater than zero. The location of this peak in the correlogram is a direct reflection of the similarity between the spatial patterning in two images. Images with similar spatial patterning will have the highest correlation in pixel values when they are directly superimposed, and the result of this is a peak at the center of the correlogram—the images do not need to be significantly shifted relative to each other for the spatial patterning to overlap. Images with dissimilar spatial patterning will have the highest degree of correlation in pixel values when one is shifted relative to the other (e.g. shifting one image relative to the other gets the patterning in the images to overlap), resulting in a

peak in the correlogram that is displaced from the center. The amount the correlogram peak is spatially offset from the center of the correlogram can be quantified, and used as a measure of the similarity of the spatial patterning in two images (Fig. 4-5). Finally, the shape of the peak in the correlogram is related to the nature of the patterning; focal patterning will generate a more focal (circular) peak, while more distributed patterning will generate a more elongated peak (e.g. there is overlap in the two patterns over a larger range of spatial shifts). For both piriform and amygdala, normalized cross-correlation was performed for all pairwise combinations, in both possible configurations (e.g. MOR 1-3 A x MOR 28 A, and MOR 28 A x MOR 1-3 A). The location of the maximum correlation coefficient in correlograms was determined by transforming the matrix of correlation values into a linear array and using the "max" function to find the maximum value in the array, followed by the data cursor feature to find the X and Y coordinates of the maximum correlation coefficient in each correlogram. For each pairwise comparison, the location of the maximum correlation coefficient for the configuration where the distance between the location of the maximum correlation coefficient and the center of the correlogram was the smallest was used to generate scatterplots. Because non-overlapping pixels can potentially be assigned a real number value (due to subtracting of the means) in the calculation of the Pearson correlation coefficient, artifacts can be introduced in the correlogram at the edges, which represent correlation coefficients calculated under conditions where few pixels are overlapping between the template and the source images. We therefore also performed normalized cross-correlation analysis using an alternative data padding method to control for the possibility that the edge artifacts cause changes in the spatial position of the correlogram coefficient maximum.

Template images tiled as a 3x3 array (Fig. 3d) were generated for all individual images, and the normalized cross-correlation was then calculated for all pairwise combinations of single and tiled images, as previously described. Running the NormXCorr2 algorithm using the tiled templates returns a correlogram that resembles a 3x3 grid with additional data points at the edges, but in which the block in the center has been subject to analysis without the source image ever sliding off into a region that has no overlap. Because the template image is tiled, the region of overlap between the sliding image and the template will always contain the same set of pixel values, though the spatial order of these pixels will be offset. The result is that, for computing the center block of the 3x3 cross-correlogram, the mean image pixel value and the standard deviation of image pixel values used to calculate the Pearson coefficient are constant as this region of the tiled image slides across the template; this effectively avoids the introduction of the edge artifacts described above. The resulting matrices of correlation coefficients were plotted using the "surf" function. These matrices were either left uncropped (and therefore include the correlations between all 9 panels plus the edges), were cropped to the equivalent spatial displacements as were generated in the initial analysis with zero padding (and which therefore contain offset peaks that are directly comparable between the two methods), or were cropped such that the source image only was allowed to slide for 50% of its length on any axis across the template image. This final crop limits all of the values in the correlation matrix to those in which half or more of the values in the correlation matrix arise from correlations between the image and the center tile (rather than the adjacent tiles in the template). The X,Y coordinates of the maximum correlation coefficient were extracted from the "equivalent" correlograms using the "max" and "find" functions on a

submatrix representing the correlation coefficient values within and surrounding the center peak of the correlogram (e.g. the peak closest to the center of the correlogram, not the peaks near the edge of the correlogram in the equivalent view). Once again, for each pairwise comparison, the location of the maximum correlation coefficient for the configuration where the distance between the location of the maximum correlation coefficient and the center of the correlogram was the smallest was used to generate scatterplots. The scatterplots generated using the two different methods are qualitatively and quantitatively similar (Fig. 4-7), and the correlograms generated by the two methods are qualitatively similar as well (Fig. 8), suggesting that our analyses are robust to possible correlation artifacts caused by differences in the degree of pixel overlap between the two methods.

Genetics. Construction of MOR1-3-IRES-GFP animals was achieved as follows: A 7.8 kb genomic clone containing the complete MOR1-3 open reading frame plus 5.3 kb upstream and 1.5 kb downstream sequence was mutagenized by PCR to insert a PacI restriction site 5 bp after the stop codon. An IRES-GFP-ACN cassette was cloned into the PacI site to prepare the targeting vector (the ACN cassette is described in Bunting et al., Genes Dev 13: 1524, 1999.). Following electroporation into 129SvEv-derived mouse ES cells, genomic DNA from G418-resistant colonies was screened by Southern blotting with AflII to detect homologous recombination using a 400 bp probe 5' of the targeting vector (7.4 kb wild-type allele versus 12.7 kb targeted allele). Chimeras obtained from recombinant clones by standard mouse procedures were mated to C57BL/6J females to obtain heterozygous MOR1-3-IRES-GFP mice that had deleted the neo^R selection marker

in the male germline. Construction of the MOR 174-9-IRES-GFP animals was achieved as follows: Two genomic fragments containing the MOR174-9 5' flanking sequence plus open reading frame (3.4 kb, XmaI sites) and 3' flanking sequence (2.7 kb, SalI sites) were isolated by PCR from mouse genomic DNA, with restriction sites present in the primers. These two homologous arms were cloned into an IRES-GFP-ACN vector to obtain the targeting construct. Homologous recombinant clones were identified by EcoRI-digested genomic DNA blots (5.2 kb wild-type allele versus ~10 kb targeted allele) using a 300 bp probe 5' of the construct. Mice were obtained from recombinant ES cells as described for MOR1-3-IRES-GFP strain. MOR28-IRES-GFP was previously described (see Shykind et al., Cell 117:801, 2004). Note that MOR28 is also known as MOR 244-1. The OMP-IRES-spH and M72-IRES-GFP animals were obtained from the Jackson Labs.

Figure 1.

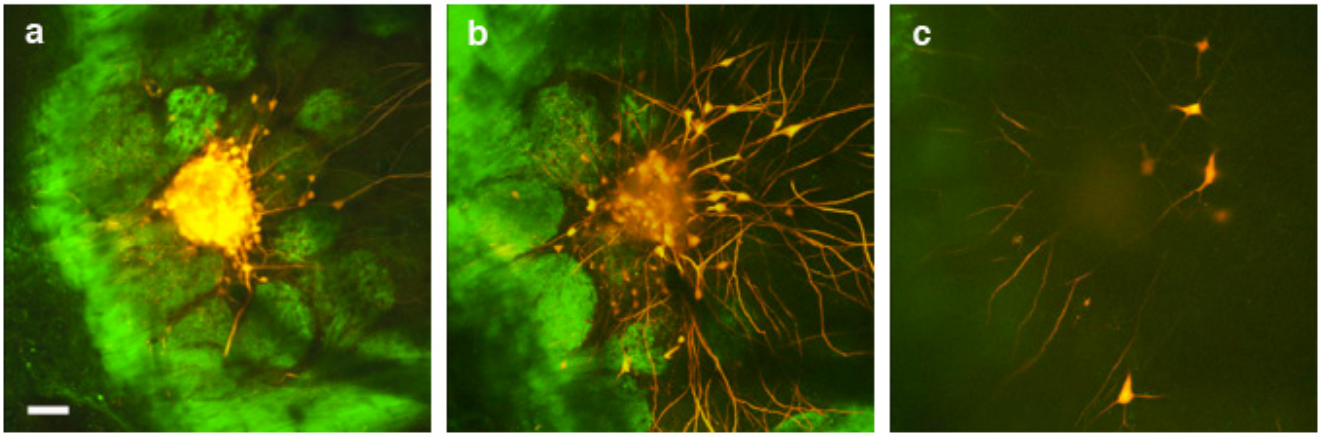

Figure 1. Examples of TMR labeling at different depths in the olfactory bulb. (a) Z-projection of images taken in the glomerular layer of a bulb in which a single glomerulus has been electroporated with TMR dextran (red). A number of labeled periglomerular cells can be seen flanking the labeled glomerulus; note that often these cell bodies cannot be disambiguated from the glomerular border (scale bar = 60 μM; green = synapto-pHluorin). **(b)** Z-projection of images taken in the external plexiform layer of the bulb. Several putative tufted cells can be seen to the right of the glomerulus. Note that the number of cells labeled, the distributed location and varying size of the cell bodies of the putative tufted cells, and the bright shadow of the labeled glomerulus make it difficult to accurately count the number of tufted cells labeled using our method. **(c)** Z-projection of images taken in the mitral cell layer of the bulb. The large cell body size, the distinct laminar location of cell bodies, and their distance from the glomerular layer (~200-300 μM) make it possible to quantify the number of labeled cells in the mitral cell layer.

Figure 2.

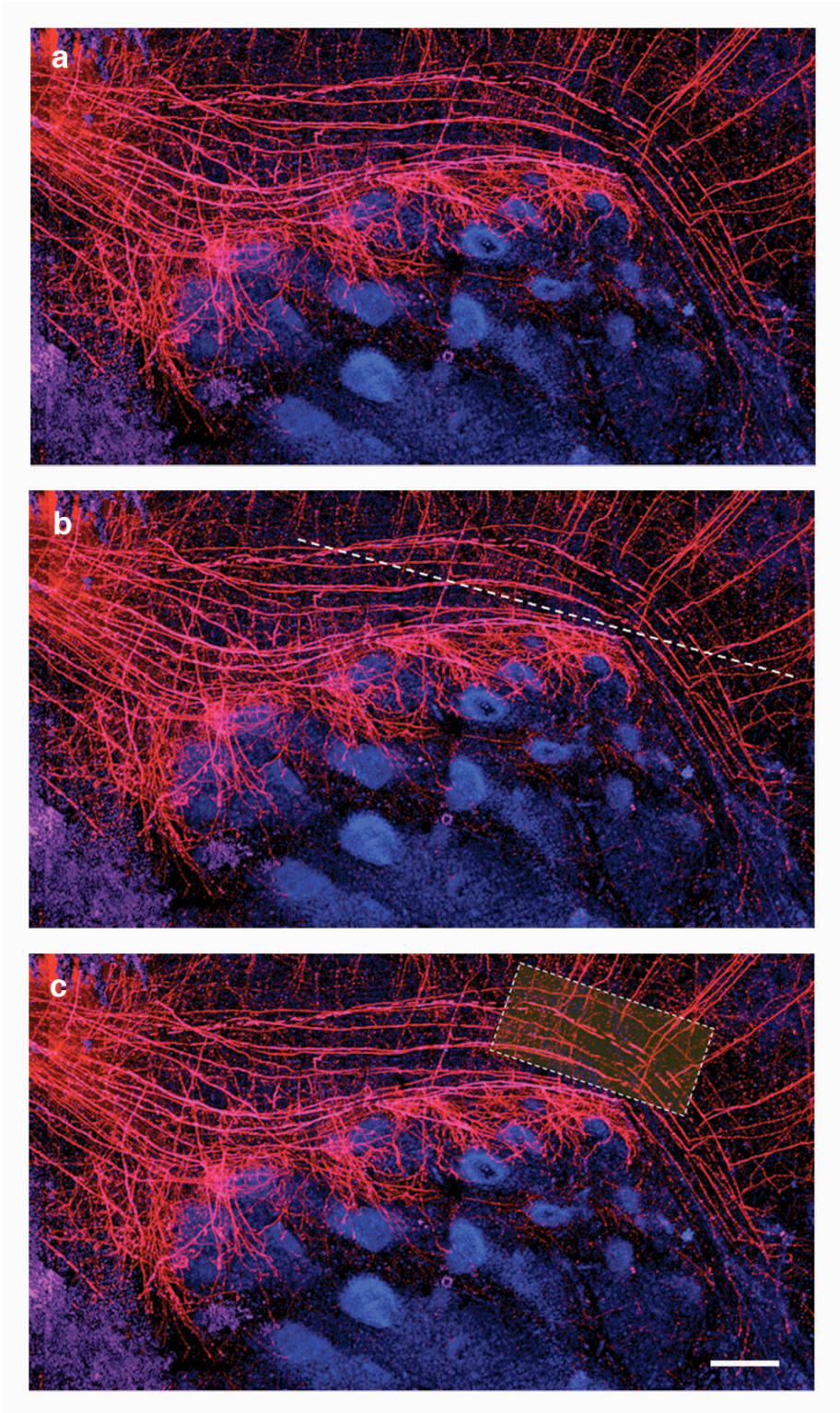

Figure 2. Putative mitral cell and tufted cell axon streams are visually distinguishable in the posterior lateral olfactory tract. (a) The appearance of the LOT after the labeling of a single glomerulus with TMR dextran (scale bar = 400 μM). **(b)** Two separate axon fiber tracts can be distinguished in the posterior aspect of the LOT (separation highlighted by dotted line). **(c)** The fibers in the superior, putative mitral cell axon tract (yellow box) are quantified to control for differences in number of axons labeled using our method. The axons in this tract can be followed all the way to the cortical nuclei of the amygdala. The number of labeled axons we count in this tract are similar to the number of neurons in the mitral cell layer counted in z-stacks taken of the olfactory bulb after electroporation.

Figure 3.

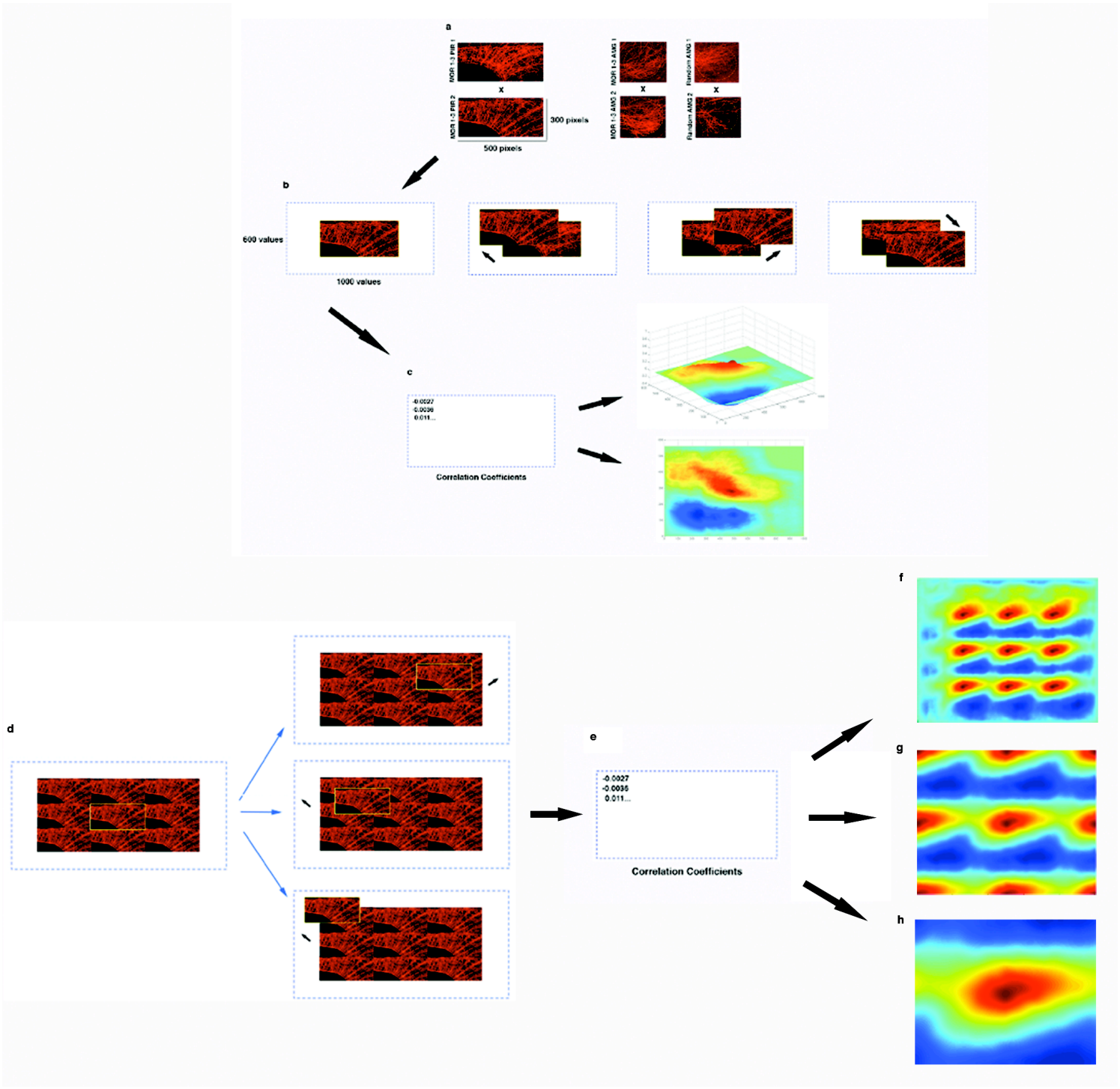
a
MOR 1-3 PIR 1
MOR 1-3 PIR 2
300 pixels
500 pixels
MOR 1-3 AMS 1
MOR 1-3 AMS 2
Random AMS 1
Random AMS 2
b
600 values
1000 values
c
Correlation Coefficients
d
e
Correlation Coefficients
f
g
h

Figure 3. Normalized cross-correlation analysis can be used to quantify the similarity of the spatial patterning in two images. (a) Examples of the images of piriform cortex and the posterolateral nucleus of the cortical amygdala used in normalized cross-correlation analysis. The source images are registered to a template image and filtered (see Methods) before being uploaded into Matlab, where they are represented as matrices of pixel values (e.g. piriform images would be represented as 500 x 300 matrices of pixel values if the images are 500 x 300 pixels in size). **(b)** The cross-correlation between the pixel values in each image is calculated when the images are directly superimposed (left-most panel) and calculated again as one image is shifted relative to the other, repeatedly in all directions (e.g. one image is shifted to the top left, top right, bottom right, and so on, as illustrated). **(c)** The result of these calculations is a matrix of correlation coefficients. The size of the matrix of correlation coefficients is the sum of the lengths of the input source and template images in each axis minus one (e.g. a 500x300 source image correlated to a 500x300 template image would result in a 999x599 correlation matrix) because such a matrix can accommodate the entire range of possible spatial shifts of one image with regard to the other, while maintaining at least one pixel worth of overlap (e.g. if images were placed side by side lengthwise, the two images would be 1000 pixels long, and 600 pixels wide if the same was done for width). These correlation coefficients range from -1 to 1, with -1 reflecting perfect anticorrelation and 1 reflecting perfect correlation of pixel values. This matrix can be plotted as a correlogram (panels on right). Two ways of displaying this correlogram are illustrated; on top, a three-dimensional correlogram is used, where the correlation coefficient values are represented on the Z-axis, and the pixel values for width and length are represented on the X and Y

axes, respectively. The data is plotted using a heatmap representation, where warm colors reflect locations of high pixel correlation, and cool colors represent areas of low correlation. Each location in the correlogram corresponds to the correlation coefficient calculated for a spatial shift of one image relative to the other (i.e. **(b)**). The bottom correlogram is simply the correlogram on top rotated 90 degrees towards the viewer. **(d)** Because normalized cross correlation analysis can be subject to edge artifacts where the two images have little overlap, we also implemented a data padding strategy to validate the data generated by traditional normalized cross correlation. By tiling the template, the source image can be slid across the entire central template tile without the source image encountering a region of zero overlap. Because of the phasic nature of the tiled template image, the overall set of pixel values in the region of overlap is held constant, and therefore the mean image pixel value and the standard deviation of image pixel values used to calculate the Pearson coefficient **(e)** are also constant as this region of the tiled image slides across the template. While the source image will slide off the template at the edges (see **d**, bottom example), the source image never leaves the tiled template image as it samples the center tile. (**f**) Output correlograms from the tiled analysis appear to be a 3x3 array, with minor errors apparent at the edges; within this array an artifact-free tile appears in the center of the correlogram, and represents the correlation between the image and the template under conditions where the image never slides off the tiled template. **(g)** To directly compare the position of the maximum correlation coefficient between this method and the zero-padding method we crop this correlogram such that it represents a similar spatial distribution of displacements. Note that the calculated values in the outer 50% of this correlogram represent displacements in which the source image overlaps

more extensively with the outer tiles in the template than with the center tile, giving this correlogram a phasic appearance. The center tile, however, clearly lacks the edge artifacts apparent at the edges of **(f)**. **(h)** Cropping out the outer 50% of displacements from the image in **(g)** generates a correlogram in which the all of the included values represent an overlap of 50% or more of pixels between the image and the central tile. In this example of cross-correlation of two piriform cortices, this correlogram reveals a single peak in the center, consistent with this brain region containing similar patterns of projection.

Figure 4.

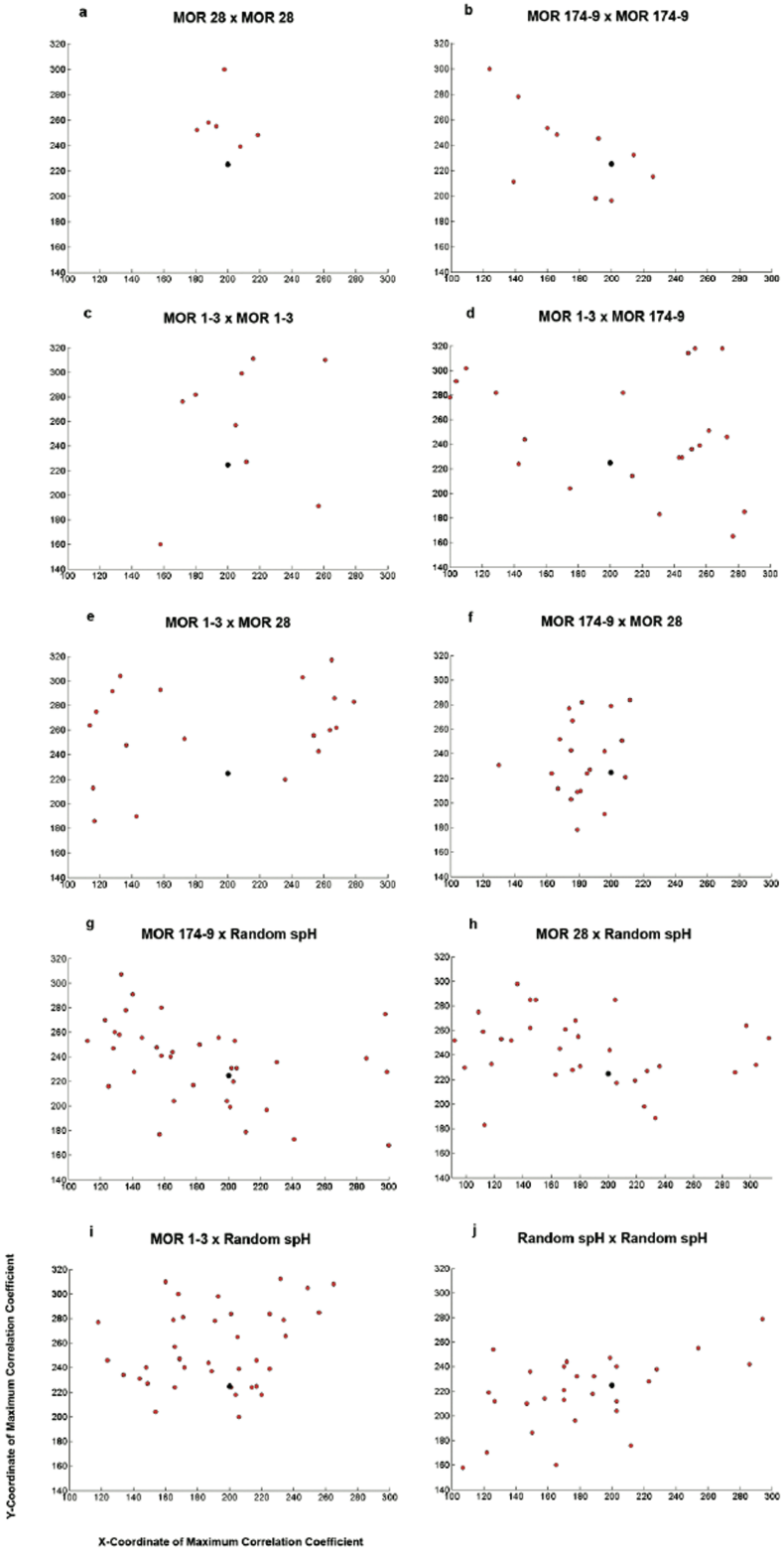
a
MOR 28 x MOR 28
b
MOR 174-9 x MOR 174-9
c
MOR 1-3 x MOR 1-3
d
MOR 1-3 x MOR 174-9
e
MOR 1-3 x MOR 28
f
MOR 174-9 x MOR 28
g
MOR 174-9 x Random spH
h
MOR 28 x Random spH
i
MOR 1-3 x Random spH
j
Random spH x Random spH
Y-Coordinate of Maximum Correlation Coefficient
X-Coordinate of Maximum Correlation Coefficient

Figure 4. Correlograms generated by the normalized cross-correlation of posterolateral amygdala innervation patterns are more similar within than across glomerulus types when using two single images as the inputs for cross-correlation analysis. The location of the maximum correlation coefficient value in cross-correlograms is closer to the center of the correlogram (represented by black dot) and more homogeneous when cross-correlation is performed on two images from the same glomerulus **(a)-(c)** than when cross-correlation is performed using images from two different glomeruli **(d)-(j)**. **(f)** Note that MOR 28 x MOR 174-9 distances are similar to those seen for within-glomerulus comparisons; this is in accord with the large degree of overlap seen in the pattern of projections from these glomeruli in the posterolateral amygdala.

Figure 5.

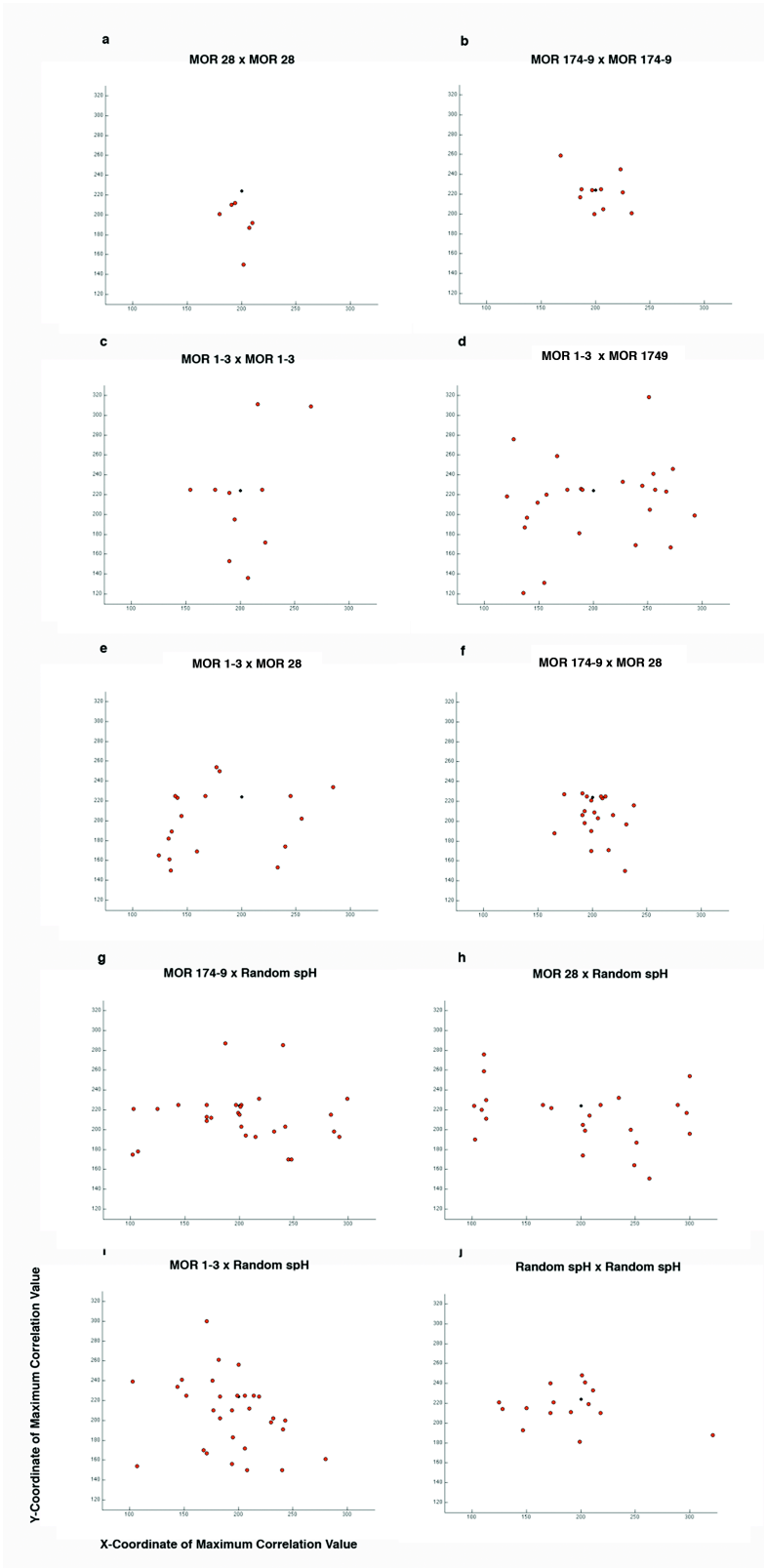
a
MOR 28 x MOR 28
b
MOR 174-9 x MOR 174-9
c
MOR 1-3 x MOR 1-3
d
MOR 1-3 x MOR 1749
e
MOR 1-3 x MOR 28
f
MOR 174-9 x MOR 28
g
MOR 174-9 x Random spH
h
MOR 28 x Random spH
i
MOR 1-3 x Random spH
j
Random spH x Random spH
Y-Coordinate of Maximum Correlation Value
X-Coordinate of Maximum Correlation Value

Figure 5. Correlograms generated by the normalized cross-correlation of posterolateral amygdala innervation patterns are more similar within than across glomerulus types when using a single source image and a 3x3 tiled template image as the inputs for cross-correlation analysis. The location of the maximum correlation coefficient value in cross-correlograms is closer to the center of the correlogram (represented by black dot) and more homogeneous when cross-correlation is performed on two images from the same glomerulus **(a)-(c)** than when cross-correlation is performed using images from two different glomeruli **(d)-(j)**. Note the qualitative and quantitative similarity of the scatterplots generated using two different modes of normalized cross-correlation analysis.

Figure 6.

	Variance of X Coordinate of Maximum Correlation Coefficient	Variance of Y Coordinate of Maximum Correlation Coefficient
MOR 28 x MOR 28	190.9	455.4
MOR 174-9 x MOR 174-9	1161.3	1163.8
MOR 1-3 x MOR 1-3	1234.9	2892.5
MOR 1-3 x MOR 28	4237.2	2142.2
MOR 1-3 x MOR 174-9	4603.7	2403.8
MOR 28 x MOR 174-9	330.9	976.7
Mean Within Glomerulus Type	862.3 +/- 412	1503.9 +/- 886.4
Mean Across Glomerulus Type	3057.3 +/- 1674.6	1840.9 +/- 537

Figure 6. The variance of the distributions of the X and Y location of the maximum correlation coefficient in correlograms is greater when comparing across glomerulus type than when comparing within glomerulus type (X/Y location calculated from correlograms generated using two single images for normalized cross-correlation analysis).

Figure 7.

	Variance of X Coordinate of Maximum Correlation Coefficient	Variance of Y Coordinate of Maximum Correlation Coefficient
MOR 28 x MOR 28	125.5	518.8
MOR 174-9 x MOR 174-9	402.9	350.9
MOR 1-3 x MOR 1-3	910.2	3409.0
MOR 1-3 x MOR 28	2717.4	1158.2
MOR 1-3 x MOR 174-9	2986.4	1758.5
MOR 28 x MOR 174-9	324.6	473.0
Mean Within Glomerulus Type	479.5 +/- 281.4	1462.2 +/- 1215.6
Mean Across Glomerulus Type	2009.5 +/- 1036.2	1130.0 +/- 454.8

Figure 7. The variance of the distributions of the X and Y location of the maximum correlation coefficient in correlograms is greater when comparing across glomerulus type than when comparing within glomerulus type (X/Y location calculated from correlograms generated using a single image and a 3x3 tiled image for normalized cross-correlation analysis).

Figure 8.

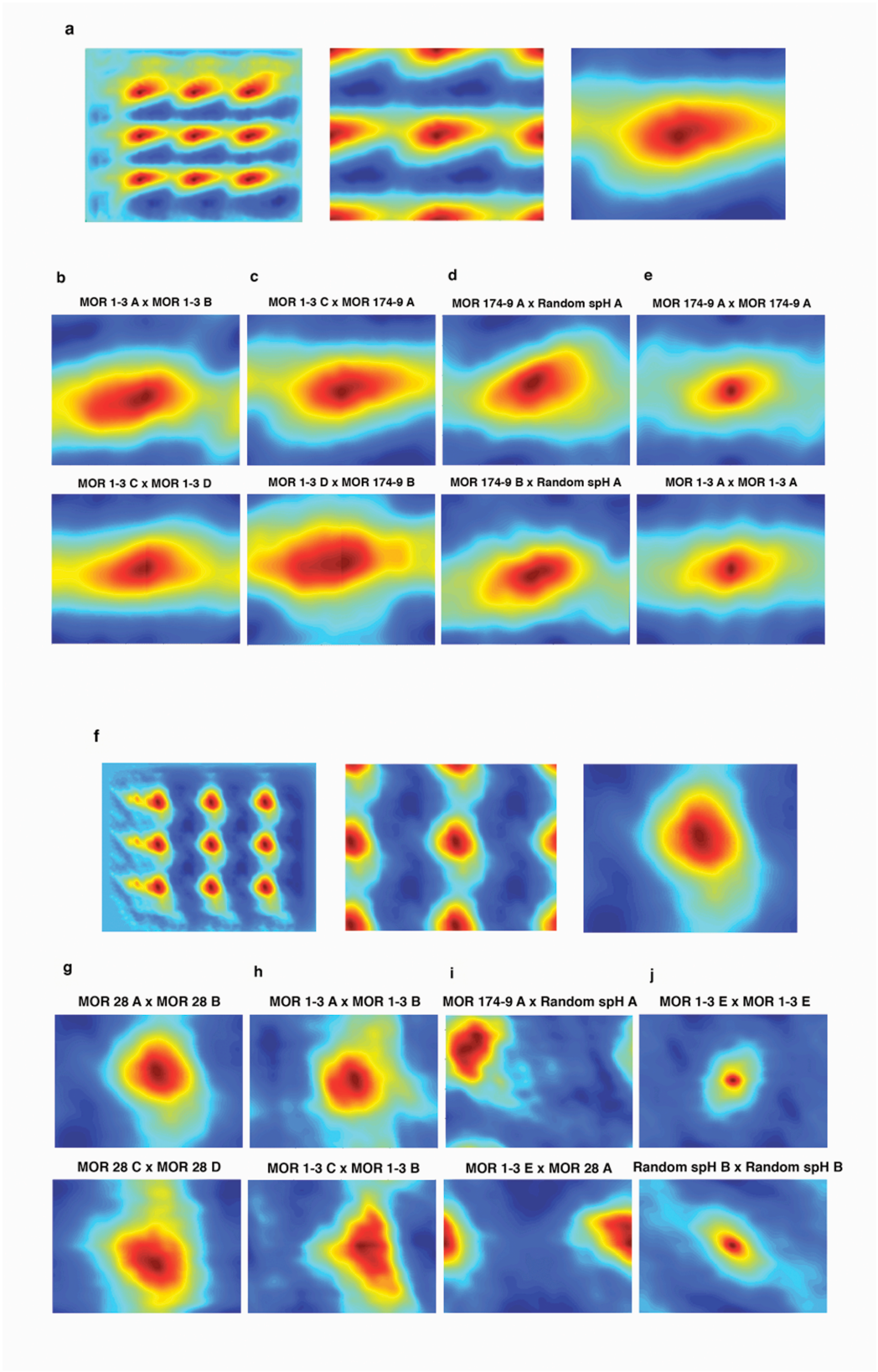
a
b
MOR 1-3 A x MOR 1-3 B
c
MOR 1-3 C x MOR 174-9 A
d
MOR 174-9 A x Random spH A
e
MOR 174-9 A x MOR 174-9 A
MOR 1-3 C x MOR 1-3 D
MOR 1-3 D x MOR 174-9 B
MOR 174-9 B x Random spH A
MOR 1-3 A x MOR 1-3 A
f
g
MOR 28 A x MOR 28 B
h
MOR 1-3 A x MOR 1-3 B
i
MOR 174-9 A x Random spH A
j
MOR 1-3 E x MOR 1-3 E
MOR 28 C x MOR 28 D
MOR 1-3 C x MOR 1-3 B
MOR 1-3 E x MOR 28 A
Random spH B x Random spH B

Figure 8. Correlograms generated using a single source image and a 3x3 tiled template image as inputs for normalized cross-correlation analysis are similar to those generated using a single untiled template image. (a) Cross-correlation performed using a single projection pattern source image and a 3x3 tile of projection pattern images as the template image. This approach is used to address potential edge artifacts generated by non-overlapping pixels at the edges of the correlogram. Output correlograms from the tiled analysis **(a, left)** appear to be a 3x3 array, with minor errors apparent at the edges, but an artifact-free tile in the center of the correlogram representing the correlation between the image and the template under conditions where the image never slides off the tiled template. **(a, center)** To directly compare the position of the maximum correlation coefficient between this method and the zero-padding method we crop this correlogram such that it represents a similar distribution of displacements. Note that the calculated values in the outer 50% of this correlogram represent displacements in which the source image overlaps more extensively with the outer tiles than with the center tile, giving this correlogram a phasic appearance. The center tile, however, lacks the edge artifacts apparent at the edges of **(a, left)**. **(a, right)** Cropping out the outer 50% of displacements from the image in **(a, center)** generates a correlogram in which the all of the included values represent an overlap of 50% or more of pixels between the image and the central tile. In this example of cross-correlation of two piriform cortices, this correlogram reveals a single peak in the center, consistent with this brain region containing similar patterns of projection. **(b)** Spatial correlograms (top and bottom) plotted using the matrix of correlation coefficients generated by normalized cross-correlation of two MOR 1-3 piriforms, and depicted using the 50% cropping method

similar to **(a, right). (c)** Correlograms similar to **(b)** from cross-correlation of MOR 1-3 and MOR 174-9 piriforms. **(c)** Correlograms similar to **(d)** from cross-correlation of two piriforms of different glomerular types. **(e)** Autocorrelograms generated using methods similar to **(d)** in which a labeled piriform is compared to itself. **(f)** Images similar to those in **(a)** except comparing projection patterns within two amygdalae rather than two piriform cortices. **(g)** Spatial correlograms plotted using the matrix of correlation coefficients generated by normalized cross-correlation of MOR 28 projection patterns within the cortical amygdala. These data are depicted using the 50% cropping method, similar to **(b-e)**. **(h)** Correlograms similar to **(g)** from cross-correlation of MOR 1-3 projection patterns within the cortical amygdala. **(i)** Correlograms similar to **(g)** of PLCo projection patterns from different glomerulus types. Note that because the correlogram was cropped to only 50% of the potential overlap, where there are significant spatial shifts we observe that the peak appears to "wrap around" the correlogram, an effect that occurs because of the phasic nature of the tiled template. This result demonstrates that in many cases the correlation maximum for different glomeruli are actually offset from each other by more than 50% of the width of our raw images. **(j)** Autocorrelograms of the PLCo from two labeled glomeruli (top and bottom) correlated with themselves. Note that correlograms generated using a single source image and a 3x3 tiled template image are similar to those generated using two single images as inputs for both piriform cortex and amygdala projection patterns.

APPENDIX B

CHAPTER 3 METHODS

Mice. Adult (12-30 weeks of age) male and female M71 transgenic mice and their littermate controls were used for functional imaging experiments of the olfactory bulb and piriform cortex. M71 transgenic mice were generated as previously described in Fleischmann et al., 2008. Briefly, M71 odorant receptor cDNA followed by an internal ribosome entry site (IRES)-tau-lacZ cassette was inserted into a plasmid containing the tet_O promoter and an exogenous intron with splice donor and acceptor sites, and an SV40 polyadenylation sequence was placed directly after the tau-lacZ gene stop codon. This construct was separated from vector sequence by agarose gel electrophoresis and microinjected into the pronuclei of fertilized eggs. Genomic DNA isolated from the tails of resultant mice was analyzed by PCR and Southern blotting to identify transgenic founders by standard protocols. Ten mouse lines bearing the tet_O-M71-IRES-tau-lacZ construct were crossed with mice harboring OMP-IRES-tTA (Yu et al., 2004) to generate mice that express both the M71 transgene and OMP-IRES-tTA. The line of M71 trangenic mice ("M71transgenic mice") we have used displays expression of the M71 receptor in over 95% of all olfactory sensory neurons.

X-Gal and Immunohistochemical Staining. M71-IRES-tau-lacZ-expressing neurons were visualized in whole-mount preparation using X-gal (GIBCO-BRL), a chromogenic substrate for lacZ, as previously described (Gogos et al., 2000). Immunohistochemistry

was performed on 16 μM cryosections of tissue that was prefixed in 1% freshly prepared paraformaldehyde (EMS) for 60 min. followed by decalcification in 0.5 M EDTA, 1 x PBS for 18 hr at 4^{o} C and embedding in OCT (Sakura) on dry ice. Anti-lacZ antiserum (Biogenesis) was used at 1:1000 dilution; anti-M50 antiserum (Lomvardas et al., 2006) was used at 1:2000 dilution; and anti-GFP antiserum was used at 1:1000 dilution (Molecular Probes and Jackson Labs) and counterstained with TOTO-3, 1:1000 (Molecular Probes). Stained sections were visualized using a Bio-Rad MRC 1024ES confocal microscope.

RNA In Situ Hybridization. Tissue was prepared as described for immunohistochemistry. Two-color RNA in situ hybridization was carried out on 16 μM cryosections using riboprobes labeled with either digoxigenin or FITC (Roche) by either T7 or SP6 RNA polymerase (Promega). Hybridizations were carried out as described (Vassar et al., 1993), and dig-labeled probes were detected using sheep anti-digoxigenin-HRP (horseradish peroxidase, Roche) and visualized with the fluorogenic HRP substrate, Cy3-tyramide, following manufacturer's instructions (Perkin-Elmer TSA system). For the second color, slides were treated with sodium azide (0.05%) in TNB buffer (Perkin-Elmer TSA kit) for 60 min. at room temperature to inactivate the first HRP-labeled antibody. FITC-labeled riboprobes were then detected by sheep anti-FITC-HRP (Roche) and visualized with the fluorogenic HRP substrate FITC-tyramide. Nuclei were counterstained with TOTO-3 at 1:1000 (Molecular Probes).

EOG Recordings. A preparation of the medial surface of the olfactory turbinates was superfused (150 ml/hr) with artificial cerebrospinal fluid (ACSF) at room temperature. Local field potentials were recorded with an ACSF-filled glass pipette (2-4 MΩ) placed on the surface of the olfactory epithelium and were amplified by a Multiclamp 700A amplifier (Molecular Devices, Sunnyvale, CA), filtered at 1 kHz, and digitized at 5 kHz (ITC-18; Instrutech, Mineola, NY). Data were collected and analyzed using Axograph X and IGOR Pro (Wavemetrics, Lake Oswego, OR). A second pipette containing the odorant cocktail diluted in ACSF was placed within 100 μM of the recording electrode using a micromanipulator. Odorants were delivered as brief puffs (30 psi, 100 ms) using a Picospritzer II (Parker). Responses to three odorant puffs, delivered 1 min. apart, were obtained at each location and averaged. Puffs of ACSF alone did not elicit changes in local field potential.

In Vivo Imaging. Imaging experiments were performed on adult mice (8 to 10 weeks old). Homozygous OMP-synaptopHluorin mice (Bozza et al., 2004) were acquired from The Jackson Laboratory (Bar Harbor, ME) and crossed with mice harboring the M71 transgene and OMP-IRES-tTA. Mice were anaesthetized using ketamine/xylazine (100 mg/kg and 10 mg/kg, Henry Schein Veterinary, Inc.); the dorsal-lateral surface of the olfactory bulb was exposed, and a custom-cut glass coverslip was placed over the area sealed in place with a layer of 2% agarose. For CGP46381 use, the coverslip was removed, and 1mM CGP46381 in ACSF was bath-applied for 30 min. Animals were maintained at 37 ^{o} C using a feedback-controlled heating pad (Fine Science Tools, Inc.) and depth of anaesthesia was monitored by foot pinch and whisking responses throughout

the imaging experiment. Imaging was performed using a custom-modified Prairie Technologies Ultima two-photon microscope with two tunable pulsed IR lasers (910 nm; Coherent, Chameleon Ultra II). Images concurrent with odor administration were acquired as a T series via the Prairie View software; for each trial, 90 images were taken at a rate of ~2.5 Hz and a resolution of 256 x 256 pixels using a 16x water immersion objective (Olympus, 0.8 N.A.). Odors (ethyl acetate, isoamyl acetate, acetophenone, and eugenol) were diluted in dipropylene glycol to achieve a final concentration of 1% or 10% (vol./vol.) (Sigma Aldrich, Inc.) and were delivered to the animals from a distance of ~1 cm using a custom-made manifold. Each odor, as well as a blank consisting of dipropylene glycol only, was pseudorandomly presented eight times to the animal at each imaging site. Odor delivery lasted for 3 s in each trial. A Z-stack was taken at each imaging site to aid in offline analysis and alignment.

Image and Data Analysis. All image processing and data analysis was performed in ImageJ and Matlab using custom-written software. Pseudocolor maps were generated by calculating the average percent change ($\Delta F/F$) elicited by an odor at each site on a pixel by pixel basis by calculating an average image for the preodor baseline (images 5-11 of the 90 image series) and an average image for the odor sampling period (images 31-37) and dividing the average odor-sampling image by the average preodor baseline image for each trial. The resulting pictures were then averaged across all eight trials, pseudocolored, and superimposed upon an image of the glomeruli during resting fluorescence at the site. An ROI-based analysis was performed to determine the mean $\Delta F/F$ in response to each odor, as well as the percent change after drug application.

Circular ROIs encompassing identifiable glomeruli were manually chosen for each site. For each ROI, the mean value of all of the pixels falling within the boundaries of the ROI was calculated for each image in the T series and then used to calculate a ΔF/F value as described previously (mean pixel value at time T/mean baseline pixel value). The ΔF/F values were then averaged across trials and plotted across time, and the maximum ΔF/F value for each glomerulus was calculated. Glomeruli were classified as responsive or nonresponsive based on the mean and standard deviation of the distribution of the maximum ΔF/F values in response to dipropylene glycol. The response threshold was set at two standard deviations above the mean ΔF/F, corresponding to a value of 0.84% in M71 transgenics and 0.63% in controls. Glomeruli from all experiments (M71 transgenic N = 4, control N = 5) were then classified as responsive or nonresponsive using an automatic thresholding program in Matlab. Mean ΔF/F in response to odor was calculated by averaging the maximum ΔF/F values of responsive glomeruli to an odor in control animals and averaging the maximum ΔF/F values of all glomeruli to acetophenone in M71 transgenics.

Behavioral Testing. Mice were adapted to a reverse 12-hour light/dark cycle and water restricted (~1-1.5 ml per day to maintain 85%-90% of baseline weight) for 1 week prior to training and testing. Training and testing were performed using the Slotnick operant conditioning paradigm (Bodyak and Slotnick, 1999) and a liquid-dilution, eight-channel olfactometer (Knosys, Lutz, FL). In this paradigm, one of two odors was paired with a water reward following a 2 s delay (S+ odor). The other odor was not paired with a reward (S- odor). The S+ and S- odors were presented in a fixed random order, and the

readout of the assay was the number of licks during the 2 s interval following the odor pulse. Each experiment consisted of 200 odor presentations, and the data are presented in blocks of 20 trials. All odorants were purchased from Sigma Aldrich (highest grade available) and were dissolved in light mineral oil. The fraction of correct licks was calculated as the number of correct licks/total number of licks and averaged for mice with the same genotype. Successful odor discrimination was defined when the fraction of correct licks surpassed 75% correct.

Rabies-GCaMP3 Injections. Mice were anaesthetized with ketamine/xylazine (100mg/kg / 10mg/kg, Sigma-Aldrich), and temperature was maintained near 37 ^{o} C using a heating pad for small animals (Snuggle Safe, Amazon). Supplements of ketamine/xylazine (0.03-0.05 cc) were given upon evidence of whisking by animals to maintain anaesthesia. The scalp was removed, and membrane overlying the skull was cleared using a microblade (Roboz). An aluminum headpost cut from square bar (Small Parts) was attached to the skull using RelyX luting cement (Henry Schein). The skin overlying the cheek and zygomatic bone was removed, and vessels on or over the zygomatic bone were cauterized (Fine Science Tools). The muscle above and attached to the zygomatic bone was peeled away, and the bone was removed with microscissors (Roboz). The membrane and muscle holding the jawbone and associated tissue in place were then slightly peeled back to allow access to the skull underneath. A dental drill was used to thin the bone directly overlying the lateral olfactory tract (LOT) from the location where it intersects with the middle cerebral artery to the approximate location of the anterior olfactory nucleus (AON), and fine forceps (#55, Fine Science Tools) were used

to remove the thinned skull and dura underneath. Using a micromanipulator and injection assembly kit (Narishige; WPI), 3,000-3,500 nl of rabies-GCaMP3 virus (a gift of I. Wickersham and H. Sebastian Seung, MIT) was slowly pressure injected via a pulled glass pipette at five locations; three approximately equidistant locations directly underneath the LOT (normal to the surface of the brain), and two locations ~500 μM deep to the surface of the brain in the anterior portion of the exposed area (approximate endopiriform cortex). After injections were complete, the craniotomy was covered with silicone sealant (WPI), and the surgical exposure was covered with a layer of lidocaine jelly (Henry Schein Veterinary) followed by a layer of silicone sealant. Afterwards, animals were placed back in a clean home cage and allowed to recover for 5-10 days. Animals were not used for functional imaging experiments if more than 8 days had elapsed since injection.

AAV-GCaMP3 Injections. Mice were anaesthetized with ketamine/xylazine (100 mg/kg / 10 mg/kg, Sigma-Aldrich), and temperature was maintained near 37 ^{o} C using a heating pad for small animals (Snuggle Safe, Amazon). Metal ear bars were used to hold the head of the animal in a fixed position on a stereotaxic instrument with attached micromanipulator (SR-5M, Narishige) for pressure injection of AAV-GCaMP3 virus (AAV2/1.hSynap.GCaMP3.3.SV40 at a viral titer of 4.3 x 10^{13} GC/ml, Penn Vector). Using surgical scissors (Roboz) a small incision was made in the skin overlying the skull, and a cotton swab was used to clean the surface of the skull of blood and debris (Puritan). Care was taken to ensure that the surface of the skull was level before beginning the injection procedure. A dental drill was used to make a craniotomy ~1 mm in diameter at

injection coordinates determined using an anatomical atlas (3.9 mm to the right of the midline, 0.6 mm posterior to bregma, 4.0 mm ventral to the pial surface, Paxinos and Franklin, 2004). Over the course of 5-10 minutes, 500-1,000 nl of virus was pressure injected into the approximate center of piriform cortex via a pulled glass pipette and injection kit (WPI). Approximately 1 min. after the termination of the injection process, the pipet was slowly retracted from the brain. Animals were allowed to recover for 7-14 days, and not used for imaging if more than 14 days had elapsed since injection.

Olfactory Bulb Imaging. Mice were anaesthetized with ketamine/xylazine (100 mg/kg / 10 mg/kg, Sigma-Aldrich), and temperature was maintained at 37 º C on a feedback-controlled heating pad (Fine Science Tools). Supplements of ketamine/xylazine (0.03-0.05 cc) were given upon evidence of whisking by animals to maintain anesthesia. The scalp was removed, and membrane overlying the skull was cleared using a microblade (Roboz). An aluminum headpost cut from square bar (Small Parts) was attached to the skull using RelyX luting cement (Henry Schein). The borders of the exposure were covered with silicone sealant (VWR). The skull overlying the olfactory bulb was thinned using a dental drill (KaVo) and removed with forceps, and the dura was peeled back using fine forceps (Fine Science Tools). Finally, a small circular coverslip cut from a Corning cover glass (#2870-18) using a diamond scriber (VWR) was then placed over the exposed bulb and sealed in place using 2% agarose to minimize movement of the brain. Animals were then moved to a two-photon microscope rig (Ultima, Prairie Technologies) for imaging. A 16x objective at 2x zoom was used to focus on the mitral cell layer of the olfactory bulb (~300-400 μM below the pial surface; 0.8 NA, Nikon), and a Ti-Sapphire

laser (Coherent) was tuned to 910 nm for experiments. On each trial (during which one odor was delivered 8 seconds after the start of imaging), images were acquired at a size of 256 x 256 pixels and a framerate of 2.53 Hz, and each trial lasted a total of ~30 seconds (70 images). A total of 2-3 spatially distinct sites (often consisting of the posterior, medial, and anterior dorsal surface of the bulb) were imaged in each mouse.

Piriform Cortex Imaging. Mice were anaesthetized with ketamine/xylazine (100 mg/kg / 10 mg/kg, Sigma-Aldrich), and temperature was maintained at 37 ^{o} C on a feedback-controlled heating pad (Fine Science Tools). Supplements of ketamine/xylazine (0.03-0.05 cc) were given upon evidence of whisking by animals to maintain anesthesia. The scalp was removed, and membrane overlying the skull was cleared using a microblade (Roboz). An aluminum headpost cut from square bar (Small Parts) was attached to the skull using RelyX luting cement (Henry Schein). The skin overlying the cheek and zygomatic bone was removed, and vessels were cauterized (Fine Science Tools). The muscle attached to the zygomatic bone was peeled away, and the bone was removed with microscissors (Roboz). The cheek muscle overlying the jawbone was removed with microscissors, and the vessels overlying the jawbone were cauterized. Afterwards, the membrane holding the jawbone in place against the skull was severed and the upper half of the jawbone extracted and cut away using microscissors. A large craniotomy (~3 mm x 2 mm) was made over the piriform cortex by thinning the skull with a dental drill (KaVo) and removing the bone and underlying dura with fine forceps (Fine Science Tools). Finally, a rectangular coverslip cut from a Corning cover glass (#2870-18) using a diamond scriber (VWR) was then placed over the exposed cortex and sealed in place

using 2% agarose to minimize movement of the brain. Animals were then moved to a two-photon microscope rig (Ultima, Prairie Technologies) for imaging. A 40x objective was used to focus on layer 2 and occasionally layer 3 of the piriform cortex (~200 μM and ~300 μM below the pial surface, respectively; X NA, Nikon), and a Ti-Sapphire laser (Coherent) was tuned to 910 nm for experiments. On each trial (during which one odor was delivered 8 seconds after the start of imaging), images were acquired at a size of 256 x 256 pixels and a framerate of 2.53 Hz, and each trial lasted a total of ~30 seconds (70 frames). A total of 2-3 spatially distinct sites (consisting of both more anterior and posterior areas of piriform cortex) were imaged in each mouse.

Mitral/Tufted Cell Imaging Stimulus Delivery. Odor stimuli for a given experiment consisted of one of three odor sets: a set of 15 odors at 1/10,000 vol./vol. dilution (pure odorants purchased from Sigma Aldrich and Pherotech and diluted in mineral oil: amyl acetate, acetophenone, (S+) citronellol, ethyl acetate, eugenol, farnesene, heptanal, 2-hexanone, α-ionone, isobutyraldehyde, limonene, pinene, 2,4,5-trimethylthiazoline (TMT), valeraldehyde, and the diluent mineral oil as a "blank" control odorant), a set of odors at 1/100 vol./vol. dilution in mineral oil (acetophenone, a 50/50 mixture of acetophenone and ethyl acetate, ethyl acetate, 2-hexanone, isoamyl acetate, and the diluent mineral oil as a "blank" control odorant), and a set of three odors at multiple concentrations (1/100, 1/1,000 and 1/10,000 vol./vol. dilutions of acetophenone, ethyl acetate, and 2-hexanone). Odorants were presented in pseudorandom order using a 64-channel olfactometer controlled by a custom-written Matlab program (Island Motion). Using a 200 μl pipet tip, 40 μl of odorant was placed on a Whatman syringe filter, and a

small teflon male luer piece (Island Motion) was placed in the large aperture of the filter (Whatman Puradisk glass microfiber syringe filters, 13 mm). The smaller aperture of these filters was placed inside a teflon manifold with 8 bored holes (Island Motion), and the exposed end of the luer was connected to a single channel of the olfactometer via teflon and polyethylene tubing (Neptune Research). A tube connected to a continuously running carrier air stream (~1.2 l/min) was connected to the center of the manifold. A second tube was connected to the other side of the manifold; this tube terminated in a female luer piece, and the opening of this female luer piece (large opening) was positioned ~1 mm in front of the animal's nostrils. Odorized air was generated by opening a solenoid valve on the olfactometer, which released air (~100 ml/min) through the tubing and syringe filter connected to a single valve, thereby adding an odorized airflow to the continuously running carrier stream. Medical air of the highest purity was used as both our carrier and odorized air sources (TechAir). Each odor was presented for ~2 seconds (frames 15-21 of a synchronized two-photon image acquisition trial), with an approximately 90 second intertrial interval. Each odor was delivered a total of four times (4 trials) at a given imaging site. Between experiments, olfactometer valves and tubing were deodorized by continuous flushing with medical air for 12-24 hours. The manifold and teflon pieces inserted into the manifold or odorized filters were cleaned in a bath of 70% ethanol overnight with continuous agitation.

Rabies Histological Processing. During preliminary experiments performed to optimize the injection parameters for labeling mitral and tufted cells with rabies-GCaMP3, a series of mice were sacrificed 3-8 days after injection of rabies-GCaMP3 (see "Rabies-

GCaMP3 Injections" in Methods) and their brains saved for histological processing. Animals were deeply anaesthetized with 0.3 cc ketamine/xylazine (100 mg/kg / 10 mg/kg, Sigma-Aldrich), and sacrificed by transcardial perfusion with 13 ml PBS, followed by 10 ml 4% paraformaldehyde. After perfusion was complete, the brain was removed and placed in 4% paraformaldehyde for 24-48 hours. A vibtratome was then used to make coronal slices through the olfactory bulb and piriform cortex (85 μM slices through bulb; 200 μM slices through cortex); these slices were counterstained overnight in 1/1,000 NeuroTrace 435 (Invitrogen) in PBS and mounted in Vectashield (Vector Labs) for imaging on a Zeiss 710 confocal microscope (Zeiss) using a 10x water immersion objective (Zeiss 0.45 NA).

Pixel-Based Image Analysis. Heatmap images of odor-evoked activity in the olfactory bulb and piriform cortex were generated using a custom-written Matlab program. Images from all four trials were first loaded into Matlab and blurred using a Gaussian filter (bin size = 6 x 6 pixels; $\sigma = 3$). A mean baseline image was then calculated for each trial by averaging the pixel values in images 3-11 (taken during a baseline period before the start of odor delivery). For each individual trial, the percent change in pixel value ($\Delta F/F$) was calculated for each image taken over the majority of a single trial (images 1-40) by dividing the pixel values in each image by the mean pixel values calculated for the baseline period. Finally, these average $\Delta F/F$s across trials were used to calculate the mean $\Delta F/F$ over images 18-24, a time period typically corresponding with the maximum odor-evoked response in mitral and tufted cells. The results of this average $\Delta F/F$ calculation for images 18-24 were then plotted using the "colormap" function in Matlab.

ROI-Based Image Analysis. A custom-written Matlab program was used to perform an ROI-based analysis of olfactory bulb and piriform cortex neuron activity. For each odor stimulus at a given site, images from each trial (1-70 for each of the four trials/presentations of that odor) were compiled into a single folder and renumbered (0001-0280). Compiled mages were then loaded from this folder into an interface that enabled both automatic and manual ROI drawing. ROIs were manually chosen using an average image generated using the "Z project" function in ImageJ (NIH) (generated from the images corresponding to trial 1 for mineral oil). For mitral and tufted cells, ROIs were drawn around the soma, which was clearly visible due to high expression of GCaMP3 and whose borders were easy to differentiate. For piriform neurons, ROIs were drawn to encompass the nucleus but not the very edge of the cell body, to avoid signal contamination from tightly packed neighboring neurons that also expressed GCaMP3. The percent of responsive cells observed in the olfactory bulb and piriform cortex using these ROIs was similar to that observed using our pixel-based analysis, demonstrating that the nature of these ROIs does not significantly bias the outcome of our cell-based analysis. After ROIs for a given imaging site were chosen, the percent change in pixel value ($\Delta F/F$) across each individual trial for all the pixels within each ROI was calculated for all images by dividing the mean pixel value within a given ROI in each image by the mean pixel value for that ROI calculated during a pre-odor baseline period. The average response of each cell during the interval typically corresponding to the maximal odor-evoked change in fluorescence (images 18-24) was calculated by averaging the mean $\Delta F/F$ value for each ROI across these images. These average $\Delta F/F$ values for each cell were the $\Delta F/F$ values used to construct plots of the percent of cells with $\Delta F/F$s within a

given interval, as well as the histogram plots of the ΔF/Fs of cells (e.g. Fig. 17). To calculate the number of odor-responsive neurons, we first determined the mean, median, and standard deviation of the distribution of responses (average ΔF/Fs across images 18-24) to mineral oil across several littermate controls, and used the median plus a number of standard deviations as our threshold for "responding" (mitral and tufted cells = 2SD above the median, corresponding to 6.31% ΔF/F, and piriform neurons = 3SD above the median, corresponding to 4% ΔF/F); all neurons with an average ΔF/F value across frames 18-24 that was above these ΔF/Fs were counted as "responsive" to a given odor. Topographic maps of active mitral and tufted cells and piriform neurons (e.g. Fig. 11) were constructed by placing a blue dot at the location of each responsive cell using Photoshop (Adobe). The percent of odor-responsive neurons at a given site was calculated by dividing the number of neurons responding to a given odor by the total number of ROIs at that site (e.g. Fig. 10). The tuning breadth of neurons (e.g. the number of odors each cell responds to) was calculated by determining the sum of how many odors drove a given cell above threshold during the aforementioned interval for each ROI at a given site. A graphical representation of tuning breadth was generating by calculating binary arrays noting the ROIs that respond to each odor (e.g. cell responds to odor = 1, cell does not respond = 0), generating a master array consisting of these binary arrays, and plotting this master array using the "pcolor" function (e.g. Fig. 13). Interval histograms of ΔF/Fs for an imaging site were generated by calculating the number of ROIs that displayed ΔF/Fs in a given bin (e.g. 0-2.5% ΔF/F, 2.51-5% ΔF/F, etc.) for each odor, and then plotting the resulting array using the "bar" function. Response traces (e.g. Fig. 9) of ΔF/Fs for single trials as well as the average response across all four trials for a

given cell of interest were generated in the following manner: first, the "plot Z axis profile" function in ImageJ was used to get the mean grayscale pixel value for an ROI in each image for each trial. The mean grayscale pixel values for an ROI in every image (1-70) for each of the four trials were then uploaded into Matlab; the percent change in pixel value ($\Delta F/F$) across each individual trial for the ROI was calculated for all images in each individual trial by dividing the mean grayscale pixel value in each image by the mean grayscale pixel value for the ROI calculated during a pre-odor baseline period. The $\Delta F/F$ values for the four individual trials were also averaged together to generate the average $\Delta F/F$ values across trials. Both the individual trial and average trial traces were then plotted in Matlab using the "plot" function. Each point in the plotted trace reflects the average $\Delta F/F$ values across three frames (e.g. frames 1-3 = 1 on the x-axis).

Statistics. All errorbars are +/- standard error of the mean (SEM). P-values were generated by performing the Kolmogorov-Smirnov (K-S) test for significant differences in distributions of values ($\alpha = 0.05$).

Generation of Rabies-GCaMP3. Deletion-mutant rabies virus expressing mCherry and GCaMP3 ("RV-1mC5GCaMP3") was made by cloning the mCherry and GCaMP3 genes into the viral genome vector cSPBN-4GFP (Wickersham et al., 2010) and then following the protocol described in detail in (Wickersham et al., 2010).

APPENDIX C

CHAPTER 4 METHODS

Behavior. A modified home cage assay similar to that used in Kobayakawa et al., 2007 was used to categorize odors as innately aversive, innately attractive, or innately neutral to mice. A clean Plexiglas cage (e.g. a clean home cage without bedding material) was divided into a small (~1/3 of the cage) and a large (~2/3rds of the cage) compartment by placing a moveable curtain made of parafilm (Fisher Scientific). Adult male mice (8-12 weeks) of the C57BL/6 strain that were naïve to odor stimulus presentation were allowed to habituate to the modified cage for 5 minutes before presentation of an odor stimulus. After habituation, 50 µl of an undiluted odorant was placed on a rectangular strip of filter paper and the paper was placed into the small compartment of the modified cage. A videocamera was used to record the mouse's response to the odor stimulus for 3 minutes after placement of the filter paper, and post-hoc analysis was performed on the recorded footage to quantify the amount of time the animal spent investigating the odor (snout within 1 cm of the filter paper), the amount of time the animal spent freezing (motionless except for movement associated with breathing), and the amount of time the animal spent away from the odor (in the large compartment of the modified cage). The normalized time spent away from the odor was then calculated ((mean time spent in large compartment when test odor is present) – (mean time spent in large compartment when stimulus is odorless diluent)) and used to classify odors as aversive, attractive or neutral.

Olfactory Bulb Imaging. To generate maps of glomeruli responsive to odorants at near-threshold concentrations, adult male mice (8-12 weeks old) expressing the pH-sensitive indicator of synaptic release, synapto-pHluorin, in all olfactory sensory neurons (OMP-spH mice, The Jackson Laboratory) were anaesthetized with ketamine/xylazine (100 mg/kg / 10 mg/kg, Sigma-Aldrich), and temperature was maintained at 37 ^{o} C using a feedback-controlled heating pad (Fine Science Tools). Supplements of ketamine/xylazine (0.03-0.05 cc) were given upon evidence of whisking by animals to maintain anaesthesia. The scalp was removed, and membrane overlying the skull was cleared using a microblade (Roboz). An aluminum headpost cut from square bar (Small Parts) was attached to the skull using RelyX luting cement (Henry Schein). The borders of the exposure were covered with silicone sealant (VWR). The skull overlying the olfactory bulb was thinned using a dental drill (KaVo) and removed with forceps, and the dura was peeled back using fine forceps (Fine Science Tools). Finally, a small circular coverslip cut from a Corning cover glass (#2870-18) using a diamond scriber (VWR) was placed over the exposed bulb and sealed in place using 2% agarose to minimize movement of the brain. Animals were then moved to a two-photon microscope rig (Ultima, Prairie Technologies) with attached CCD camera (Hamamatsu) for imaging. A mercury lamp was used to illuminate the surface of the bulb, and the HCImage software package (Hamamatsu) was used to acquire images at ~3 Hz (100 images per trial). To image responses of periglomerular and granule cells, mice were anaesthetized with ketamine/xylazine (100 mg/kg / 10 mg/kg, Sigma-Aldrich), and temperature was maintained at 37 ^{o} C using a feedback-controlled heating pad (Fine Science Tools). Supplements of ketamine/xylazine (0.03-0.05 cc) were given upon evidence of whisking

by animals to maintain anesthesia. The scalp was removed, and membrane overlying the skull was cleared using a microblade (Roboz). An aluminum headpost cut from square bar (Small Parts) was attached to the skull using RelyX luting cement (Henry Schein). The borders of the exposure were covered with silicone sealant (VWR). The skull overlying the olfactory bulb was thinned using a dental drill (KaVo) and removed with forceps, and the dura was peeled back using fine forceps (Fine Science Tools). Finally, a small circular coverslip cut from a Corning cover glass (#2870-18) using a diamond scriber (VWR) was then placed over the exposed bulb and sealed in place using 2% agarose to minimize movement of the brain. Animals were then moved to a two-photon microscope rig (Ultima, Prairie Technologies) for imaging. A 16x objective at 2x zoom was used to focus on the glomerular layer (~50-100 μM) or granule cell layer of the olfactory bulb (~300-400 μM below the pial surface; 0.8 NA, Nikon), and a Ti-Sapphire laser (Coherent) was tuned to 910 nm for experiments. On each trial (during which one odor was delivered 8 seconds after the start of imaging), images were acquired at a size of 256 x 256 pixels and a framerate of 2.53 Hz, and each trial lasted a total of ~30 seconds (70 images).

Stimulus Delivery. To generate maps of glomerular responses to odorants at near-threshold concentrations, odor stimuli for a given experiment consisted of a concentration series of three odorants (the lowest concentration of an odor that reliably evokes glomerular responses, as well as the concentrations that correspond to two orders of magnitude above the threshold concentration, vol./vol. in mineral oil) suggested to have innate behavioral relevance to mice based on previously published behavioral or gas

chromatography experiments, as well as a "blank" control (mineral oil) and a positive control that reliably evokes robust glomerular responses (1/1,000 vol./vol. TMT). Odorants were purchased from Sigma Aldrich (2-heptanone, 4-heptanone, 2-hexanone, butyric acid, eugenol, butyraldehyde, 2-mercaptoethanol, 2-methylbutyric acid) and Pherotech (2,4,5-trimethylthiazoline (TMT), 2-propylthietane, 2,5-dimethylpyrazine), or were custom synthesized by Chemtos (4-Methoxy-2-methylbutane-2-thiol (MMB), 3-Mercapto-3-methylbutan-1-ol (3-Merc)). Odorants were presented in pseudorandom order using a 64-channel olfactometer controlled by a custom-written Matlab program (Island Motion). Using a 200 µl pipet tip, 40 µl of odorant was placed on a Whatman syringe filter, and a small teflon male luer piece (Island Motion) was placed in the large aperture of the filter (Whatman Puradisk glass microfiber syringe filters, 13 mm). The smaller aperture of these filters was placed inside a teflon manifold with 8 bored holes (Island Motion), and the exposed end of the luer was connected to a single channel of the olfactometer via teflon and polyethylene tubing (Neptune Research). A tube connected to a continuously running carrier air stream (~1.2 l/min) was connected to the center of the manifold. A second tube was connected to the other side of the manifold; this tube terminated in a female luer piece, and the opening of this female luer piece (large opening) was positioned ~1 mm in front of the animal's nostrils. Odorized air was generated by opening a solenoid valve on the olfactometer, which released air (~100 ml/min) through the tubing and syringe filter connected to a single valve, thereby adding an odorized airflow to the continuously running carrier stream. Medical air of the highest purity was used as both our carrier and odorized air sources (TechAir). Each odor was presented for ~2 seconds (frames 15-21 of a synchronized two-photon image acquisition

trial), and ~120 seconds elapsed between trials. Each odor was delivered a total of three times (3 trials) at an imaging site. Between experiments, all of the constituent valves and tubing of the olfactometer were deodorized by continuous flushing with medical air for 12-24 hours. The manifold and teflon pieces inserted into the manifold or odorized filters were cleaned in a bath of 70% ethanol overnight with continuous agitation. To image periglomerular and granule cell responses, the same procedures were used, but a different set of odorants were delivered (acetophenone, ethyl acetate, 2-hexanone, isoamyl acetate, all at 1/100 vol./vol. dilution, as well as the odorless diluent mineral oil).

Image Analysis. Heatmap images of odor-evoked activity in the olfactory bulb were generated using a custom-written Matlab program. Images from all three trials were first loaded into Matlab and blurred using a Gaussian filter (bin size = 6 x 6 pixels; $\sigma = 3$). A mean baseline image was then calculated for each trial by averaging the pixel values in images 3-11 (taken during a baseline period before the start of odor delivery). For each individual trial, the percent change in pixel value ($\Delta F/F$) was calculated for each image taken over the majority of a single trial (images 1-40) by dividing the pixel values in each image by the mean pixel values calculated for the baseline period. Finally, these average $\Delta F/F$s across trials were used to calculate the mean $\Delta F/F$ over images 27-38, a time period that typically corresponds with the maximum of the odor-evoked synapto-pHluorin signal. The results of this average $\Delta F/F$ calculation were then plotted using the "colormap" function in Matlab. Heatmaps of periglomerular and granule cell activity were generated in a similar fashion, except that the mean $\Delta F/F$ was calculated over images 18-24.

Generating Maps of Glomerular Activity. Average ΔF/F plots were used to generate maps of glomerular activity for each odor using ImageJ and Photoshop (Adobe). The "magic wand" tool was used to eliminate color corresponding to low ΔF/Fs (< 1%) in the average ΔF/F plots for each odor stimulus, and each of these images was superimposed on an image of the resting fluorescence of the bulb. In this manner, one master image of the resting fluorescence of the bulb overlaid with aligned images of glomeruli responsive to each odorant was generated. To allow for the comparison of odor-evoked patterns of glomerular activity across animals for the same odor as well as across odors within the same animal, Powerpoint (Microsoft) was used to place a circle centered on each active glomerulus in these images.

Statistics. All errorbars are +/- standard error of the mean (SEM). The Student's t-test was used to test for significant differences in behavioral data (α= 0.05 and 0.01).

Plasmid Electroporation. Mice were anaesthetized with ketamine/xylazine (100mg/kg / 10mg/kg, Sigma-Aldrich), and temperature was maintained at 37 ^{o} C a feedback-controlled heating pad (Fine Science Tools). The scalp was removed, and membrane overlying the skull was cleared using a microblade (Roboz). An aluminum headpost cut from square bar (Small Parts) was attached to the skull using RelyX luting cement (Henry Schein). The borders of the exposure were covered with silicone sealant (VWR). The

skull overlying the olfactory bulb was thinned using a dental drill (KaVo) and removed with forceps, and the dura was peeled back using fine forceps (Roboz). Animals were placed under a two-photon microscope (Ultima, Prairie Technologies), and a 16x objective was used to focus on a single glomerulus (0.8 NA, Nikon). A Ti-Sapphire laser (Coherent) was tuned to 880 nm for experiments. Pulled glass pipettes (Sutter, 5-6 μM tip) were backfilled with a solution containing 1 μl of plasmid DNA ("minicircles," X, Inc. encoding EGFP) at a concentration of ~300 μg/μl, 5 μl PBS, and 4 μl 3000 MW tetramethylrhodamine dextran (12.5 mg/ml in PBS, Invitrogen), and filled halfway with 0.9% w/v NaCl. The pipette was mounted on an electrode holder (WPI)/manipulator (Luigs and Neumann), and its tip directed to the three-dimensional center of a glomerulus under two-photon guidance. Current was applied to the pipette using a stimulator (50 V, 30 ms pulses at 2 Hz for 5 min., Grass SD-9 stimulator). The black lead of the stimulator was connected to the animal via an alligator clip on the foot. After electroporation, the bulb was coverslipped and covered in 2% agarose and silicone sealant for protection, and the animal was returned to a clean home cage to recover for 48 hours.

Histological Processing. Mice were sacrificed 2 days after electroporation of plasmid and their brains saved for histological processing. Animals were deeply anaesthetized with 0.3 cc ketamine/xylazine (100 mg/kg / 10 mg/kg, Sigma-Aldrich) and sacrificed by transcardial perfusion with 13 ml PBS, followed by 10 ml 4% paraformaldehyde. After perfusion was complete, the brain was removed and placed in 4% paraformaldehyde for 24-48 hours. A vibtratome was then used to make coronal slices through the olfactory

bulb and piriform cortex (85 μM slices through bulb; 200 μM slices through cortex); these slices were counterstained overnight in 1/1,000 NeuroTrace 435 (Invitrogen) in PBS (Invitrogen) and mounted in Vectashield (Vector Labs) for imaging on a Zeiss 710 confocal microscope (Zeiss).